NORTHWESTERN UNIVERSITY

X-ray Studies of Ion Adsorption at Charged Titania-Electrolyte Interfaces

A DISSERTATION

SUBMITTED TO THE GRADUATE SCHOOL

IN PARTIAL FULFILLMENT OF THE REQUIREMENTS

for the degree

DOCTOR OF PHILOSOPHY

Field of Materials Science and Engineering

By

Vaibhav Kohli

EVANSTON, ILLINOIS

December 2009

ABSTRACT

X-ray Studies of Ion Adsorption at Charged Titania-Electrolyte Interfaces

Vaibhav Kohli

Interaction of counter ions with charged solid-electrolyte interfaces plays an important role in wide ranging chemical and environmental processes including ion adsorption, colloidal stability, and electrokinetic transport. A complete molecular-level characterization of the counter-ion profile near the interface is critical to understanding the interfacial reactivity.

Resonant anomalous X-ray reflectivity (RAXR), and crystal truncation rod (CTR) techniques were used to directly measure the vertical density profiles of Rb^+ and Sr^{2+} at the rutile $TiO_2(110)$-electrolyte interface. These results are the first experimental confirmation of a recent molecular dynamics prediction that the adsorbed ion structure is distributed between multiple inner-sphere sites (i.e., tetra-dentate and bi-dentate) rather than a single site (i.e., tetra-dentate) as thought from previous investigations. Rb^+ and Sr^{2+} are found to be specifically-adsorbed with coverages of 0.080 ± 0.003 and 0.40 ± 0.07 monolayers respectively, and average heights of 3.72 ± 0.03 Å and 3.05 ± 0.16 Å above the interface respectively.

A new generalized model-independent approach was developed for the analysis of long-period x-ray standing waves (XSW) data. The approach is applicable to various reflection geometries, including simple x-ray mirrors, and multi-layers, and is valid for XSW in an attenuating medium. The formalism allows direct extraction of the amplitudes and phases of the elemental structure factor from the measured long-period XSW data, leading to a fully model-independent recovery of the elemental distribution. The method is demonstrated by extracting

the 1D profile of Ti normal to the surface for a $TiO_2/Si/Mo$ tri-layer sample on a Si substrate, using Ti-Kα fluorescence yield measured in *ex situ* and *in situ* environments.

Using long period XSW, X-ray fluorescence (XRF) and X-ray reflectivity (XR), it is shown that titania nanofilms grown by atomic layer deposition (ALD) exhibit significantly enhanced properties for ion adsorption as compared to single crystalline rutile surfaces. This is expressed by a >2-fold higher total ion coverage on the nano-titania surface compared to rutile. The significance of these observations in the context of Electrochemical Capacitors (EC) is discussed. These results demonstrate that use of nanometer thick layers provides an additional degree of control that can be used as a way to fully optimize EC energy storage characteristics.

Approved

_____

Professor Michael J. Bedzyk

Department of Materials Science and Engineering

Northwestern University

Evanston, IL

ACKNOWLEDGEMENTS

TABLE OF CONTENTS

LIST OF FIGURES

LIST OF TABLES

Chapter 1 : Introduction

1.1 Applications of the Charged Solid-Electrolyte Interface

A solid surface can acquire an electric charge when brought in contact with an aqueous solution, resulting either from charging of a functional group present on the surface, or adsorption of ionic species from the solution onto the surface[1, 2]. A surface charge can also arise as a result of an isomorphic replacement in the lattice near the surface (for e.g. substitution of Si^{4+} by Al^{3+} in a silicate lattice)[1].

Interaction of the charged solid-liquid interface with counter ions plays an important role in various environmental and chemical processes including ion adsorption at electrolyte-electrode interfaces, colloidal stability (i.e. the stabilization of the colloidal particles against coagulation that occurs as a result of the electrostatic forces near the charged surface of the particles) and sedimentation, and growth and dissolution of minerals in aqueous environments[1-5].

The above interaction is a key to understanding various electro-kinetic phenomena such as electrophoresis, and electroosmosis[1, 2]. Electrophoresis is the process involving the movement of colloidal particles (having charged surface) relative to a stationary electrolyte, while electroosmosis involves movement of the electrolyte ions relative to a stationary charged surface, both processes occur in presence of an applied electric field (Fig. 1.1 and 1.2). Applications of the above phenomena range from biological separation, for e.g. separation of proteins based on their size and charge differences, to de-watering of soils near a hazardous waste area[2].
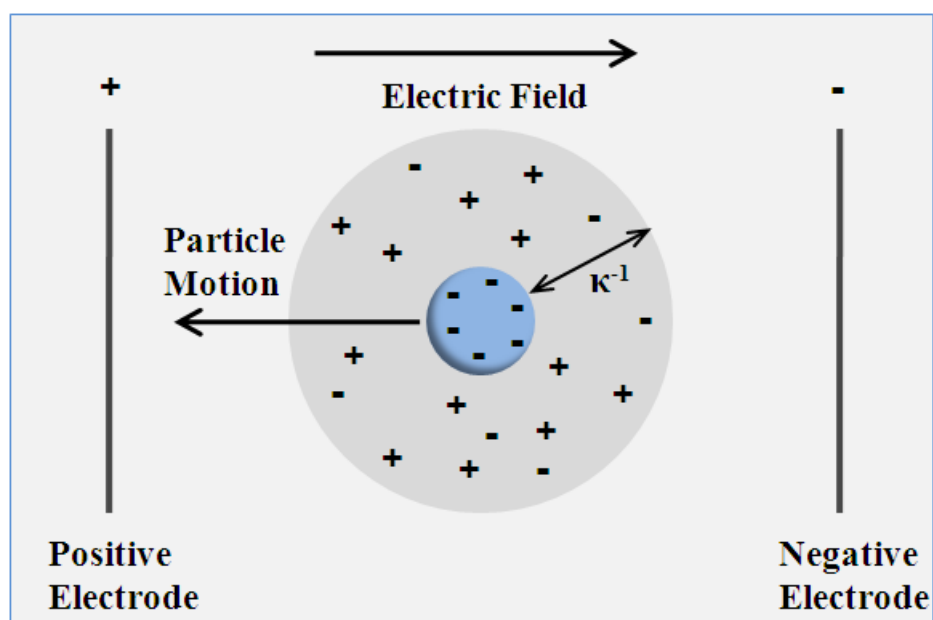
Figure 1.1: Electrophoresis of a charged particle in presence of an applied electric field. A negatively charged particle (blue sphere) in an electrolyte is depicted, with an electrical double layer of width κ^{-1} surrounding the particle. The external electric field pointing to the right causes the particle to drift leftwards.
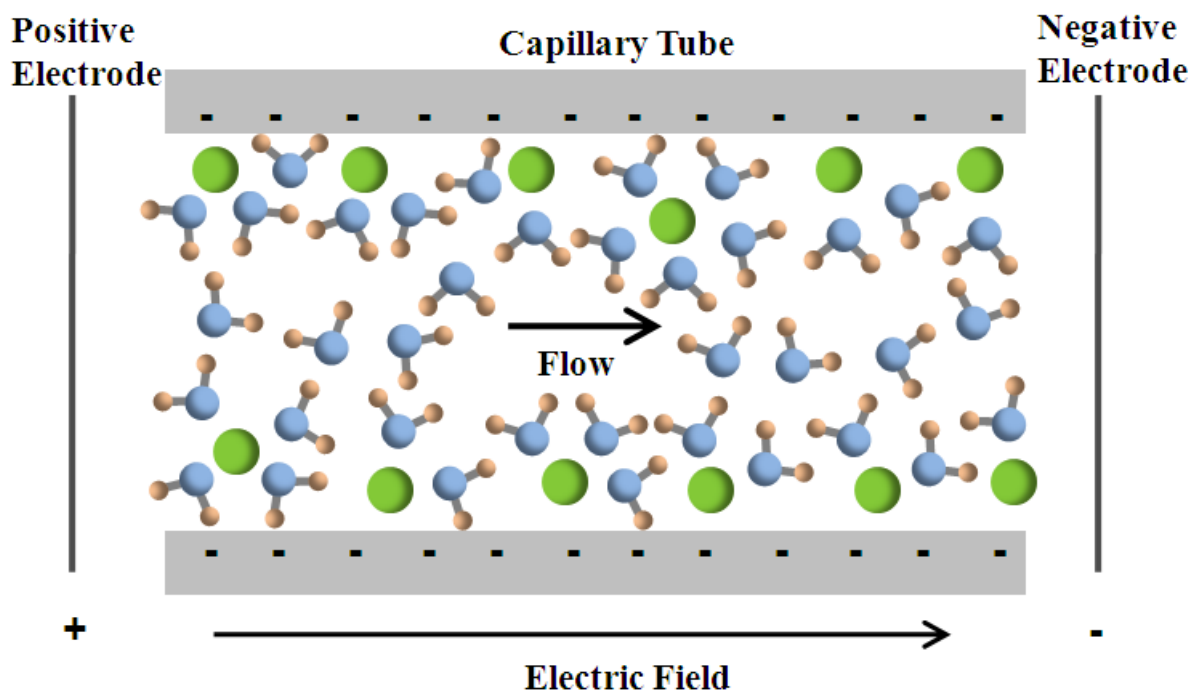
Figure 1.2: Electro-osmosis of an electrolyte in a capillary tube. The negative charge on the inner walls of a capillary leads to segregation of positively charged particles (in the electrolyte) near the walls. When an external electric field is applied, the positively charged particles (green spheres) drift towards the negative electrode, also pushing the solvent particles to move with them. This process plays an important role in fluid flow through micro- or nano-sized capillaries, since it provides an alternative to the use of high pressure gradients to generate the flow.
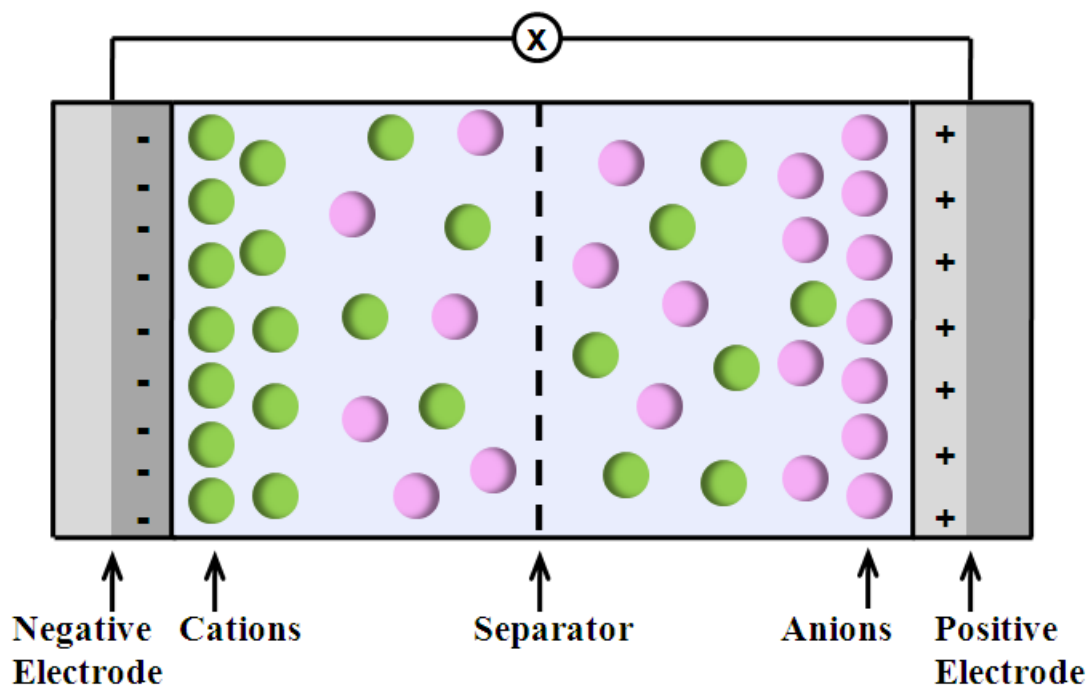
Figure 1.3: Schematic of an electrochemical capacitor (EC). The ECs utilize the charge separation at the electrode-electrolyte interface as the mechanism to store and deliver energy. This is unlike conventional batteries where energy is delivered as a result of a chemical reaction. A single cell EC consists of two electrodes. The cations and anions are attracted to the negative and positive electrodes respectively. The ECs can be classified as electrical double layer type or pseudo-capacitor type, depending on whether the ions are held near the charged interface by simple electrostatic forces, or whether they are adsorbed at the interface, respectively.
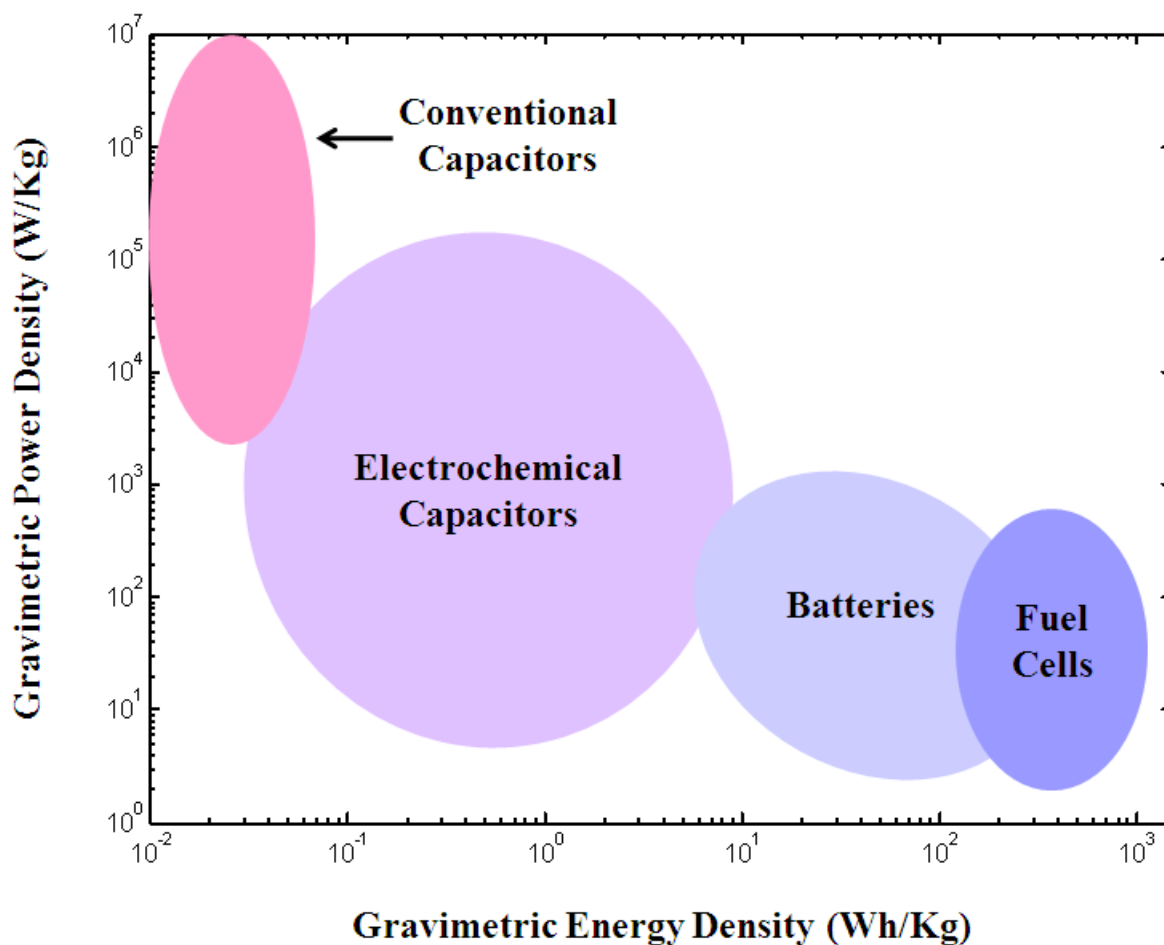
Figure 1.4: Power and Energy densities of various energy storage devices. Electrochemical capacitors (EC) can yield orders of magnitude higher power densities compared to batteries; however, they have much lower energy densities. The ECs fall in between conventional capacitors and batteries (both in terms of energy density and power density) on this Raygon plot.

The understanding of the charged liquid-solid interface is also crucial to the area of micro-fluidics, i.e., fluid flow through micro- or nano-sized channels. The liquid flow through these narrow channels is typically controlled by applying an electric field along the channel (rather than the conventional approach of using a pressure gradient), and the motion of charged electrolyte particles depends on both the applied electric field as well as the net field resulting from the charged interface and the counter-ion distribution[2].

The counter ion interaction with electrolyte-electrode interfaces is the basis of modern energy storage devices, such as electrochemical capacitors (EC, schematic shown in Fig. 1.3)[6-10]. The ECs store energy as a result of the charge separation that occurs at the interface. This is fundamentally different from conventional energy storage, such as batteries, where energy is delivered after certain chemical reactions (such as oxidation of a metallic anode) take place[11]. Since the ion distribution can respond swiftly to changes in potential, the ECs offer much higher rates of charging and discharging, and can deliver orders of magnitude higher power density compared to batteries (Fig. 1.4)[6]. The ECs are also unique due to their high life cycles, unlike batteries where life is limited due to deterioration of the electrode that occurs as part of the charging/discharging which involves structural changes of the electrode. In spite of the several advantages offered by ECs, their applications are currently limited by their energy density which remains lower than that of batteries (Fig 1.4). To gain further insight into the functioning of ECs, it is important to understand the ion-electrode interaction at the nano-scale level.

1.2 A Classic Description of the Ion Distribution

Since the counter ions present in an electrolyte that is in contact with a charged surface are attracted to the surface, it is expected that their distribution near the solid-electrolyte interface will be different from their distribution in the bulk electrolyte. This counter ion distribution is often referred to as the electrical double layer (EDL), so called because the interfacial system can be seen as a double layer of charges where the layer of charge on the surface holds an equal and opposite charge compared to the net charge held by the layer of distributed ions[1, 12].

Various models have been used to describe the distribution of ions near the interface[1, 2, 12-14]. The simplest model is an idealized capacitor model where the ions are considered to be located at a sharp plane above the charged interface (similar to a parallel plate capacitor). This model is however unrealistic, since any thermal motion would diffuse the ion distribution. A classic description of the ion distribution is given by the Poisson-Boltzmann theory[1, 2], where the distribution normal to the surface is controlled by the Boltzmann factor (the exponential in the eqn. below),

$$n_i(z) = n_i(\infty) \, e^{-\frac{v_i \, e \, \psi(z)}{k_B \, T}} \qquad\qquad (1.2.1)$$

Here, $n_i(z)$ and $n_i(\infty)$ denote the concentration of the ith ionic species at a height z above the surface, and at infinite distance from the surface (i.e. in bulk electrolyte), respectively. v_i denotes the valency of the ith ionic species, $\psi(z)$ is the net potential at the position z, T is the temperature in Kelvin, and k_B is the Boltzmann constant. The general description of the potential variation is given by the Poisson equation[1],

$$\frac{d^2\psi}{dz^2} = -\frac{\rho(z)}{\varepsilon} \tag{1.2.2}$$

where, $\rho(z) = \sum_i v_i\, e\, n_i(z)$, is the net charge density at height z, and ε is the permittivity of the solution. Combining eqn. 1.2.1 and 1.2.2 gives the Poisson-Boltzmann equation[1] that describes the variation of potential with height and thus determines the distribution of ions,

$$\frac{d^2\psi}{dz^2} = -\frac{e}{\varepsilon}\sum_i v_i\, n_i(\infty)\, e^{-\frac{v_i\, e\, \psi(z)}{k_B T}} \tag{1.2.3}$$

The above equation is simplified for $v_i\, e\, \psi(z) < k_B T$, where a first order Taylor's expansion can be applied to the exponential term. Since, $\sum_i v_i\, n_i(\infty) = 0$, based on electro-neutrality in the bulk solution, eqn. 1.2.3 can be written as,

$$\frac{d^2\psi}{dz^2} = -\frac{e^2}{\varepsilon k_B T}\sum_i v_i^2\, n_i(\infty)\, \psi(z) \tag{1.2.4}$$

This is called the linearized Poisson-Boltzmann equation, also referred to as the Debye-Huckel theory[1], and has the following solution,

$$\psi(z) = \psi(0)\, e^{-\frac{z}{L_D}} \tag{1.2.5}$$

The above eqn. shows that the potential varies exponentially with height, i.e. follows a diffuse distribution. Here $\psi(0)$ is the potential at the z=0 (or the surface), and L_D denotes the Debye-length, which is given according to,

$$L_D = \left[\frac{e^2}{\varepsilon k_B T}\sum_i v_i^2\, n_i(\infty)\right]^{-2} \tag{1.2.6}$$

The Debye length is a characteristic of the thickness of the diffuse distribution. The above eqn. shows that the diffuse layer thickness simply depends on the ionic strength of the electrolyte $\left(\text{ionic strength equals } \frac{1}{2}\sum_i v_i^2 \, n_i(\infty) \right)$. The diffuse layer thickness therefore decreases with increase in the ion concentration and ion valency.

The Debye-Huckel theory described above is valid only for small potentials (i.e., $v_i \, e \, \psi(z) < k_B \, T$). The more general result is obtained by Gouy-Chapman theory, however the potential variation from this theory no longer has the simple form shown in eqn. 1.2.5. For a symmetric electrolyte (i.e. when both cations and anions have same valence number, v), it can be shown that rather a function of potential, τ $\left(\text{where, } \tau = \dfrac{\exp\left(\frac{v \, e \, \psi(z)}{2 \, k_B \, T}\right) - 1}{\exp\left(\frac{v \, e \, \psi(z)}{2 \, k_B \, T}\right) + 1} \right)$, varies exponentially with height[1]. While the Gouy-Chapman theory (as well as the Debye-Huckel theory) describes the diffuse distribution of ions, it does not take into account any ions adsorbed at the interface. A more realistic picture is described by the Gouy-Chapman-Stern model that includes an additional adsorbed layer of ions (also called the Stern layer), in addition to the Gouy-Chapman distribution.

1.3 Physical Picture of Ion Adsorption

Visualization of the ions near the charged liquid-solid interface can be simplified with the aid of a physical picture, such as the one shown in Fig. 1.5. The ions at the interface can be held either simply by attractive electrostatic forces from the charged surface, or they can be physically or chemically adsorbed at the surface. In this picture of ion adsorption, the ion distribution is
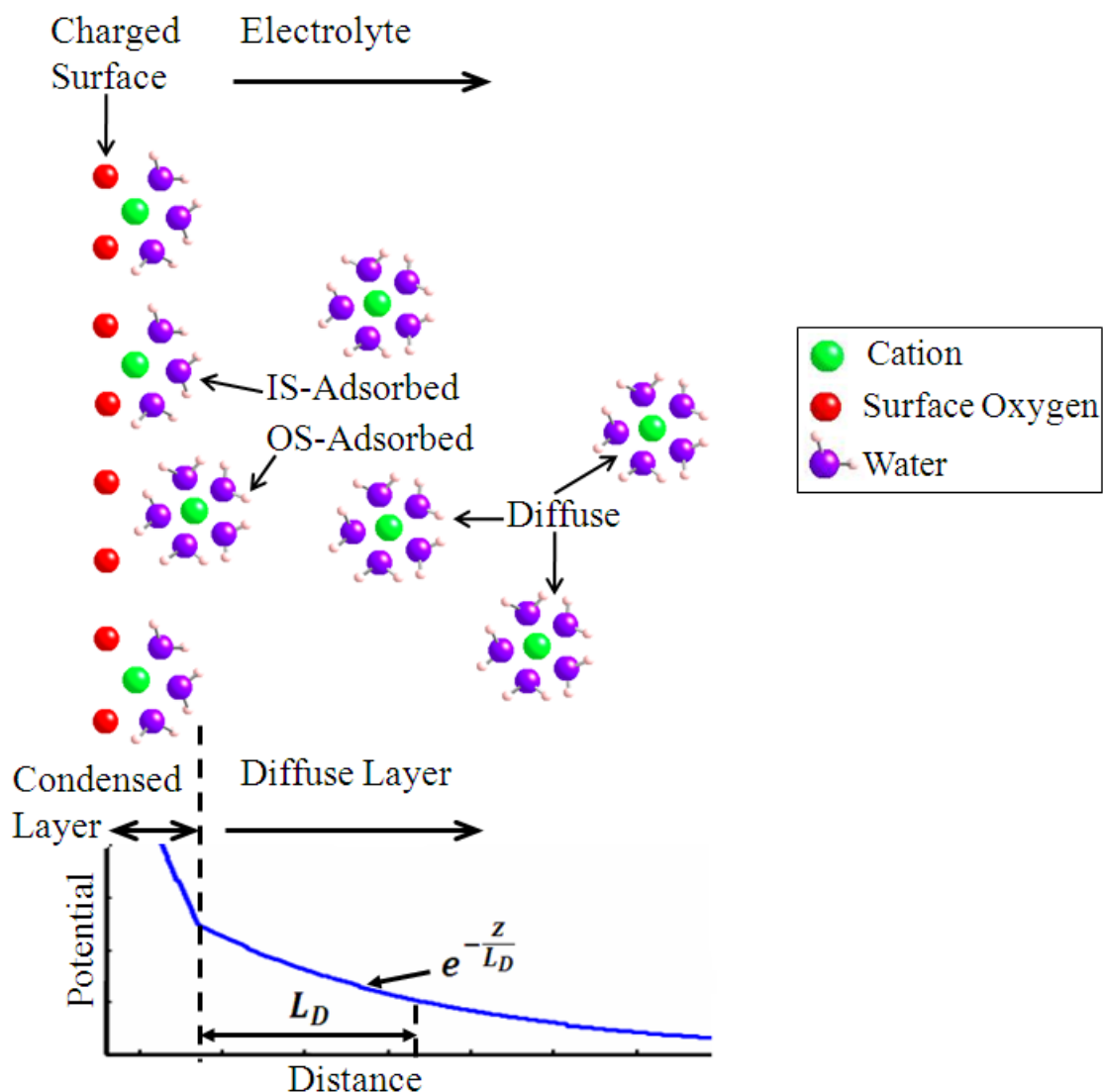
Figure 1.5: A physical picture describing the interaction of ions with charged liquid-solid interface. The ion distribution can be classified into a condensed layer and a diffuse layer, depending on the mechanism of interaction, and the distance from the interface. The condensed ions can either be chemically bonded to the surface (for e.g. to the surface oxygen atoms shown in red above) as inner-sphere (IS) species, or they can form an outer-sphere (OS) complex where they are held to the interface in fully hydrated form as a result of electrostatic and van der Waals forces.

broadly classified into a condensed part referring to the ions adsorbed at the interface, and a diffuse part representing ions that extend further away into the electrolyte[15].

The ions in aqueous environments (for e.g. metal cations like Rb^+ or Na^+) typically exist as hydrated species, where they are bonded to multiple water molecules surrounding them (for e.g., Rb^+ has a hydration number of six at room temperature[16]). As these ions approach the counter-charged interface, they can get adsorbed above the interface, either staying in hydrated form, i.e. as outer-sphere species (OS), or stripped off of their hydration shell and chemisorbed at the surface, i.e. as inner-sphere species (IS)[4].

Each of these ionic species (i.e. IS, OS and diffuse) possesses different characteristics and behaves as a different chemical entity[4]. For example, the OS species are conventionally regarded as less strongly bound to the interface compared to IS species. Therefore the OS species can be more easily displaced by the presence of any background or competing ionic species. Also, the IS species that are bonded to the surface atoms (such as surface oxygens) are thought to typically exist at well defined heights above the surface (corresponding to the possible bonding geometries). On the other hand, the OS species can show a significant distribution width, since they are not directly bonded to the surface atoms, but are only held by electrostatic, or van der Waals forces. Both the IS and OS typically exist within one or two nanometers height above the interface, which is in contrast to the large spread of the diffuse part (which could be up to tens of nanometers)[15].

The different structural characteristics of the above species pose different set of challenges in their measurements. Often, the characterization tool that best suits the measurement

of one species is not helpful in obtaining information about the other. Consequently, current understanding about the ion distribution has resulted from a wide array of theoretical and experimental approaches. X-ray based tools have been on the forefront in terms of direct measurements of the adsorbed ion structure[17-19]. Mineral surfaces have been a natural choice for studying ion adsorption, and various minerals studied include calcite, mica, orthoclase, rutile, quartz, alumina, and hematite[20-29]. These previous efforts have strengthened the physical picture described in this section, by providing evidence for the presence of specifically-adsorbed ions above the interface (i.e. IS species located at a particular site above the inteface). More recently, co-existence of IS and OS species has also been observed on mica, orthoclase, alumina, and hematite surfaces[20, 21, 26]. Efforts in this thesis are directed towards probing the ion distribution at the TiO_2-electrolyte interface, and hence the next section is devoted to providing background about this system.

1.4 Ion Interaction with the TiO_2 – Electrolyte Interface

The applications of TiO_2 are wide ranging, from preservation of ancient statues to potential use in spintronic devices[30]. TiO_2 exists in three crystalline forms, Rutile, Anatase, and Brookite. Out of the three, the rutile form is the most stable phase[30]. Consequently, the previous studies on ion adsorption on TiO_2 have been primarily based on the rutile form. From the perspective of understanding the ion distribution at the aqueous-mineral interfaces, rutile also offers the advantage that it has a simple structure compared to most other minerals. Bulk rutile
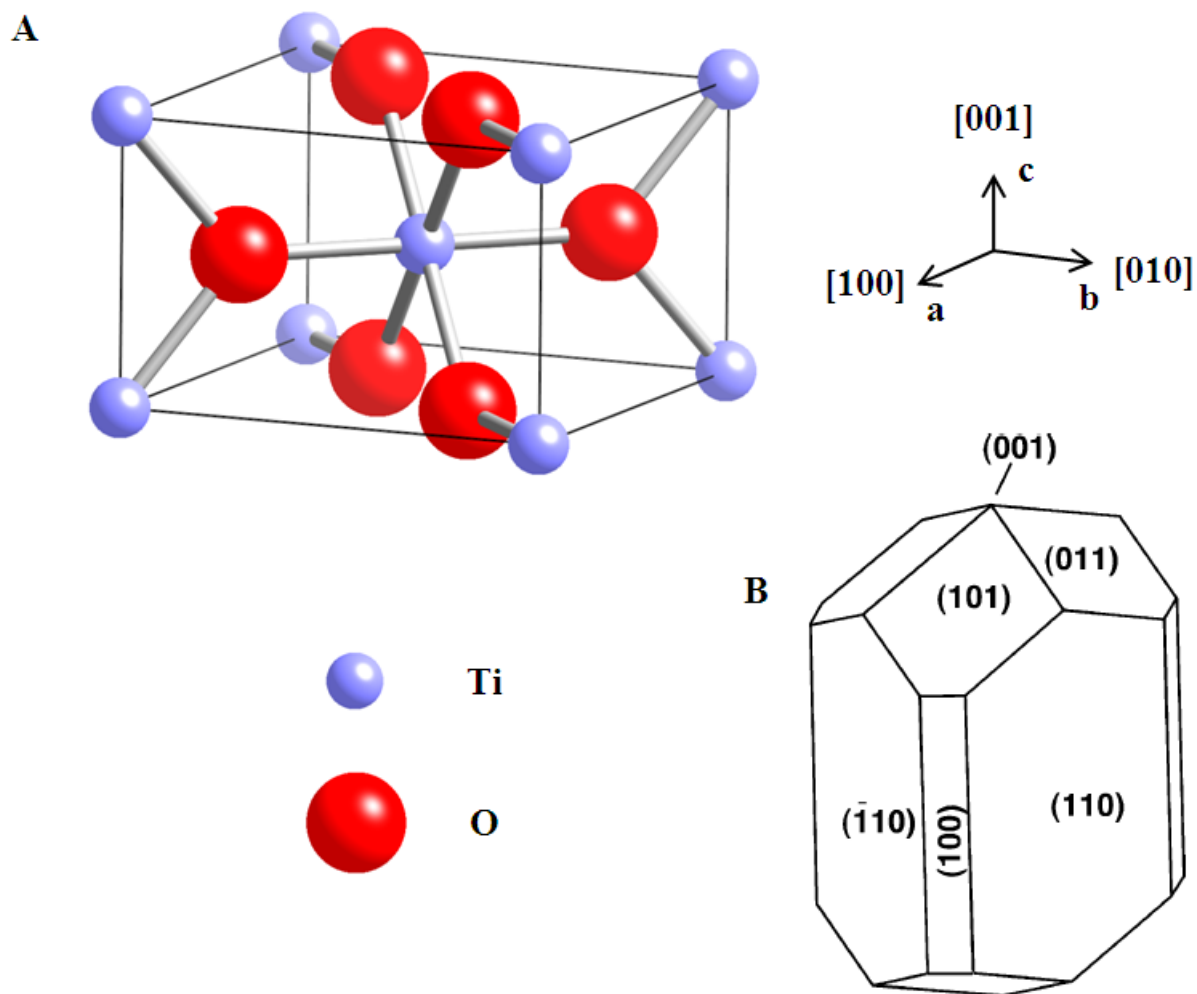
Figure 1.6: Rutile TiO_2 bulk structure, and the most stable surface orientations. (A): The rutile bulk unit cell is a tetragonal structure, with dimensions, a=b=4.594 Å, and c=2.959 Å. (B): The (110) surface the most stable surface of rutile, as indicated by the Wulff-net construction based on calculations of surface energy. The facet that occupies the largest area (i.e., 110) indicates the most stable surface. Figure adapted from Reference [30].

has a tetragonal structure, with a=b=4.594 Å, and c=2.959 Å, where the Ti atoms are octahedrally (six-fold) coordinated with the O atoms (Fig. 1.6)[31].

The (110) surface of rutile is the most stable surface based on the Wulff construction (Fig. 1.6)[30, 32]. In vacuum, this surface is known to be terminated with a row of bridging oxygens (BO) protruding from the surface, which are attached to two Ti atoms on the surface plane. The surface also has a row of Ti atoms with a five-fold coordination (under-coordinated). When in contact with an aqueous environment, the six-fold coordination of these Ti are restored due to water (or hydroxyl) adsorption, giving rise to another row of protruding oxygens, called the terminal oxygens, or TO (Fig. 1.7). The rutile (110) surface is preferred for ion adsorption studies, because of its surface charging mechanism (discussed below) that allows an easy control of surface charge simply by changing electrolyte conditions.

Two models have been typically used to describe the charging behavior on the rutile (110) surface: the non-hydroxylated and the hydroxylated surface model[33]. Under the neutral charge conditions, the non-hydroxylated surface is described as the surface where none of the BO sites are hydroxylated, and the terminal oxygen exist as $TiOH_2$ species from the adsorption of a water molecule above the five-fold coordinated Ti. In this case, the surface charge arises from de-protonation of the $TiOH_2$ sites as the solution pH is increased. The neutral hydroxylated surface on the other hand is described as resulting from dissociative adsorption of water with the hydroxyl group adsorbing onto the five-fold coordinated Ti and the proton bonding to the BO sites, resulting in $TiOH^-$ and BOH^+ species. In this case, the surface charge arises from the de-protonation of the bridiging hydroxyl sites. Both the models agree in that the mechanism of surface charging on the rutile (110) surface is the protonation and deprotonation of the surface
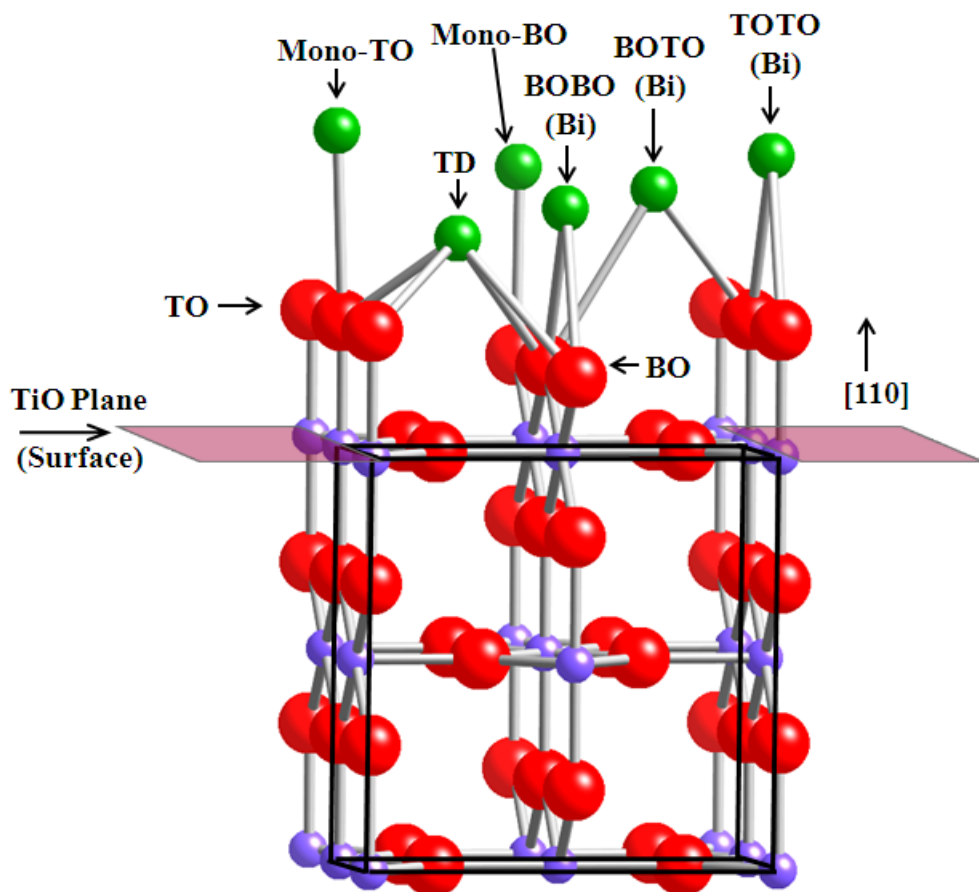
Figure 1.7: Schematic of the (110) surface of rutile TiO_2. Two rows of surface oxygens are present on the surface (when in contact with an aqueous electrolyte), the bridging (BO) and the terminal (TO) oxygens. The unrelaxed Ti-O plane is referred to as the surface plane. The tetragonal surface unit cell boundaries are highlighted by black lines. Six possible sites for inner-sphere adsorption on the surface are shown, these include a tetra-dentate site (TD), three bi-dentate sites (BOBO, BOTO, and TOTO), and two mono-dentate sites (Mono-BO and Mono-TO).

oxygens (BO or TO). The surface charge can therefore be controlled simply by changing the solution pH, and this serves as an advantage in studying the rutile surface.

Rutile has a point of zero *net proton charge* of pH 5-6, as observed by previous powder titration measurements[23, 34]. The surface is negatively charge in contact with aqueous solutions with pH higher than this limit, with an increase in the net negative charge with increasing pH. This makes it attractive to study *cation* adsorption on rutile, since the cations are naturally (electrostatically) attracted to the surface (and may also be adsorbed above the surface attached to the surface oxygens). Various cations that have been probed previously on the rutile surface include Rb^+, Na^+, Sr^{2+}, Ca^{2+}, Zn^{2+} and Y^{3+}. Previous studies on ion adsorption at the rutile-electrolyte interface[29, 35-42] have involved both theoretical tools, such as molecular dynamics (MD) simulations[38], density functional theory (DFT) calculations[23, 43], and surface complexation models[35, 36, 42, 44-50], as well as experimental tools, such as x-ray reflectivity (XR)[25], x-ray standing waves (XSW)[22, 23], x-ray absorption spectroscopy (such as XAFS)[51, 52], and powder titrations[23, 34, 53-55].

There are six possible sites of inner-sphere adsorption on the rutile surface (Fig. 1.7)[25]. These include a tetra-dentate site, where the adsorbed ion is bonded to four surface oxygens (two BOs and two TOs), three bi-dentate sites, where the ion is bonded to two surface oxygens (BOBO, TOTO, and BOTO), and two mono-dentate sites, where the ion is bonded to only one surface oxygen, either the BO or the TO. Each of these sites differ in terms of the vertical distance from the surface, which makes it possible to distinguish between them and predict the actual adsorption site even if only the one-dimensional interfacial structure normal to the surface is known.

Previous XR and XSW studies revealed that various cations, including Rb^+, Sr^{2+}, and Y^{3+} adsorb as single inner-sphere species, occupying the tetra-dentate site[22, 23, 25]. The above three cations were located at heights of 3.44 ± 0.03 Å, 3.07 ± 0.07 Å, and 2.75 ± 0.07 Å above the surface respectively. The behavior of Zn^{2+} was however exceptional, and it was found to be adsorbing in two distinct inner-sphere sites, a mono-dentate site (above the BO site), and a bi-dentate site (TOTO), based on the XSW measurements. Molecular dynamics (MD) simulations showed reasonable agreement with the experimental results, confirming the tetra-dentate site to be the primary adsorption site for most cations. In the case of Zn^{2+} however there were significant discrepancies between the x-ray and the simulations[23], although these were later resolved[24]. More recent MD simulations have raised numerous questions (discussed in next section) about the conventional picture of ion adsorption, and shown that the double layer structure on the rutile surface is yet to be fully understood.

1.5 Unanswered Questions

Recent molecular dynamics (MD) simulations[56] of ion adsorption at the rutile-electrolyte interface have shown that in addition to the primary adsorption tetra-dentate site, there are also additional bi-dentate sites that form a significant fraction of various adsorbed cations, including Rb^+, Na^+, Sr^{2+}, and Ca^{2+}. These bi-dentate sites were not seen with previous experimental XR and XSW studies. This recent prediction has raised an important question about the ion distribution on the rutile surface: whether the condensed ions are occupying a single

inner-sphere (IS) site, as thought previously, or is the adsorption structure more distributed (i.e. multiple IS sites)?

The MD simulations have also predicted that only a small fraction of the adsorbed cations (<10%) are adsorbed as outer-sphere (OS) species on rutile[56]. Recent cation adsorption studies at the mica-electrolyte interface using resonant anomalous x-ray reflectivity (RAXR) found that a significant proportion (>50%) of the divalent cations (Sr^{2+}) adsorb as outer-sphere (OS) species on mica[20]. Similar OS species have also been recently detected on other mineral surfaces[21, 26]. Previous XSW measurements on rutile showed that the Sr^{2+} distribution is largely unaffected by the presence of background electrolyte, thereby suggesting the absence of OS species[22]. However, the presence of a weakly bound OS species on the surface may not be visible to the XSW measurements. Therefore further measurements are needed to ascertain whether there are any OS adsorbed species on rutile or if all the condensed ions are bound only as IS species.

The structural measurement of the diffuse part of the electrical double layer has remained a challenge, although the evidence of the presence of this part has existed since long ago[15] (the details about the difficulty in measuring the diffuse part are discussed in Chapter 5, for e.g. see Fig. 5.4). The only previous measurements of the diffuse part have been the demonstration by Bedzyk et al.[19], and later by Wang et al.[57]. Knowing what fraction of the total ions are present in the diffuse part vs. the condensed part, and understanding the factors that could affect this distribution is an important factor in several applications of the double layer phenomenon. In particular, this is especially important in electrochemical capacitors (EC) since numerous efforts have been aimed at increasing the energy density of ECs, and the diffuse ions are detrimental to

the energy density as they are located at further distances from the interface[58]. This thesis addresses the issues highlighted above, and aims to further the understanding of the ion distribution at liquid-solid interfaces. The next section gives a synopsis of the work presented ahead in the thesis.

1.6 Overview of this Thesis

A background of the various experimental techniques used in this study, namely, crystal truncation rod (CTR), resonant anomalous x-ray reflectivity (RAXR), multi-layer x-ray reflectivity (ML-XR), and multi-layer x-ray standing waves (ML-XSW), is provided in Chapter 2. This chapter also describes the typical experimental setup used during the measurements reported in the thesis.

Chapter 3 reports the vertical distribution of cations (Rb^+ and Sr^{2+}) at the rutile TiO_2-electrolyte interface as measured using CTR and RAXR, at dilute ion concentrations. The effect of a background electrolyte (Na^+) on the Sr^{2+} distribution is also investigated in this chapter (as an indirect probe of any outer-sphere species, in addition to the direct probe by measuring the ion structure using RAXR). Comparison between the observed results and the previous theoretical predictions aims to bring a better understanding of the ion adsorption at the rutile-aqueous interface.

A new model-independent way of long period XSW analysis is reported in Chapter 4. This formalism is derived for XSW in an absorbing medium, for the case of a specular reflection. The applicability of this formalism extends to various reflection geometries including simple x-

ray mirrors, and multi-layers. The formalism is demonstrated by extracting the 1-D profile of Ti normal to the surface for a TiO_2/Si/Mo tri-layer on a Si substrate using the Ti-Kα fluorescence yield measured in air and under an aqueous electrolyte.

In Chapter 5, the adsorption behavior of a nano-film of titania is investigated with relevance to applications in electrochemical capacitors (EC). Ion coverages and distribution observed on the nanofilm using x-ray fluorescence (XRF) and long period XSW are used (in conjunction with the results of surface titrations and predictions of a multi-site complexation model) to highlight how the novel characteristics shown by the nanofilm compared to rutile TiO_2 can be attractive for ECs.

The ongoing and future work relevant to this thesis is mentioned in Chapter 6, separated in two segments. The first segment describes the XR and XSW measurements conducted on a Si/Mo periodic multi-layer (PML). Results concerning the characterization of the multi-layer structure, as well as measurements of ion (Rb^+) fluorescence yields under different electrolyte conditions are reported. Future challenges with this project are also highlighted. The second segment of this chapter presents the feasibility of using a cavity-array structure to measure the diffuse part of ion distribution. It demonstrates through simulations that model-independent reconstruction of the diffuse ion profile inside the cavities is possible using resonant and non-resonant x-ray reflectivity. A summary of the thesis work is presented in the final chapter (Chapter 7).

Chapter 2 : Experimental Techniques and Setup

2.1 Crystal Truncation Rod (CTR) X-ray Reflectivity

2.1.1 Basics of Surface X-ray Diffraction

In the limit of weak scattering, or the kinematical approximation, the amplitude (complex) of x-rays scattered from a system, is proportional to the so called *structure factor* of the electron density distribution, $\rho(\boldsymbol{r})$, within the system[59-61]. The structure factor, $F(\boldsymbol{Q})$, which is the Fourier transform of $\rho(\boldsymbol{r})$, is given by,

$$F(\boldsymbol{Q}) = \int \rho(\boldsymbol{r})\, e^{i\,\boldsymbol{Q}.\boldsymbol{r}}\, d\boldsymbol{r} \qquad\qquad (2.1.1)$$

Here $\boldsymbol{r}$ denotes the position vector, and, $\boldsymbol{Q} = \boldsymbol{k_R} - \boldsymbol{k_I}$, is the wave-vector transfer (or the momentum transfer), where $\boldsymbol{k_I}$ and $\boldsymbol{k_R}$ are the incident and reflected wave-vectors respectively. In vacuum, the magnitude of the wave-vector is given by, $k = 2\pi/\lambda$, where λ is the x-ray wavelength.

The condition of diffraction from a crystalline lattice is given by the constructive interference of the waves scattered from different scatterers (atoms) within the lattice. In general, this condition is given by the Laue equation, which state that in a diffraction experiment, a maxima in the scattered intensity is obtained whenever the wave-vector transfer Q becomes equal (in orientation and magnitude) to a reciprocal lattice vector[61, 62]. In case of a 3D infinite lattice, scattering is therefore confined to delta functions in reciprocal space, centered at, $\boldsymbol{Q} = H\,\boldsymbol{a}^* + K\,\boldsymbol{b}^* + L\,\boldsymbol{c}^*$, where $\boldsymbol{a}^*$, $\boldsymbol{b}^*$, and $\boldsymbol{c}^*$ are the reciprocal lattice vectors corresponding to

the primitive vectors of the real space (a, b, and c), and H, K and L are integers. The reciprocal

lattice vector a^* is defined as having an orientation along $b \times c$ (cross product), and a magnitude

given by $a^*.a = 2\pi$ (dot product)[62]. For a lattice with the primitive vectors normal to each

other, $a^* = 2\pi/a$.

For a crystal with a surface (i.e., a finite size in one direction, e.g. a cleaved crystal),

scattering is no longer confined only to the delta functions mentioned above for the case of 3D

infinite lattice. Rather, rods of intensities are produced (in reciprocal space) which are

perpendicular to the surface and run through the Bragg peaks. These are called the crystal

truncation rods or CTR[59]. This can be explained in terms of the structure factor, by writing the

electron density distribution, $\rho(r)$, for a lattice which is truncated along the Z direction, as

$\rho(r) = \rho(r)^{3D} \, s(z)$, where $\rho(r)^{3D}$ is the density distribution for the 3D infinite lattice, and $s(z)$

is a step function centered at the surface. The structure factor can now be written as, $F(Q) =$

$FT\,[\rho(r)^{3D}] \otimes FT[s(z)]$, following the convolution theorem, where FT denotes Fourier

transform, and $\otimes$ is the convolution operator[60, 61]. While FT of $\rho(r)^{3D}$ is a series of delta

functions centered at the Bragg peaks (e.g. $Q_z = L\,2\pi/a$), the FT of $s(z)$ is proportional to

$1/iQ_z$, where Q_z is the Z component of the wave-vector transfer. The convolution of the FT of

these two functions leads to a non-zero intensity even away from the Bragg peaks. While the

intensity is still maximum at the Bragg peaks, it varies as $1/Q_z^2$ away from the peaks reaching

minimum value half-way between two Bragg peaks, at the so called anti-Bragg points (e.g.

$Q_z = L\,\pi/a$, for odd integer L). The shape of the CTR, particularly away from the Bragg peaks,

is very surface sensitive, and this makes CTR a valuable tool in studying the surface structure
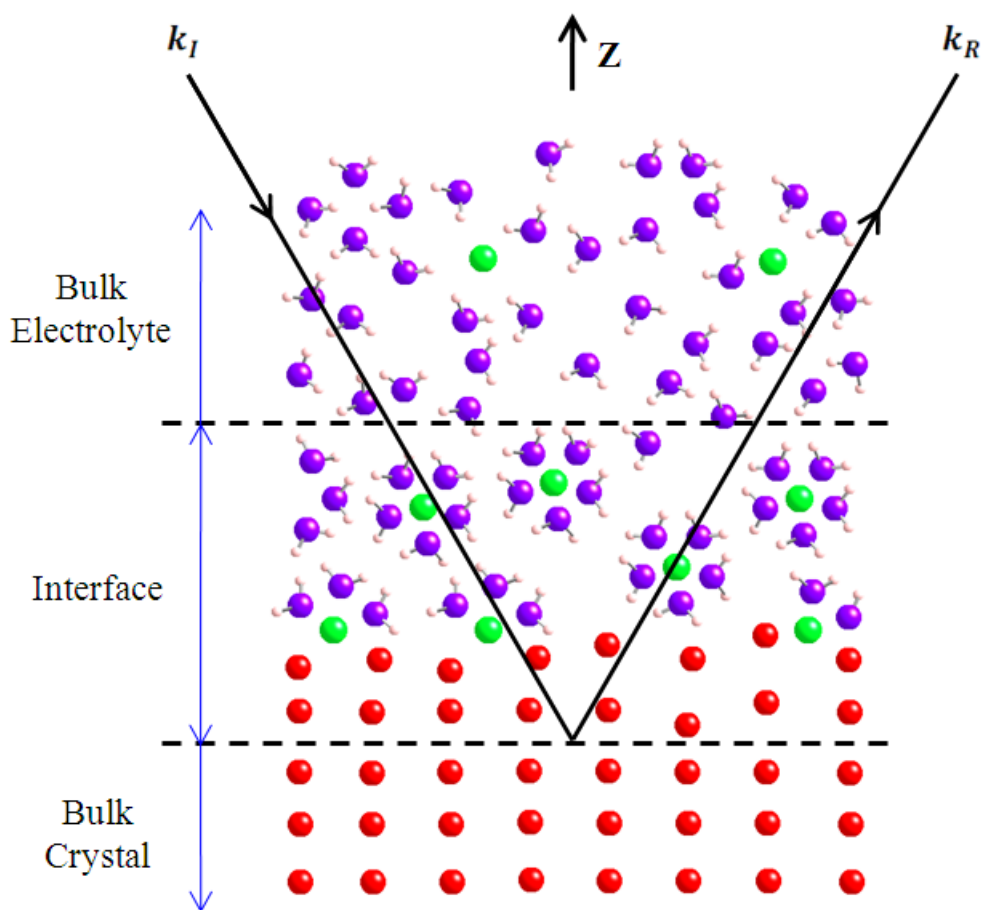
Figure 2.1: X-ray reflectivity to probe the structure near a crystal-electrolyte interface. The interfacial region that can extend over a few nanometers in height includes relaxations and reconstructions of the crystal surface, as well as the ordering of the fluid due to adsorption of water or ionic species near the surface. The x-ray reflectivity analysis can be simplified by separating the system into the bulk region, i.e., bulk crystal and bulk electrolyte, and the interfacial region whose structure is to be determined, as described previously(Reference[17]).

(such as termination, and relaxations), adsorbates on the surface, and also the interfacial structure when this surface is in contact with another medium, such as an electrolyte (Figs. 2.1 and 2.2).

2.1.2 Probing the Crystal-Electrolyte Interface

Of particular interest is the crystal-electrolyte interfacial system, such as a mineral-water interface (Fig. 2.1). In this case the total structure factor of the system F_T can be divided into the following components, as described previously[17, 18],

$$F_T(Q) = F_{Bulk-crystal}(Q) + F_{Interface}(Q) + F_{Bulk-electrolyte}(Q) \qquad (2.1.2)$$

Here $F_{Bulk-crystal}$ denotes the structure factor of the semi-infinite bulk crystal, $F_{Bulk-electrolyte}$ is the structure factor of the semi-infinite bulk electrolyte layer, and $F_{Interface}$ is the structure factor of the interfacial region corresponding to the relaxed unit cells near the crystal surface, and any adsorbate species, such as adsorbed water or ion layers (Fig. 2.2). In the above eqn. the squared total structure factor (i.e., $|F_T(Q)|^2$) can be obtained from the measured CTR data (as described in section 2.1.3), and the interfacial structure can then be obtained by comparing the measured $|F_T(Q)|^2$ with model calculated values.

The structure factor of the bulk crystal is calculated using the relation, $F_{Bulk-crystal} = F_{UC} F_{CTR}$, which is based on the fact that the truncated crystal can be represented as a semi-infinite array of a repeating unit cell. Here F_{UC} is the structure factor of the unit cell, and F_{CTR} is the CTR-form factor[17]. For the case of specular scattering, Q is oriented along the Z direction, and F_{CTR} is given simply by, $F_{CTR} = \frac{1}{1-e^{-iQc}}$, where c denotes the lattice spacing of the crystal in

A

$$F_{NR}(Q) = \int \rho_T(z)\, e^{i\,Qz}\, dz$$

B
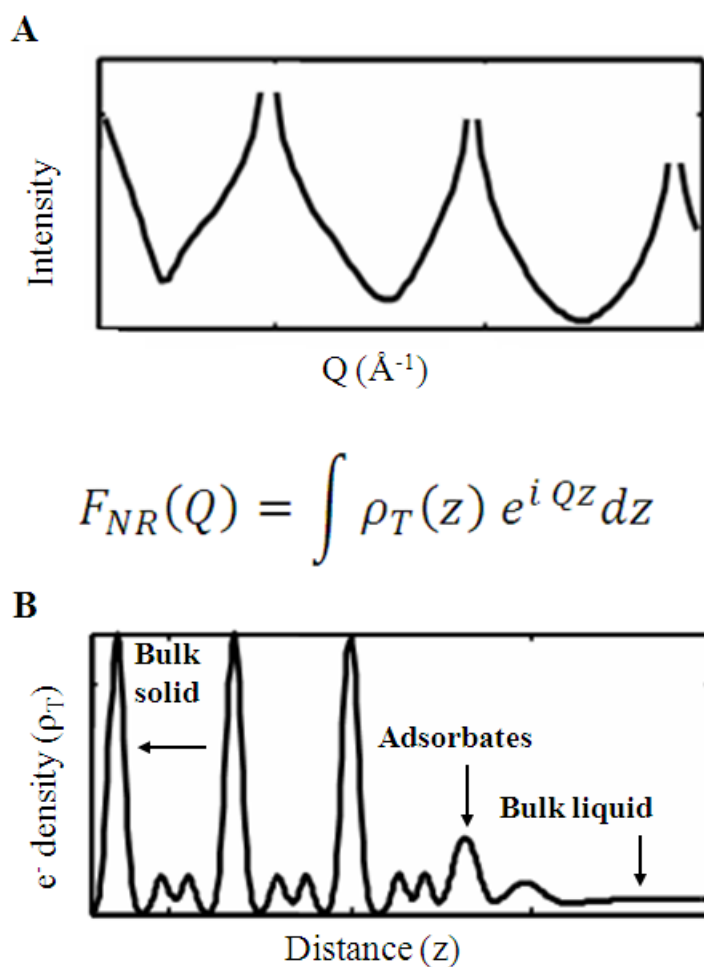
Figure 2.2: Crystal truncation rod (CTR) measurement and interfacial structure. The specular CTR measurement involves recording the surface scattered intensities as a function of 1-D momentum transfer, Q (shown in A). For a non-resonant measurement, the incident x-ray energy is far away from the absorption edge of all the elements in the system. The measured reflectivity is proportional to the squared structure factor (referred to as the F_{NR}, or non-resonant structure factor), which is the Fourier transform of the vertical electron density distribution (ρ_T) within the system (shown in B).

the Z direction[17]. The unit cell structure factor is given by, $F_{UC} = \sum_j \theta_j \, e^{-\frac{1}{2}Q^2 u_j^2} \, e^{i Q z_j}$, where θ, u and z denote the occupancy, vibrational amplitude, and position respectively of an atom in the unit cell, and the summation is over all the atoms in the unit cell. $F_{Interface}$ is calculated in the same way (i.e., the same expression described above for F_{UC}), except only the near-surface region that is expected to relax is included in the summation, for e.g., one or two unit cells below the interface. $F_{Interface}$ also includes the contribution from adsorbed water, and any adsorbed ion layers. The structure factor of bulk electrolyte layer, $F_{Bulk-electrolyte}$, can be calculated either using a featureless model (i.e., an error-function), or using a layered fluid model as described previously[18].

2.1.3 Obtaining Structural Information from Measured Data

The first step in obtaining structural information from the measured CTR data is to obtain the net scattered intensity (i.e., the total integrated intensity minus any background that could be due to sources such as diffuse scattering) of the scattered x-rays corresponding to a reflection condition Q. This can be obtained using a 2D detector, such as a CCD detector[63] (the integrated intensity can also be obtained with a point detector by measuring a rocking scan around any reflection condition, Q, where the sample is rotated around the reflection condition, while the detector is held fixed). The procedures for obtaining integrated and background subtracted scattered intensities using a CCD detector have been described in detail previously[63].

The second step involves converting the net scattered intensity into absolute reflectivity (R_{abs}) of the crystal-aqueous system. The net scattered intensity should be normalized by

extrinsic transmission factors corresponding to transmission of x-rays through any filters used during the experiment and through the path traversed by x-rays in air before reaching the detector, to obtain the *intrinsic* scattered intensity. The reflectivity is then obtained by normalizing the *intrinsic* scattered intensity by the incident flux which can be measured using an ion chamber placed upstream of the sample during the measurements. The measured ion chamber signal in counts/second should be converted to x-ray photons/second in order to calculate the reflectivity in absolute units.

The third step involves obtaining the squared intrinsic total structure factor, $F_T(Q)$, of the crystal-electrolyte interface from the measured absolute reflectivity. This can be done using the relation below[17],

$$|F_T(Q)|^2 = \frac{R_{abs}}{\left(\frac{4\pi \, r_e}{Q \, A_{uc}}\right)^2 T_{cell}(Q) \, |B(Q)|^2} \tag{2.1.3}$$

Here r_e = 2.818 x 10^{-5} Å is the classical electron radius, and $T_{cell}(Q)$ is the transmission of x-rays through the sample cell (i.e. the bulk electrolyte film above the sample surface, as well as the plastic film, e.g. Kapton, used to enclose the electrolyte, in the thin-film sample cell arrangement). The factor $|B(Q)|^2$ denotes the reduction in reflectivity due to the roughness on the crystal surface. The surface roughness can be modeled as a β-factor described previously (where the nth partially occupied layer above the ideally flat surface has an occupancy of β^n)[64]. For the β-factor roughness model, $|B(Q)|^2$ is equal to $\frac{(1-\beta)^2}{1+\beta^2-2\beta \cos (Qc)}$, where c is the spacing between the partially occupied layers[64]. Once $|F_T(Q)|^2$ is known (using eqn. 2.1.3), the interfacial structure can be obtained using a model-dependent analysis using eqn. 2.1.2.

Further details about the model-dependent analysis of the CTR data are provided in Chapter 4, where the technique is applied to the rutile TiO_2-electrolyte interface.

2.2 Resonant Anomalous X-ray Reflectivity (RAXR)

2.2.1 Brief Introduction

Resonant anomalous x-ray reflectivity or RAXR makes use of the energy dependence of the atomic scattering factor at x-ray energies near the absorption edge of the element of interest to specifically probe elemental distribution[27, 65]. In an RAXR experiment, the reflectivity of the sample is measured as a function of incident x-ray energy in the vicinity of the absorption edge of the element to be probed, at a fixed wave-vector transfer (Q_0). Such spectra are collected at a series of Q_0 values, in order to enable a direct imaging of the elemental profile. Unlike conventional scattering methods, where the only information that is measured at different Q values is the modulus squared of the structure factor (reflectivity), the RAXR technique includes also the phase information in the energy spectra. When the total electron density profile is known (from separately measured reflectivity vs. Q, measured at incident energy far away from the absorption edge of the element), the RAXR enables direct retrieval of the amplitude and phase of the structure factor of the resonant species. Fourier inversion of these amplitudes and phases corresponding to the different Q_0, gives the structure of the resonant species[65].

A

B

C

D

RAXR spectrum   total structure   resonant atom's   resonant atom
                                            spectroscopy   distribution

$$I(Q_o, E) = |\; F_{NR}(Q) \;+\; (f_R'(E) + i\, f_R''(E)) \times \mathcal{F}(Q)\,|^2$$
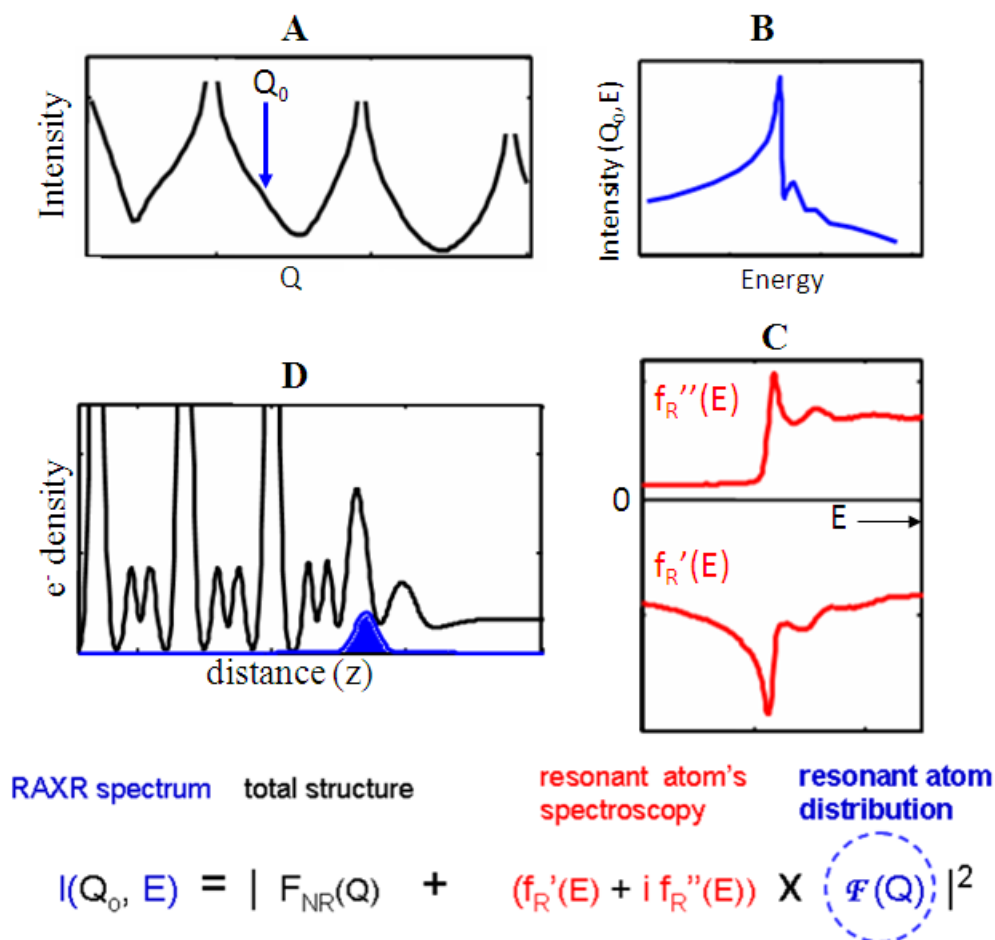
Figure 2.3: Resonant anomalous x-ray reflectivity (RAXR) technique to measure the distribution of a specific element at the liquid-solid interfaces. The non-resonant crystal truncation rod (CTR) measurement yields the total electron density variation (black line in D), following a conventional model based analysis. The RAXR measurements (shown in B) that involve recording scattered intensities as function of incident x-ray energy at a fixed $Q=Q_0$ (and the knowledge of element's anomalous dispersion terms shown in C) reveal information about the specific structure of the element of interest (blue distribution in D).

2.2.2 Fundamentals of RAXR

The form factor of an atom, $f^0(Q)$, is simply the Fourier transform of the electron density distribution within the atom, and is a function of the scattering angle (or the wave-vector transfer, Q). The precise x-ray scattering amplitude of the atom, however, includes the effect of absorption of x-rays as they pass through the atom, and the fact that electrons are not free but rather bound to the atom. These effects are particularly important near the absorption edge, and can be included as energy dependent corrections (also known as anomalous dispersion terms) to the atomic scattering factor, $f(Q, E)$[60],

$$f(Q, E) = f^0(Q) + f'(E) + if''(E)$$
(2.2.1)

Here $f'(E)$ and $f''(E)$ are the energy dependent corrections to the real and imaginary part of the atomic scattering factor respectively (the Q-dependence of these terms is typically negligible), and $f^0(Q)$ is the scattering factor when the anomalous terms are negligible (i.e., at energies far away from the absorption edge).

The reflectivity of a system (such as an oxide-electrolyte interface) is proportional to the square of the total structure factor of the system. When the incident x-ray energy is far away from the absorption edge of all the elements in the system, the dispersion terms (f' and f'') are negligible, and the total structure factor of the system, also called the non-resonant structure factor, $F_{NR}(Q)$, can be written as[65],

$$F_{NR}(Q) = \sum_j \theta_j f_j^0(Q) \, e^{i \, Q \, z_j} \, e^{-\frac{1}{2}\sigma_j^2 Q^2} = A_{NR}(Q) \, e^{i \, \Phi_{NR}}$$
(2.2.2)

Here θ_j, and σ_j denote respectively the occupancy and width (*rms*) of the jth atom with form factor $f_j^0(Q)$, and located at position z_j. The summation is over all the atoms in the system (i.e. not just the element of interest). A_{NR} and Φ_{NR} denote the amplitude and phase of the non-resonant structure factor respectively.

At the incident x-ray energies close to the absorption edge of any specie in the system, however, the dispersion corrections f' and f'' of that specie must be included in its atomic form factor, and the total structure factor in this case if given by[65],

$$F(Q,E) = \sum_j \theta_j\, f_j(Q,E)\, e^{i\,Q\,z_j}\, e^{-\frac{1}{2}\sigma_j^2\,Q^2} \tag{2.2.3}$$

Here $f_j(Q,E)$ is the atomic scattering factor described in eqn. 2.2.1, and includes the anomalous dispersion terms. The above expression for $F(Q,E)$ can be separated into the non-resonant and the resonant components[65],

$$F(Q,E) = \sum_j \theta_j\, f_j^0(Q)\, e^{i\,Q\,z_j}\, e^{-\frac{1}{2}\sigma_j^2\,Q^2} + \sum_k \theta_k\, \left[f_k'(E) + i f_k''(E)\right] e^{i\,Q\,z_k}\, e^{-\frac{1}{2}\sigma_k^2\,Q^2}$$

$$= F_{NR}(Q) + F_R(Q,E) \tag{2.2.4}$$

Here $F_R(Q,E)$ is the structure factor of the resonant species. Notice that the summation k is only over the resonant atoms, while the summation j is over all the species in the system. If the x-ray energy is such that the anomalous dispersion of only one kind of species is significant, the resonant structure factor can be written as[65],

$$F_R(Q,E) = [f'(E) + if''(E)] \sum_k \theta_k \, e^{i\,Q\,z_k} \, e^{-\frac{1}{2}\sigma_k^2\,Q^2} = [f'(E) + if''(E)] \, A_R(Q) \, e^{i\,\Phi_R} \quad (2.2.5)$$

Here A_R and Φ_R denote the amplitude and phase respectively of the structure factor corresponding to the distribution of the resonant element.

Since in an RAXR experiment, the energy spectra (i.e. reflectivity vs. energy) is measured at a fixed Q, we denote it by Q_0 (Fig. 2.3). The measured RAXR intensity which is proportional to the magnitude squared of $F(Q_0, E)$, can be normalized to the intrinsic non-resonant reflectivity to obtain[65],

$$\left| \frac{F(Q_0,E)}{F_{NR}(Q_0)} \right|^2 = 1 + |f'(E) + if''(E)|^2 \left[\frac{A_R(Q_0)}{A_{NR}(Q_0)} \right]^2$$

$$+ 2 \left[f'(E) \frac{A_R(Q_0)}{A_{NR}(Q_0)} \right] \cos[\Phi_{NR}(Q_0) - \Phi_R(Q_0)]$$

$$+ 2 \left[f''(E) \frac{A_R(Q_0)}{A_{NR}(Q_0)} \right] \sin[\Phi_{NR}(Q_0) - \Phi_R(Q_0)] \qquad (2.2.6)$$

The above equation gives insight into the fact that the shape of the measured RAXR spectra is sensitive to the phase difference $\Phi_{NR}(Q_0) - \Phi_R(Q_0)$, and it therefore depends on the resonant atom location for a known $\Phi_{NR}(Q_0)$.[65]. The magnitude of the modulation in the RAXR spectra, on the other hand depends on the relative size of $A_R(Q_0)$ with respect to $A_{NR}(Q_0)$, and therefore depends on the coherent coverage of the resonant element distribution at any Q_0 (i.e., it depends on the total elemental coverage and the distribution width)[65].

2.2.3 Data Analysis

The analysis of the RAXR data requires the knowledge of the complex non-resonant structure factor, i.e. $A_{NR}(Q_0)$ and $\Phi_{NR}(Q_0)$, which can be obtained from the analysis of the non-resonant reflectivity data (i.e., based on the model of total electron density profile that best explains the non-resonant reflectivity). The anomalous dispersion terms can be obtained by measuring the x-ray absorption spectra for the element of interest (for e.g. by measuring x-ray transmission vs. energy) which yields $f''(E)$, and using the difference Kramers-Kronig relationship[66] to obtain $f'(E)$. Once the complex $F_{NR}(Q_0)$ and the anomalous dispersion terms are known, the RAXR spectra can be fit in a model-independent way, based on eqn. 2.2.6 to obtain a $A_R(Q_0)$ and a $\Phi_R(Q_0)$ corresponding to the spectrum measured at Q_0. Each of the measured spectra can be fit separately to obtain an amplitude and phase for that spectrum[65]. This set of amplitudes and phases can then simply be Fourier transformed according to eqn. below to obtain the distribution of the element of interest,

$$\rho(z) = \frac{1}{2\pi} \sum_j \left\{ A_R(Q_{0,j}) \; e^{i\,\Phi_R(Q_{0,j})} \; e^{-iQ_{0,j}\,z} \; \Delta Q_{0,j} \right\} \tag{2.2.7}$$

Here $\rho(z)$ is the distribution of the element of interest normal to the surface, $Q_{0,j}$ denotes the Q_0 value for the jth energy spectra, and ΔQ denotes the difference in Q_0 between the different energy spectra.

A model based analysis of the RAXR data can be conducted by performing a simultaneous fit of the complete set of measured spectra. In this case the resonant structure factor is calculated based on the assumed model, i.e., using eqn. 2.2.5, and eqn. 2.2.6 is then used to fit

the normalized RAXR data. Here, θ_k, z_k and σ_k that represent the kth layer of the resonant element distribution are used as fit parameters. The resonant element distribution obtained from the model based analysis should be compared with the model-independently obtained profile to check for consistency between the two approaches. This is important as the model-independently retrieved profile can have several artifacts that arise as a result of the Fourier transform of the A_R and Φ_R at discrete Q_0 values. For example, the model-independently obtained profile can be resolution limited when the distribution widths are smaller than the resolution of the experiment[65]. The experimental resolution is given by, $\frac{\pi}{Q_{max} - Q_{min}}$, where Q_{max} and Q_{min} denote the high and low Q_0 range of the set of the measured RAXR spectra. The real-space range over which the profile can be model-independently recovered (also called the Fourier window) from the RAXR data is given by $\frac{2\pi}{\Delta Q}$, where ΔQ denotes the sampling frequency of the spectra.

2.3 Multilayer X-ray Reflectivity

2.3.1 Reflection from a Single Interface

When an x-ray plane wave passing through a medium 1 (with refractive index n_1) encounters an interface with a different medium (medium 2, with refractive index n_2), the wave is split into a wave that transmits into the medium 2, and a wave that reflects back into the medium 1 (Fig. 2.4). From the boundary conditions of the wave-fields at the interface, two important relations concerning the incident, reflected and transmitted waves and the media properties, can be derived[60],
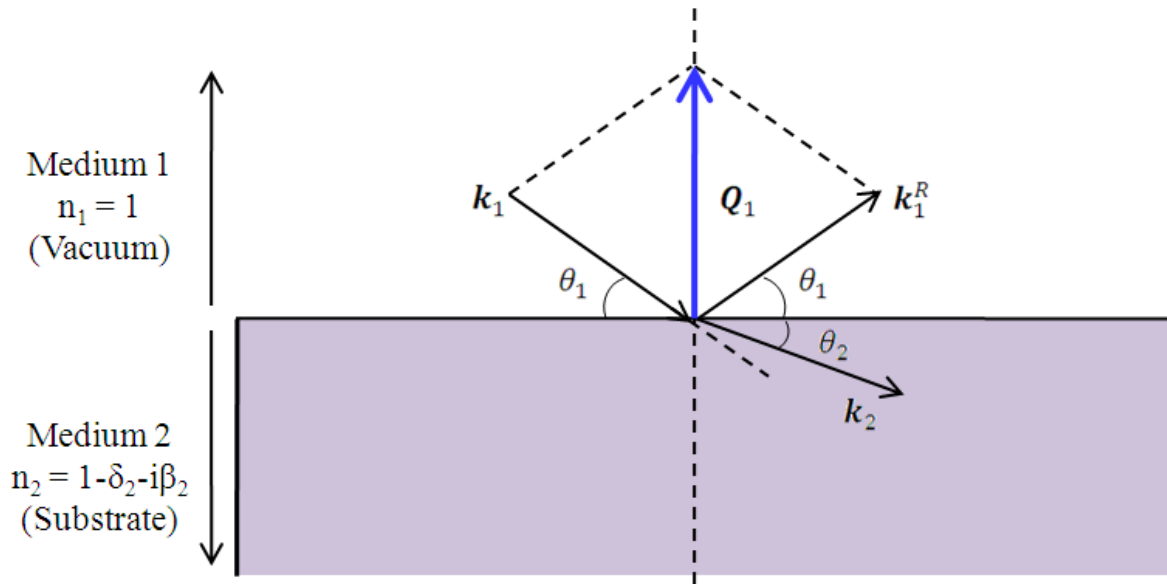
Figure 2.4: Reflection and transmission of x-rays at an interface between two semi-infinite media. Here, a vacuum-substrate interface is depicted. The incident and reflected wave-vectors are denoted by k_1 and k_1^R respectively, while the transmitted wave-vector inside the substrate is denoted by k_2. Since $n_2 > n_1$ for x-rays, we have $\theta_2 < \theta_1$, following Snell's law. The momentum transfer Q_1 is along the surface normal direction for the specular reflection geometry.

$$n_1 \cos\theta_1 = n_2 \cos\theta_2 \qquad (2.3.1)$$

$$r_{1,2}^F = \frac{n_1 \sin\theta_1 - n_2 \sin\theta_2}{n_1 \sin\theta_1 + n_2 \sin\theta_2} \qquad (2.3.2)$$

The first relation above is known as the Snell's law, which shows that the wave-vector component parallel to the interface remains unchanged as the wave transmits from one medium to the other. The second relation gives the Fresnel reflection coefficient, $r_{1,2}^F$, which is the ratio of the reflected wave amplitude (complex) to the incident wave amplitude[60]. Here θ_1 and θ_2 denote the angle between the travelling wave and the interface in medium 1 and 2 respectively. The refractive index of a medium is a complex quantity, given by, $n = 1 - \delta - i\beta$.

2.3.2 Reflection from a Film of Finite Thickness

Here we are interested in the expression for reflectivity from a film of finite thickness on a semi-infinite substrate. This is required to obtain the more general expression for reflectivity from a multi-layer derived in the next section. Consider the case of media 1, 2, and 3 where medium 2 represents the film with finite thickness, and media 1 and 3 are semi-infinite extending above and below the medium 2 respectively. In this case, the reflectivity at the medium 1 - medium 2 interface is not given simply by the Fresnel coefficient described previously as it would be if the medium 2 were semi-infinite. This is because the wave transmitted into the film (second medium) experiences multiple scattering from the interfaces above and below the film which must be included to obtain the correct reflection coefficient referred to as $r_{1,2}^D$, where D stands for *dynamic* to emphasize the inclusion of multiple reflections (as opposed to the kinematical limit, where these events are ignored). It can be shown that $r_{1,2}^D$ is given by[60],

$$r_{1,2}^D = \frac{\left(r_{1,2}^F + r_{2,3}^F \, p_2^2\right)}{\left(1 + r_{1,2}^F \, r_{1,2}^F \, p_2^2\right)} \tag{2.3.3}$$

Here $p_2 = e^{i\frac{Q_2 t_2}{2}}$ is the phase-factor that takes into account the phase-retardation and amplitude attenuation of the wave as it travels through the thickness t_2 of the film. Q_2 represents the wave-vector transfer inside the film.

2.3.3 Reflection from a Multilayer

The expression for the reflectivity coefficient from a multi-layered system can be derived using the Fresnel coefficients for the individual interfaces and taking into account the multiple reflections within each of the finite layers (Fig. 2.5). Consider now a system of N media, where the first and the Nth media are semi-infinite, while all other media (2 to N-1) are finite in thickness. In this case, the reflection coefficient at the top interface, or $r_{1,2}^D$ can be calculated using the Parratt's recursive formalism[60, 67, 68]. In this formalism, first the reflection coefficient at bottom-most interface (between media N-1 and N) is calculated, which is simply the Fresnel coefficient, since the Nth layer is semi-infinite. Then the reflection coefficient at each interface up is calculated from the reflection coefficient at the interface below, using the relation in eqn. 2.3.3. This process is iterated until the reflection coefficient at the top-most interface is obtained. In this thesis, a modified form of Parratt's formalism is used, where the roughness of each interface is taken into account by multiplying the Fresnel reflectivity coefficient at that interface with a Debye-Waller type factor (below) based on the *rms*-width of the interface.

The following notations are used in the equations below. Layer number is denoted by subscript j (j=1 to N), interface number is denoted by j-1,j (the interface between j-1 and jth
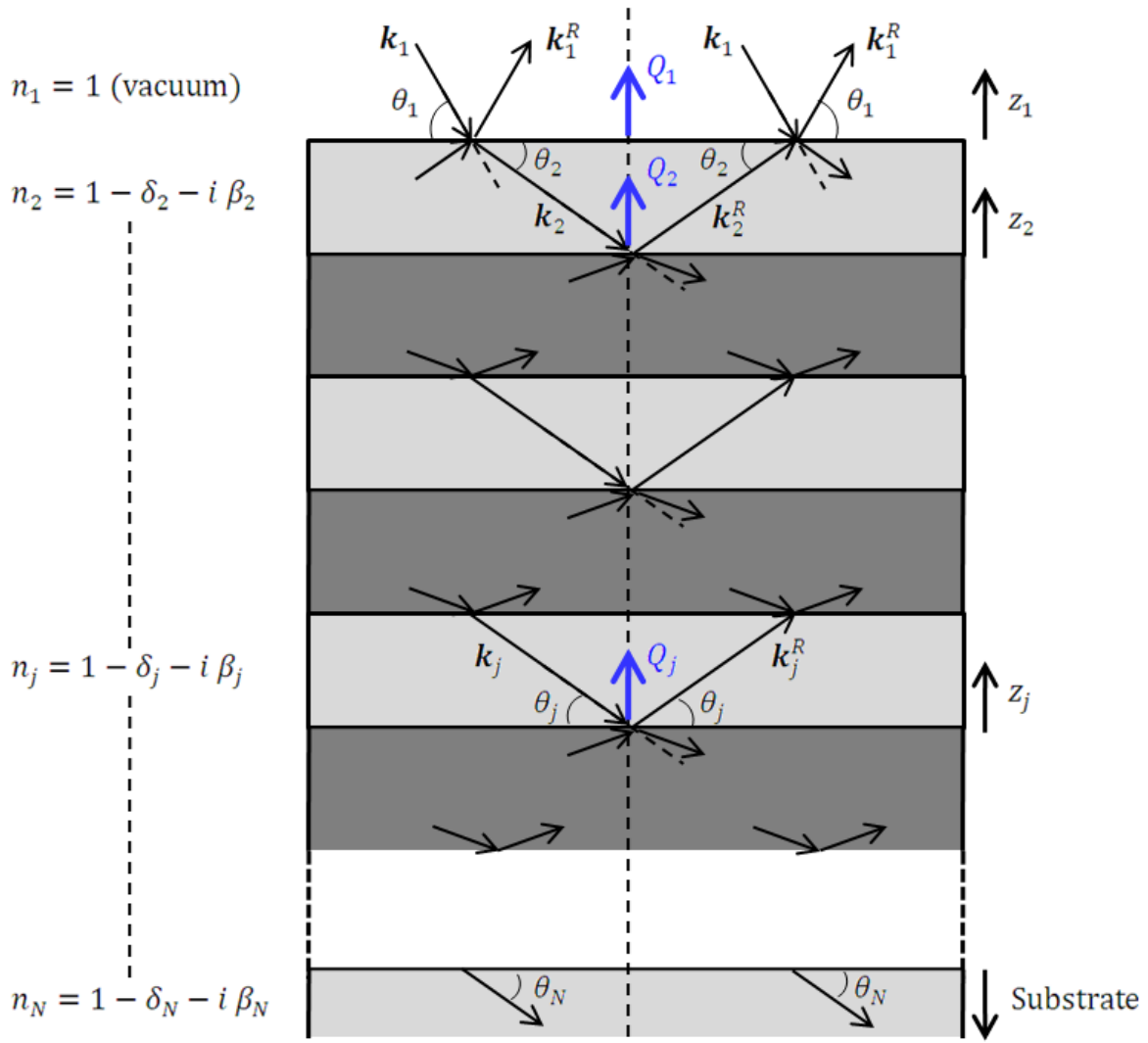
Figure 2.5: Reflection and transmission of x-rays at the various interfaces in a multi-layer sample. The calculation of reflection coefficients at these interfaces (except the interface between the N-1 and Nth layers) should include multiple reflection components inside the different layers, especially for low angles of incidence. These reflection coefficients can be calculated using Parratt's recursive formalism. The momentum transfer inside the jth layer is given by, $Q_j = 2 k_j \sin \theta_j$, and is a complex quantity for all layers (except for the top vacuum layer).

layers). For the jth layer, n_j is the refractive index, k_j is the complex wave-vector in that layer, θ_j is the incident angle (from the interface) inside that layer, Q_j is the momentum transfer, and t_j is the layer thickness. For the interface between j-1 and j^{th} layer, $\sigma_{j-1,j}$ is the interfacial roughness, $r^F_{j-1,j}$ is the Fresnel reflection coefficient, and $r^D_{j-1,j}$ is the (dynamical) reflection coefficient based on Parratt's formalism. The real and imaginary parts of a complex number are denoted by ' and " respectively. In the jth layer, we have,

$$n_j = 1 - \delta_j - i\,\beta_j \qquad (2.3.4)$$

$$k_j = n_j\,\frac{2\pi}{\lambda} \qquad (2.3.5)$$

$$\sin\theta_j = \sqrt{1 - \left(\frac{n_1}{n_j}\,cos\theta_1\right)^2} \qquad (2.3.6)$$

$$Q_j = 2\,k_j\,\sin\theta_j \qquad (2.3.7)$$

The reflection coefficient at the interface between medium j-1 and j, referred to as , $r^D_{j-1,j}$, can be expressed by the two equations below,

$$r^D_{j-1,j} = r^F_{j-1,j}, \text{for j} = N \qquad (2.3.8a)$$

$$r^D_{j-1,j} = \frac{\left(r^F_{j-1,j} + r^D_{j,j+1}\,p_j^2\right)}{\left(1 + r^F_{j-1,j}\,r^D_{j,j+1}\,p_j^2\right)}, \text{where,}\, p_j = e^{i\,\frac{Q_j t_j}{2}}, \text{for j} = 1 \text{ to } N-1 \qquad (2.3.8b)$$

Here, $r^F_{j-1,j}$ is given by the following relation,

$$r_{j-1,j}^{F} = \frac{(Q_{j-1} - Q_j)}{(Q_{j-1} + Q_j)} \; e^{-\frac{1}{2}\sigma_{j-1,j}^{2} \; Q_{j-1}' \, Q_j'} \tag{2.3.9}$$

2.4 Long Period X-ray Standing waves

2.4.1 XSW Introduction

Since the first demonstration forty years ago that X-ray standing waves (XSW) can be used to determine the location of impurity atoms in single crystals[69], the technique has been applied to measure the distribution of specific elements near or within complex structures including synthetic[70, 71] and natural crystals[72, 73], surfaces[74-77], thin films[78] and multilayers[79-82], and fluid-crystal interfaces[23, 83, 84]. The target atomic species are selected via characteristic X-ray fluorescence (XRF), or photoelectron or Auger signals.

The XSW has been utilized in various configurations, shown in Fig. 2.6, including diffraction from bulk crystals (Bragg single crystal XSW)[85], total-external reflection from x-ray mirrors (TR or TER XSW)[86, 87], and reflection from periodic multilayer (PML XSW)[79-82]. These techniques have differing sensitivities and strengths. For the Bragg single crystal case the XSW period is equivalent to the diffraction-plane spacing. As such, it is ideal for locating elemental structures and distributions that are correlated to the substrate lattice with sub-Angstrom resolution. When applied to interfaces, it is most readily applied to distributions that occur within one lattice spacing of the surface because of the modulo-d ambiguity[74] arising from the fact that the measurements are made only at the Bragg diffraction condition defined by the crystal lattice. At much smaller scattering angles (2θ), the TER and PML cases generate a
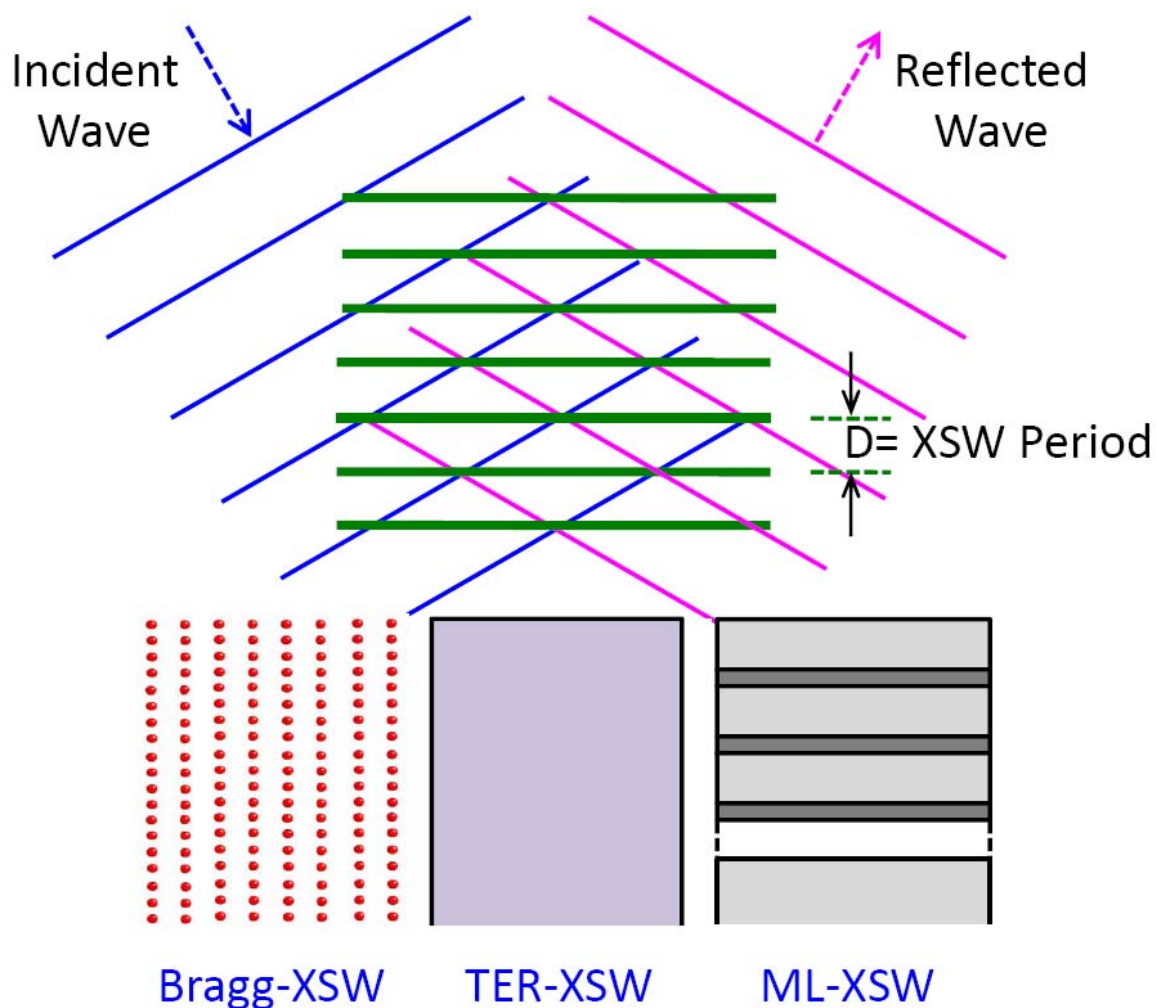
Figure 2.6: X-ray standing waves (XSW) generated in various geometries. XSW results from the interference between incident and reflected waves. A strong reflected wave can result either through Bragg diffraction from a single crystalline lattice (Bragg-XSW), or through total external reflection from an x-ray mirror (TER-XSW). The strong reflectivity around the Bragg peaks of a multi-layer can also be utilized to generate standing waves (ML-XSW). TER and ML modes offers the advantage of long XSW periods at low angles (since XSW period $D = 2\pi/Q$).

so-called "long-period" XSW with a period D=λ/(2sinθ) that is much longer and can vary continuously; thereby providing sensitivity to extended elemental 1D distributions that are much broader and are located further above the reflecting surface.

2.4.2 XSW inside a Thin Film

When an x-ray plane wave is reflected from an interface between any two media, a standing wave is formed above the interface as a result of superposition of incident and reflected electric fields (E-fields)[74, 85]. Now consider the case of a thin film on a substrate (Fig. 2.7). The topmost vacuum layer is called medium 1, the thin film is medium 2, and the substrate is medium 3. The refractive indices n_2 and n_3, are given by, $n_j = 1 - \delta_j - i\,\beta_j$ (while $n_1 = 1$) . X-rays reflected from the 2,3 interface (referred to as 'the interface' in this derivation) result in standing wave formation inside the medium 2. The total E-field inside medium 2 can be written as,

$$\varepsilon_2^T(\mathbf{r}, t) = \varepsilon_2(\mathbf{r}, t) + \varepsilon_2^R(\mathbf{r}, t) = \mathbf{E}_2\, e^{-i\,(\mathbf{k}_2 \cdot\, \mathbf{r}\, -\, \omega t)} + \mathbf{E}_2^R\, e^{-i\,(\mathbf{k}_2^R \cdot\, \mathbf{r}\, -\, \omega t)} \tag{2.4.1}$$

where $\mathbf{E}_2$ and $\mathbf{E}_2^R$ denote respectively the complex amplitude of the incident and reflected E-fields just above 2,3 interface (at z=0), and $\mathbf{k}_2$ and $\mathbf{k}_2^R$ denote the incident and reflected wave-vectors respectively. The magnitude of both the wave-vectors is given simply by $k_2 = \frac{2\pi}{\lambda}\left(1 - \delta_2 - i\,\beta_2\right)$. If $r_{2,3}^D$ is the complex reflectivity coefficient at the 2,3 interface ($=\varepsilon_2^R/\varepsilon_2$, which is simply the Fresnel coefficient in this case since the medium 3 is semi-infinite), we have,

$$\varepsilon_2^T(\mathbf{r}, t) = \mathbf{E}_2\, e^{-i\,(\mathbf{k}_2 \cdot\, \mathbf{r}\, -\, \omega t)}\left[1 + r_{2,3}^D\, e^{-i\,\mathbf{Q}_2 \cdot\, \mathbf{r}}\right] \tag{2.4.2}$$
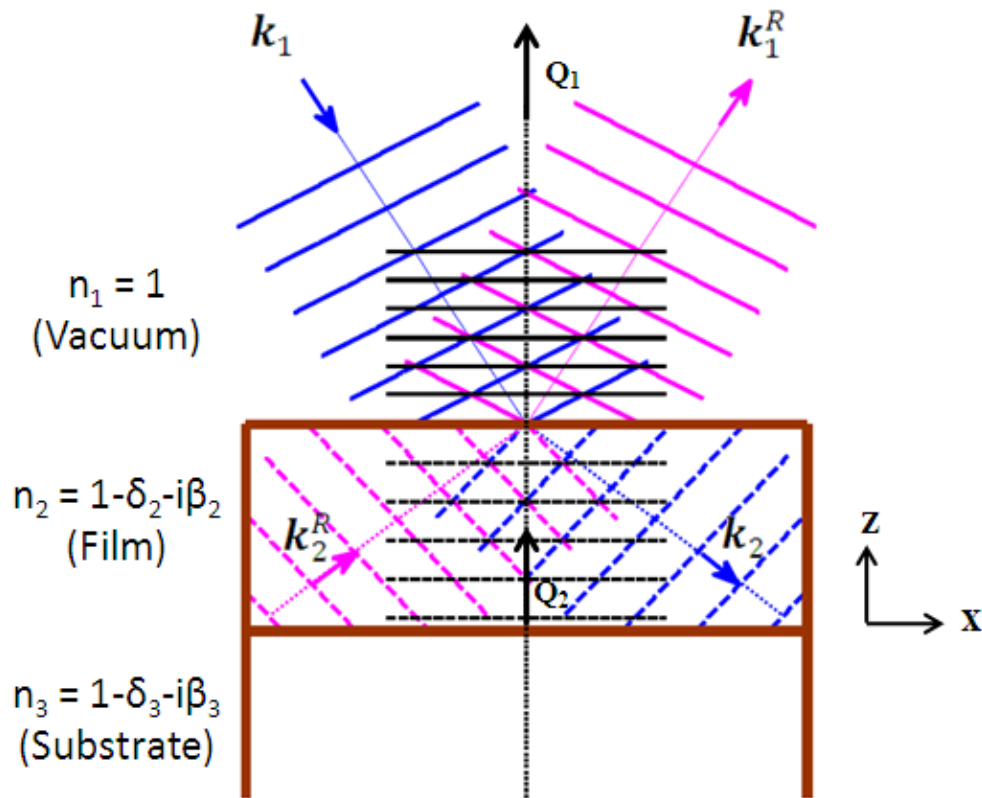
Figure 2.7: Long period x-ray standing waves (XSW) generated by interference between incident and specularly reflected x-rays. The case shown is of a film (refractive index n_2) on a substrate (refractive index n_3). The incident and reflected waves are shown in blue and magenta respectively, while the XSW antinodes are shown in black. The XSW is generated both in vacuum, as well as within the film (because of the presence of the reflection from the film-substrate interface).

where $\boldsymbol{Q_2} = \boldsymbol{k_2^R} - \boldsymbol{k_2}$ is the wave-vector transfer in the medium 2. By the law of reflection, $\boldsymbol{Q_2}$ is oriented along the surface normal direction, and $\boldsymbol{Q_2}.\boldsymbol{r} = Q_2\,z$, where z is the height above the 2,3 interface. The complex quantity Q_2 is described as, $Q_2 = Q_2' - iQ_2''$. The total E-field intensity in medium 2, normalized to the incident E-field intensity in vacuum, can now be written as,

$$I_2(Q_2, z) = \frac{|\varepsilon_2^T|^2}{|E_1|^2} = \frac{|E_2(Q_2)|^2}{|E_1|^2}\; e^{+\,Q_2'' z}\; \left|1 + r_{2,3}^D\, e^{-i\,Q_2\,z}\right|^2 \tag{2.4.3}$$

Here the factor $e^{+\,Q_2'' z}$ represents the attenuation of the incident wave in the second medium that includes both the linear absorption as well as extinction (i.e. attenuation of the evanescent wave that occurs for incident angles below the critical angle). Therefore Q_2'' is an effective linear absorption coefficient.

2.4.3 XSW inside a Multi-Layer

For a multi-layered system, consisting of N layers (where layer 1 and N are semi-infinite), the total electric field intensity in the jth layer can be written in terms of the height z_j above the interface between the jth and $j+1^{th}$ layer,

$$I_j(Q_j, z_j) = \frac{|E_j(Q_j)|^2}{|E_1|^2}\; e^{+\,Q_j'' z_j}\; \left|1 + r_{j,j+1}^D\, e^{i\,Q_j\,z_j}\right|^2 \tag{2.4.4}$$

Here, $|E_j(Q_j)|^2$ is the complex electric field amplitude of the incident wave just above the interface between the j and $j+1^{th}$ layer, and is given by the two equations below,

$$|E_j(Q_j)|^2 = |E_1|^2, \text{for } j = 1 \tag{2.4.5a}$$

$$|E_j(Q_j)|^2 = E_{j-1}(Q_{j-1}) \frac{\left(1 + r_{j-1,j}^F\right) p_j}{\left(1 + r_{j-1,j}^F r_{j,j+1}^D p_j^2\right)}, where\ p_j = e^{i\frac{Q_j t_j}{2}}, for\ j = 2\ to\ N-1 \qquad (2.4.5b)$$

When an element in a medium interacts with the standing wave in that medium, it produces x-ray fluorescence, when the incident x-ray energy is greater than the absorption edge of the element. This is a result of photoelectric effect, and in the dipole approximation, the fluorescence yield Y(Q) from the element is given by $Y(Q) = \int \rho(z)\, EFI(Q, z)\, dz$, where $\rho(z)$ is the elemental density distribution, and $EFI(Q, z)$ is the net electric field intensity distribution. The net yield produced from an element interacting with the standing wave field produced by a multi-layer is given by,

$$Y(Q) = \sum_j \int \rho(z_j)\, I_j(Q_j, z_j)\, dz_j \qquad (2.4.6)$$

Here z_j denotes the position in the layer j with respect to the interface between the medium j and j+1.

2.5 Experimental Setup

The measurements reported in this thesis (i.e., CTR, RAXR, XSW and XR) were conducted at beamlines 33-BM, 6-ID, 11-ID, and 33-ID, at the Advanced Photon Source (APS) at Argonne National Laboratory (ANL). The typical experimental setup for these measurements is shown in Figs. 2.8 and 2.9. The x-rays are generated using an undulator, a wiggler, or a bending magnet source[60]. A double crystal monochromator (Si, or diamond crystals) is then used to select a particular x-ray energy for the measurement. The monochromatic beam typically goes through a
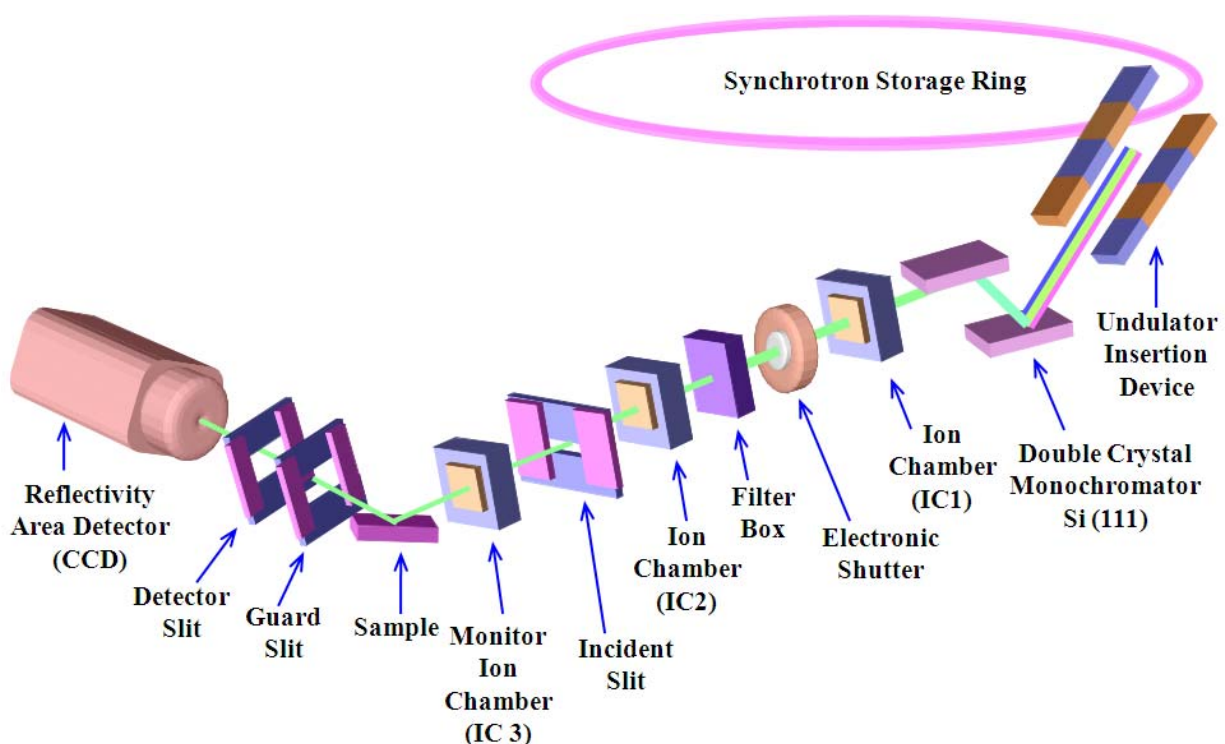
Figure 2.8: Schematic of the experimental setup for the resonant anomalous X-ray reflectivity (RAXR), and crystal truncation rod reflectivity (CTR) experiments. Electrons circulating in the synchrotron ring are oscillated by an insertion device such as an undulator (or a wiggler) to produce intense x-ray radiation, useful for reflectivity experiments. Typically a Si(111) monochromator is used to select a particular energy suitable for the measurement. Higher harmonics of the undulator are rejected using x-ray mirrors (not shown), which can also be used to focus the beam. Inside the experimental hutch, an electronic shutter is used to turn the beam on and off. Attenuating materials (such as Al, Mo, Ti) are used as filters to reduce the x-ray intensity when required. The beam size (vertical and horizontal) is defined by the 'incident slit'. The flux incident on the sample is tracked by the 'monitor' ion chamber (IC3). The reflectivity from the sample can be measured using a 2D detector, such as the CCD detector shown here.
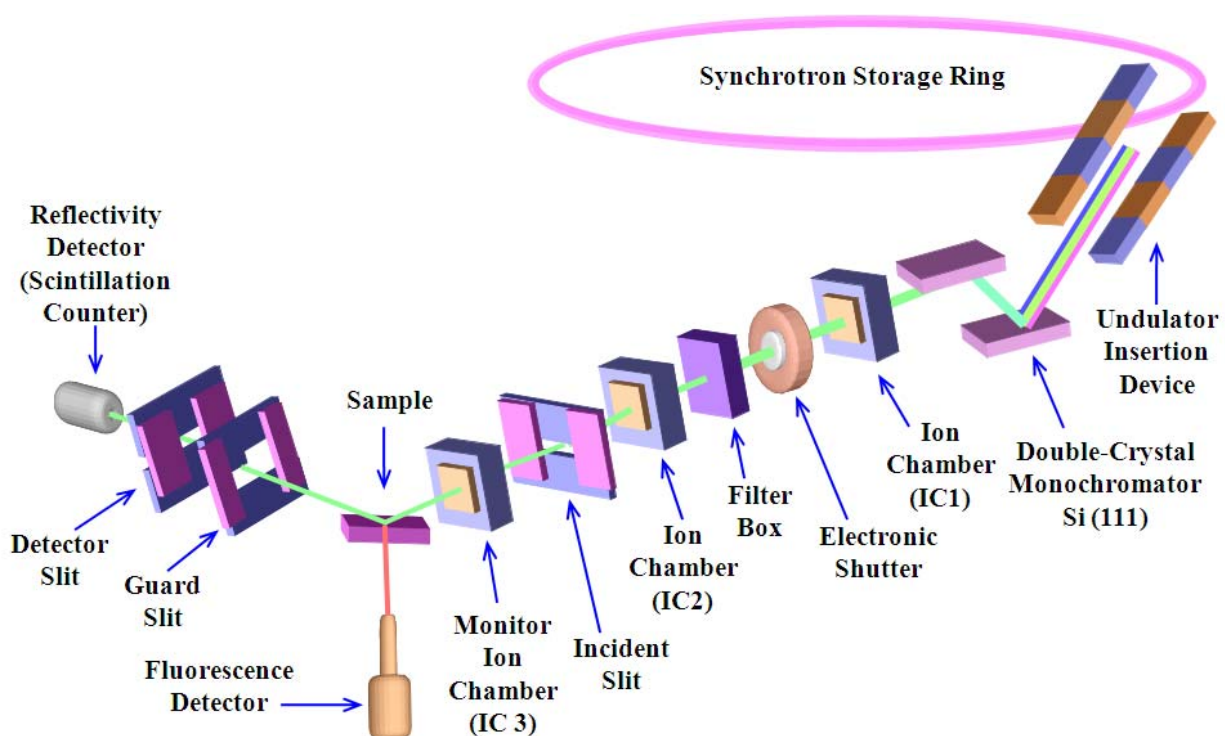
Figure 2.9: Schematic of the experimental setup for the X-ray standing waves (XSW), and low-angle X-ray reflectivity (XR) experiments. Two sets of detectors are used for the XSW experiments, a reflectivity detector (scintillation counter) that measures the reflected x-rays in the vertical scattering plane, and a fluorescence detector placed pointing perpendicular to the scattering plane that measures the x-ray fluorescence from the sample.

set of focusing optics (such as x-ray mirrors) before entering the experimental hutch. The x-ray mirrors are also useful in rejecting the very high energy radiation (such as higher harmonics). An electronic fast shutter can be used inside the experimental hutch to turn the beam on or off during the course of the measurements. The vertical and horizontal beam size can be chosen depending on the experiment, using a 'beam defining slit'. An ion chamber, referred to as the 'monitor', is placed downstream of the beam defining slit, and upstream of the sample to monitor the incident beam flux during the measurements. The sample cell is mounted on a 'goniometer' on a four-circle or a six-circle diffractometer (for e.g. Huber). The reflected x-ray intensity can be measured using either a point detector, such as Cyberstar, or using a 2D area detector (CCD), mounted on the detector arm. A 'guard slit' is used on the detector arm to reduce the background signal (such as that due to diffuse x-ray scattering). A 'detector slit' is also used on the detector arm downstream of the 'guard slit', when a point detector (typically a scintillation detector, such as Cyberstar) is used, and it should be opened when collecting data using the 2D detector (e.g. CCD). In an XSW experiment, an additional detector is needed to measure the x-ray fluorescence from the sample, this is done using a solid state detector (such as Vortex) which is oriented perpendicular to the vertical scattering plane. The beam flux during the experiment can be controlled using x-ray filters (e.g. Mo or Al), which can be placed either upstream of the sample to reduce the incident flux, or on the detector arm (of either the reflected, or the fluoresced x-rays). For the RAXR measurements, or an energy scan, however, it is preferable to place the filters upstream of the monitor ion chamber, to avoid an extrinsic slope in the measured RAXR spectra (arising from the change in transmission through the filters vs. x-ray energy). When the filters are used downstream the monitor ion chamber, the filter transmission correction

needs to be applied to the data before the analysis. The ion chamber settings (i.e., the sensitivity, voltage to frequency converter gain, gas type, and chamber length) should be noted during the experiment, as these are required to convert the ion chamber count rate to the x-ray beam flux in photons/second, and to convert the measured scattered intensities to absolute reflectivity.

Chapter 3 : Rb$^+$ and Sr^{2+} Adsorption at the Rutile TiO$_2$ (110) – Electrolyte Interface Observed with Resonant Anomalous X-ray Reflectivity

3.1 Introduction

A complete molecular-level characterization of the adsorbed ion distribution is critical to understanding the reactions that occur at the charged liquid-solid interface. Chapter 1 highlighted the importance of rutile TiO$_2$ (110) surface as a model oxide surface for studying ion adsorption, as well as described the previous ion adsorption work done on this system. It also presented the important questions that have been raised as a result of recent molecular dynamics (MD) simulations that predicted that various cations adsorb at multiple inner-sphere (IS) sites that were not seen in previous x-ray results. These simulations had found that the tetra-dentate site represented ~80 percent of the total adsorbed ions (IS and OS) for the case of Rb$^+$, while it accounted for only ~60 percent of the total adsorption of Sr^{2+}. The simulations also predicted that ~5-10 percent of the adsorbed ions (Rb$^+$ and Sr^{2+}) were adsorbed as an OS species. This prediction of the simultaneous multi-site adsorption of ions on rutile surface, previously thought to adsorb solely as IS species at the tetra-dentate site, has yet to be confirmed experimentally.

XSW measurements of Rb$^+$ adsorption on rutile at *dilute* ion concentrations (1mM, pH 11) found no evidence for specific adsorption[23]. Multi-site complexation (MUSIC) model based analysis of surface titration measurements[22] on the other hand found a specifically

adsorbed coverage of 0.08 Rb^+ monolayers (ML) under the same conditions (Here, 1 ML is defined as one ion per rutile surface unit cell area, $A_{UC} = 19.22Å^2$). From measurements of proton release as a function of pH for rutile powders[23], in contact with Rb^+ solution at a higher ion concentration (0.03 M), it can be inferred that the surface should have a charge of ~-0.018 $e/Å^2$ at pH 11. If this surface charge were fully compensated by the adsorbed Rb^+ ions, a total coverage of 0.35 ML Rb^+ would be expected (at 0.03 M concentration and pH 11), including all the IS/OS and diffuse ionic species. Although, it is expected that the total Rb^+ coverage would be lower at dilute ion concentrations at the same pH (~factor of 2 lower at 1mM than at 0.03M, at pH 11), as inferred from rutile powder titrations for different electrolyte ionic strengths[54, 55]. Previous X-ray reflectivity (XR) measurements done at a substantially *higher* Rb^+ concentration (1M) had found these ions to be adsorbed as IS species (at the tetra-dentate site). This technique however lacked the capability to probe the element-specific distribution of Rb^+ and relied instead on measuring the changes in the total interfacial structure caused by the adsorbing ions.

Previous measurements of Sr^{2+} adsorption on rutile using XSW detected a single layer of specifically adsorbed ions located at the tetra-dentate site[22]. These measurements also revealed that the IS-adsorbed ions had a coherent fraction of ~0.5. The coherent fraction is a measure of the degree of order of the adsorbed species. In the context of the simple adsorption picture where the IS species adsorbed at a specific site are considered to be ordered, this observation implies that the measured IS species accounted for only ~one-half of the total Sr^{2+} coverage. The remaining ions were apparently "missing" in the XSW measurements. Other explanations of a reduced coherent fraction could be the disorder as a result of cation motion, or even adsorption at multiple sites as predicted by MD simulations[38, 56]. If this apparent disorder in the Sr^{2+}

distribution were due to the simultaneous adsorption of an OS species (as seen recently at the muscovite-electrolyte interface[20]), it is expected that this distribution would be modified by a background electrolyte (e.g., Na^+)[4], since the OS species could be weakly bound in comparison to the specifically adsorbed IS species. Previous XSW measurements showed that the Sr^{2+} distribution is largely unaffected by the presence of background electrolyte. However, the presence of a weakly bound OS species on the surface may not be visible to the XSW measurements.

Consequently, there remain numerous unanswered questions, even for this simple system. Do Rb^+ ions adsorb in the same tetra-dentate site at dilute concentrations as they do at high concentrations? Or is the adsorption structure more distributed? Does the Sr^{2+} profile consist of a single IS adsorption site? Or, are there multiple, or possibly less-ordered, adsorption sites (including OS species) for Sr^{2+} that account for the apparently "missing" Sr^{2+} in the XSW measurements?

Resonant anomalous x-ray reflectivity (RAXR) technique described in Chapter 2 has been used recently to probe the distribution of cations and anions at mineral-electrolyte interfaces, including quartz, mica, orthoclase, alumina and hematite[20, 21, 26, 27]. This technique is similar to Bragg XSW in that it can image directly elemental distributions at and above an interface. One difference between RAXR and Bragg-XSW is that RAXR can probe more extended ion distributions while Bragg XSW[85, 88] has an ambiguity in distinguishing heights that are separated by distances greater than the substrate lattice spacing. Studies of cation adsorption at mica-electrolyte interface using RAXR[20] showed that Rb^+ adsorbs as a single inner-sphere species, while Sr^{2+} adsorbs both as inner and outer-sphere species. This observation,

coupled with the gaps in our knowledge of cation adsorption on rutile, prompted us to determine if the adsorbed Sr^{2+} is adsorbed exclusively as a single IS species on rutile, or it has a more complex adsorption structure (i.e., coexistence of the IS species with additional IS or OS species), and whether there is any specific adsorption of Rb^+ at dilute ion concentrations.

Here we report the vertical distribution of Rb^+ and Sr^{2+} at the rutile (110)-electrolyte interface obtained with crystal truncation rod x-ray reflectivity (CTR) and RAXR measurements. Two solution conditions were used in probing Sr^{2+} adsorption, without and with an added background electrolyte (NaCl), to test the sensitivity of the ion distribution to the ionic strength. Sr^{2+} without background electrolyte will be referred to the Sr^{2+} solution, while the solution with Na^+ is called "Sr^{2+} with Na^+" solution throughout this paper.

3.2 Experimental

3.2.1 Materials

Measurements were conducted on rutile(110) single crystals with the sample held in contact with an aqueous solution in a thin-film cell[22]. The samples used for the Rb^+ and Sr^{2+} measurements had sizes of 10x10x1mm and 25x5x1mm crystals respectively, and were obtained from Princeton Scientific. The sample used for the Sr^{2+} measurements was mechanically polished using a colloidal silica suspension. Both the crystals were cleaned, sequentially with acetone, methanol, and de-ionized water repeatedly before annealing (at ~250°C and 350°C respectively for the Rb^+ and Sr^{2+} measurements), cooling and storage in deionized water.

Solutions used for the three measurements were 1mM Rb(OH) at pH 11, 0.1mM $Sr(OH)_2$ at pH 10.3, and 0.1mM $Sr(OH)_2$ with 30mM added NaCl at pH 10.3. The Sr^{2+} solutions were prepared in a CO_2-free environment to prevent precipitation of Sr^{2+}. During the Sr^{2+} measurements, the atmosphere above the sample cell was controlled by flowing helium gas contained by a thin Kapton film to minimize the possibility of dissolved CO_2.

3.2.2 Methods

The details about the crystal truncation rod x-ray reflectivity (CTR), and resonant anomalous x-ray reflectivity (RAXR) techniques can be found in Chapter 2. The CTR measurements (also referred to as the non-resonant measurements) reported here were conducted at incident x-ray energies of 13.2 keV for Rb^+ and 14 keV for Sr^{2+}, which are each about 2 keV below the K-shell absorption edges of these elements. The RAXR measurements of reflectivity vs. x-ray energy were collected near the K-shell absorption edges of Rb^+ and Sr^{2+} at fixed Q_0, for 12-14 different Q_0 values ranging from 0.25 Å^{-1} to 3.7 Å^{-1}. For the sake of clarity, the RAXR data are normalized to the intrinsic non-resonant reflectivity (obtained from the CTR analysis) at the same Q_0 and at the same solution conditions. Each RAXR spectrum was measured over an energy range of ±400 eV centered at the Rb^+ and Sr^{2+} absorption edges.

Rb^+ and Sr^{2+} measurements were conducted at beamlines 11-ID-D and 6-ID-B, respectively, at the Advanced Photon Source (APS) at Argonne National Laboratory. Initial measurements towards this effort were also conducted at the beamline 33-ID-D. The incident x-ray beam size at the sample was ~0.15 × 1 mm (vertical × horizontal) for the Rb^+ measurements and ~0.1 x 0.5 mm for the Sr^{2+} measurements, both using a vertical scattering plane. Anomalous

dispersion terms of the ions' atomic scattering factors (Rb^+ and Sr^{2+}) were obtained from x-ray absorption spectra measured in transmission geometry through a 2 mm thick aqueous solution with a 0.1 M ion concentration. The real-part of the anomalous dispersion terms were obtained with a difference Kramers-Kronig transform[20, 66]. Both the CTR and RAXR data were collected using a x-ray CCD area detector[63]. The procedures for obtaining integrated and background subtracted x-ray reflectivity data using a CCD area detector have been described previously[63]. In brief, a CCD image at a given scattering condition, Q, simultaneously images the reflected beam and the background so that a fully background subtracted reflectivity signal can be obtained in a single image.

The vertical spatial resolution of these measurements is given by $\pi/\Delta Q$, where ΔQ is the momentum transfer range of the data. The current measurements have a resolution of 0.6 Å for the CTR data, and ~1 Å for the RAXR data. The reported plots of the vertical electron density profiles (both total and element-specific) obtained from the CTR and RAXR analyses include a broadening term to include the experimental resolution, as described previously[17].

The un-relaxed rutile (110) surface unit cell[23, 89] referred to in this paper is the tetragonal structure with lateral unit cell dimensions of 6.497 x 2.959 Å, and a vertical unit cell spacing of $c = 2d_{110} = 6.497$ Å, where d_{110} is the rutile *110* Bragg plane spacing. The surface structure is shown in Fig. 1.7, which consists of a Ti-O plane terminated by bridging and terminal oxygen sites (abbreviated as BO and TO respectively). It is often useful to express the momentum transfer (Q) in reciprocal lattice units[62] as $L = Q/(2\pi/c)$. The Bragg peaks of the bulk structure oriented in the [110] direction therefore occur at L=2, 4, 6, etc. as the vertical spacing of the Ti-O planes along [110] is $d_{110} = c/2$.

3.2.3 System Stability

Repeated fiducial measurements of L=0.7 RAXR spectra were performed (Fig. 3.9) during the course of the Sr^{2+} measurements to check for systematic errors. The scattering condition of L=0.7 was chosen since its shape is indicative of the average height of the ion distribution as well as the total ion coverage. The reflectivity at this scattering condition also was high enough so that reasonable counting statistics could be obtained quickly. We found that the resonant phase (i.e., average height) and resonant amplitude (i.e., total occupancy) extracted from these spectra showed a standard deviation of repeated observations of ~5%, and ~20%, respectively. This compares to a statistical uncertainty of ~2% and ~4% in the resonant phase and amplitude respectively for the individual spectra. This reveals that the system showed some systematic variation with time. It is not well understood what causes this variability, although it was minimized by repeatedly flushing the sample with fresh solution during these measurements. All of these repeated spectra were included in the model-dependent fits, which is why the χ^2 from the fits was relatively larger for the Sr^{2+} and Sr^{2+} with Na^+ data sets. The reported uncertainties in Sr^{2+} height and coverage reflect these systematic uncertainties based on the repeated fiducial measurements.

3.3 Results

3.3.1 CTR and RAXR Data

First, we provide a qualitative assessment of the experimental data. The measured x-ray reflectivity data for the Rb^+, Sr^{2+} and Sr^{2+} with Na^+ solutions is shown in Fig. 3.1, plotted as reflectivity vs. Q (and L). The data are presented in absolute reflectivity, showing the intrinsically low reflectivity signals (10^{-5}-10^{-9}), especially away from the bulk Bragg diffraction peaks. All three data sets have similar reflectivities near the Bragg peaks, which is expected since the reflectivity near Bragg peaks is dominated by the bulk crystal structure. Differences between the three data are most apparent near the minima in the reflectivity occurring near the anti-Bragg positions (L=1, 3, 5), where the reflectivity is most sensitive to the interfacial structure. Reflectivity in this region is also sensitive to an extrinsic factor associated with surface roughness, with a higher roughness resulting in a greater decrease in the reflectivity near the anti-Bragg regions compared to an ideally flat surface. The three surfaces studied have a similar reflectivity magnitude at the anti-Bragg position L=5, which suggests that these surfaces have similar roughnesses. This, however, can be ascertained only after a complete analysis of the data (next section) since other factors (e.g., the presence of an adsorbed layer near the interface) can also substantially change the reflectivity near the anti-Bragg positions. The Rb^+ and Sr^{2+} data have distinctly different locations of their reflectivity minima (especially near L = 3). This suggests that there are differences in the total interfacial structure for the two ions. On the other hand, the differences in reflectivity data for Sr^{2+} with and without added Na^+ are relatively small indicating that background electrolyte does not significantly change the total interfacial structure.
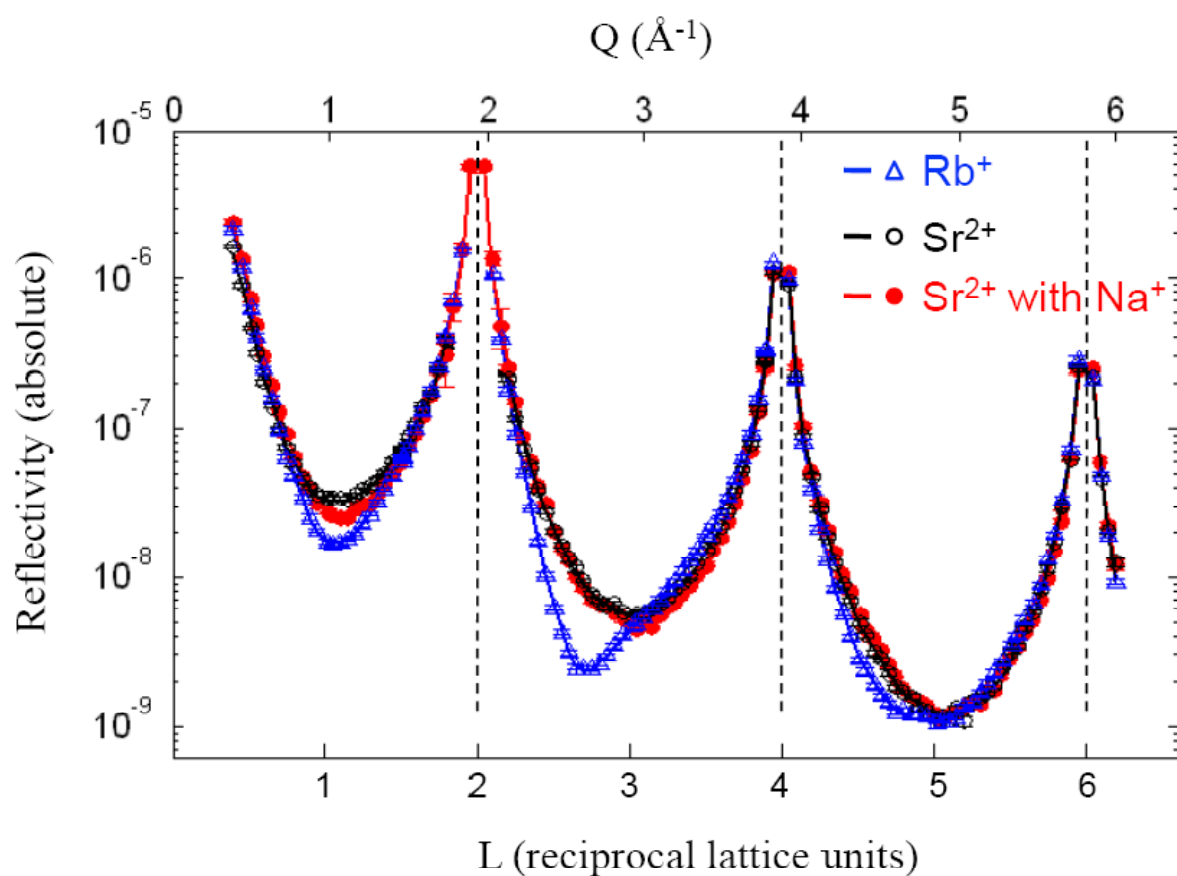
Figure 3.1: X-ray reflectivity (XR) analysis of the rutile (110) - electrolyte interface. Symbols show the XR data in absolute units, for the following electrolytes, 1mM Rb$^+$ at pH 11 (blue triangles), 0.1mM Sr^{2+} at pH 10.3 (black open circles), 0.1mM Sr^{2+} with 30mM Na$^+$ at pH 10.3 (red filled circles). The lines are fits based on the parameters shown in Table 3.1. Both Q and L values are shown on the x-axes, where Q = $(2\pi/c)*L$, and c = 6.497 Å is the vertical rutile (110) surface unit cell spacing. The dashed vertical lines show the Q and L positions of the first three Bragg peaks.

The Sr^{2+} data show a lower reflectivity in the low Q region ($Q < \sim 0.8$ Å^{-1}) in comparison to the Rb^+ and Sr^{2+} with Na^+ cases. This appears to be due to an extrinsic difference associated with a larger solution film thickness for this measurement. The attenuation of X-ray signal from the solution film in the thin-film cell geometry is significant mostly in the low Q region due to the increased path length of x-rays through the solution at low incident angles.

Selected RAXR spectra are shown in Fig. 3.2, chosen to have similar scattering conditions (i.e., L) to enable direct comparison between the three sets of data (the complete set of RAXR data can be found in Figs. 3.4 to 3.7). The RAXR data are normalized by the intrinsic non-resonant reflectivity (corresponding to the same scattering condition and the same solution condition) obtained from the fit of the CTR data (next section). The details of data normalization procedure for RAXR spectra are fully described in elsewhere[65]. The spectra are offset vertically for clarity. The similar offsets for the three data sets corresponding to each L (except L=1.1) illustrate that the non-resonant reflectivity is typically similar for the three solution conditions. Of the spectra shown, the spectra at L=0.7 conveys direct information about the average height and total coverage of the adsorbed ion distribution. It can be seen that there are distinct differences in the shape of the L=0.7 spectra for Rb^+ and Sr^{2+}. This suggests differences in the average height of the two ions above the surface. Also note that the fractional modulation in the spectra at the absorption edge is much smaller for Rb^+ as compared to Sr^{2+}, which suggests a relatively smaller total coverage of Rb^+ specifically adsorbed at the surface. On the other hand, comparing the Sr^{2+} and Sr^{2+} with Na^+ cases, it can be seen that the L=0.7 spectra is similar both in terms of shape and modulation, which suggests that the presence of Na^+ did not significantly alter the average height and the coverage of adsorbed Sr^{2+}.
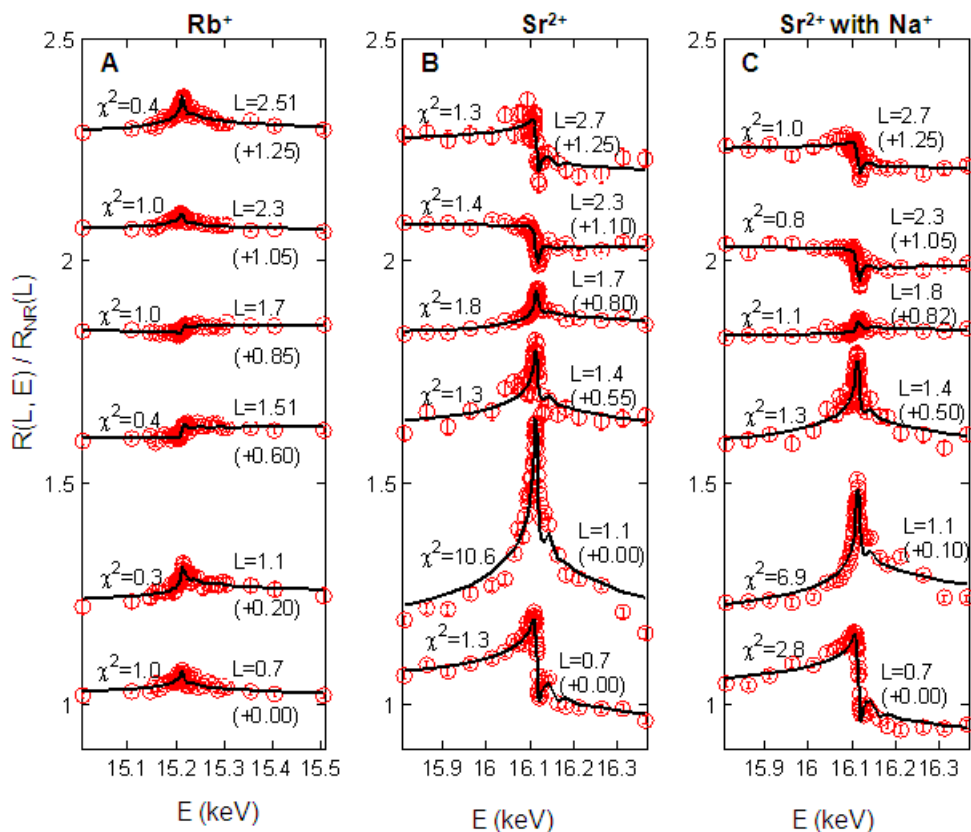
Figure 3.2: Resonant anomalous x-ray reflectivity (RAXR) analysis of ions adsorbing at the rutile (110) - electrolyte interface. Representative RAXR spectra normalized by the intrinsic non-resonant reflectivity are shown for the three solutions, A: Rb^+, B: Sr^{2+}, C: Sr^{2+} with Na^+. The data points are shown as red circles, while lines are model-independent fits of each spectra. Only data within ±200 eV of the absorption edge is plotted for clarity. Each RAXR spectrum shown was measured at a fixed 'L' value indicated on the spectra. The spectra are vertically offset by offset amounts indicated in parenthesis, with increasing L order from bottom to top. Fit quality for each spectrum is indicated by the χ^2 value shown towards the left side of each curve.

Another distinct difference between Rb^+ and Sr^{2+} is in their apparent distribution widths. For Sr^{2+}, there is a significant decrease in fractional intensity modulation in the RAXR spectra with increasing L, while the modulations in the Rb^+ spectra remain similar in magnitude with increasing L. The decrease in modulation of the spectra with increasing L is consistent with an intrinsically broadened effective width of the ion distribution. This can be confirmed only from the complete analysis (next section) because the fractional RAXR modulation is also influenced by the magnitude of the non-resonant structure factor. The higher effective width of the ion distribution can have contributions from the intrinsic distribution width at a particular site (e.g., a vibrational amplitude) as well as the intrinsic ion distribution (i.e., due to multiple adsorption sites). These data therefore suggest that the effective width of the Sr^{2+} distribution is larger than that of Rb^+. Similarly, comparing the Sr^{2+} and Sr^{2+} with Na^+ spectra, it appears that the decrease in the modulation of the RAXR spectra with increasing L is somewhat larger for Sr^{2+} with Na^+ case (Sr^{2+} with Na^+ has a smaller modulation for L=1.8, 2.3, 2.7 compared to Sr^{2+}) suggesting that the Sr^{2+} distribution in presence of Na^+ has a larger effective width.

3.3.2 Data Analysis

The CTR data were analyzed by least squares fitting by comparison to the reflectivity calculated using a model of a rutile(110)–water interfacial system, following previously established procedures[17, 25]. This model includes a surface unit cell that was allowed to relax (up to a depth of two Ti-O planes), the surface oxygens BO and TO, the interfacial water structure, and the bulk water. Only the vertical relaxations of the atoms were included in the analysis since the specular reflectivity is insensitive to lateral structural displacements. The positional origin used in the calculations is the unrelaxed surface Ti-O plane (Fig. 1.7), to which
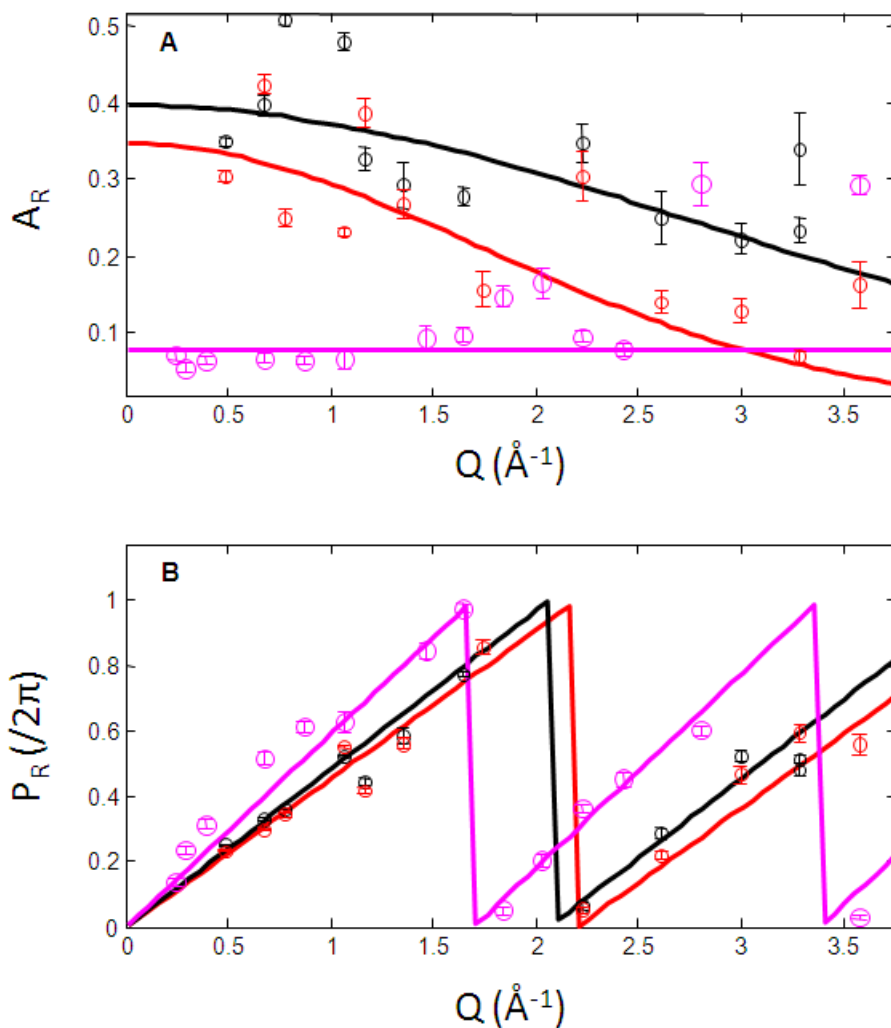
Figure 3.3: RAXR-derived ion structure factor amplitudes and phases. Amplitudes (A), and phases (B), obtained from model-independent (circles), and model-dependent (lines) analysis of the RAXR spectra measured on the rutile (110)-electrolyte interface, for the following electrolytes: Rb^+ (magenta), Sr^{2+} (black), Sr^{2+} with Na^+ (Red, for model I reported in the text).
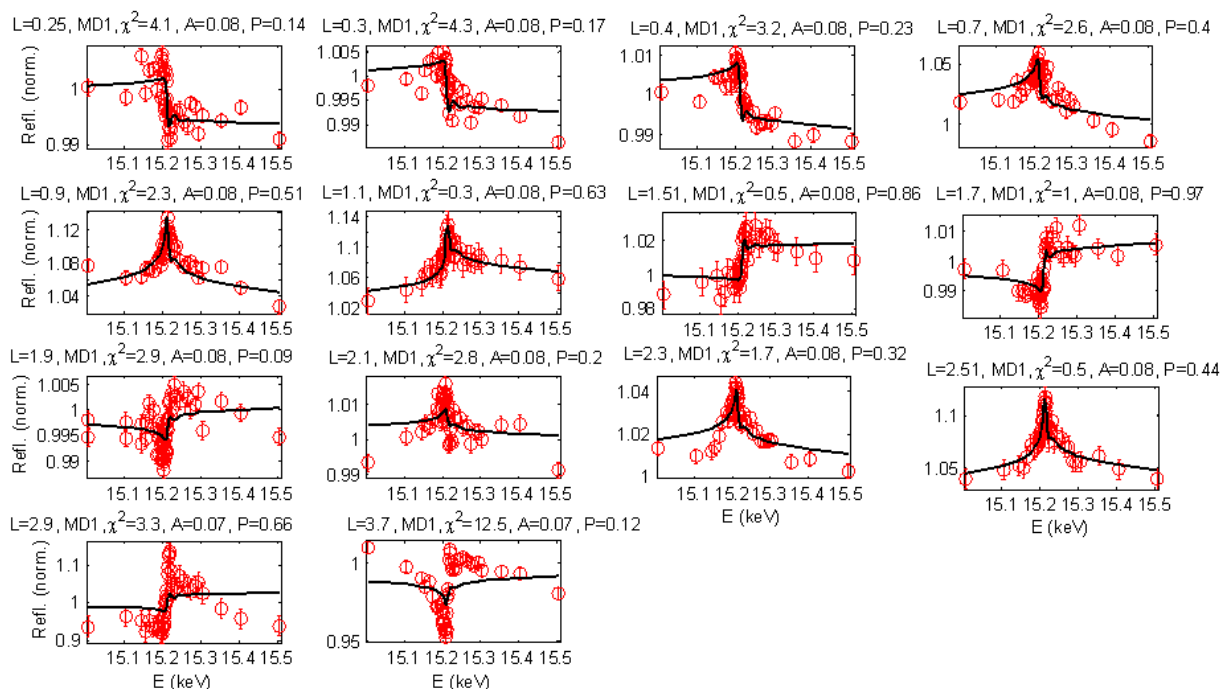
Figure 3.4: Rb^{+} RAXR results. Complete set of RAXR data for 1mM Rb^{+} at pH 11, at the rutile-electrolyte interface. Red circles are the data, and black lines are model-dependent fits. The spectra are normalized to the intrinsic non-resonant reflectivity as described in the text. The sub-title above each plot shows the scattering condition (L), the fit quality (denoted by χ^2), and the resonant amplitude (A) and phase (P) of that spectra from the RAXR analysis (MD1 denotes model-dependent fit using a single Gaussian layer).
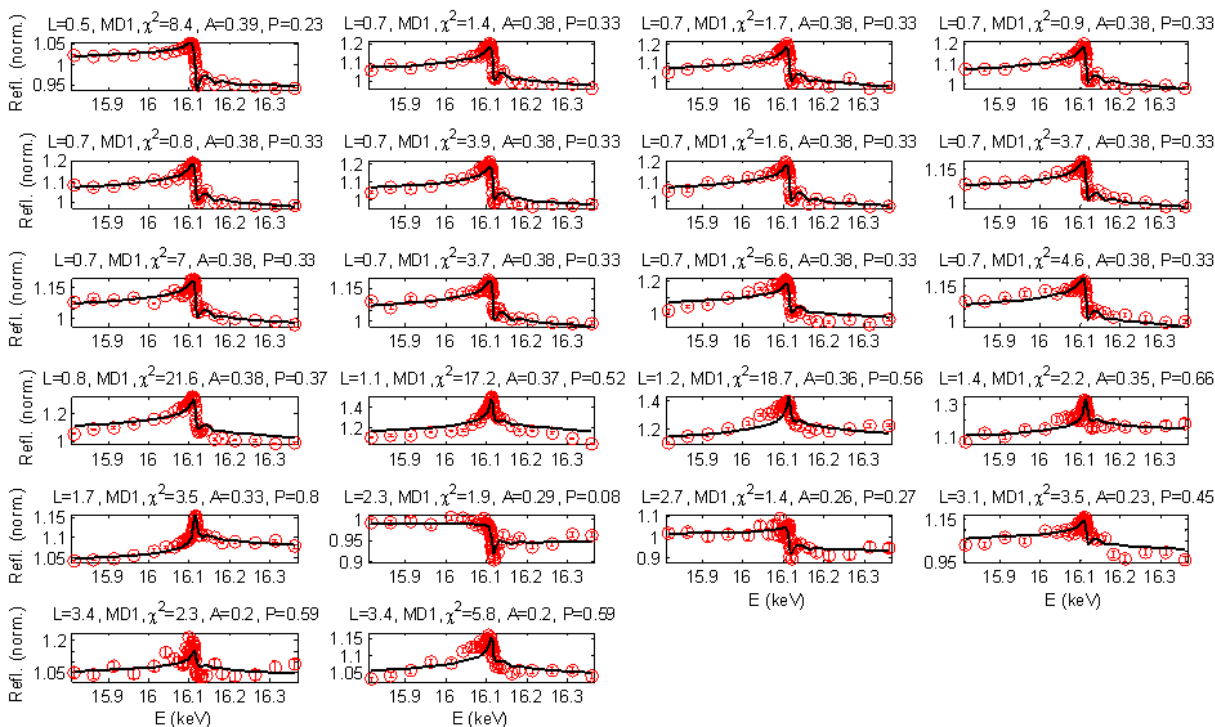
Figure 3.5: Sr^{2+} RAXR results. Complete set of RAXR data for 0.1mM Sr^{2+} at pH 10.3, at the rutile-electrolyte interface. Red circles are the data, and black lines are model-dependent fits. The spectra are normalized to the intrinsic non-resonant reflectivity as described in the text. The subtitle above each plot shows the scattering condition (L), the fit quality (denoted by χ^2), and the resonant amplitude (A) and phase (P) of that spectra from the RAXR analysis (MD1 denotes model-dependent fit using a single Gaussian layer).
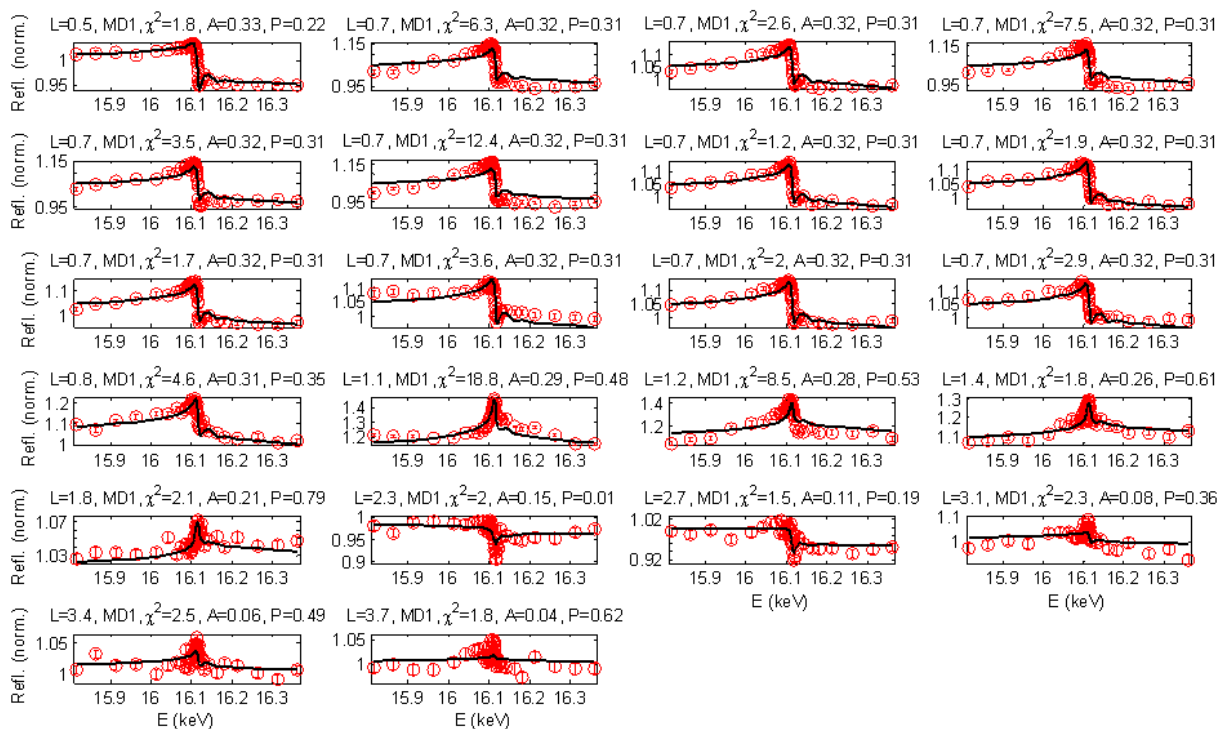
Figure 3.6: Sr^{2+} with Na^+ RAXR results, for model I reported in the text. Complete set of RAXR data for 0.1mM Sr^{2+} with 30mM Na^+, at pH 10.3, at the rutile-electrolyte interface. Red circles are the data, and black lines are model-dependent fits for the case of model I reported in the paper. The spectra are normalized to the intrinsic non-resonant reflectivity as described in the text. The sub-title above each plot shows the scattering condition (L), the fit quality (denoted by χ^2), and the resonant amplitude (A) and phase (P) of that spectra from the RAXR analysis (MD1 denotes model-dependent fit using a single Gaussian layer).
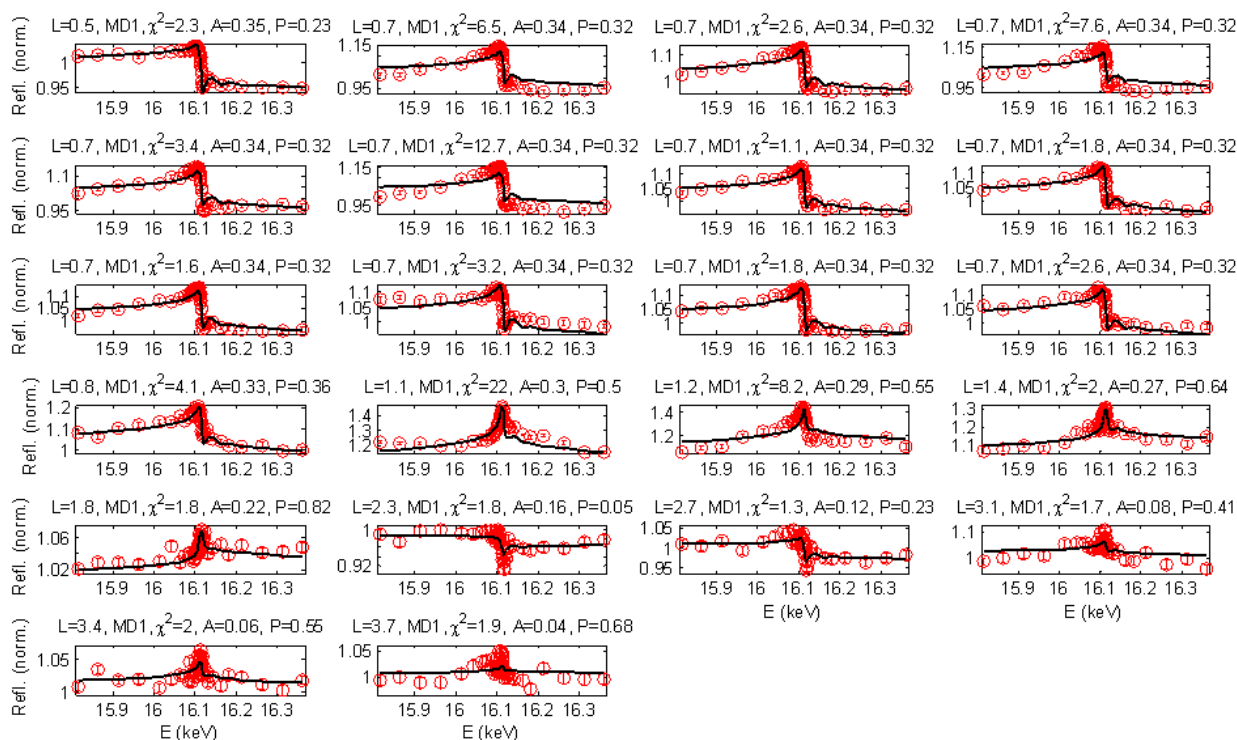
Figure 3.7: Sr^{2+} with Na^{+} RAXR results, for model II reported in the text. Complete set of RAXR data for 0.1mM Sr^{2+} with 30mM Na^{+}, at pH 10.3, at the rutile-electrolyte interface. Red circles are the data, and black lines are model-dependent fits for the case of model II reported in the paper. The spectra are normalized to the intrinsic non-resonant reflectivity as described in the text. The sub-title above each plot shows the scattering condition (L), the fit quality (denoted by χ^2), and the resonant amplitude (A) and phase (P) of that spectra from the RAXR analysis (MD1 denotes model-dependent fit using a single Gaussian layer).

all results on the elemental distributions obtained by RAXR are referenced. Structural parameters used in the fit are summarized in Table 3.1. Two parameters were used to model the relaxation of the surface Ti-O plane: the average displacement of the plane from its ideal location, δZ_1, and the splitting between the two Ti atom heights in this plane, Δ_1. The relaxation of the second TiO plane was minimal ($\delta Z_2 < 0.005$Å). Including additional relaxation parameters (e.g., a splitting parameter for the second plane and the relaxations of deeper planes) did not further improve the quality of fit. The adsorbed water was modeled as a single Gaussian layer with parameters describing its height and occupation, while the bulk water structure was based on the layered water model[90] with parameters describing the first water layer position (z_{BW}), the water layer spacing (d_{BW}), the first layer root-mean-square (*rms*) width (u_{BW}), and a parameter describing the increase in *rms* width with distance from the surface[90] ($ubar_{BW}$). Extrinsic parameters needed to fit the data included a scale factor, a water-equivalent film thickness (t_{BW}) to account for attenuation of x-rays through the solution layer and the Kapton film above the sample, and a parameter that describes the surface roughness (β)[64].

The CTR data were fit in a two step process. The first step involved fitting the interfacial structure with only water molecules in the interfacial region, i.e., the "oxygen-equivalent" structure[26]. This structure was used to calculate the initial non-resonant structure factors needed as input for the RAXR analysis. The RAXR data were then fit to obtain the ion distribution, characterized by a height, coverage and distribution width. This preliminary ion adsorption structure was then incorporated in a second CTR analysis as a fixed ion layer and the remaining interfacial structure was allowed to vary to optimize the fit to the CTR data. This second non-resonant structure was then used to re-analyze the RAXR data. This process was

repeated until convergence was reached such that the ion profile parameters stayed within the parameter uncertainties (Table 3.2), revealing the final ion profile obtained from the RAXR analysis. The final CTR structure is referred to as the converged structure. Convergence was achieved in the ion profile parameters in 1-2 iterations for Rb^+ and Sr^{2+} data sets. For Sr^{2+} with Na^+ case, the converged structure had what appeared to be unphysical displacements of the BO and TO, and hence the initial structure (model I in Tables 3.1 and 3.2) based on oxygen-equivalent model is reported for this case (the converged structure parameters are listed in Table 3.3). This structure however has a deficiency in that the Sr^{2+} density obtained from RAXR analysis slightly exceeds the total density from CTR (Fig. 3.8C) over a short distance range, which is unphysical. We also used a featureless water model (i.e., described by an error-function profile)[25] for the Sr^{2+} with Na^+ data set. In this case, the CTR-RAXR iterative analysis led to two different structures with same ion coverage and width within systematic uncertainties, but a difference of ~0.2 Å in height, with one of the structures having apparently unphysical relaxations of BO and TO in the total structure. We therefore report the more feasible converged structure (Fig 3.8D) for the Sr^{2+} with Na^+ case, while including the differences in the ion heights for the two structures in the reported uncertainties (model II in Table 3.2).

The RAXR data were fit (Fig. 3.2) using both model independent[65] as well as model dependent approaches. The model-independent approach involved fitting each spectrum separately to reveal the amplitude and phase of the element-specific structure factor from each spectrum. This information then yields the density profile by Fourier inversion[65]. In contrast, the model-dependent approach fits all of the spectra simultaneously based on a model that is chosen based on the model-independent results. The model-independent results were indicative
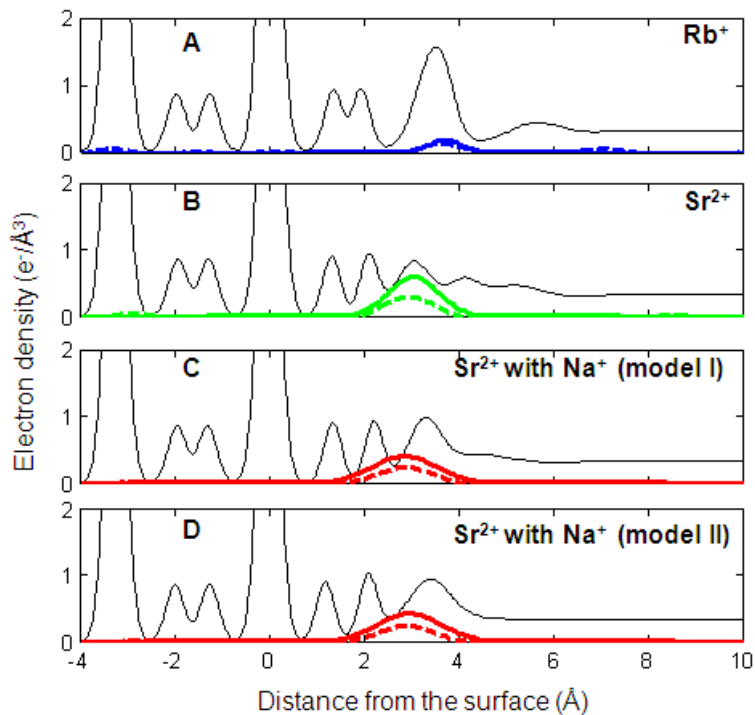
Figure 3.8: Total and element-specific density profiles from CTR and RAXR analyses. Electron density profiles plotted vs. distance from the surface Ti-O plane, for A: Rb^+, B: Sr^{2+}, C: Sr^{2+} with Na^+ (model I) and D: Sr^{2+} with Na^+ (model II). Thin black lines show the total electron density profile obtained from the model that best fit the XR data. The ion density profiles (shown in blue, green and red, respectively for Rb^+, Sr^{2+} and Sr^{2+} with Na^+) obtained from model-independent analysis of RAXR data are shown as thick dashed lines, while the more precise results obtained from model-dependent analysis are shown as thick solid lines. The two results shown for the Sr^{2+} with Na^+ case used different models to fit the XR data (see text for explanation). Both the total and element-specific density profiles are plotted to include the experimental resolution as described previously.
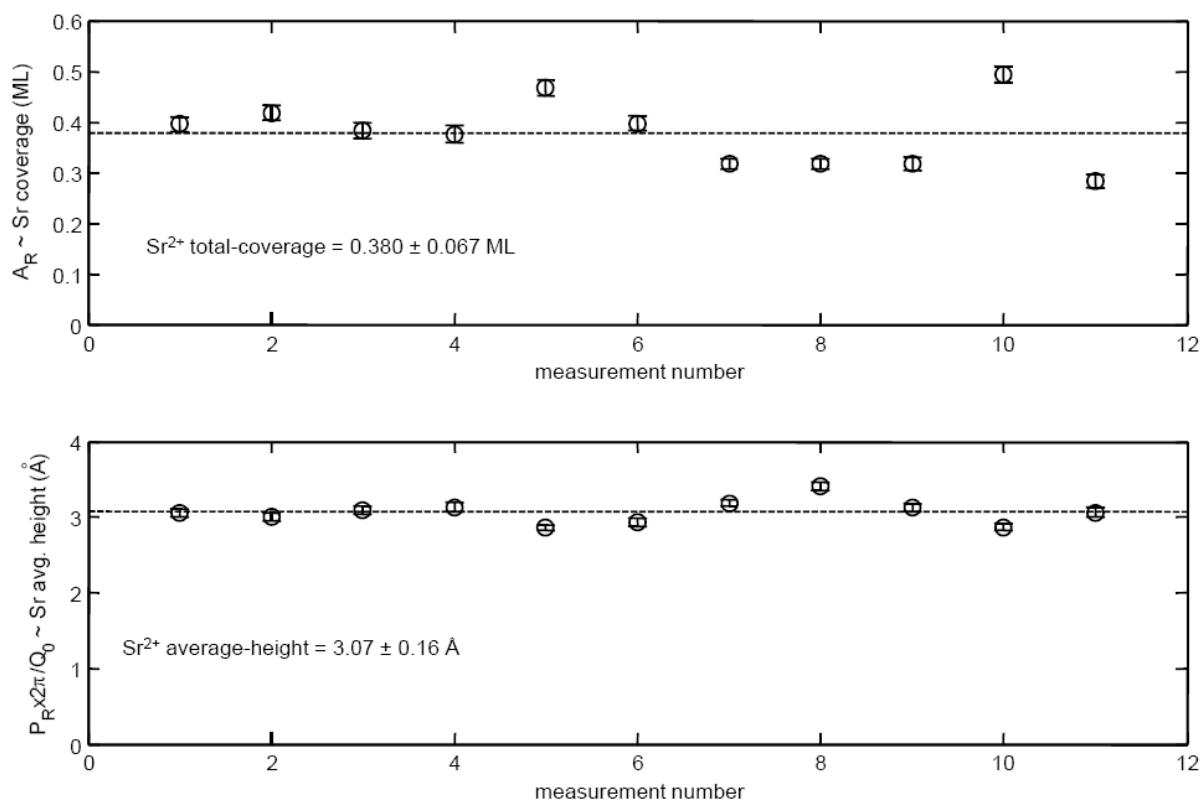
Figure 3.9: Evaluation of systematic errors and system stability in RAXR measurements of 0.1mM Sr^{2+} at pH 10.3. Top and bottom plots show the resonant amplitude A_R, and phase P_R (multiplied by $2\pi/Q_0$) values, respectively, of repeated measurements of the L=0.7 RAXR spectra during the course of the full set of Sr^{2+} data collection. The horizontal dotted lines indicate the average value of repeated measurements. These low-Q resonant amplitude and phase are indicative of the total-coverage and average-height of the ion distribution respectively.

Table 3.1: Final values of parameters from fitting of XR data, uncertainties of the last digits are shown in parenthesis.

	Rb^+	Sr^{2+}	Sr^{2+} with Na^+ [a] (model I)	Sr^{2+} with Na^+ [b] (model II)
Fit quality[c]				
χ^2	0.75	1.38	1.57	2.90
Surface relaxations				
δBO (Å)	0.079 (9)	0.05 (8)	0.07 (6)	-0.1 (1)
δTO (Å)	-0.03 (2)	0.12 (6)	0.23 (4)	0.10 (5)
δZ_1 (Å)	0.009 (1)	0.029 (5)	-0.014 (6)	-0.014 (8)
Δ_1 (Å)	-0.005 (7)	-0.07 (2)	-0.069 (9)	0.01 (1)
δZ_2 (Å)	0.0052 (8)	0.001 (2)	-0.004 (1)	-0.001 (2)
Adsorbed water and ion				
z_{AW} (Å)	3.446 (6)	4.1 (1)	3.27 (4)	3.4 (1)
occ_{AW} (ML)	2.70 (5)	0.8 (2)	1.6 (7)	0.6 (9)
$u_{AW}{}^d$ (Å)	0.28	0.28	0.28	0.28
$z_{ION}{}^e$ (Å)	3.72	3.05	-	3.13
$occ_{ION}{}^e$ (ML)	0.078	0.40	-	0.38
$u_{ION}{}^e$ (Å)	0.1	0.35	-	0.61
Bulk water				
type	layered	layered	layered	un-layered
d_{BW} (Å)	0.74 (3)	1 (2)	2 (2)	-
u_{BW} (Å)	0.45^d	0.5 (5)	0.8 (5)	0.45^d
$ubar_{BW}$ (Å)	1.6 (2)	1.4 (7)	1 (1)	-
z_{BW} (Å)	5.60 (4)	5.1 (2)	4.3 (3)	-
Extrinsic				
t_{BW}(water thickness^f, μm)	13 (2)	44 (5)	12 (5)	16 (7)
β (surface roughness)	0.176 (5)	0.16 (2)	0.16 (3)	0.18 (2)

[a] Oxygen-equivalent model for adsorbate structure, see explanation in text.
[b] A featureless bulk water profile used in this case.
[c] Fit quality denoted by deviation parameter, $\chi^2 = 1/(N-n) \sum(y-y_{calc})^2/\varepsilon^2$, where y denotes the data, y_{calc} the calculation, ε the uncertainty in the data, and the summation is over N data points. Here n is the number of fitting parameters.
[d] Parameter fixed during the fit.
[e] Value based on the penultimate RAXR data analysis in the XR/RAXR iterative analyses procedure described in text. The final RAXR analysis parameters and their uncertainties are listed in Table 3.2.
[f] Thickness of solution layer and a 8μ thick Kapton film.

Table 3.2: Parameters from fitting of RAXR data

	Rb$^+$	Sr^{2+}	Sr^{2+} with Na$^+$ (model I)	Sr^{2+} with Na$^+$ (model II)
Fit quality[a]				
χ^2 (model indep.)	1.3	2.4	1.7	1.7
χ^2 (model dep.)	3.1	5.6	4.2	4.3
Adsorbed Ion Structure				
z_{ION} (Å)	3.72 (3)	3.05 (16)[b]	2.85 (7)[b]	2.95 (+20/-7)[b]
occ$_{ION}$ (ML)	0.080 (3)	0.40 (7)[b]	0.35 (9)[b]	0.37 (9)[b]
u_{ION} (Å)	0.1[c]	0.35 (2)	0.57 (3)	0.58 (2)

---

[a] Fit quality denoted by deviation parameter, $\chi^2 = 1/N \ \sum(y - y_{calc})^2 / \varepsilon^2$, where y denotes the data, y_{calc} the calculation, ε the uncertainty in the data, and the summation is over N data points.
[b] Systematic uncertainty is shown since it was larger than the derived statistical error.
[c] Parameter fixed during fit.

Table 3.3: Final values of parameters from fitting of XR data, for Sr^+ with Na^+ case using layered water(iterated structure). This is the converged structure that had unphysical relaxations of BO and TO. This problem was not present when a featureless (i.e. error function) water profile is used (see main text). Uncertainties are shown in parenthesis.

	Sr^+ with Na^+
Fit quality	
χ^2	1.38
Surface relaxations	
δBO (Å)	-0.34 (2)
δTO (Å)	0.58 (6)
δZ_1 (Å)	0.008 (4)
Δ_1 (Å)	-0.09 (1)
δZ_2 (Å)	-0.007 (2)
Adsorbed water / ion	
z_{AW} (Å)	3.40 (4)
occ_{AW} (ML)	1.2 (3)
u_{AW}^a (Å)	0.28
z_{ION}^b (Å)	3.13
occ_{ION}^b (ML)	0.374
u_{ION}^b (Å)	0.62
Bulk water	
type	layered
d_{BW} (Å)	1.1 (7)
u_{BW} (Å)	0.5 (3)
$ubar_{BW}$ (Å)	1.4 (3)
z_{BW} (Å)	5.3 (1)
Extrinsic	
t_{BW}(water thickness μ)	8 (4)
β (surface roughness)	0.16 (2)

[a] Parameter fixed during fit.
[b] Ion layer parameters based on RAXR analysis.

of a single layer distribution for both Rb^+ and Sr^{2+} (observed from the amplitude and phase variation vs. Q of the spectra shown in Fig. 3.3). The assumed model of the ion distribution was a Gaussian layer with three parameters that were allowed to vary during the model-dependent fit. These were the layer height (z_{ION}), occupancy (occ_{ION}) and distribution width (u_{ION}). A single layer was sufficient to fit the data as the use of additional layers did not improve the quality of the fit. The density profiles obtained from these analyses are shown in Fig. 3.8. The density profiles from the two independent analyses (i.e., model-independent and model-dependent) agree quite well showing the internal consistency in the results. However, the model-independent coverage underestimates the intrinsic coverage of the ion distribution because of the absence of data the near Q=0.

This analysis reveals that both the Rb^+ and Sr^{2+} profiles can be described as a single layer above the rutile surface within the resolution of the current data. Rb^+ adsorbs at a greater height than Sr^{2+} (3.72±0.03 Å vs. 3.05±0.16 Å, respectively) as expected due to the larger ionic radius of Rb^+. Rb^+ also adsorbs with a lower coverage (0.080±0.003 ML vs. 0.40±0.07 ML, respectively, Figure 3.8 and Table 3.2). The width of the Rb^+ layer was found to be 0±0.2 Å, while that for Sr^{2+} was 0.40±0.07 Å. The weak variation in Rb^+ RAXR signals (Fig. 3.2) over the entire range of Q, leads to insensitivity to the actual distribution width, except to specify an upper limit of 0.2 Å. Therefore the parameter was fixed at the value of 0.1 during the final CTR analysis, as that is a typical value observed in previous studies[25]. Also shown in Table 3.2 are the RAXR analyses for the Sr^{2+} with Na^+ case based on the two different models of the non-resonant structure factor described above. The differences in the Sr^{2+} with Na^+ layer parameters for the two models are within the parameter uncertainties (ion coverages of 0.37±0.09 and

0.35±0.09 ML respectively, and ion heights of 2.95±0.07 and 2.85±0.07Å respectively, for model II and model I). While there appears to be a small decrease in the Sr^{2+} height in presence of Na^+ (by 0.1 to 0.2 Å), in comparison to Sr^{2+} without Na^+ (3.05±0.16 Å), this difference is within the systematic uncertainties in this measurement. We therefore conclude that the Sr^{2+} coverage and height are unaltered by presence of a background electrolyte within experimental uncertainties. One important difference between the Sr^{2+} and Sr^{2+} with Na^+ profiles is that the Sr^{2+} width is larger by ~0.25 Å in presence of Na^+.

3.4. Discussion

3.4.1 Comparison with Previous XSW and XR Results

Our results reveal specific adsorption of Rb^+ at 1mM which was not detected in previous XSW measurements[23], although it was measured at similar experimental conditions. In an XSW measurement, it is difficult to detect the coherently adsorbed component of an ion distribution when it is overwhelmed by incoherent contributions (e.g., diffuse ion distribution, the bulk ion concentration). In contrast, the RAXR measurement is interface-specific, and the observed modulation at these dilute ion concentrations is due solely to the adsorbed ions. The difference in results from XSW and RAXR therefore appears to be due to the incoherent fluorescence that obscured the intrinsic Rb^+ ordering in the XSW measurements. The Rb^+ layer height from our results is 0.28 Å higher than the previous results obtained at a higher concentration and pH (1M Rb^+, pH 12) using XR[25]. XR alone however is not capable of

providing element-specific information and measures only the total interfacial electron density. It is insensitive to small fractions of Rb^+ at sites other than the primary site. We cannot rule out however the possibility that this difference is intrinsic and associated with the different solution conditions.

The Sr^{2+} height measured here using RAXR (3.05±0.16 Å) is in excellent agreement with the previous XSW-measured height of 3.07±0.07 Å[23]. A more direct comparison with the XSW results can be made if we use our RAXR-derived Sr^{2+} distribution (i.e., ion coverage and distribution) to calculate the coherent coverage at the L=2 scattering condition associated with the rutile *110* reflection used in the XSW measurement. Our measured ion coverage and distribution correspond to an equivalent XSW coherent coverage of 0.31 ± 0.06 ML (compared to XSW measured coherent coverages, 0.16 – 0.44 ML). Therefore the RAXR and XSW results are quantitatively consistent in terms of the RAXR-measured ion height, and coverage.

We also calculate the coherent fraction, f, associated with the RAXR results by normalizing our L=2 coherent coverage by the observed Sr^{2+} occupancy, i.e., $f(Q) = A(Q)/occ_{ION}$ = 0.78. This value is lower than unity due to the reduction in coherent fraction with increasing Q because of the width of the ion distribution (u_{ION} = 0.35 ± 0.02 Å). This highlights that part of the nominally "missing" Sr^{2+} associated with the XSW coherent fraction was a result of the 22% reduction in $f(Q)$ from the intrinsic ion distribution width. This explains roughly half of the missing ions in the XSW measurement[22]. Additional contributions to the reduced XSW coherent fraction may include outer-sphere adsorbed Sr^{2+} as well as the presence of a diffuse profile.

Table 3.4: Estimation of adsorbed ion heights above the surface Ti-O plane for the six different inner-sphere (IS) adsorption sites. The estimation is based on simple geometrical closed packing, assuming the ions as solid spheres. The ionic radii assumed for the estimation are 1.49 Å for Rb^+, 1.13 Å for Sr^{2+}, and 1.40 Å for O^{2-}. The estimation assumes the bridging and terminal oxygens at ideal (bulk terminated) positions.

Site	Rb^+ height (Å)	Sr^{2+} height (Å)
Tetra-dentate (TD)	3.43	2.80
Bi-dentate (BOTO)	3.93	3.49
Bi-dentate (BOBO)	3.75	3.32
Bi-dentate (TOTO)	4.46	4.03
Mono-dentate (BO)	4.16	3.80
Mono-dentate (TO)	4.87	4.51

Our results also show that the Sr^{2+} distribution does not change significantly in terms of coverage and ion height (within ±0.1Å) in the presence of a background electrolyte, NaCl. This is consistent with previous XSW studies that found that even changing the background Na^+ concentration by three orders of magnitude did not affect the XSW-measured Sr^{2+} height and coverage[22]. It is expected that any OS species would be readily displaced by the background electrolyte[4]. The lack of any significant change in the average height or coverage is consistent with our conclusion that Sr^{2+} ions are adsorbed only as IS species. The observation of an increase in the distribution width for Sr^{2+} with Na^+ was unexpected. However, the calculated L=2 coherent fraction corresponding to these RAXR results is 0.51 in comparison to the XSW measured coherent fraction of ~0.6 for the same background electrolyte concentration. Therefore the measured root-mean-square width ($u_{ION} = 0.58 \pm 0.02$ Å) is in very good agreement with the XSW results.

3.4.2 Ion Binding Sites and Surface Speciation

As mentioned in Chapter 1, each of the six possible sites for inner-sphere adsorption of ions on the rutile (110) surface (Fig. 1.7) is nominally located at different vertical distances from the surface. This makes it conceptually possible to distinguish between them and infer the actual adsorption site from the measured one-dimensional ion profiles. We calculated the vertical heights for these sites (Table 3.4) with respect to the ideally terminated surface based on geometrical close packing constraints (i.e., the ions touching the surface oxygens to which they are bonded). This calculation was based on simple spherical model for the ion and surface oxygens with both BO and TO oxygens assumed to have the same ionic radius. This is different

from the more rigorous geometrical estimate by Predota et al[38], which included ion-oxygen distances based on pair correlation functions derived from molecular-dynamics simulations.

Our measured Rb^+ height of 3.72±0.03 Å is close to three possible adsorption sites. These include the tetradentate site (3.43 Å), and two bidentate sites, BOBO (3.75Å) and BOTO (3.93Å) (see Fig. 1.7 for the adsorption geometries at these sites). If the Rb^+ ions are assumed to occupy only a single IS site, the BOBO bidentate site is the site closest to our measured ion height. However, previous MD simulation work[56] has predicted a multi-site Rb^+ distribution, with dominant adsorption at the tetradentate site at 3.55 Å, and a weak adsorption (14% occupancy) at the bidentate height at 4.25 Å. We therefore re-analyzed the data with a two layer model with heights fixed at the tetradentate and bidentate heights found by MD[56] and allowed only the occupancies to vary. The total occupancy was unchanged (0.078±0.009) with primary adsorption in the tetradentate site (occupation of 91% ± 8%), and with a minority bidentate component (9% ± 9%). This model had a 5% increase in χ^2 (3.25 compared to 3.1 for the model in Table 3.2). While this difference is small, it is nevertheless a significant change in the quality of fit, and this is due primarily to the use of constrained ion heights obtained independently in the MD results. Our measured Rb^+ height (3.72±0.03 Å) can be compared with the *average* ion height from the MD results. Based on the reported relative occupancies of the multi-site IS species from MD[56], we calculated the average height of the IS Rb^+ distribution to be 3.66 Å, which is within 0.1 Å of the Rb^+ height from our results. Finally, we also estimated an average root mean squared width (σ_{avg}) of the multi-site IS Rb^+ based on the MD results. This was done by taking into account the *rms* widths of the individual tetra-dentate and bi-dentate layers from the MD results, and the relative occupancies of Rb^+ in these layers. We found σ_{avg} ~0.3 Å, which is comparable to, but

somewhat greater than, the ion width reflected by our Rb^+ RAXR data (0±0.2 Å). This comparison suggests that our results generally are consistent with the multi-site IS adsorption predicted by MD in terms of the ion heights and distributions, albeit with some quantitative discrepancies in the rms widths, although the present data do not have the spatial resolution to resolve the multiple IS sites (the current RAXR measurements have ~1 Å resolution).

In the case of Sr^{2+}, the *primary* adsorption site can be identified as the tetra-dentate since that is the site closest to our measured height of 3.05±0.16 Å. However, this measured value is 0.25 Å higher than the location of the tetra-dentate site expected based on our simple geometrical estimation (2.80 Å), indicating the possibility of a multi-site adsorption. The MD simulations had predicted that in addition to the primary tetra-dentate site, Sr^{2+} also occupies two bi-dentate sites (~20% and 10% occupation at the BOTO and TOTO sites, located at 3.55 Å and 4.05 Å, respectively)[56]. In fact, our measured Sr^{2+} distribution width (0.35±0.02 Å) is significantly larger than the *rms* width expected for species adsorbed at a single IS site (which is typically ~0.1 for Sr^{2+} based on MD results). The average distribution width (σ_{avg}) corresponding to the multi-site IS distribution predicted by MD is ~0.3 Å, which is in very good agreement with our measured Sr^{2+} width. This suggests that the experimentally measured single-layer height is actually an average of multiple unresolved sites (i.e., due to Sr^{2+} being distributed between the tetra-dentate and the two bi-dentate sites). The RAXR measured height (3.05±0.16 Å) also shows excellent agreement with the previous XSW measurement (3.07±0.07 Å), indicating that this result is robust. Previous density function theory (DFT) calculations found that the tetradentate Sr^{2+} is at a height of 2.85 Å[23], which is quite similar to our simple geometric estimate for this site. That the height for the tetradentate site is lower than our measured average height

(3.05±0.16 Å) is qualitatively consistent with a multi-site IS adsorption scheme for Sr^{2+}. We note, however, that there is a substantial discrepancy in the absolute Sr^{2+} height obtained by RAXR, XSW and DFT when compared with that predicted by MD. The average height corresponding to the multi-site distribution predicted by MD is 3.41 Å. There appears to be an overall height offset (for Sr^{2+}) between the MD predictions and the other results (i.e., RAXR, XSW and DFT). For example, the MD prediction for the tetradentate site is ~0.4 Å higher than that predicted by DFT. The source of this discrepancy is unclear.

The presence of minority IS sites in addition to the dominant tetradentate site for cation adsorption on rutile agrees qualitatively with previous surface complexation prediction[36], although the current results suggest that the minority sites are bidentate, rather than the predicted monodentate. This apparent presence of bidentate components is consistent with both MD[56] and recent MUSIC model predictions[46]. For Sr^{2+}, however, the present results show a greater tendency for the presence of multiple adsorption sites than predicted by the MUSIC model[46].

The rutile surface with a negative surface charge was previously suggested to be hydroxylated[33, 38] in which the TO sites exist primarily as adsorbed hydroxyl groups, and surface charge arises from the de-protonation of the BO sites (see Chapter 1 for further information about the hydroxylated and non-hydroxylated surfaces). While the x-ray measurements do not directly reveal the surface complexation, insight can be obtained by comparison of these results with the MD simulations that are able to differentiate between the hydroxylated and non-hydroxylated surfaces. We compared our measured ion heights with the average height corresponding to the distributions predicted by MD for the two surfaces. For the Sr^{2+} case, the average height predicted for the non-hydroxylated surface was ~0.1 Å higher than

that for the hydroxylated surface, and therefore our measured height is closer to the hydroxylated case. For Rb^+ however, the two surfaces were not distinguishable just based on the average height predicted by MD (since the same average height of ~3.66 Å was predicted for both surfaces). A significant difference between the MD results for the two surfaces, both in case of Rb^+ and Sr^{2+}, was that the non-hydroxylated surface was predicted to have comparable occupancies at the bidentate and tetradentate sites, while the hydroxylated surface had a dominant adsorption at the tetradentate site (with secondary bi-dentate adsorption). We tried to explain the RAXR results by fitting the data with fixed ion heights based on the MD results of a non-hydroxylated surface, and allowing the occupancies to vary. The final structure had only one ion layer with non-zero occupancy. This suggests that the hydroxylated surface model is in better agreement with the RAXR data.

3.4.3 The Uncharacterized Portion of Ion Profile

Our measured Sr^{2+} distribution width shows good agreement with the average IS width expected from the multi-site IS adsorption predicted by MD simulations for the hydroxylated surface[56]. The simulations had also predicted that 5% of Sr^{2+} is present in the form of an OS species. While our results do not show evidence for an OS component, we can estimate an upper limit on the amount of Sr^{2+} adsorbed as an OS species based on the uncertainties in our measured ion height. We calculate the average height of a Sr^{2+} distribution containing both IS and OS species, with inner-sphere layer parameters based on our measurements, and the outer-sphere layer height and width based on the MD predictions reported previously (~6.0 Å and ~0.5 Å respectively). With these assumptions, we can estimate that the outer-sphere occupancy of ≤ 6 % leads to average heights that are consistent with our measurement uncertainties (±0.16 Å).

The observation of a predominant IS distribution of Sr^{2+} on rutile raises a question: why does Sr^{2+} adsorb as an IS species on rutile, when it adsorbs as a mixture of IS and OS species on other mineral surfaces, such as muscovite mica? Recent surface complexation models[36] reveal that the free energy for the ion adsorption reaction can be separated into three components: an electrostatic energy component resulting from either a repulsive or attractive interaction between the ion and the near-surface species (e.g. surface oxygen or near-surface substrate metal atom), a Born solvation energy component associated with the free energy of hydrated ions, and a free energy component intrinsic to the adsorbing ionic species. The solvation term, which opposes IS-adsorption and is primarily dependent on the inverse of the dielectric constant of the substrate, can determine whether the ions adsorb as IS or OS species. Specifically, it was predicted that the solvation term would be negligible for high dielectric constant materials, such as rutile, thus favoring IS adsorption. Therefore our observation of a lack of OS species on rutile appears to be consistent with these predictions. Park et al. recently suggested that IS/OS partitioning on mica is controlled by the change in the electrostatic and hydration energies between the two species[91]. Because the dielectric constant of rutile is >10 times that of mica, the hydration energy difference between IS and OS is expected to be significantly lower on rutile, thereby promoting IS speciation. Additionally, in case of rutile, the surface charge is located at the BO and TO sites which are situated (at ~1.3 and 2.0 Å respectively) above the surface, unlike mica which has a fixed lattice charge that is distributed at sites below the surface. This suggests that there will be a larger electrostatic energy difference between the IS vs. OS sites on rutile as compared to mica, which would tend to further stabilize the IS species on the rutile surface.

Since the previous XSW results had found that the IS species accounted for approximately half of the total adsorbed Sr^{2+} based on the XSW coherent fraction of 0.55, our limit of <6% of OS ions, combined with an expected 22% reduction in L=2 coherent fraction (as obtained from our RAXR results) based on our IS distribution width, apparently does not account for all of the remaining ions. This suggests that the presence of an OS species does not fully explain the differences in RAXR and XSW measurements. This implies that some of the unaccounted for Sr^{2+} could either be extrinsic (e.g., associated with variations in the bulk ion concentration) or intrinsic (e.g., present in the diffuse double layer). Our measured Rb^+ coverage of 0.080±0.003 ML, which shows excellent agreement with the previous MUSIC model prediction of specifically-adsorbed Rb^+ coverage[22], apparently explains only part of the total Rb^+ coverage (i.e., including IS/OS and diffuse species) expected under these conditions[54, 55]. We see no evidence of significant OS adsorption for Rb^+ which is in agreement with results on other minerals. It is therefore likely that any remaining Rb^+ ions are present in the diffuse layer. Based on linearized Poisson-Boltzmann theory[1], it is expected that a diffuse layer of monovalent ions will have a Debye length of ~100 Å (at 1mM concentration). Probing this broadly distributed portion of the ion distribution will require measurements at much lower scattering angles ($Q<0.1 Å^{-1}$) than those included here.

3.5 Conclusions

These results have extended the understanding of ion adsorption at the rutile–electrolyte interface by direct measurements of adsorbed Rb^+ and Sr^{2+} distributions[92]. X-ray reflectivity

and resonant anomalous x-ray reflectivity techniques were applied to probe the distribution of these ions at dilute concentrations and it was found that both Rb^+ and Sr^{2+} adsorb as inner-sphere species above the surface. Our measured Rb^+ height is in good agreement (within 0.1 Å) with the average height of the multi-site inner-sphere Rb^+ distribution predicted by the MD simulations[56] that included both tetradentate and bidentate IS adsorption. The measured Sr^{2+} distribution confirms the previous XSW results in terms of Sr^{2+} height and coverage. We find that our measured Sr^{2+} vertical distribution width (0.35±0.02 Å) is significantly broader than the typical width expected for an adsorbed species at a single IS site (~0.1 Å based on MD results) and is consistent with the multi-site inner-sphere species predicted by MD simulations[56] (with a mixture of tetradentate and bidentate adsorption modes). This shows that part of the apparently "missing" Sr^{2+} from previous XSW measurements was the result of the multi-site ion distribution. These results are therefore the first experimental confirmation of the multi-site adsorption distribution of cations at the rutile-electrolyte interface as predicted by MD[56]. Our results for both Rb^+ and Sr^{2+}, in comparison with previous MD simulations, confirm that the rutile surface is hydroxylated, in agreement with earlier conclusions by Predota et al[38]. The background electrolyte (Na^+) was found to have no significant effect on the adsorbed Sr^{2+} height and coverage within the systematic errors of our measurements, while we observe an increase in the width of the Sr^{2+} layer in presence of Na^+. It is not clear how the presence of Na^+ would increase the width of the Sr^{2+} distribution, although the present results might suggest that this is achieved through a electrolyte-dependent partitioning between the different adsorption sites. Our results do not find any significant outer-sphere species of Sr^{2+} on rutile as predicted by MD simulations (the simulations had predicted 5% of Sr^{2+} in the OS), however we can place an upper

limit of ~6% on the amount in the outer-sphere if present at the height predicted by MD. The understanding of the multi-site IS adsorption behavior can be furthered by measuring the Sr^{2+} distribution in presence of a competing species that is also expected to be strongly IS-adsorbed (such as another divalent cation, e.g. Zn^{2+}), and observing the changes in the partitioning of Sr^{2+} at the different IS sites.

Chapter 4 : A Direct-Method for Imaging Elemental Distribution Profiles with Long-Period X-ray Standing Waves

4.1 Introduction

An introduction to the basics of XSW was provided in Chapter 2. Analysis of XSW data has traditionally relied on model-dependent approaches. That is, the predictions of models of the elemental distribution were used to explain the observed fluorescence yield modulation. In the case of single crystal Bragg-XSW, it was shown that the phase of the XSW corresponds to the phase of the element-specific structure factor at the momentum transfer of the Bragg reflection condition[93]. The amplitude and phase of a Fourier coefficient of XRF-selected atomic density (i.e., the coherent fraction and coherent position) can therefore be obtained directly from the fluorescence yield modulation.[76, 94] Comparison of these measured amplitudes and phases for different $H=hkl$ reflections with the model-calculated values allows the structure to be determined. For the long-period XSW, model-calculated fluorescence yields are typically compared with experimental data and fit through least-squares approaches. In all cases, the comparison between data and model-calculations is done after the X-ray reflectivity data are analyzed so that the XSW electric field intensity is known.

While the phase-sensitivity of XSW data has been long acknowledged, it was demonstrated only recently that elemental distributions can be obtained directly from the

experimental Bragg-XSW data through a fully model-independent analysis. This is obtained by Fourier-inversion of the set of *hkl* Fourier amplitudes and phases obtained from each Bragg reflection. This was shown for the case of impurity atom distributions within a crystal[95], as well as for species located above the crystal surface[88, 96-98]. This model-independent XSW analysis has only been applied to single crystal Bragg-XSW measurements. Recently Bedzyk demonstrated a different model-independent approach that is applicable to the TER-XSW regime[99]. Specifically, he showed that the fluorescence yield measured near the substrate critical angle can be converted to a modified-yield whose inverse Fourier transform directly recovers the elemental distribution of interest. This approach is limited to the TER-XSW regime because it assumes that the phase of the reflected wave that participates in XSW varies linearly with scattering angle. Nevertheless, it shows that such model-independent approaches are applicable, in principle, to the long-period XSW regime.

Here we describe a generalized model-independent method for reconstructing elemental distribution profiles from XSW data. This approach is valid for the long-period XSW including TER and PML regimes. It also explicitly includes absorption so that it is applicable both within a material and above a reflecting surface. This approach makes use of the known complex reflectivity coefficients (determined from the reflectivity analysis) and assumes that the element-specific structure factor varies slowly enough with momentum transfer, Q, so that the fluorescence yield variation within a given Q-interval, $|Q- Q^0| < \Delta Q/2$ (where Q^0 and ΔQ are the center and width of the Q-interval, respectively), can be described by a fixed amplitude, $A(Q^0)$, and phase, $P(Q^0)$, of the element-specific structure for that Q-interval. Where necessary, the amplitude and phase variation within a given interval can be described by a linear Taylor series

expansion. The formalism is applied to analyze Ti-Kα yield for a tri-layer system consisting of a TiO$_2$ thin film grown on a Si/Mo bi-layer on a Si substrate, with the sample in air (*ex situ*) and in contact with an aqueous solution (*in situ*).

4.2 Model-Independent Method

4.2.1 XSW Fluorescence Yield in an Attenuating Medium

Refer to the case of interface between two *absorbing* media, 2 and 3 (medium 1 being the vacuum layer), discussed in Chapter 2 (Fig. 2.7). The expression for total E-field intensity in medium 2 given in eqn. 2.4.3 can be simplified as,

$$I_2(Q_2, z) = \frac{|\boldsymbol{\varepsilon}_2^T|^2}{|E_1|^2} = \frac{|E_2(Q_2)|^2}{|E_1|^2} \; e^{+Q_2'' z} \; \left[1 + R_2 \, e^{-2 Q_2'' z} + 2\sqrt{R_2} \, e^{-Q_2'' z} \cos\{v_2 - Q_2' z\}\right] (4.2.1)$$

Here the factor $e^{+Q_2'' z}$ represents the attenuation of the incident wave in medium 2 that includes both the linear absorption as well as extinction (i.e. attenuation of the evanescent wave that occurs for incident angles below the critical angle). Therefore Q_2'' is an effective linear absorption coefficient. The pre-factor representing the E-field intensity at z=0 just above interface 2,3 is obtained from the relation,

$$|E_2(Q_2)|^2 = |E_1|^2 \; |T_{1,2}|^2 e^{-Q_2'' t_2} \tag{4.2.2}$$

where $T_{1,2}$ is the transmission coefficient at the vacuum/medium-2 interface based on Parratt's formalism[60, 67], and t_2 is the thickness of medium 2. Setting $|E_1|^2 = 1$, we obtain the normalized E-field intensity at any height z within medium-2 as,

$$I_2(Q_2, z) = |E_2(Q_2)|^2 \left[e^{+Q_2'' z} + R\, e^{-Q_2'' z} + 2\sqrt{R_2}\, \cos(v_2 - Q_2' z) \right] \qquad (4.2.3)$$

The first exponential term in the above equation represents the attenuation of the incident beam, the positive sign denotes that the beam is attenuated with *decreasing* height above the interface. The second exponential represents the attenuation of the reflected beam, which is attenuated with increasing height above the interface. The third term which is a result of coherent interference between the incident and reflected waves is unaffected by the attenuation in the medium.

Based on the dipole approximation for the photoelectric effect, the fluorescence yield from an element with distribution $\rho(z)$ within medium 2 is given by,

$$Y(Q_2) = \int_{z=0}^{t_2} \rho(z)\, I_2(Q_2, z)\, dz \qquad (4.2.4)$$

Here it is assumed that the effective absorption length in medium-2 for the emitted fluorescent X-ray is much larger than $\frac{t_2}{\sin(\alpha)}$ where α is the fluorescence emission take-off angle. Substitution of the Eq. (4.2.3) into the above expression, and expanding the cosine term yields,

$$Y(Q_2) = |E_2(Q_2)|^2 \left[Y_0(Q_2) + R_2(Q_2)\, Y_0(-Q_2) + \sqrt{R_2(Q_2)}\, \{ F^*(Q_2) \exp(iv_2) + \right.$$

$$\left. F Q2 \exp{-\acute{v}2} \right. \qquad (4.2.5)$$

The first term in the equation above, $Y_0(Q_2) = \int_{z=0}^{t_2} \rho(z) \, e^{+ Q_2'' z} \, dz$, is the yield due to the incident beam only, i.e., the yield when R=0. And here,

$$F(Q_2) \equiv \int_{z=0}^{t_2} \rho(z) \, e^{\, i \, Q_2' z} \, dz = \rho^{2D} \, A(Q_2) \, \exp[i \, 2\pi \, P(Q_2)] \qquad (4.2.6)$$

is the structure factor (or Fourier transform) of the XRF-selected elemental distribution, $P(Q_2)$ the phase of the structure factor, and $A(Q_2)$ the amplitude of the normalized structure factor $F(Q_2)/\rho^{2D}$. Here $\rho^{2D} = \int_{z=0}^{t_2} \rho(z) \, dz$ is the 2D atom number density of the fluorescing species, also referred to as the total coverage. The yield can be normalized to ρ^{2D},

$$\frac{Y(Q_2)}{\rho^{2D}} =$$

$$|E_2(Q_2)|^2 \left[\frac{Y_0(Q_2)}{\rho^{2D}} + R_2(Q_2) \frac{Y_0(Q_2)}{\rho^{2D}} + 2\sqrt{R_2(Q_2)} \, A(Q_2) \cos\{v_2(Q_2) - 2\pi P(Q_2)\} \right] \qquad (4.2.7)$$

We now consider two cases of interest in which the above expression can be simplified. The first is a limiting case of a narrow distribution located significantly above interface 2,3, with an average height z_0, and distribution width Δz. When $\Delta z \ll 1/Q_2''$, (the effective absorption length), the variation of the attenuating exponential factor in the expression for $Y_0(Q_2)$, over the range of Δz can be neglected, to obtain,

$$\frac{Y(Q_2)}{\rho^{2D}} \cong$$

$$|E_2(Q_2)|^2 \left[e^{+ Q_2'' z_0} + R_2(Q_2) \, e^{- Q_2'' z_0} + 2\sqrt{R_2(Q_2)} \, A(Q_2) \cos\{v_2(Q_2) - 2\pi P(Q_2)\} \right] \qquad (4.2.8)$$

Here the center of the distribution, z_0, is an unknown quantity, along with A and P, which can be determined from the analysis of the $Y(Q_2)$ data, as illustrated later in this paper. We also note that $z_0 = 2\pi P(Q_2)/ Q_2$ in the limit of $Q_2 \to 0$.

The other case of interest is for distributions that are located near interface 2,3 ($z \ll 1/Q_2''$), where Eq. (4.2.7) can be simplified by applying a first order Taylor series expansion to the exponential term in the expression for $Y_0(Q_2)$,

$$Y_0(Q_2) \cong \int_{z=0}^{t_2} \rho(Z) \left[1 + Q_2'' z\right] \, dz = \rho^{2D} + Q_2'' <z> \rho^{2D} \qquad (4.2.9)$$

where $<z> = \frac{\int_{z=0}^{t_2} \rho(z) z \, dz}{\rho^{2D}}$ is the average height of the distribution. The term $Y_0(-Q_2)$ is also expanded similarly, to obtain,

$$\frac{Y(Q_2)}{\rho^{2D}} \cong |E_2(Q_2)|^2 \left[1 + R_2(Q_2) + 2 \sqrt{R_2(Q_2)} \, A(Q_2) \cos\{v_2(Q_2) - 2\pi P(Q_2)\} \right.$$

$$\left. + <z> Q_2'' \left(1 - R_2(Q_2)\right)\right] \qquad (4.2.10)$$

We now evaluate the first order term in the expansion of the attenuation factor, $e^{+ Q_2'' z}$, used in the above derivation, for the case of an elemental distribution in an aqueous medium (in which case the attenuation length of 17 keV X-rays in water is ~10 mm). At the critical angle of the aqueous medium (Q = 0.022 Å^{-1}), the contribution of this term to the fluorescence yield is less than one percent for distribution widths less than ~1200 Å, and becomes smaller with increasing angles (since it is inversely related to Q). Since the Ti distribution probed in this study

is only ~10-20 Å thick, it is reasonable to exclude this attenuation term. In this case, the expression for fluorescence yield becomes,

$$\frac{Y(Q_2)}{\rho^{2D}} \cong |E_2(Q_2)|^2 \left[1 + R_2(Q_2) + 2\sqrt{R_2(Q_2)}\, A(Q_2) \cos\{v_2(Q_2) - 2\pi\, P(Q_2)\}\right] \qquad (4.2.11)$$

In an XSW experiment Y is measured, while R and v are known (in principle) from analysis of the reflectivity measurement. The only unknowns therefore are $A(Q_2)$ and $P(Q_2)$ which can be extracted from the data using the model-independent method discussed below. This equation is similar to that used in Bragg-XSW analysis with the difference that here A and P are continuous functions of Q_2, whereas in the Bragg-XSW case, A and P are treated as constants referring to a specific Bragg diffraction condition.

Applying a first order Taylor series expansion to A and P over a region of width ΔQ_2 centered at $Q_2 = Q_2^0$, we obtain: $A(Q_2) = A_{Q_2=Q_2^0} + \left(\frac{dA}{dQ_2}\right)_{Q_2=Q_2^0} (Q_2 - Q_2^0)$, and $P(Q_2) = P_{Q_2=Q_2^0} + \left(\frac{dP}{dQ_2}\right)_{Q_2=Q_2^0} (Q_2 - Q_2^0)$, and substituting in Eq. (4.2.11),

$$\frac{Y(Q_2)}{\rho^{2D}} = |E_2(Q_2)|^2 \left[1 + R_2(Q_2) + 2\sqrt{R_2(Q_2)} \left(A_0 + \frac{dA_0}{dQ_2}(Q_2 - Q_2^0)\right) \cos\left\{v_2 - 2\pi\left(P_0 + \right.\right.\right.$$

$$\left.\frac{dP_0}{dQ_2}(Q_2 - Q_2^0)\right)\right] \qquad (4.2.12)$$

Expanding the expression to first order in the gradient terms, the above equation transforms to,

$$\frac{Y}{\rho^{2D}} = |E_2(Q_2)|^2 \left[1 + R_2 + 2\sqrt{R_2}\, A_0 \cos(v_2 - 2\pi\, P_0) + 2\sqrt{R_2}\left\{\frac{dA_0}{dQ_2}\cos(v_2 - 2\pi\, P_0) + \right.\right.$$

$$\left.\left. A_0\, 2\pi\, \frac{dP_0}{dQ_2}\sin(v_2 - 2\pi\, P_0)\right\}(Q_2 - Q_2^0)\right] \qquad (4.2.13)$$

This shows that the the fluorescence yield near Q^0 is determined by A_0 and P_0, while the variation farther away from Q^0 is controlled increasingly by the gradient terms $\left(\frac{dA}{dQ_2}\right)_{Q_2=Q_2^0}$ and $\left(\frac{dP}{dQ_2}\right)_{Q_2=Q_2^0}$. The four unknowns in the above equation $(A_0, P_0, \frac{dA_0}{dQ_2}$ and $\frac{dP_0}{dQ_2})$ can be extracted by a model-independent fit of Eq. 4.2.13 to the measured yield data vs. Q_2 in a region of width ΔQ_2. If the entire range of data is divided into separate segments of width ΔQ_2, and each segment is fit separately to the above equation, a series of amplitudes and phases (and their gradients, if needed) can be obtained. If the chosen segment width ΔQ_2 is sufficiently small, such that there is no significant variation in the structure factor for the elemental distribution over this region, the fluorescent yield variation within each segment can be fit with just the A_0 and P_0 of that segment. The elemental distribution $\rho(z)$ can then be directly generated by the Fourier-inversion, using the relation:

$$\rho(z) = \frac{1}{2\pi} \sum_{j} \left\{ A_j \exp\left[i\, 2\pi\, P_j\right] \exp\left(-i\, Q_2^j z\right) \Delta Q_2 \right\} \qquad (4.2.14)$$

Here Q_2^j is the center of the jth segment, and the summation is over all segments into which the data is divided. The recovered profile will be intrinsic with sufficient sampling of A and P (i.e., in terms of the sampling frequency which determines the size of the Fourier window, and the maximum momentum transfer which determines the spatial resolution of the recovered profile).

Eq. (4.2.13) is also applicable to the case where the X-ray attenuation over the extent of the elemental distribution is considerable (e.g. for a 1000 Å or wider distribution in an aqueous medium), if the extra term $<z> Q_2'' \left[1 - R_2(Q_2)\right]$ is added in the expression for the

fluorescence yield (Eq. (4.2.10)). In this case however, there is an additional unknown quantity, <z>, which can be used as an extra parameter during the model independent fit of the data. Similarly, for the limiting case of a narrow distribution far away from the interface (Eq. (4.2.8)), z_0 can be used as an additional parameter during the model independent fit although its value is determined by $P(Q_2)$.

4.3 Materials and Methods

4.3.1 Sample Description

Measurements were conducted on a tri-layer system consisting of TiO_2, Si and Mo layers grown on Si substrate. The starting substrate was a 2.5 mm thick, single-side polished, 150 mm diameter Si(001) wafer. The wafer surface had a root mean square (rms) roughness of 3 Å as measured using x-ray reflectivity (Fig. 4.3). The wafer was diced into several 12-mm by 37-mm sized samples. These rectangular Si substrates were then mounted on a specially designed plate to hold the individual pieces separately, and were coated using sputter deposition with Si and Mo layers (with expected thicknesses of 540 Å and 60 Å, respectively). The top layer of TiO_2 with nominal thickness of 14 Å was then grown by atomic layer deposition (ALD)[100] using 20 consecutive 2 sec. exposures of titanium tetrachloride and water with 5 sec. purge periods. The substrate temperature was 100°C and the reactor base pressure was 1.1 torr of flowing (360 mL/min) UHP nitrogen. The samples were degreased with acetone, methanol and de-ionized water in a sonicator before the sputter deposition, before the ALD growth, and before the X-ray measurements.

Ex situ x-ray measurements were performed with the sample held in air. The *in situ* x-ray measurements were conducted in a thin-film cell geometry[17] with a Kapton film used to enclose the aqueous layer on the sample surface. The aqueous solution used for the *in situ* case was a 0.2 mM RbOH solution at pH 10.3. This solution condition was chosen as part of an effort to measure ion distributions at the oxide-water interface, the results of which will be published elsewhere.

4.3.2 Experimental

X-ray reflectivity and X-ray standing waves measurements were conducted at beamline 33BM-C at the Advanced Photon Source (APS) at Argonne National Laboratory. The incident x-ray energy during the measurements was 17.00 keV. The measured beam size at the sample was 0.05 mm-high by 1 mm-wide, with a flux of $\sim$2 x 10^{10} x-ray photons/second. The reflected intensity was measured using a Cyberstar scintillation detector, while the Ti-K_α fluorescence was collected using a SII NanoTechnology Inc. Vortex detector. An ion chamber with N_2 gas was used as monitor of the incident flux to which the data was normalized before analysis. A linear background was subtracted from the Ti-K_α yield data based on the background around the peak in the multi-channel analyzer (MCA) spectrum. A typical MCA spectrum measured *ex situ* is shown in Fig. 4.5 (see Fig. 5.1 for typical *in situ* MCA spectra). Corrections due to the detector dead-time[12] and due to the variation of the beam footprint on the sample with incident angle were applied to the yield data. Data for $Q < 0.026$ Å^{-1}, where beam footprint on the sample exceeded the sample length, were not included in the reflectivity and Ti-yield analysis.

The Ti coverage was estimated from x-ray fluorescence yield measured in both *ex situ* and *in situ* environments. Calibration of the absolute elemental coverage used the Sr-K$_\alpha$ yield from a standard sample (a Sr implanted Si wafer with 10.6 Sr/nm^2, calibrated with Rutherford backscattering[12]), taking into account the differences in the elemental absorption cross-section and the K$_\alpha$-fluorescence cross-section (yield) for the two elements, as well as the difference in the detector efficiency at the two fluorescence energies. The measured fluorescence yield was corrected for attenuation through air before reaching the detector, while additional corrections for attenuation of the fluorescence yield as well as of the incident beam through the Kapton and solution layers were included for the *in situ* measurements.

4.4 Results

4.4.1 Results from Simulations

We first demonstrate the feasibility of the model-independent formalism by applying it to simulated fluorescence yield data generated from a model calculation for incident X-ray energy of 17.00 keV. The simulated data was generated by an augmentation of Parratt's recursion formulation[68, 101, 102]. The model structure is a Si/Mo bi-layer on a Si substrate (black line in Fig. 4.1A), where the Si and Mo layers are 560 Å and 60 Å thick, respectively, that is similar to the samples investigated below in the experimental studies. The simulated reflectivity from this layered structure with $\sigma = 1$ Å *rms* interface roughnesses is shown in Fig. 4.1B. Notice that there is a sharp drop in the reflectivity at the Si critical angle corresponding to $Q_C = 0.032$ Å^{-1}.
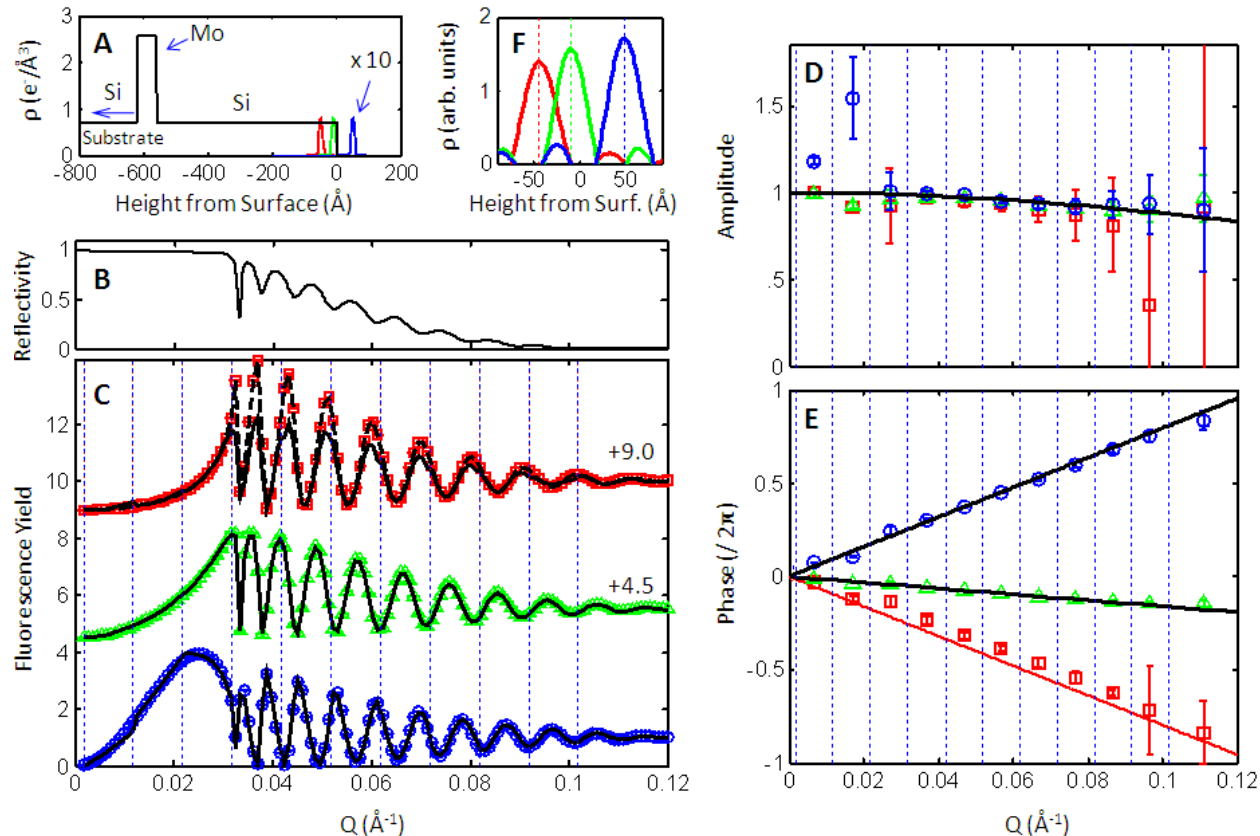
Figure 4.1: Model-independent formalism applied to simulated fluorescence yield data for Si/Mo bi-layer on Si substrate, for three assumed Gaussian elemental distributions, each with $\sigma = 5$ Å. (A): The density profile (black) used in E-field intensity calculation. The 3 elemental distributions shown are for Gaussian profiles centered at 50 Å above (blue), 10 Å below (green), and 50 Å below (red) the top Si surface. (B): Simulated reflectivity vs. Q calculation. (C): The simulated fluorescence yield data (symbols) and model-independent fits (solid lines, based on electric field intensities in vacuum). The dashed black line shown for the case of the Gaussian located 50 Å below the surface is the model-independent fit based on the use of electric field intensities inside the Si layer, and including x-ray absorption in the medium as described by Eq. (4.2.8). The data are offset vertically for clarity. (D) & (E): The model-independently derived A and P (symbols), and those based on the assumed models (lines). (F): The recovered profiles.

The target elemental profiles that will be recovered are represented by Gaussian distributions (shown in Fig. 4.1A) with widths of $\sigma = 5$ Å, centered at 50 Å above (blue), 10 Å below (green), and 50 Å below (red) the top Si surface. (In these simulations the target elemental profiles will not affect the primary E-fields by refraction or absorption). These height differences lead to differences in the simulated fluorescence yield data for the three cases (Fig. 4.1C), where the first peak in the TR region is present below the Si critical angle ($Q_C \sim 0.032$Å^{-1}) for the Gaussian located above the surface, while almost at and slightly above Q_C for the profiles centered 10 Å and 50 Å below the surface, respectively. This is consistent with a XSW node being at the top surface at $Q = 0$ and the first XSW anti-node sweeping inward toward the surface as the incident angle increases and arriving at the top Si surface when the incident angle equals Q_C for Si.

The simulated yield data is fitted with the model-independent formalism discussed above to recover the elemental profiles, first using the electric fields in vacuum (i.e. using R_I, v_I, and E_I corresponding to the air-Si interface). This is done to illustrate the situation in which the elemental profile is initially unknown. The simulated XRF yield data are assigned a fixed uncertainty of 0.1%. The data are divided into segments of width $\Delta Q = 0.01$ Å^{-1} (which gives sufficient sampling to locate distributions up to $2\pi/\Delta Q = 600$ Å above the surface) as shown by the vertical dashed lines in Fig. 4.1C, and the fluorescence yield within each segment is fitted with only two parameters corresponding to the amplitude and phase $\left(A(Q^j) \text{and } P(Q^j) \right)$. Note that the calculated fluorescence yield does not show any significant discontinuities at each segment boundary, suggesting that the chosen segment width was appropriate. The model-independently derived A and P (symbols in Figs. 4.1D and 4.1E), are compared with the

expected values of A_{calc}, and P_{calc}, (lines in Figs. 4.1D and 4.1E, respectively) that were obtained from the calculated structure factors, F, for the Gaussian profiles, given by,

$$F(Q) = \exp\left(-\frac{1}{2}\,\sigma^2 Q^2\right)\exp(i\,Q\,Z_0) \;=\; A_{calc}(Q)\,\exp[i\,2\pi\,P_{calc}(Q)] \qquad (4.4.1)$$

where Z_0 is the center and σ the width of the Gaussian layer. Using Eq. (4.2.14), the Fourier-inversion of the derived amplitudes and phases yields the density profiles (Fig. 4.1F). The recovered mean positions of the distributions in Fig. 4.1F match (within 0.5 Å) the expected Z_0 values from the original Gaussians shown in Fig. 4.1A for the cases of 10 Å below the surface and 50 Å above the surface. In these cases, the fluorescence yield data is also reproduced well by the formalism (solid lines in Fig. 4.1C). The recovered position for the Gaussian located 50 Å below the surface, however, differs from the actual position by 6 Å. In that case, the fluorescence yield data are not well-reproduced by the model-independent formalism (red line in Fig. 4.1C). This is due to the use of electric field intensities appropriate for the vacuum layer instead of those present in the silicon substrate (although this limitation was also present for the profile that was 10 Å below the surface; in that case, the change in electric field intensities was small due to its proximity to the interface).

We then used the electric field intensities inside the Si layer to fit the fluorescence yield for the Gaussian located 50 Å below the surface. This was done by using the reflection coefficients (i.e. R_2, v_2, and E_2) corresponding to the Si-Mo interface in the analysis. In this case, we used the phase gradient parameter dP/dQ_{Si} during the fit, in addition to the A and P parameters, since the distribution was at a large height with respect to the Si-Mo interface (since the Gaussian located 50 Å below the surface is at a height of 510 Å from the Si-Mo interface),

and therefore the phase variation could not be treated as constant over the segment width ($\Delta Q_{Si} =$ 0.01 Å^{-1}). In this case it was also important to include x-ray absorption inside the Si layer, which was significant below the critical angle. This was done by use of Eq. (4.2.8) and using z_0 as an additional parameter in the fit. This approach gave excellent agreement with the fluorescence yield data, both above and below the critical angle (dashed line in Fig 4.1C). The average height of the distribution was obtained simply from the parameter z_0 (Eq. (4.2.8)), which was found to be 509.9 Å with respect to the Si-Mo interface, or 50.1 Å below the top surface (close to the expected 50 Å). The height of the distribution was also obtained from the density profile reconstructed from the derived amplitudes and phases, which was found to be centered at 510 Å above the Si-Mo interface, exactly as expected. In the calculations described above for the Gaussian distributions, the model-independent calculations used the E-fields based on the Si/Mo bi-layer, and neglected any contribution to the electric field intensity due to the presence of the elemental profile. When the presence of the elemental distribution significantly alters the E-

fields, it should be included in the E-field calculations. Since the reflectivity of the system is measured in an XSW experiment along with the fluorescence yield, this is automatically included when the E-fields are based on the analysis of the experimental reflectivity data.

The analysis so far has extracted A(Q) and P(Q) of the elemental profile using $\Delta Q = 0.01$ Å^{-1}, and the gradient parameters were neglected (except for the last example in which the reflection coefficients were referenced to the Si-Mo interface and where the phase gradient term was included). We now illustrate the conditions under which fixed amplitudes and phases can be used, and when the gradient parameters become important. This is shown in Fig. 4.2 for a distribution consisting of two Gaussian layers located at and 50 Å above the surface (inset in Fig.
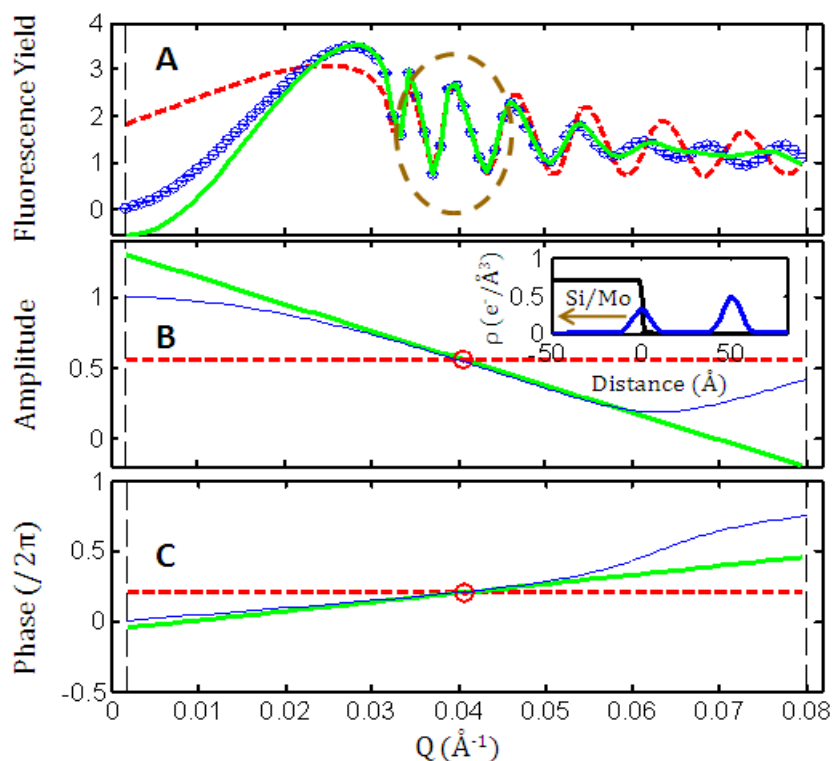
Figure 4.2: Illustration of relative benefits of model-independent analysis using fixed values of $A(Q^0)$ and $P(Q^0)$ within segment ΔQ at Q^0, vs. using linearly varying A & P within each segment. Data are simulated for a Si/Mo bi-layer on Si substrate for a 2-layer elemental distribution consisting of Gaussians centered at & 50 Å above the surface (shown in inset in B), each with $\sigma = 5$ Å. (A): The simulated fluorescence yield data (blue circles), and two model-independent calculations: without (dashed red line) & with (solid green line) the gradient terms of A & P included. In the first case, the yield is calculated using $A = A(Q^0)$ and $P = P(Q^0)$. In the second case, additional slope parameters dA/dQ and dP/dQ are included based on the gradients of A & P obtained from actual elemental structure factor at Q^0. (B) & (C): The variation of A & P, respectively, for the actual elemental distribution (blue circles), along with the model-independent calculation with fixed values defined at $Q^0 = 0.04$ Å^{-1} (red dashed lines), and when the gradient terms are included (green lines).

4.2B). The simulated fluorescence yield data (blue circles in Fig. 4.2A) is compared against two model independent calculations. The first calculation (dashed red line in Fig. 4.2A) assumes $A(Q) = A(Q^0)$, and $P(Q) = P(Q^0)$, with $Q^0 = 0.04$ Å^{-1} chosen to be at the center of the calculation range ($\Delta Q = 0.08$ Å^{-1}). Note that this calculation agrees well with the simulated data near $Q = Q^0$ extending over a Q-range where the assumed values of $A(Q^0)$ and $P(Q^0)$ (red dashed lines in Fig. 4.2B and 4.2C) approximate the actual variation of $A(Q)$ and $P(Q)$ (thin blue lines in Fig. 4.2B and 4.2C). This range of $Q = 0.035$ to 0.045 Å^{-1} is highlighted in Fig. 4.2A. However, this calculation deviates significantly from the simulated data as Q deviates significantly from Q^0. The second calculation (green line in Fig. 4.2A) shows that inclusion of the terms that describe the gradient of A and P within ΔQ (i.e., $dA/dQ(Q^0)$ and $dP/dQ(Q^0)$) substantially increases the range over which the model independent calculation agrees with the simulated data, again because this provides a better approximation for the actual variation of A and P within the segment width (blue line, Fig. 4.2B and 4.2C). From this example, it becomes evident that the choice of approach in analyzing the fluorescent yield data (i.e., using fixed amplitudes and phases for each segment, or including linear gradient terms) will depend on the specific shape of the element-specific distribution and the choice of the segment widths. Consequently, some prior knowledge of the potential physical range of the elemental distribution is helpful in choosing the segment width. The appropriateness of the chosen segment width can be directly evaluated by the ability to reproduce the observed fluorescence yield data.

4.4.2 *Ex situ* Experimental Results

The X-ray reflectivity measurements for the TiO_2/Si/Mo on Si substrate system are shown in Fig. 4.4A (magenta dots). We begin with a qualitative assessment of the data. Two distinct periods of oscillations are visible in the data. The longer oscillation period ($\Delta Q \sim 0.1$ Å^{-1}) arises from interference between x-rays reflected from the Si-Mo and Mo-Si interfaces suggesting a Mo layer thickness of $2\pi/\Delta Q \sim 60$ Å. The fine period oscillations have a ~9 times finer Q-spacing corresponding to the Si layer thickness of ~540 Å. It can be seen that the fine period oscillations in the data are weaker for $Q < 0.12$ Å^{-1}, and become strong at larger Q. This is because of the increased attenuation of x-rays passing through the top Si layer to reach the Si-Mo interface at low angles, thereby causing reduction in the interference fringes. There is also a gradual reduction in the strength of these finer-scale oscillations with increasing Q. This reduction is associated with interfacial roughness, of the interface above or below the Si layer. The observation of significant oscillations from the Mo thickness that are still pronounced at high Q suggests that the Si-Mo and Mo-Si interfaces have sharper widths than the Si/TiO_2 /Air interfaces.

A precise and quantitative analysis of these data is necessary to obtain the electric field intensities necessary to analyze the XSW fluorescence yield data. This was performed using least squares fitting by comparing the data to model calculations based on Parratt's recursion formalism[60, 67]. Interfacial roughness was incorporated as a Debye-Waller factor multiplied by the Fresnel coefficients for each interface[60]. The system was modeled as separate TiO_2, Si and Mo layers on a semi-infinite Si substrate. The refractive index parameters ($n = 1 - \delta - i\,\beta$) for the three materials were initially based on the bulk values. Two parameters were used to describe
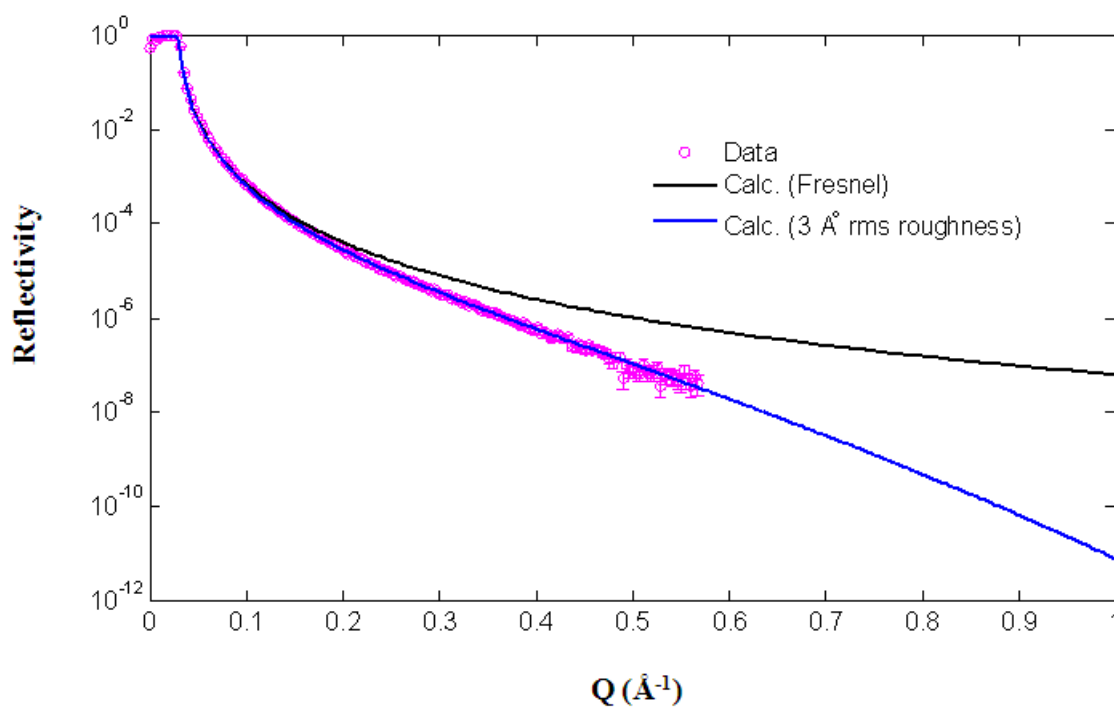
Figure 4.3: X-ray reflectivity of the Si (001) wafer, used as a substrate for the deposition of the TiO$_2$/Si/Mo layers. XR of the wafer measured in air (magenta circles), and calculation for an ideally flat interface (Fresnel reflectivity, in black line), and for interface with a 3 Å root mean square roughness (blue line). The data was measured with the Rigaku ATX-G diffractometer in the NU X-ray Lab, using Cu-Kα incident radiation (8 keV).
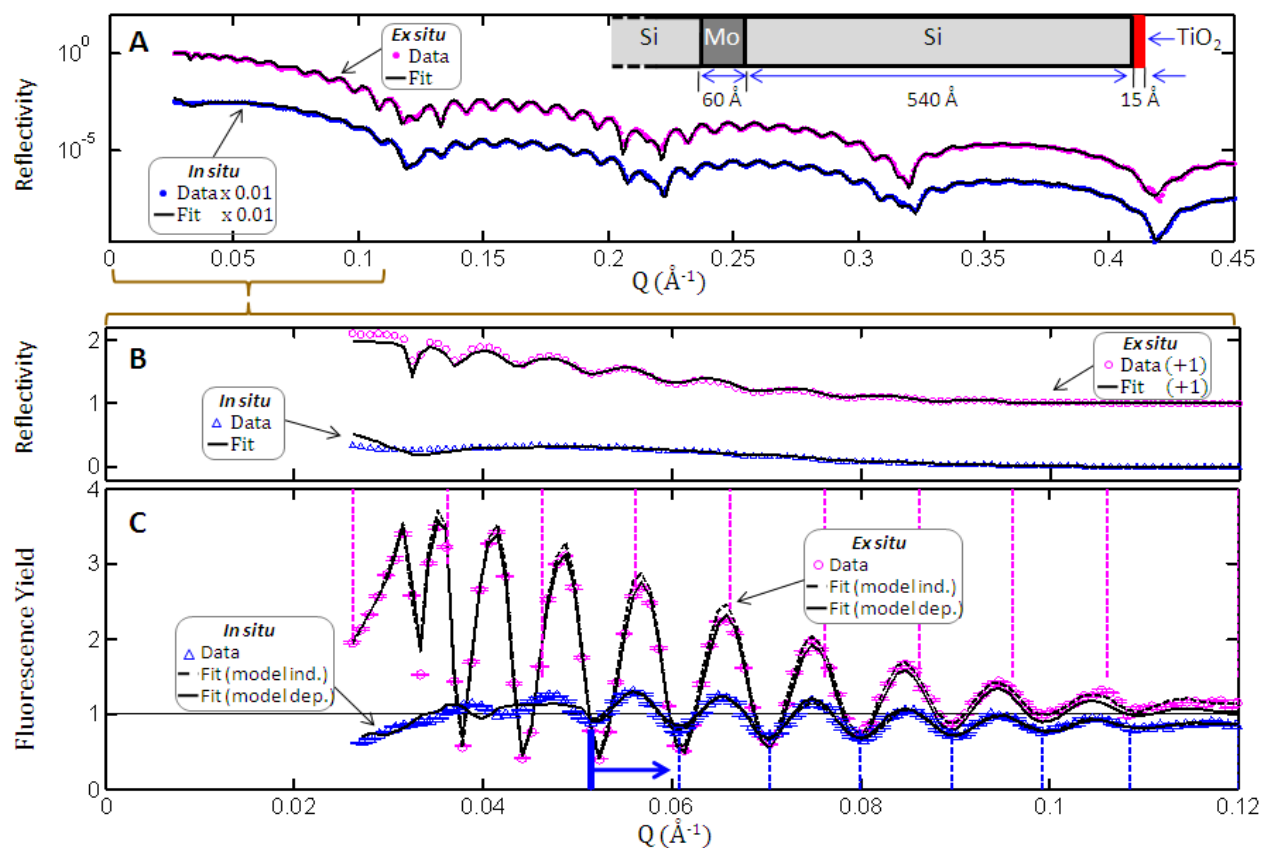
Figure 4.4: Model-independent analysis of measured *ex situ* and *in situ* reflectivity and Ti-yield

for TiO$_2$-Si-Mo-Si substrate (schematic shown in inset). (A): The reflectivity data (dots) in

absolute units (magenta: *ex situ*, blue: *in situ* multiplied by 0.01), and model fits (lines). Error-

bars in reflectivity are not shown for clarity, typical statistical uncertainty was ~0.5%, while a

minimum uncertainty of 2% based on systematic errors was assigned before analysis. B):

Highlight of the reflectivity data in Q<0.12Å^{-1} range corresponding to full Ti-yield data (circles,

panel C). The parameters derived from reflectivity analysis were based on fit of the full-range

(shown in A). C): The Ti-yield data (circles, magenta: *ex situ*, blue: *in situ*), model-independent

fits (dashed lines), and model-based fits (solid lines). Vertical dashed lines show segments into

which data were divided for model-independent analysis (using $\Delta Q = 0.01$ Å^{-1}). The blue arrow

shows the range of *in situ* data included in the fit (Q>0.05Å^{-1}).
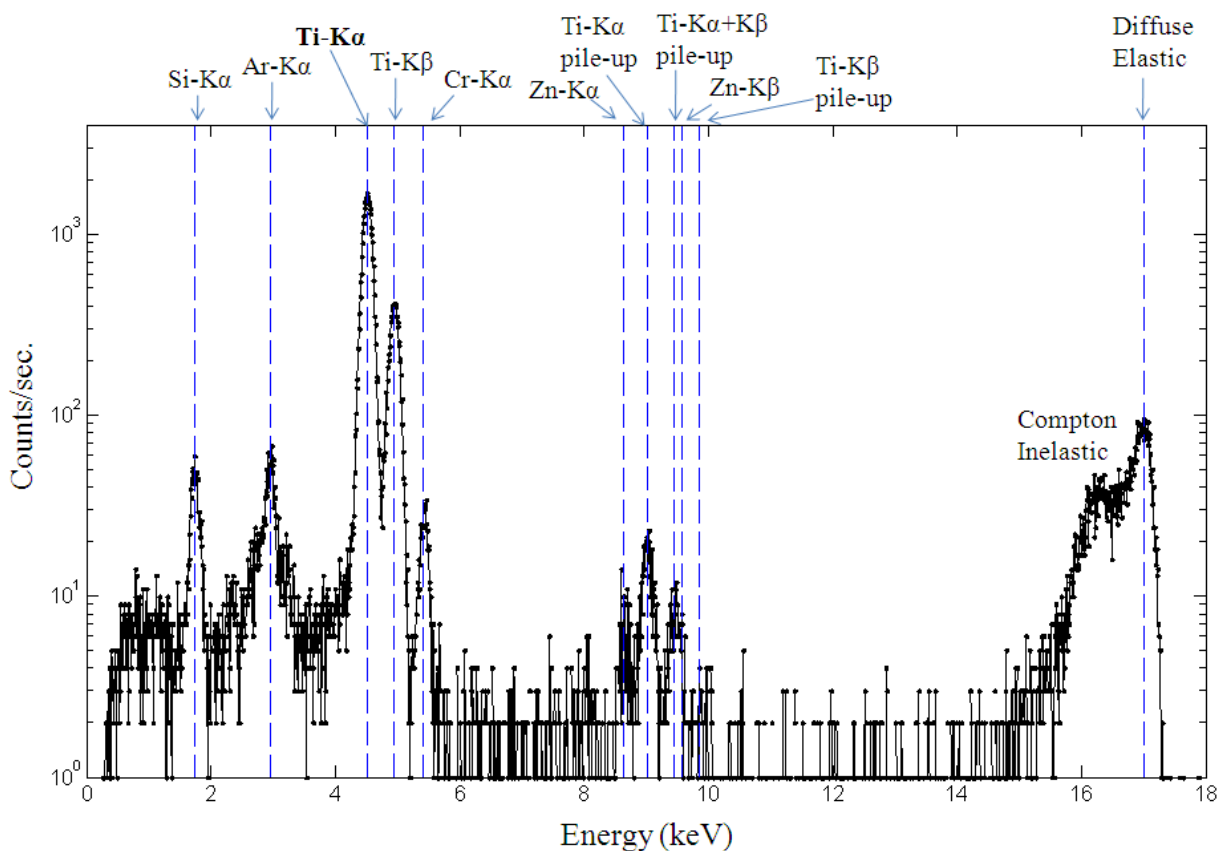
Figure 4.5: X-ray fluorescence spectrum, measured in air on the TiO$_2$/Si/Mo tri-layer sample, at Q=0.032 Å^{-1}. Measurement was on sample#1 (as described in the text). Different fluorescence lines assigned to the spectrum for the purpose of energy calibration (and identification of line of interest), are indicated. The signal of interest was the Ti-Kα fluorescence for the *ex situ* measurements.

Table 4.1: Parameters derived from the fit of the reflectivity data measured in air and under an aqueous solution.

	Ex situ **Results (Sample#1)**	*In situ* **Results (Sample#2)**
Fit quality[a]		
R-factor	0.10	0.08
χ^2	55	37
Structure [b]		
t_{TiO_2} (Å)	16.7 ± 0.1	14.9 ± 0.2
t_{Si} (Å)	549.3 ± 0.2	546.2 ± 0.3
t_{Mo} (Å)	60.67 ± 0.02	60.65 ± 0.01
X_{TiO_2} [c]	0.88 ± 0.01	0.86 ± 0.01
X_{Si}	0.97 ± 0.01	0.83 ± 0.02
X_{Mo}	1.06 ± 0.01	1.12 ± 0.01
$\sigma_{Air-TiO_2}$ (Å)	5.73 ± 0.08	5.0 ± 0.1
σ_{TiO_2-Si} (Å)	4.9 ± 0.1	5.4 ± 0.2
σ_{Si-Mo} (Å)	3.54 ± 0.02	3.40 ± 0.02
σ_{Mo-Si} (Å)	3.75 ± 0.02	3.51 ± 0.02
Extrinsic		
t_{H_2O} (μ)	0	1.39 ± 0.04
t_{Kap} (μ)	0	7.5 ± 0.1
X_{H_2O}	N/A	1[d]
X_{Kap}	N/A	1[d]
Angle avg., δQ_{Ref} (Å^{-1})	0	0.048 ± 0.001[e]

---

[a] Least- squares fit was guided by Chi-squared deviation of the data from the calculation, defined as $\chi^2 = 1/n \sum (y-f)^2/\varepsilon^2$, where y denotes the data, f the calculation, ε the uncertainty in the data, and n the number of data points. Quality of fit is also indicated by parameter R representing the average deviation of data points from calculation, or $R = 1/n \sum |(y-f)/y|$, where || denotes the absolute value.

[b] Uncertainties are based on a minimum 2 percent error-bar enforced on the data points when the statistical uncertainty was smaller.

[c] X denotes the fraction of the electron density of the layer with respect to the electron density of bulk material.

[d] Parameter fixed during the fit.

[e] A bending radius of curvature of 31 m can be estimated based on δQ_{Ref} for a vertical x-ray beam size of 50 μ.

Table 4.2: Parameters derived from model-independent and model-based analyses of the Ti-K_α x-ray standing wave data measured in-air and under an aqueous solution. Ti coverage estimate based on x-ray fluorescence measurements is also reported.

	Ex situ **Results (Sample#1)**	*In situ* **Results (Sample#2)**
Model Independent		
Fit quality		
R-factor	0.03	0.02
χ^2	19	1.9
Structure [a]		
Z_0 (Å)	- 9.3	- 10.0
Δ (Å)	~ 30	~ 30
Extrinsic		
$A_{Q=0}$	0.86	0.60
Angle avg., δQ_{Ref} (Å^{-1})	0	0.037 ± 0.001[b]
$t_{H_2O-equivalent}$ (μ) [c]	0	10.8 ± 0.6
Model Dependent		
Fit quality		
R-factor	0.05	0.02
χ^2	31	3
Structure		
Z_0 (Å)	-9.2 ± 0.3	-10.5 ± 1
Δ (Å)	21 ± 3	20 ± 3
Extrinsic		
$A_{Q=0}$	0.86[d]	0.60[d]
Angle avg., δQ_{Ref} (Å^{-1})	0	0.037 ± 0.001[b]
t_{H_2O} (μ)	0	3.8 ± 0.6
t_{Kap} (μ)	0	8.3 ± 0.7
X-ray Fluorescence		
Θ_T (Ti atoms / Å^2)	0.31[e]	0.25[e]

---

[a] The model-independent structural parameters shown were derived from the fit parameters A and P used in the fit.

[b] A bending radius of curvature of 40 m can be estimated based on δQ_{Ref} for a vertical x-ray beam size of 50 μ.

[c] This is used to calculate a_I at the water-TiO$_2$ interface needed for the model-independent analysis (accounts for attenuation of the incident x-ray beam through Kapton and solution layers).

[d] Value fixed based on the information from model-independent results.

[e] This is an estimate based on the procedure described in the experimental section. The uncertainties in this parameter were systematic and arose from the nominal attenuation corrections of the Ti-Kα fluorescence yield through air, Kapton and solution layers (for the *in situ* data), that were based on the detector geometry, as well as corrections for the detector efficiency.

the jth layer, a thickness (t_j), and a density factor (X_j) to allow for changes in the layer density with respect to the assumed bulk density of the material (shown by dashed horizontal lines in Fig. 4.6A). The refractive index used for j^{th} layer was $n_j = n_j^{Bulk} X_j$. Interfacial roughness for the interface between the j and j+1 layers was included as the parameter σ_j. The calculation (Fig. 4.4A, black line as indicated for *ex situ* case) reproduces all of the qualitative features present in the data and has an R-factor of 0.1 (defined in Table 4.1). The structural parameters determined from the fit are shown in Table 4.1 (sample#1). The Si and Mo layer thicknesses determined from the analysis are close to the values that we estimated from qualitative assessment, and the interfaces above the Si layer are indeed rougher than the ones below it. The thickness of the top TiO_2 layer is determined to be 16.7 ± 0.1 Å. The complete density profile based on this model analysis (black lines in Fig. 4.6A) was used to calculate the electric field intensities required to analyze the XSW data.

The Ti-Kα fluorescence yield data measured in air is shown in Fig. 4.4C (magenta circles). The first peak in the fluorescence yield data occurs at Q ~ 0.032 Å^{-1}, the critical angle of the system (Fig. 4.4B), which reveals that the Ti distribution is located at the surface, as expected. The yield modulations at increasing Q (Fig. 4.4C) arise from the oscillations in reflectivity due to the Si layer thickness (Fig. 4.4B).

For the model-independent analysis, the data was divided into segments of width ΔQ = 0.01 Å^{-1} (outlined in Fig. 4.4C by dashed vertical magenta lines), and fit using the model-independent formalism described above. Here the reflectivity, and the phase of the reflectivity coefficient are based on Parratt's formulation applied to the electron density model displayed in
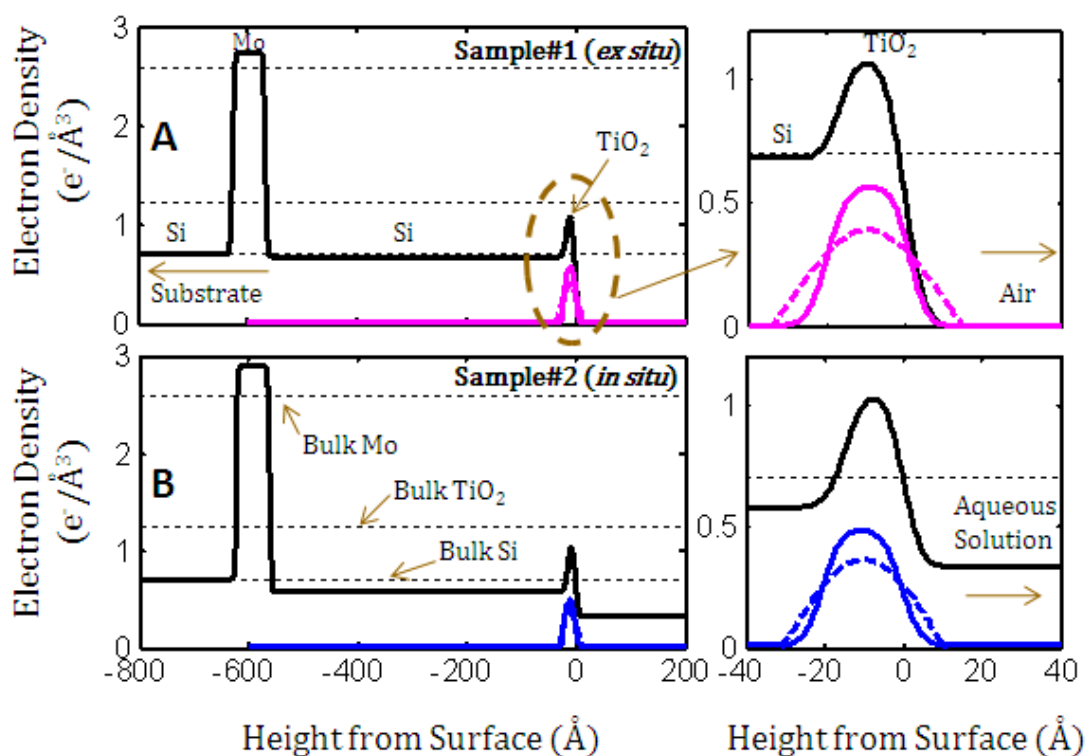
Figure 4.6: The density profiles for the $TiO_2 - Si - Mo - Si$ substrate system based on analysis of reflectivity measurements (black lines) for (A) the *ex situ* analysis, and (B) the *in situ* analysis. The horizontal black dotted lines show the expected bulk electron density of each material. These interfacial profiles include the interfacial roughness obtained by the reflectivity analysis (see Table 4.1). The TiO_2 profiles based on the analysis of Ti-yield data are also shown for model-independent (dashed) and model-based (solid) cases, these profiles are scaled to absolute units based on the Ti coverage measured from XRF.
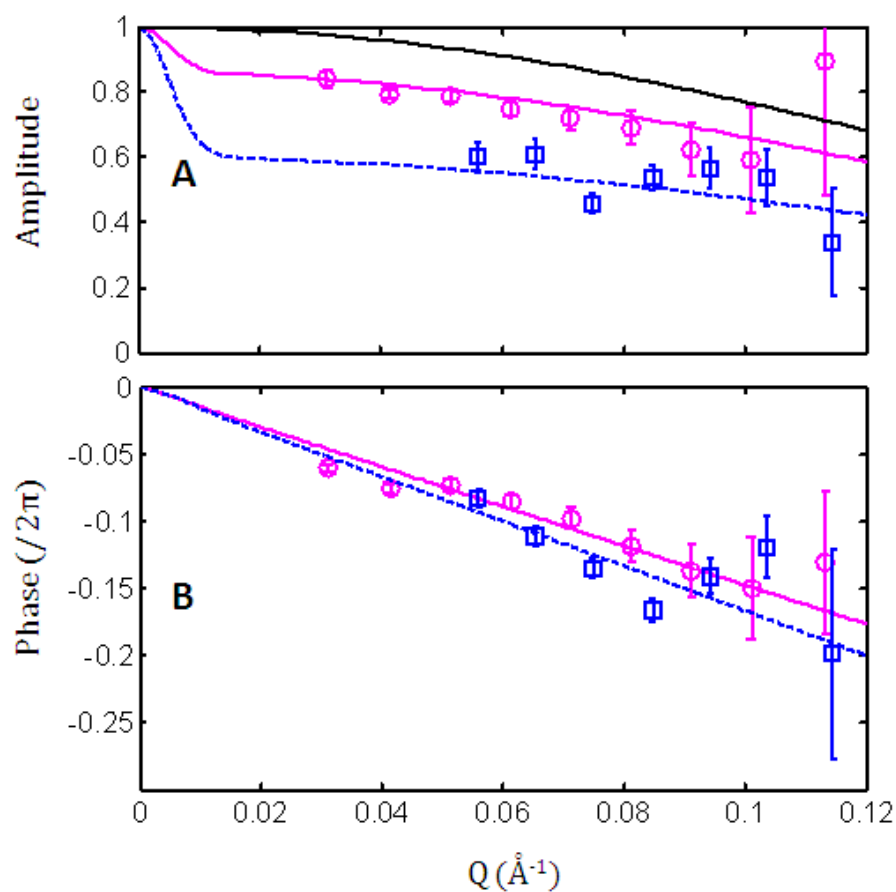
Figure 4.7: Amplitudes and (B) phases (symbols) extracted from the model-independent analysis for the sample measured in air (magenta) and in contact with an aqueous solution (blue). The A and P variation based on the model analysis are shown in lines. Note the difference in the extrapolated value of $A_{Q=0}$ for the *ex situ* and *in situ* results. Also shown are the A vs. Q variation (black line) for the *ex situ* case if the distribution were fully coherent (i.e. with $A_{Q=0} = 1$).

Fig. 4.6A. Note that this model includes an initial rough estimate (from reflectivity analysis) for the presence of the TiO_2 layer and thus R_1 and v_1 correspond to the air-TiO_2 interface. As seen in Fig. 4.4C, the model-independent fit (dashed black line as indicated for the *ex situ* case) is in very good agreement with the data, giving an R-factor of 0.02 (Table 4.2). The amplitudes and phases (A and P) derived from each segment are shown in Fig. 4.7 (magenta circles); these A and P values reveal direct information about the 1D Ti atomic density profile. The negative slope in phase variation indicates that the Ti distribution is centered *below* the surface, which is expected since the origin was chosen to be the air-TiO_2 interface. The Q-variation of the derived amplitudes and phases in the Q-range of analysis is consistent with a single layer of Ti, as expected. The extrapolation of A(Q) in the limit of Q→0 (i.e., $A_{Q=0}$) gives the value $A_{Q=0} = 0.86$ (or 86% of the total coverage). This Q = 0 value of element-specific amplitude is expected to be equal to unity for any elemental distribution. That $A_{Q=0}$ is less than unity indicates the presence of an incoherent contribution to the fluorescence yield. We will provide explanations for possible sources of this incoherency in the discussion section.

The Fourier-inversion described by Eq. (4.2.14) is then used on the set of A_j and P_j values shown in Fig. 4.7 to generate the Ti profile centered at 9.4 Å below the surface as shown in Fig. 4.6A. This Ti profile is converted to absolute units of e/Å^3 for a TiO_2 layer (Fig. 4.6A, dashed magenta line), based on the measured Ti-number density from XRF (Table 4.2) and the electron density of TiO_2 (assuming all Ti are in the form of TiO_2). This conversion is done so there can be a direct comparison of the XSW-derived profile to the adjoining electron density profile that was derived from the reflectivity analysis.

A model-based analysis was done to confirm the model-independent results; this was based on exact calculation of E-fields throughout the extent of the total structure, and use of Eq. (4.2.4) to calculate the fluorescence yield from the model Ti structure. The model used was a rectangular profile with rounded edges, represented by the product of two error-functions. The interfacial widths were fixed at the values derived from the reflectivity analysis for the air-TiO_2 and TiO_2-Si interfaces. Other parameters used during the fit were a scale factor, and the thickness and position of the Ti layer. This model-dependent fit led to an R-factor of 0.03 (solid black line in Fig. 4.4C, Table 4.2). An incoherent fraction of 0.14 (i.e., 1- $A_{Q=0}$) was assumed in the analysis based on the information from the model-independent analysis (Table 4.2). This parameter was fixed since it co-varies with the width of the Ti layer. This incoherent component was modeled as a relatively broad Gaussian layer centered at the surface. We used a width of 200 Å, which was sufficiently broad to make the structure factor for this layer insignificant over the Q-range of data studied. The amplitudes and phases of the Ti distribution including the incoherent component are plotted in Fig. 4.7 (magenta lines), indicating very good agreement with the model-independent results. The model-based density profile (Fig. 4.6, solid magenta line) shows that the Ti distribution is centered at 9.2 ± 0.3 Å below the surface, which agrees with the results derived from the model-independent analysis. This is also a good agreement with the value expected based on reflectivity, which is 8.4 Å (i.e., half of the TiO_2 layer thickness found from the reflectivity analysis), especially since reflectivity is not an element specific technique. The Ti-layer thickness of 21 ± 3 Å obtained from the model-analysis of the XSW data can be compared against that derived from two other independent methods, namely, reflectivity and x-ray fluorescence. The reflectivity measurements reveal a TiO_2 thickness of 16.7 ± 0.1 Å.

The differences are not unexpected given the poorer spatial resolution of the XSW data. Based on a $Q_{max} - Q_{min}$ defined resolution, the XSW data had a resolution of ~33 Å while the reflectivity had a 7 Å resolution. The estimate of the TiO_2 film thickness based on XRF yield is 10 Å. This value is based on the coverage of 0.31 Ti/Å^2 estimated from the measured Ti-Kα counts (at Q=0.15 Å^{-1}) using the procedure described in the experimental section, and assuming bulk density of TiO_2 to calculate the TiO_2 thickness from the coverage.

4.4.3 *In situ* Experimental Results

The *in situ* reflectivity data (Fig. 4.4A) were measured on a second sample that was nominally similar to that used for the *ex situ* measurements. The data are similar in terms of the period of oscillations suggesting similar structural parameters. The *in situ* data are characterized by a substantially diminished magnitude of oscillations in the reflectivity signal compared to the *ex situ* data, particularly in the low-Q region (Fig. 4.4B). This is due to both intrinsic and extrinsic factors. There is a reduced density contrast at the water-TiO_2 interface which reduces the visibility of these fringes. We also find that there is a bending of the sample due to stress on the sample edges from tension in the Kapton film which was used to confine the aqueous solution at the sample surface[103]. This bending of the crystal further reduces the visibility of the reflectivity fringes due to "angular averaging", because the incident beam effectively has a finite range of incident angles along the length of the beam-footprint on the sample.

The model used to fit the *in situ* reflectivity data (black line in Fig. 4.6B) was similar to that used in the *ex situ* analysis, except additional layers of water and Kapton were included.

Layer thicknesses, density factors, as well as the interfacial roughnesses were allowed to vary during the fit. An additional parameter δQ_{Ref} was used to include the effect of angular averaging, based on the treatment described by Libera[103], where the angular range over which the data are averaged at any Q is described by $\delta Q\,(Q) = \frac{Q_{Ref}}{Q}\,\delta Q_{Ref}$, where δQ_{Ref} is the angular averaging at $Q_{Ref} = 0.01$ Å^{-1}. The parameters obtained from the *in situ* analysis are listed in Table 4.1 (sample#3). The good agreement in the structural parameters for the two separately prepared samples measured under different conditions shows the reproducibility of our sample preparation conditions.

Comparison of the *in situ* Ti-yield data (Fig. 4.4C) with the *ex situ* data shows that the observed oscillation period is very similar for $Q > 0.07$ Å^{-1}, but differs significantly for $Q < 0.05$ Å^{-1}. This is due to the angular averaging described above, which is most significant at lower incident angles (Fig. 4.4B and 4.4C). As for the reflectivity data (Fig. 4.4B), the magnitude of the fluorescence yield oscillations (Fig. 4.4C) is considerably smaller for the *in situ* data.

The *in situ* Ti-yield analysis was restricted to $Q > 0.05$ Å^{-1} (as indicated by the blue arrow, Fig. 4.4C). Data outside of this range was not used for analysis because the calculations could not explain the measured fluorescence yield oscillations below $Q = 0.05$ Å^{-1}, as seen from the disagreement in the plot (Fig. 4.4C). This is because the angular averaging (δQ) at these low angles becomes larger than the period of modulations in the data. The inability to reproduce the data in this range suggests that the actual functional form for the angle-averaging at these angles was more complicated than the assumed model.

The model-independent analysis was conducted as described for the *ex situ* case, except now the electric field intensities used were calculated using the reflection at the water-TiO_2 interface (i.e. using R_2, v_2, and E_2 for that interface). The incident E-field amplitude (E_2) above the water-TiO_2 interface was based on transmission of incident x-rays through a water equivalent thickness parameter (Table 4.2) included in the fit, which accounted for the attenuation of the incident beam through the water and Kapton layers. The attenuation of the XSW over the thickness of the TiO_2 layer was, however, neglected as stated previously. During the model-independent analysis, the yield data was initially plotted as Y vs. Q_{H_2O}, where Q_{H_2O} is the momentum transfer inside the aqueous layer. The data was then divided into segments of width $\Delta Q_{H_2O} = 0.01$ Å^{-1}, and the model-independent approach was used to obtain an amplitude and a phase for each segment. These model-independently derived A and P values are plotted vs. Q_{air} (referred as Q) in Fig. 4.7 (blue squares) for a direct comparison with the *ex situ* data. The model-independent phases are similar to the *ex situ* results, implying that the center position of the Ti layer should be comparable for the two samples. The derived amplitudes on the other hand, while similar to *ex situ* case in terms of their variation with Q in the study range, differ quite clearly in terms of their magnitude. Note in particular that the extrapolated value of $A_{Q=0}$ (i.e., the coherent fraction) is ~0.60 compared to the value of 0.86 observed for the *ex situ* data.

The Fourier-inverted density profile for the *in situ* data (Fig. 4.6B, dashed blue line) was obtained using $Q_2 = Q_{H_2O}$ in Eq. (4.2.14) with the derived A and P values. This density profile is comparable to the *ex situ* case (Fig. 4.6A), showing that the formalism can be used to measure the *in situ* elemental distribution.

A model-based analysis shows good agreement with the model-independent results, both in terms of the A and P variation (Fig. 4.7, dashed blue lines), and the Ti profile (Fig. 4.6B, solid blue line). The center of the Ti distribution is 10.5 ± 1 Å below the surface, and is within error of the value derived with model-independent approach (10.0 Å). It is comparable to (but somewhat larger than) the value from the *in situ* reflectivity analysis (7.5 Å). The width of the Ti layer, 20 ± 3 Å, is comparable to the reflectivity measurement (14.9 ± 0.2 Å). The structural parameters of the Ti layer for the *in situ* measurement are within error the same as that obtained for the *ex situ* results (Table 4.2).

4.5 Discussion

We have demonstrated that this model-independent formalism can be used to extract elemental Fourier amplitudes and phases from experimentally measured long-period x-ray standing wave data to directly obtain the elemental profiles from the fluorescence yield data. It has also been shown that the formalism can be applied to measure *in situ* distributions by imaging the Ti layer under a thin solution layer. The capability of imaging under aqueous media and with long-period XSW can be very valuable in measuring extended structures such as the diffuse double layer[15] at liquid-solid interfaces.

One significant factor in interpreting these data is the experimental resolution. The width of the profiles extracted with this approach does not reflect the intrinsic width of the distribution if the intrinsic width is smaller than the experimental resolution. This is the case for the Ti profiles in Fig. 4.6, where the model-independent profiles derived from the XSW data have a

width of about 30 Å. The experimental resolution is given by $\pi/(Q_{max}-Q_{min})$, where Q_{max} (Q_{min}) is the higher (lower) end of the fluorescence yield data range. Based on the Q-ranges shown in Fig. 4.4C, the spatial resolution of the XSW results can be estimated as ~33 Å for the *ex situ* data and ~45 Å for the *in situ* data. The resolution can be improved by measuring the data to a higher Q. However, the reduction in reflectivity with increasing Q decreases the fluorescence yield modulations (thus requiring longer counting times to obtain the necessary statistical significance).

The model-independent elemental Fourier amplitudes in Fig. 4.7A revealed a significant incoherent fraction for the *ex situ* measurements and an even greater incoherent fraction for the *in situ* measurements. We propose that this incoherency is primarily induced by diffusely or incoherently scattered X-rays that are produced by the incident and reflected beams passing through the layers of surrounding media. Since these secondary scattered x-rays are incoherent, their induced Ti-Kα XRF yield will show no interference effect. This gives rise to a background fluorescence signal that is added to the XSW induced signal. Even though (for reasons of convenience) we use a secondary broad Ti distribution to mimic this incoherency effect in our model fits to the XSW data, it should be clear that the observed incoherency is due to an X-ray incoherency. This conclusion is supported by the observation that there is an increase in the incoherent fraction observed for the *in situ* XSW measurements compared to the *ex situ* measurements, since the Kapton and solution layers serve as additional sources of diffuse or incoherent scattering. When these different incoherent fractions are used in the model-dependent analyses for the two conditions (i.e. *ex situ* and *in situ*), the Ti profile parameters obtained are the same within experimental uncertainties.

The formalism described here is valid for an XSW generated by reflection from an interface. It can therefore be used for various geometries including TER and PML, and can also be extended for the single crystal Bragg-XSW case. Note however, that while Parratt's formalism can be used to obtain the reflection coefficients needed in the analysis (R and v) for the TER and PML regimes, as done in this paper, for the high-angle Bragg case these should be calculated using the precise dynamical diffraction theory for single crystals[104]. The current formalism can be compared to the previous model-independent approach that is applicable to the Bragg XSW case. In that case, the fluorescence yield measured around H^{th} order diffraction revealed the discrete amplitude and phase of the Hth order Fourier-coefficient of the 3D density distribution. Because of this, the sampling of the element-specific structure factor was limited to points in reciprocal space that satisfy the Bragg diffraction condition (and hence the modulo-d ambiguity was present). However with the current approach, the Fourier coefficients can be sampled at a substantially higher frequency through TER and PML XSW measurements, or even along the crystal truncation rods that pass through each Bragg diffraction condition. The sampling interval in this approach is only determined by the segment width chosen in the analysis which should be large enough so that the derived parameters are well defined. Because of the finer sampling, a unique reconstruction of more extended distributions becomes possible.

While the earlier and simpler formalism developed by Bedzyk[99] is also applicable for the reflection generated XSW, it is limited (in its current form) to the TER region of the data due to an assumption about the phase of the reflected wave. The present approach however places no constraints on either the magnitude or phase of the reflected wave and is valid even beyond the TER region. This means that there are no constraints on the type of layered structure that is used

to generate the standing waves, unlike the requirement of single crystals for Bragg-XSW case. Another distinguishing feature about the current approach is that it is applicable to XSW produced in an absorbing medium.

In the analysis shown in Sections 4.4.2 and 4.4.3, it was assumed that the elemental structure factor amplitude and phase are constant over the segment width ΔQ. This however induces some errors since the variation in A and P may not always be negligible. We now estimate the errors (in A and P) for the case of an elemental profile represented by a single Gaussian layer centered at a height Z_0 above the surface with width σ, over the range of data in the segment ΔQ centered around Q_0. The amplitude and phase of the profile is given by,

$A(Q) = e^{-\frac{1}{2}\sigma^2 Q^2}$, and $P(Q) = \frac{1}{2\pi} Q Z_0$. The change in A and P over the interval ΔQ, evaluated at

Q=Q_0, can thus be written as, $\Delta A = \frac{dA}{dQ} \Delta Q = \left(-Q \sigma^2 e^{-\frac{1}{2}\sigma^2 Q^2}\right) \Delta Q$, and $\Delta P = \frac{dP}{dQ} \Delta Q =$

$\frac{1}{2\pi} Z_0 \Delta Q$; and the fractional changes will be, $\frac{\Delta A}{A} = -Q \sigma^2 \Delta Q$, and $\frac{\Delta P}{P} = \Delta Q/Q$. This suggests that if a constant segment width ΔQ is used in the analysis to divide the entire range of data for the case of a Gaussian distribution, the fractional error in phase due to the neglected change over the interval ΔQ will be larger at small Q, while the errors in amplitude will be larger at higher Q depending on the width σ. Consider an example of a Gaussian profile having a width of $\sigma = 5$ Å, and sampled with a segment width, $\Delta Q = 0.01$ Å^{-1}. At Q = 0.05 Å^{-1}, the change in phase over ΔQ will be 20 %, while the change in amplitude will be 1 %. Choosing a variable segment width ΔQ through the range of the data can help in reducing these errors.

In cases where the elemental structure factor changes rapidly or non-linearly with Q, it may be important to include the gradient terms in the analysis, i.e. using four parameters A, P,

dA/dQ, dP/dQ for each segment ΔQ. These terms are particularly important for distributions that have multiple layers, as interference between the different layers can result in sharp changes in the variation of A and P as a function of Q. Since some degree of distortion will be induced in the results because of the non-linear variations of the elemental structure factor over the region ΔQ, precise structural results will still be best obtained from a conventional model analysis, using the model-independent results as the basis for building the model. If necessary, additional parameters describing the higher order changes can be included. It may also be beneficial to select smaller segment widths when the A and P variation is significant, although this may ultimately be limited by the sampling intervals of the experimental data.

4.6 Summary

We described a model-independent approach for directly obtaining elemental distribution profiles from multilayer structures by using X-ray fluorescence yield data for the case of reflection generated x-ray standing waves. The approach has been demonstrated by retrieving the Ti profile from the yield data measured both in air and under aqueous conditions. A distinguishing feature about the approach is that it allows determination of Fourier coefficients of the elemental profile at a more continuous sampling interval (in Q) than the previous model-independent approach that was applicable to Bragg-XSW where sampling was limited to Bragg diffraction condition. This finer Q-sampling enables unique measurements of structures further away from the reflecting surface. Another uniqueness of the approach is that it makes no assumptions about the magnitude or phase of the reflected wave, and is therefore valid for any

case of XSW generated through specular reflection from a multilayer structure, including periodic multilayers. The formalism can be used to extract not only the amplitudes and phases (of the elemental structure factor), but also their first or higher order gradients, making it potentially useful in directly measuring complex profiles (like multi-layered distributions) where structure factor changes with Q can be complicated. Applicability to *in situ* systems makes the technique useful in imaging element profiles at liquid-solid interfaces, such as the adsorbed ion profile at aqueous-mineral interfaces. Since the technique allows analysis of the long period standing waves data, it can also be used to image extended or diffuse elemental distributions.

Chapter 5 : Enhanced Ion Adsorption at the NanoTitania-Aqueous Electrolyte Interface

5.1 Introduction

As pointed in Chapter 1, the functioning of electrochemical capacitors (ECs) is defined by adsorption of ions at the electrolyte-electrode interface[6, 7]. These devices hold great promise for use in hybrid electric vehicles and portable electronic devices[8-10]. Despite their excellent power characteristics, their applications are currently limited by their low energy density. While there have been substantial efforts to improve EC properties, including searches for new materials and tailoring of electrode structures[7, 105-109], there remain important gaps in our understanding of how electrolyte ions interact with charged interfaces at the nano-scale. Here, we show that titania nano-films support a 2-fold increase in total ion coverage, compared to single crystalline TiO_2 in contact with the same aqueous electrolyte. Insight into the cause of this behavior is provided by probing the distribution of Rb^+ and Sr^{2+} at the nanofilm-electrolyte interface using x-ray standing waves (XSW) and x-ray reflectivity (XR).

Depending on the mechanism of interaction of ions with the electrode surface, the ECs are further categorized into double-layer and pseudo capacitors[110]. While the interaction is primarily electrostatic in double-layer capacitors, in pseudo capacitors it involves chemisorption of counter-ions and other chemical species (e.g. hydroxyls) at the interface. The small separation

between the surface and the adsorbed ions in pseudo capacitors leads to a significantly higher capacitance compared to double-layer capacitors [111].

The most commonly studied EC electrode materials have been carbon-based[108]. However energy density is limited in these materials due to their double-layer capacitive nature[9]. Metal oxides on the other hand are appealing because chemisorption is considered to be the dominant mechanism on these surfaces (i.e. pseudo capacitance). In particular, the transition metal oxides have gained interest because of their lower cost compared to other candidates, such as noble metal oxides like ruthenium dioxide[112, 113]. High surface area and nano-structured materials are considered to be important to maximize ion-electrode interactions[114]. Tailoring the electrode pore structure has been used previously as a way to achieve increased capacitance, this has been linked with ion diffusion into the pores (and resulting de-solvation of ions for small pore sizes)[115]. This phenomenon is however not yet well-understood, and it is important to further understand the fundamental processes associated with ion-electrode interactions.

Direct measurements of ion profiles at liquid-solid interfaces have been limited mostly to single crystal substrates. The crystalline rutile TiO_2 (110) surface has been particularly well-studied[23, 30, 38, 92, 116], as described in Chapters 1 and 3. Both monovalent and divalent ions are known to adsorb in distinct sites (e.g., tetradentate vs. bidentate) where they are in direct contact with the surface oxygens. Here we show that the use of titania nanofilms leads to a substantial improvement in its adsorption capacity, and provide new insight into the mechanism by which this is achieved.

5.2 Methods

5.2.1 Sample Preparation

The sample used during surface titration measurements was a silica gel powder (Silicycle S10040M with nominal surface area 100 m^2/gm) coated with a 14 Å amorphous titanium dioxide film using Atomic Layer Deposition (ALD)[100]. The ALD growth used 20 consecutive 120 sec. exposures of titanium tetrachloride and water separated by 120 sec. purge periods. The substrate temperature was 100°C and the reactor base pressure was 1.1 torr of flowing (360 mL/min) UHP nitrogen. The planar sample used for the x-ray measurements was the tri-layer system consisting of TiO_2, Si and Mo layers grown on Si substrate, characterized in Chapter 4. The samples were degreased with acetone, methanol and de-ionized water in a sonicator before each growth step, as well as before the X-ray measurements. The X-ray measurements were conducted in a thin-film cell geometry[17] with a 8 μm-thick Kapton film used to enclose the aqueous layer on the sample surface. Representative AFM images measured on the bi-layer samples, uncoated and coated with nano-titania layer, are shown in Figs. 5.2 and 5.3 respectively.

5.2.2 X-ray Measurements

X-ray measurements were conducted at sector 33-BM-C at the Advanced Photon Source (APS) at Argonne National Laboratory. The incident x-ray energy during these measurements was 17keV, with a measured beam size (at the sample) of 0.05 mm x 1 mm along the vertical and horizontal directions, respectively. Further details about XR and XSW measurements procedure can be found in Chapter 4. Typical *in situ* X-ray fluorescence spectra measured under de-ionized water (DIW) and under an electrolyte solution (containing Rb^+) are shown in Fig. 5.1.
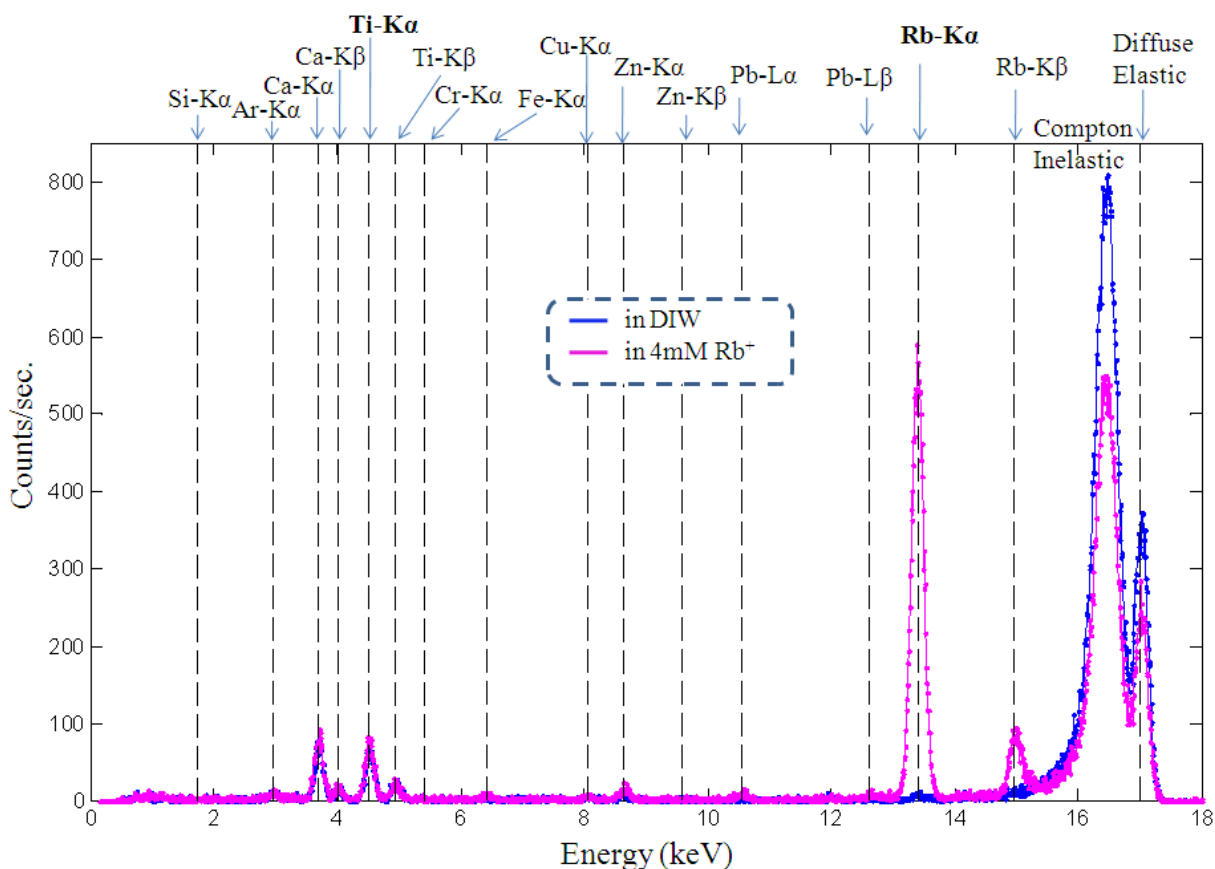
Figure 5.1: X-ray fluorescence spectrum, measured *in situ,* on the TiO_2/Si/Mo sample, at Q=0.032 Å^{-1}. Two MCA spectra are shown corresponding to the measurement in DIW (blue), and in 4mM Rb$^+$ electrolyte (magenta), on sample#3. Different fluorescence lines assigned to the spectrum for the purpose of energy calibration (and identification of line of interest), are indicated. The signals of interest were the Ti-Kα and Rb-Kα fluorescence lines.
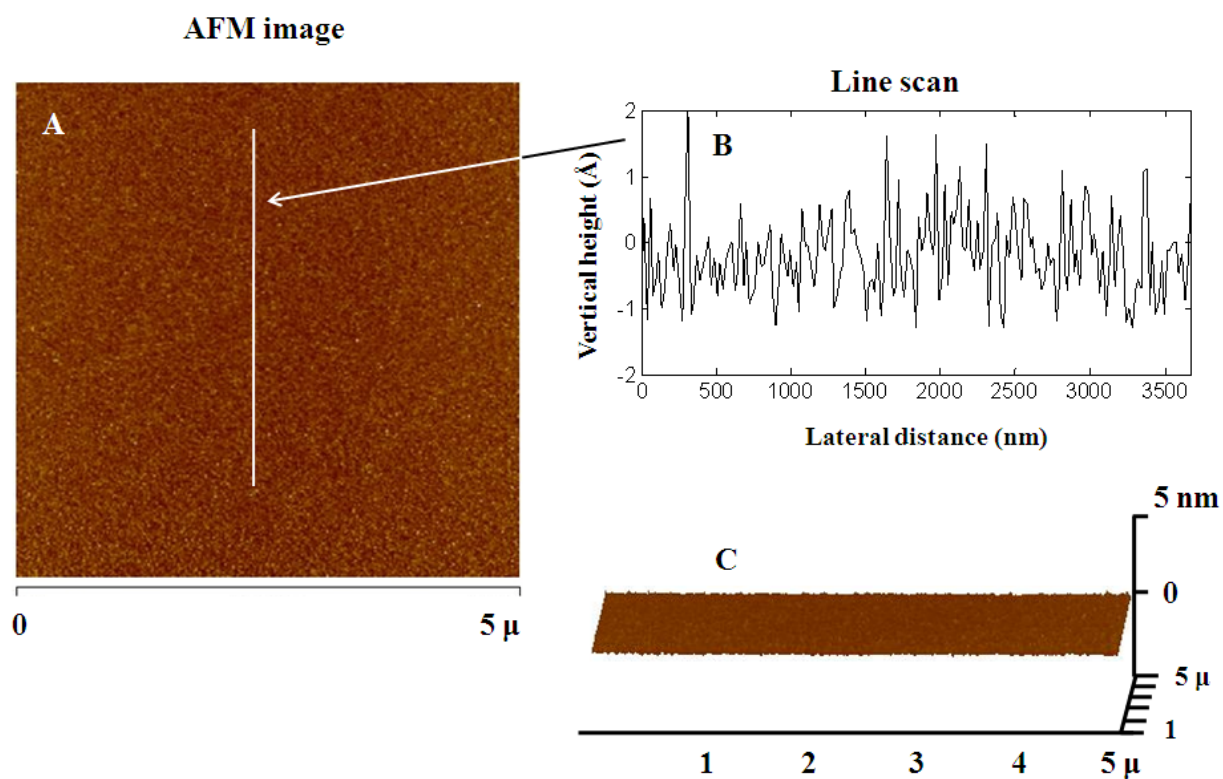
Figure 5.2: A representative AFM image of the Si/Mo bi-layer substrate surface, uncoated with the titania nano-film. (A) A 2D image of a 5 μ x 5 μ lateral area of the surface. (B) A line scan showing the vertical height variation vs. lateral position along the line marked in A. (C) A 3D plot of the surface topography, showing the surface height variation along the 25 μ² lateral region.
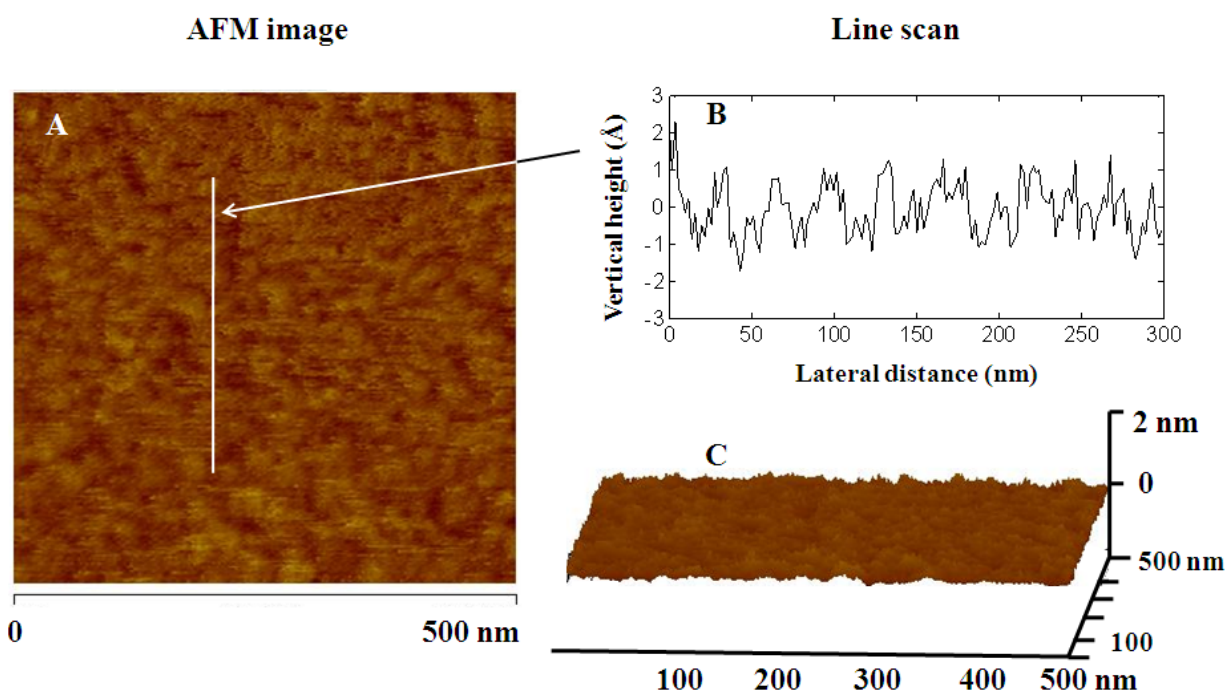
Figure 5.3: A representative AFM image of the surface of titania nanofilm coated on the Si/Mo bi-layer substrate. (A) A 2D image of a 500 nm x 500 nm lateral area of the surface. (B) A line scan showing the vertical height variation vs. lateral position along the line marked in A. (C) A 3D plot of the surface topography, showing the surface height variation along the 0.25 μ^2 lateral region.

The X-ray results discussed in this chapter refer to the measurements on sample referred #3. Complete set of XR and XSW measurements on different samples and under different electrolytes can be found in Tables 5.3 to 5.6 and Fig. 5.9.

The ion 2D-density (i.e., total number of ions per unit surface area) was measured using x-ray fluorescence yield measured at $Q = 0.15$ Å^{-1}. Calibration of the absolute elemental 2D-density used the Sr-K$_\alpha$ yield from a Si wafer standard implanted with 0.106 Sr/Å^2, independently calibrated with Rutherford backscattering[12]. While calibrating the Rb$^+$ 2D-density, the difference in the elemental absorption cross-section and the K$_\alpha$-fluorescence cross-section (yield) for the two elements, as well as the difference in the detector efficiency at the two energies was taken into account. The attenuation of the incident and fluorescence x-rays through the Kapton, electrolyte layer, and air was included in the coverage estimation.

5.2.3 X-ray Analysis

The reflectivity data analyses procedure has been described in Chapter 4. The analysis of the ion and Ti yield XSW data was conducted first using the recently developed model independent formalism[117], which was followed by a final model-dependent analysis. The details of the Ti yield analysis have been reported elsewhere[117].

The ion (Rb$^+$/Sr^{2+}) distribution was modeled as a condensed component that was represented by a Gaussian layer whose position and width were allowed to vary, and a diffuse component that was represented by an exponentially decaying profile with the fraction of ions in the diffuse profile being allowed to vary. The position and decay length of the diffuse profile

were fixed during the fit because these parameters were not uniquely determined by the data (Fig. 5.4 shows that most of the information concerning the diffuse ion distribution is present in
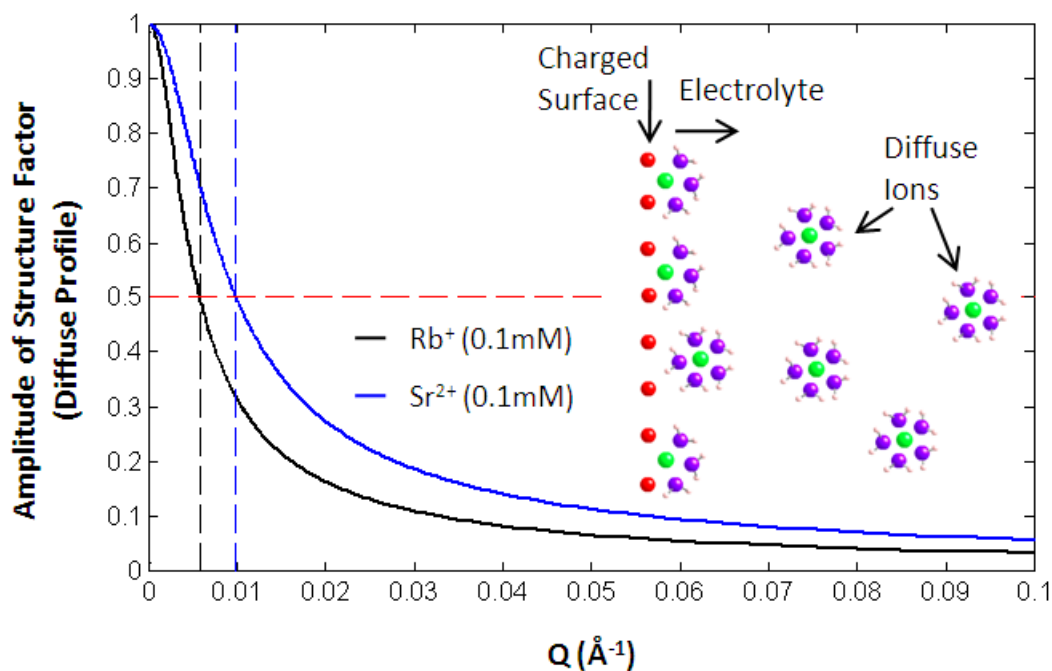
Figure 5.4: Importance of the low-Q data in obtaining information about the diffuse part of ion distribution at the charged liquid-solid interface. Calculated amplitude of the structure factor of diffuse exponential profiles (inset shows a schematic of the difuse ions) for Rb^+ and Sr^{2+}, shown in black and blue respectively, with Debye lengths L_D of 304 Å and 176 Å respectively, expected based on linearized Poisson-Boltzmann theory for 0.1mM ion concentration. The vertical dashed lines show the $Q_{1/2}$ position. This position corresponds to the momentum transfer Q where the structure factor decays to half of its maximum value (as Q increases from zero). $Q_{1/2}$ is equal to $\sqrt{3}/L_D$. The sensitivity to the diffuse profile is therefore reduced to one half at $Q = Q_{1/2}$, and decreases further at higher Q.

the very low-Q data, i.e., Q<0.01Å^{-1}). The position of the diffuse layer was fixed at 5 Å above the surface as this is a typical height where the bulk disordered water layer is expected to begin[25]. The decay lengths were obtained based on the linearized Poisson-Boltzmann theory[1] (which gave decay lengths of 304 Å and 176 Å respectively for Rb^+ and Sr^{2+} at 0.1mM concentration). The condensed layer heights were determined with respect to the titania surface by making use of the relative ion-Ti distances and the measured Ti-film thickness. The condensed ion-Ti separations, Δ_{Ion-Ti} = 4.3 ± 1 Å for Rb^+, and 8 ± 1 Å for Sr^{2+}, were revealed by XSW, while the Ti layer center is known from XR analysis (Z_{Ti} = -7.5 ± 0.1 Å, i.e., below the titania-electrolyte interface).

The measured 2D density of ions from XRF includes both the intrinsic contribution (referred to as the total coverage, including the ions in condensed and diffuse layers), and the extrinsic contribution (due to the bulk ions from the electrolyte layer). The total intrinsic ion coverages were determined from the measured 2D ion density by subtracting the number of ions in the bulk electrolyte layer (determined from the known bulk ion concentration and the measured electrolyte layer thickness derived from the Ti-yield analysis).

5.3 Results and Discussion

We first evaluate the surface charging properties of a 1 nm thick titania layer grown using atomic layer deposition (ALD)[100] on a high surface area silica gel powder (83.5 ± 0.7 m^2/gm, as measured on coated powders using the N_2 Brunauer-Emmett-Teller method or BET). The
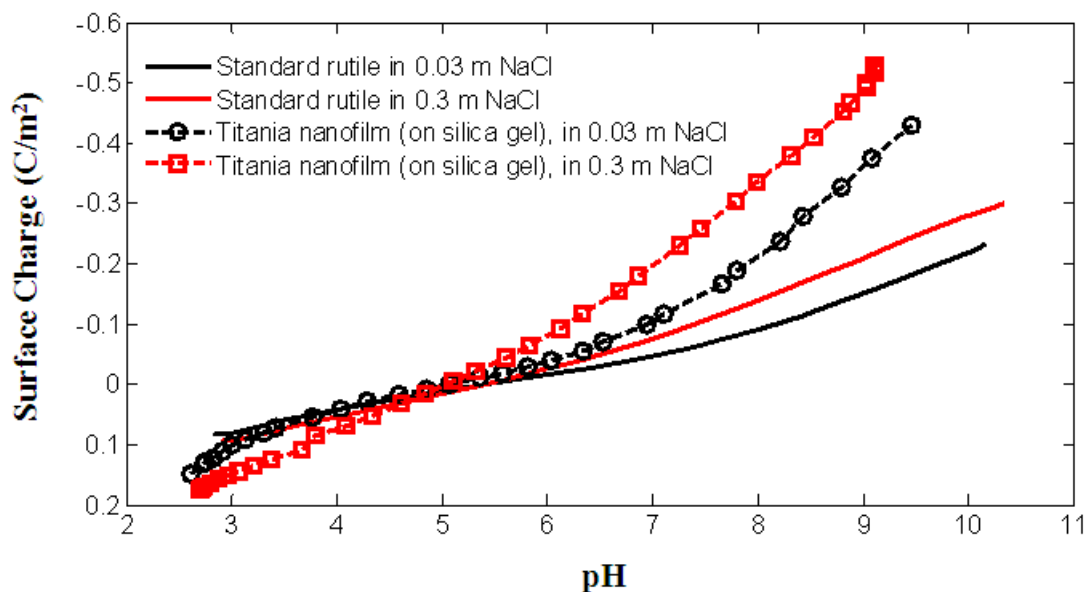
Figure 5.5: Surface charging behavior of titania nano-film surfaces, in comparison to rutile surfaces. Symbols and dashed lines indicate measurements on the nanofilm, while solid lines show the rutile measurements. Surface charge density is plotted as a function of solution pH for 0.03 m (black) and 0.3 m (red) NaCl as background electrolyte. The crossing point of the charging curves for the two background electrolyte strengths is indicative of the point of zero charge (*pzc*) of the surface. The nanofilm has a *pzc* of ~5.1, which is quite close to that of rutile (5.4). The nanofilm develops approximately double the surface charge compared to rutile at elevated pH.

surface charge evolution was measured as a function of solution pH in presence of 0.03 m and 0.3 m NaCl (Fig. 5.5). The charging curves show that the point of zero charge or *pzc* of the nano-titania film, assumed to be the pH of the crossing point of the curves for the two ionic strengths, is similar to that observed for well-crystalized rutile submicron powders with the (110) crystal face predominant (pH 5.4)[23]. This shows that the ALD-grown titania forms a continuous and impervious film on silica surfaces, because the pzc of silica is much lower. A significant difference between the nano-titania and rutile is that the nanofilm develops >2-fold higher surface charge density at pH's far from pzc compared to rutile.

An understanding of this novel behavior was obtained by observing the coverage and the distribution of adsorbed ions (Rb^+ and Sr^{2+}) on the nano-titania surface. We used the same titania nanofilms grown using ALD on a planar Si/Mo bi-layer substrate (consisting of Si and Mo layers of 540 Å and 60 Å, respectively, on a Si substrate; Fig. 5.6B) whose structure was optimized for these X-ray measurements. The interfacial structure of the multilayer in contact with aqueous electrolyte was measured using x-ray specular reflectivity (XR). The XR data (Fig. 5.6A) reveal a TiO_2 nanofilm thickness of 14.9 ± 0.2 Å, and a density that is reduced by 14% from that of bulk rutile (other structural parameters can be found in Table 4.1, sample#3). The element-specific XSW measurements confirmed the presence of a conformal titania film.

The X-ray fluorescence (XRF) and XSW were then used to reveal the coverages of the cations adsorbing on the titania nano-film surface. The XSW-measured vertical ion distribution combined with the XRF-measured ion 2D-density, allowed measurement of both the total ion coverages (i.e. the surface excess of ions, including the condensed and diffuse layers), and the specifically-adsorbed coverages (i.e., the condensed layer).
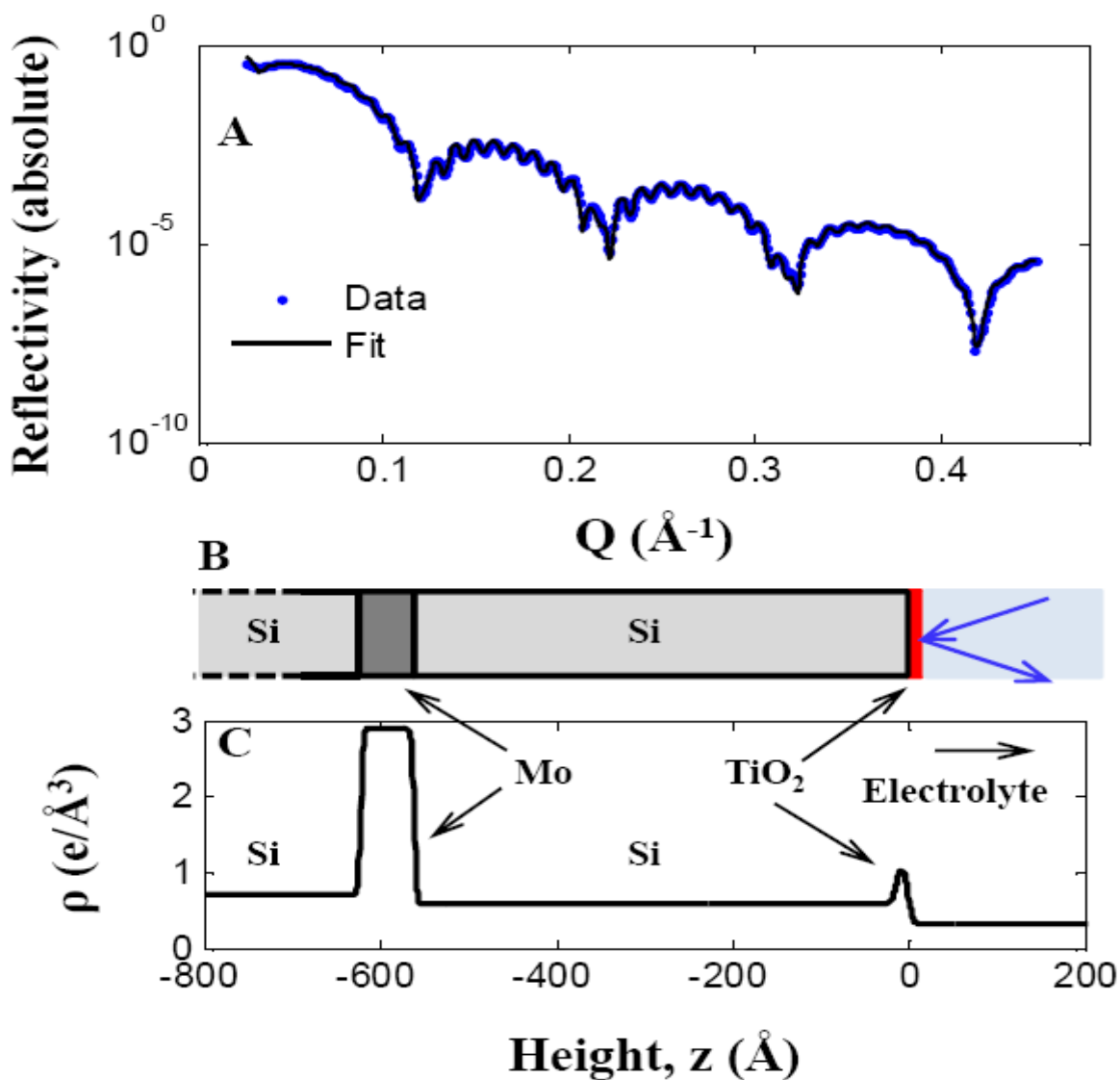
Figure 5.6: *In situ* X-ray reflectivity analysis of the TiO_2/Si/Mo tri-layer. XR data (blue dots), and the fit (black line) based on Parratt's recursion formalism. Inset shows the electron density variation of the model corresponding to the best fit of the data (measured on sample#3). A schematic of the sample is also shown; the blue arrows depict the incident and reflected x-rays at the electrolyte-nanofilm interface.

The measured *total* ion coverages on the planar nanofilm are 0.014 $Rb^+/Å^2$ and 0.033 $Sr^{2+}/Å^2$ (at 0.1mM RbOH and 0.1mM $Sr(OH)_2$, at pH 10 and 10.3, respectively, refer Table 5.1). The total Rb^+ coverage increased to 0.032 $Rb^+/Å^2$ at 1mM Rb^+ and pH 11. These measured coverages are significantly higher than those calculated for crystalline rutile powder surfaces using multi-site complexation (MUSIC) model[46] at the same electrolyte compositions. For example, the nanofilm Sr^{2+} coverage (0.033 $Sr^{2+}/Å^2$) is twice that calculated for rutile (~0.016 $Sr^{2+}/Å^2$) at the same solution ion concentration and pH (Table 5.1). The nanofilm Rb^+ coverage (0.014 $Rb^+/Å^2$, at 0.1mM) is ~3.5 times higher than that calculated for rutile (~0.004 $Rb^+/Å^2$). This >2-fold enhancement in the total ion coverages on the nanofilm compared to rutile is similar to the increase in surface charge observed for the nano-titania coated powder samples as compared to rutile powders (Fig. 5.5). This demonstrates that the planar substrates show the same behavior as the powder substrates, and shows that the results are general for the ALD-grown TiO_2 films. This observed enhancement in surface charge density for the nanofilm might be due to a higher density of surface adsorption sites compared to the perfect rutile (110) surface. However, it could also be associated with a possibly different stoichiometry of the nano-film, due to for e.g., presence of oxygen vacancies in the film, which may also explain the observed lower film density.

Significant differences were also observed in the *specifically adsorbed* ion coverages, between that observed on the nano-titania and that calculated for rutile using the MUSIC model[46] for the same conditions (Table 5.1). The measured specifically adsorbed coverage of 0.009 $Rb^+/Å^2$ on the nanofilm is ~3-fold higher than the MUSIC model calculation for the rutile

Table 5.1: Ion coverages observed on the Nano-Titania using XSW+XRF (on sample#3), compared with MUSIC model calculations for rutile TiO_2 as well as to previous powder titration work on rutile TiO_2. The uncertainties in the total ion coverages were primarily systematic, with a variability of ~6% for Sr^{2+}, and ~30% for Rb^+ based on equivalent measurements on different samples. These errors are due to uncertainties in attenuation corrections that were applied to the measured fluorescence yield (see methods section in text), because the exit angle of the emitted fluorescence used for these corrections was estimated from the detector geometry.

	Nano-Titania	**Rutile TiO$_2$**
	Ion coverage in #/Å^2 (measurement/calculation conditions)	
Rb$^+$		
Specifically-adsorbed Rb$^+$	0.009 (0.1mM, pH 10) - XRF+XSW	0.003 (0.1mM, pH 10) - MUSIC model
Total Rb$^+$ (intrinsic)	0.014 (0.1mM, pH 10) - XRF+XSW	0.004 (0.1mM, pH 10) - MUSIC model
Total Rb$^+$ (intrinsic)	0.032 (1mM, pH 11) - XRF+XSW	~0.010 (1mM, pH 11) - MUSIC model
Sr^{2+}		
Specifically-adsorbed Sr^{2+}	0.027 (0.1mM, pH 10.3)- XRF+XSW	0.016 (0.1mM, pH 10.3) - MUSIC model
Total Sr^{2+} (intrinsic)	0.033 (0.1mM, pH 10.3)- XRF+XSW	~0.016 (1mM, pH 10.3) - MUSIC model

surface (0.003 $Rb^+/Å^2$). This enhanced specifically adsorbed coverage of Rb^+ is similar to the increase in *total* ion coverage. Similarly, the specifically adsorbed Sr^{2+} coverage is ~2-fold higher than the calculation for the rutile surface, consistent with the enhancement observed for the total Sr^{2+} coverage.

The behavior shown by the two cations was further investigated by measuring the vertical profiles of these ions at the interface. An initial assessment of the XSW data (i.e., fluorescence yield vs. momentum transfer Q, Fig. 5.7) shows that the modulations of the Sr^{2+} yield are shifted towards lower Q with respect to the Ti yield while the modulations in the Rb^+ yield appear to be un-shifted. This immediately suggests that the average vertical ion-Ti separation or $\Delta_{\text{Ion-Ti}}$ is larger for Sr^{2+} compared to Rb^+. A complete analysis (Table 5.2) reveals that specifically adsorbed Rb^+ is centered at a depth of 3.2 ± 1 Å *below* the nano-titania film surface, unlike the specifically-adsorbed Sr^{2+} that is centered at the surface within the experimental uncertainties (with a height of 0.5 ± 1 Å). Here, all heights are referenced to the inflection point (i.e., z=0) of the error-function density profile of the nanofilm-electrolyte interface which had an interfacial *rms* roughness, $\sigma = 5.0 \pm 0.1$ Å. This implies that while Sr^{2+} specifically-adsorbs equally well at all the exposed areas of the surface (i.e. both above and below the average height of the rough surface), Rb^+ apparently specifically-adsorbs preferentially *below* the average surface plane (i.e., in the valleys of the rough surface).

The specifically adsorbed height of Rb^+ on the nano-titania surface is in contrast to recent measurements on single crystalline rutile (110) surface (using resonant anomalous x-ray reflectivity[92]), where Rb^+ was found to be located at a height of 2.1 Å *above* the surface plane (the height of 2.1 Å above the surface plane is equivalent to a height of 3.72 Å from the rutile
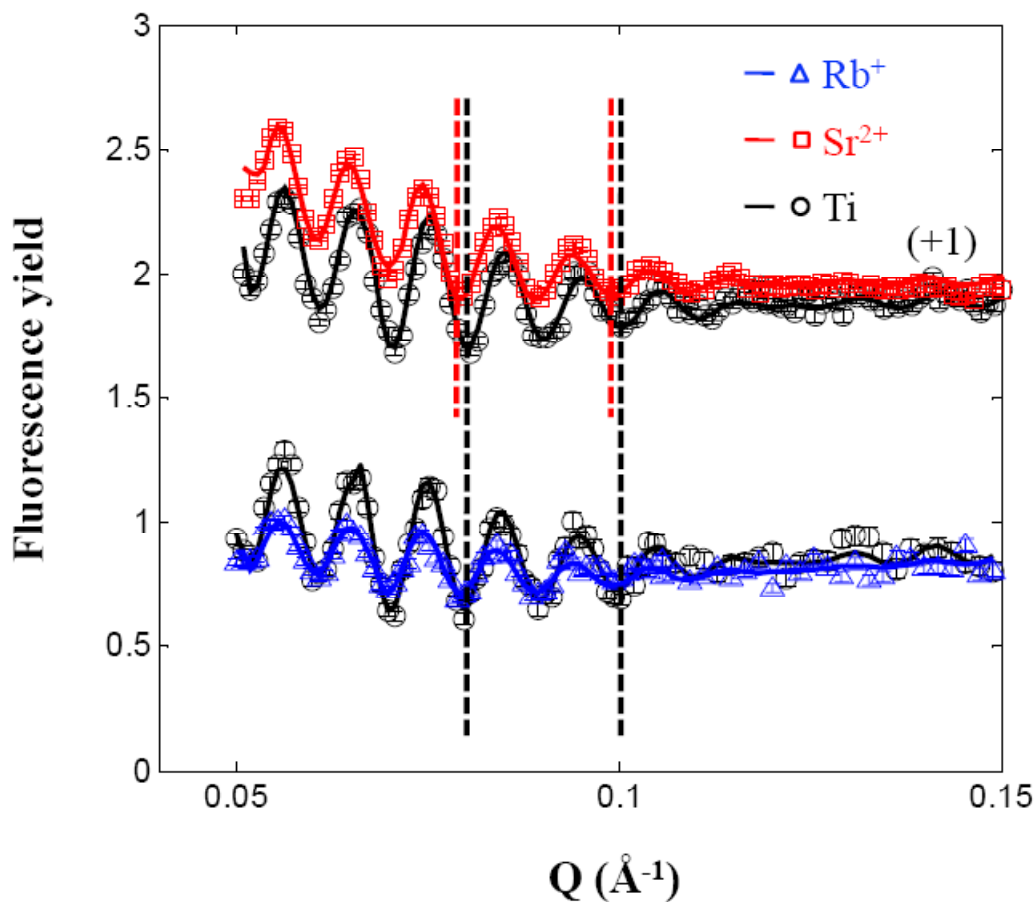
Figure 5.7: XSW analysis of ions adsorbing at the nanotitania-electrolyte interface. XSW data (symbols, measured on sample#3) and the model dependent fits (lines) for measurements under two different aqueous electrolytes, Rb^+ and Sr^{2+}. The Ti-yield (black circles) was measured at the same time as the ion yield (blue triangles: Rb^+, red squares: Sr^{2+}) for each case. The dashed vertical lines indicate that there is a Q-shift in the Sr^{2+} yield with respect to the Ti yield, while the Rb^+ yield is unshifted. The Ti and Sr^{2+} yields measured with the Sr^{2+}-electrolyte have been vertically offset by +1 for clarity.

Table 5.2: Parameters derived from the fit of XSW data for the Ti- and ion (Rb^+/Sr^{2+})- yield measured on sample#3.

Measurement for:-	RbOH 0.1mM		Sr(OH)$_2$ 0.1mM	
	Ti-XSW	Rb-XSW	Ti-XSW	Sr-XSW
Structure				
Z_0 (Å)	-10.1 ± 1	-5.8 ± 0.9	-12.8 ± 1	-4.8 ± 0.6
Δ (Å)[a]	17 ± 5	n/a	22 ± 3	n/a
σ (Å)[b]	n/a	11 ± 3	n/a	10 ± 2
$x_{Diffuse}$ (%)	n/a	34 ± 11	n/a	18 ± 8
L_D (Å)	n/a	304	n/a	176
Extrinsic				
Θ_{inc}	0.4	0.4	0.4	0.4
Angle avg., ΔQ_{ref} (Å^{-1})	0.036±0.001	0.037±0.001	0.037±0.001	0.039±0.001
tH_2O (μ)	6 ± 2	6 ± 1	2.6 ± 0.3	2.7 ± 0.3
tKap (μ)	8 ± 2	11 ± 1	8.8 ± 0.7	1.9 ± 0.3

[a] The Ti distribution is represented by a rectangular profile of width Δ, centered at Z_0, with interfacial roughnesses that are fixed to that obtained from X-ray reflectivity analysis.
[b] The ion profile includes condensed and diffuse components. The condensed component is represented by a Gaussian function with an rms width, σ, and centered at Z_0. The Debye length of the diffuse part is fixed based on the value expected from linearized Poisson-Boltzmann theory. $x_{Diffuse}$ is the fraction of total adsorbed ions present in the diffuse layer. Ions present in the bulk solution were also included based on bulk fraction determined from measured total coverage and measured solution thickness.
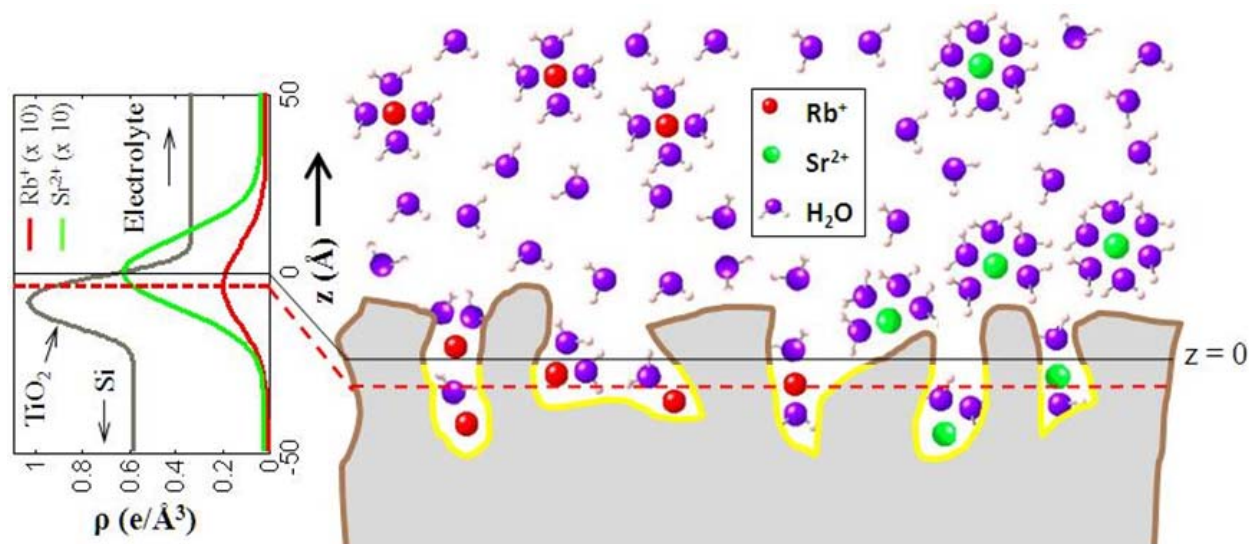
Figure 5.8: Schematic showing the interaction of ions at the electrolyte-titania nanofilm interface. Rb^+ (left) and Sr^{2+} (right). The Rb^+ ions are preferentially adsorbed in the pores below the surface while Sr^{2+} adsorb equally both above and below the rough surface (the black horizontal line shows the zero surface height). The ions that are part of the diffuse double layer are also shown. The plot shows the electron density profiles of the ions (red: Rb^+, green: Sr^{2+}) and the total electron density profile obtained from reflectivity (brown). The ion profiles shown are in absolute units (increased by a factor of 10 for clarity) based on the ion coverages obtained from XRF and XSW analyses.
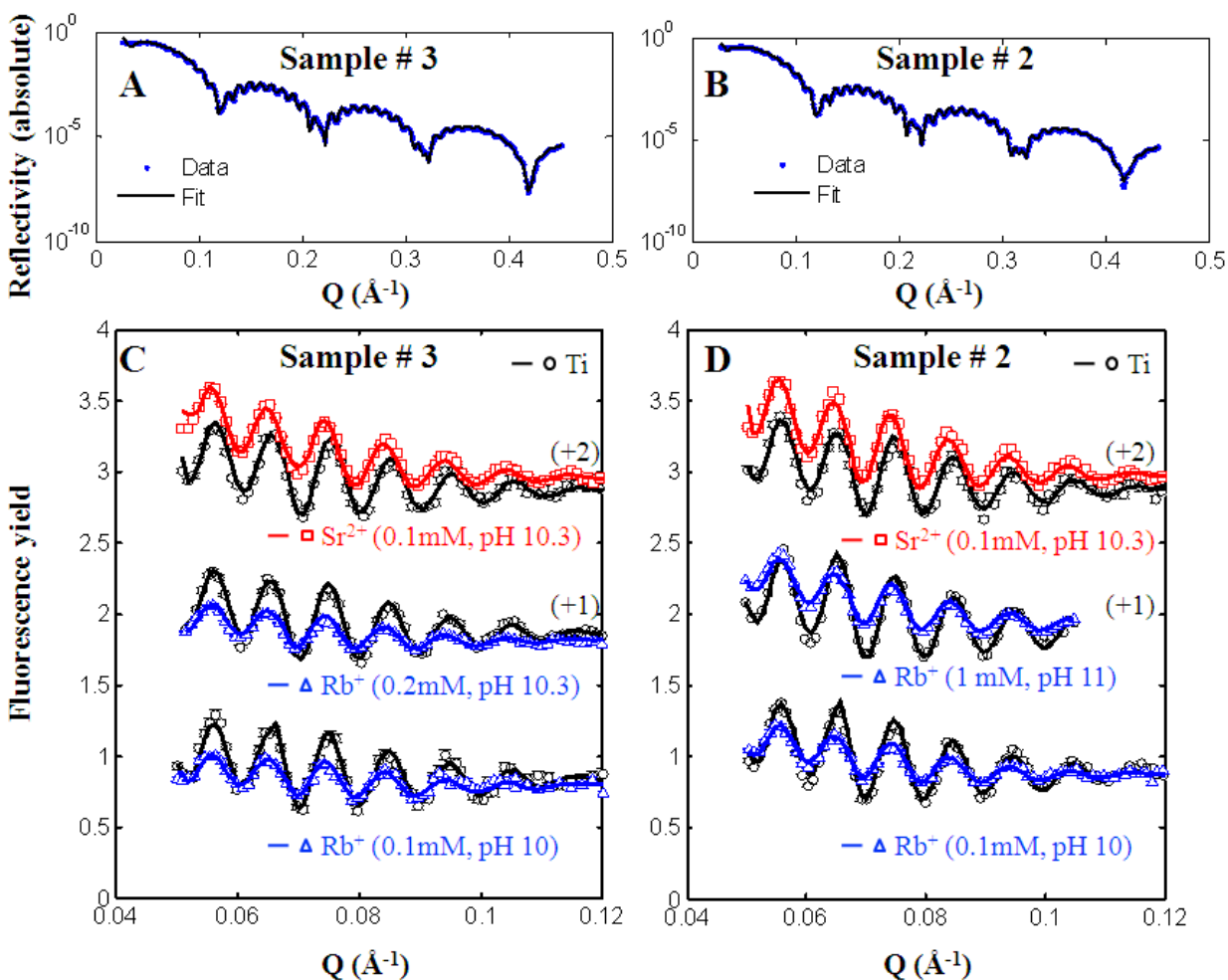
Figure 5.9: XR and XSW (titania and ion, i.e., Rb$^+$ and Sr^{2+}, fluorescence yield) analysis of data measured on two different samples, and under different electrolyte conditions. A and B: XR data (dots) and model based fits (lines) for measurements on sample#3 and 2 respectively. The electrolytes used for the XR measurements were Rb$^+$ 0.2mM pH 10.3, and Rb$^+$ 1mM pH 11 for samples 3 and 2 respectively. C and D: Ti and Ion XSW data (symbols) and model fits (lines) for samples 3 and 2 respectively. The electrolyte composition is indicated below each pair of curves. In each pair, the Ti-yield (black circles) was measured simultaneously with the ion yield (blue triangles: Rb$^+$, red squares: Sr^{2+}). The data are vertically offset for clarity.

Table 5.3: Estimation of Ti and Rb^+/Sr^{2+} coverages, from measured x-ray fluorescence and x-ray standing waves data, on different samples and under different electrolytes.

	Ti coverage, total, in #/19.22$Å^2$ (estimated TiO_2 thickness[a] in parenthesis)	Total ion coverage, i.e., measured 2D density – bulk ions[b]), in #/19.22$Å^2$ (expressed as % of measured 2D density in parenthesis[c])
Sample # 2		
Rb^+ 0.1mM	4.78 (7.8 $Å$[d])	0.19 (82%)
Rb^+ 1mM	3.97 (6.4 $Å$[d])	0.62 (66%)
Sr^{2+} 0.1mM	4.53 (7.4 $Å$[d])	0.68 (93%)
Sample # 3		
Rb^+ 0.1mM	4.54 (7.4 $Å$[e])	0.26 (93%)
Rb^+ 0.2mM	4.98 (8.1 $Å$[e])	0.36 (79%)
Sr^{2+} 0.1mM	4.85 (7.9 $Å$[e])	0.64 (96%)

Table 5.4: Position of the peak in the condensed ion distribution with respect to the average surface height of the titania-electrolyte interface (z=0), for data measured on different samples and under different electrolytes. The condensed ion height from the TiO_2 surface is obtained from the TiO_2 layer center determined from reflectivity, and the Ion – Ti separation determined from XSW.

Electrolyte	Sample # 3	Sample # 2
Rb^+ 0.1mM, pH 10	- 3.2 ± 1 $Å$	- 3.6 ± 1 $Å$
Rb^+ 0.2mM, pH 10.3	- 2.2 ± 1 $Å$	n/a
Rb^+ 1.0mM, pH 11	n/a	- 2.4 ± 1 $Å$
Sr^{2+} 0.1mM, pH 10.3	+ 0.5 ± 1 $Å$	- 0.9 ± 2 $Å$

---

[a] Thickness estimation based on assumption of bulk TiO_2 density in the film.
[b] Ion 2D density measured from x-ray fluorescence, while bulk coverage estimated from known ion concentration in bulk solution and solution thickness known from model-independent analysis of Ti fluorescence yield.
[c] Total intrinsic coverage of ions (including condensed or diffuse layers) expressed as fraction of the total measured 2D density which also includes the bulk solution contribution. This fraction was useful in the final model dependent XSW analysis of the ion yield.
[d] Compare against the value of TiO_2 thickness based on reflectivity, which is 13.5 ± 0.3 $Å$ for this sample.
[e] Compare against the value of TiO_2 thickness based on reflectivity, which is 14.9 ± 0.2 $Å$ for this sample.

Table 5.5: Parameters derived from fit of reflectivity data measured *in situ* (under aqueous electrolyte), on sample#2. Reflectivity analysis parameters for data measured on samples #1 and #3 are shown in Table 4.1.

	In situ results (sample#2)
X-ray Reflectivity	
Fit quality [a]	
R^2	0.019
Structure [b]	
t_{TiO_2} (Å)	13.5 ± 0.3
t_{Si} (Å)	547.9 ± 0.3
t_{Mo} (Å)	60.98 ± 0.01
X_{TiO_2} [c]	0.90 ± 0.02
X_{Si}	0.82 ± 0.02
X_{Mo}	1.099 ± 0.006
$\sigma_{Air-TiO_2}$ (Å)	5.4 ± 0.1
σ_{TiO_2-Si} (Å)	5.6 ± 0.2
σ_{Si-Mo} (Å)	3.45 ± 0.02
σ_{Mo-Si} (Å)	3.57 ± 0.02
Extrinsic	
t_{H_2O} (μ)	2.34 ± 0.08
t_{Kap} (μ)	7.3 ± 0.2
X_{H_2O} [d]	1
X_{Kap} [d]	1
Angle avg., ΔQ_{Ref} (Å^{-1})	0.048 ± 0.001

---

[a] Fit quality described by parameter R-squared or $R^2 = 1/n \sum \{ (y\text{-}f)^2 / y^2 \}$, where *y* denotes the data, *f* the calculation, and *n* number of data points.

[b] Uncertainties are based on a minimum 2 percent error-bar enforced on the data points when the statistical uncertainty was smaller.

[c] X denotes the fraction of the electron density of the layer with respect to the electron density of bulk material.

[d] Parameter fixed during the fit.

Table 5.6: Elemental distribution from model-dependent analyses of Ti and ion (Rb^+/Sr^{2+}) fluorescence yield, for data measured on different samples, and under different electrolytes.

	Ti yield analysis			Ion yield analysis		
Sample# 3	*Solution conditions:-*			*Solution conditions:-*		
	Rb^+ 0.1mM	Rb^+ 0.2mM	Sr^{2+} 0.1mM	Rb^+ 0.1mM	Rb^+ 0.2mM	Sr^{2+} 0.1mM
Structure						
Z_0 (Å) x -1	10.1 ± 1	10.5 ± 1	12.8 ± 1	5.8 ± 0.9	5.2 ± 0.9	4.8 ± 0.6
Δ (Å)[a]	17 ± 5	20 ± 3	22 ± 3	n/a	n/a	n/a
σ (Å)[b]	n/a	n/a	n/a	11 ± 3	12 ± 2	10 ± 2
$x_{Diffuse}$ (%)	n/a	n/a	n/a	34 ± 11	25 ± 12	18 ± 8
L_D (Å)	n/a	n/a	n/a	304	215	176
Extrinsic						
Θ_{inc}	0.4	0.4	0.4	0.4	0.4	0.4
Angle avg., ΔQ_{ref} (Å^{-1})	0.036±0.001	0.037±0.001	0.037±0.001	0.037±0.001	0.037±0.001	0.039±0.001
tH_2O (μ)	6 ± 2	3.8 ± 0.6	2.6 ± 0.3	6 ± 1	3.5 ± 0.5	2.7 ± 0.3
tKap (μ)	8 ± 2	8.3 ± 0.7	8.8 ± 0.7	11 ± 1	12.1 ± 0.5	1.9 ± 0.3
Sample# 2	*Solution conditions:-*			*Solution conditions:-*		
	Rb^+ 0.1mM	Rb^+ 1.0mM	Sr^{2+} 0.1mM	Rb^+ 0.1mM	Rb^+ 1.0mM	Sr^{2+} 0.1mM
Structure						
Z_0 (Å) x -1	9.1 ± 1	11.0 ± 0.8	10.0 ± 2	5.9 ± 0.5	6.6 ± 0.8	4.1 ± 0.7
Δ (Å)	17 ± 4	13 ± 6	19 ± 4	n/a	n/a	n/a
σ (Å)	n/a	n/a	n/a	11 ± 2	9 ± 2	10 ± 2
$x_{Diffuse}$ (%)	n/a	n/a	n/a	32 ± 7	18 ± 17	6 ± 12
L_D (Å)	n/a	n/a	n/a	304	96	176
Extrinsic						
Θ_{inc}	0.4	0.4	0.4	0.4	0.4	0.4
Angle avg., ΔQ_{ref} (Å^{-1})	0.035±0.001	0.035±0.001	0.036±0.001	0.036±0.001	0.035±0.001	0.037±0.001
tH_2O (μ)	2.8 ± 0.7	3.1 ± 0.6	3 ± 1	2.6 ± 0.2	3.0 ± 0.7	2.7 ± 0.4
tKap (μ)	7.8 ± 0.8	7.6 ± 0.7	8 ± 1	9.3 ± 0.3	4.8 ± 0.6	1.7 ± 0.4

---

[a] Ti distribution represented by a rectangular profile of width Δ and centered at Z_0, the roughness of the edges is fixed at the interfacial roughness derived from reflectivity analysis.

[b] Ion profile includes a condensed and a diffuse part. Condensed part is represented by the Gaussian of width σ and centered at Z_0. The Debye length of the diffuse part is fixed based on the value expected from linearized Poisson-Boltzmann theory. $x_{Diffuse}$ is the fraction of total adsorbed ions present in the diffuse layer.

(110) Ti-O plane). These differences appear to be due, at least in part, to the different morphologies of the nano-titania film and rutile sufaces. The surface roughness of the nanofilm (σ = 5.0 ± 0.1 Å) is larger in comparison to that observed on rutile (110) ($\sigma \sim$ 1.5 Å)[92]. More importantly, the ~few nm lateral surface domain size of the nano-titania film (Supplementary Fig. 5.3) is much smaller than the typical ~µm-sized atomically flat terraces separated by elementary steps observed previously on rutile surfaces[22]. Higher roughness and smaller domain size of the nanofilm could be due to a higher effective surface porosity. The specifically-adsorbed Rb^+ being centered below the average surface plane might therefore be a result of a preferential adsorption inside the surface pores (Fig. 5.9). This would support previous studies that found that the electrode pore size directly controls EC capacitance[115].

Key insight into these results is obtained by exploring the vertical Rb^+ distribution. The fraction of specifically adsorbed Rb^+ and Sr^{2+} located below the average surface height (in the presumed pores) can be estimated if we assume that the condensed layer ions are conformal with the surface roughness, but with a different interaction strength for the inner and outer-surfaces (i.e., below and above z=0, respectively). The measured average condensed layer ion height specifies the ratio of the inner- and outer-surface coverages: $\theta_{inner}^C / \theta_{outer}^C$ (where, e.g., θ_{inner}^C is the condensed ion coverage at the inner surface). We find that $\theta_{inner}^C / \theta_{outer}^C$ is ~9 for Rb^+, compared to ~1 for Sr^{2+}. Thus the majority of specifically-adsorbed Rb^+ ions apparently are located inside the surface pores. It is not clear why Rb^+ shows this anomalously increased specific-adsorption tendency at the inner surfaces of the nano-titania (i.e., in the surface pores). This can be associated with the fact that surface charges within the ~nm-scale surface pores cannot be screened effectively by the more extended diffuse layer (having a characteristic ~30

nm Debye length) thereby stabilizing specific adsorption within these confined spaces. This suggests that interfacial electrode porosity can be used as a way to increase the fraction of condensed layer ions in ECs, thus resulting in enhanced energy densities.

5.4 Conclusion

These results demonstrate that titania nanofilms exhibit significantly enhanced properties for ion adsorption as compared to single crystalline rutile surfaces[118]. This is expressed by a >2-fold increase in the total amount of interacting ions, and a ~9-fold enhancement of specific adsorption of monovalent ions within the pores defined by the surface roughness. These results show that surface morphology is a critical factor for improving EC properties, as it offers a way to tune the pseudo- vs. double-layer- capacitive nature of the electrode-ion interaction by controlling the distribution of ions in the condensed and diffuse layers. The use of nanofilms for ECs is attractive for a number of reasons. First, EC energy storage characteristics are defined by interactions at the material surface, and therefore it is likely that only nm-thick layers are needed to achieve the appropriate characteristics. Second, advanced growth technologies such as atomic layer deposition offer an attractive way to create uniform nano-coatings even on high surface area materials that are needed for viable energy storage devices. The present results demonstrate that use of nanometer thick layers provides an additional degree of control that can be used to fully optimize materials properties.

Chapter 6 : Ongoing and Future Work

6.1 XR and XSW Measurements on a Periodic Multilayer

6.1.1 Introduction

X-ray standing waves in the total-external reflection (TER) and multi-layer (ML) configurations offers the advantage that a wide range of substrate structures can be chosen to generate the XSW, unlike the case of Bragg-XSW which is limited to single crystalline substrates. Earlier in this thesis (Chapter 5), a tri-layer sample consisting of layers of TiO_2, Si and Mo was used to probe the ion distribution at the TiO_2 - electrolyte interface, where the XSW measurements were carried out using the strong reflection of the tri-layer through the low scattering angle range (Q ~ 0 - 0.12 Å^{-1}). Here instead we use a Si/Mo periodic multi-layer (PML) sample as the substrate (coated with a TiO_2 nano-film), and use the TER region and the strong reflection around the multilayer Bragg peaks to measure elemental fluorescence yields in the PML-XSW mode. Measurements reported aim to characterize the multi-layer structure, as well as probe the ion distribution at the TiO_2-electrolyte interface.

6.1.2 Experimental

The sample used during these measurements was a TiO_2 coated Si/Mo multi-layer grown on a Si substrate (Fig. 6.1 shows a schematic of the multi-layer). The TiO_2 layer was expected to be ~ 10 Å thick, and was grown using atomic layer deposition (ALD). The multi-layer structure was expected to be 20 bi-layers of Si and Mo, where the Si and Mo layer thicknesses in each bi-layer were expected to be 160 Å and 26 Å respectively, based on an earlier characterization of
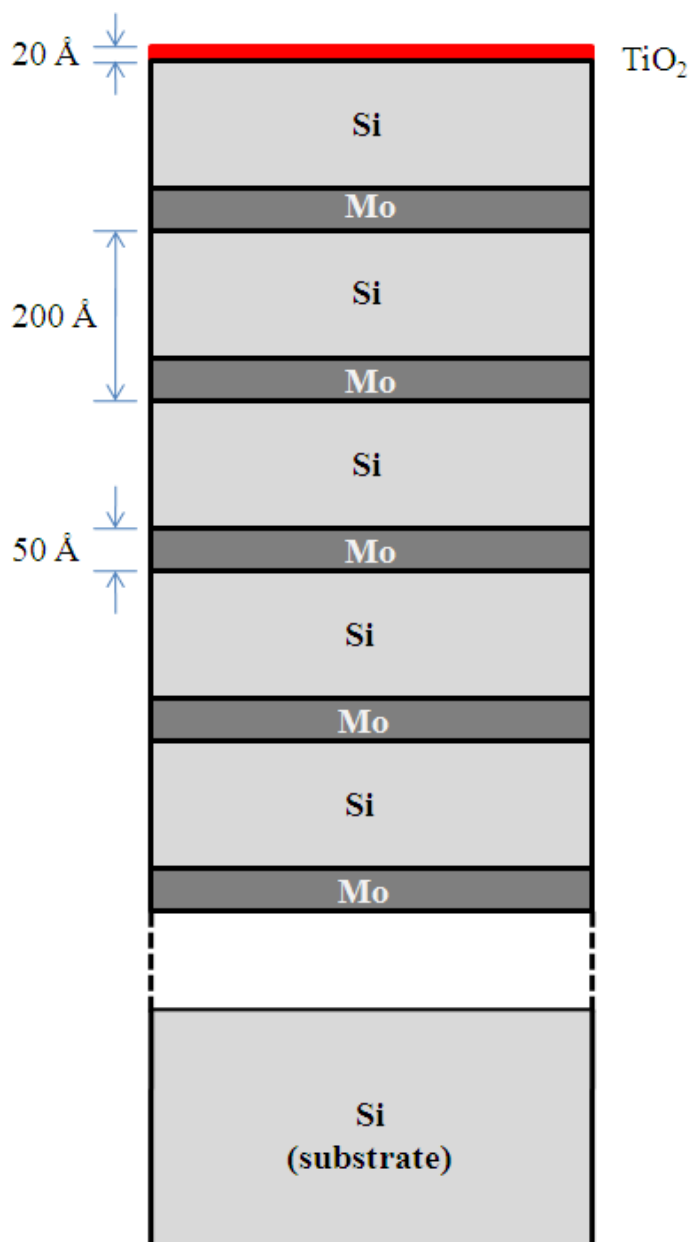
Figure 6.1: Schematic of a periodic multi-layer with adjacent low and high density materials, 200 Å Si / 50 Å Mo. A thin film of TiO_2 (20 Å) on the surface is shown in red. The relative dimensions of the thicknesses of different layers are preserved in the plot (i.e., 1:1 scale in *relative* thicknesses).

these multi-layers[82]. The samples were de-greased with acetone, methanol and de-ionized water in a sonicator before the x-ray measurements. The measurements were conducted both *ex situ* (in air), and *in situ* in contact with electrolyte solutions (containing Rb^+ or Sr^{2+}). The *ex situ* measurements were conducted at sector 11-ID-D at the APS at Argonne National Laboratory, with an incident x-ray energy of 9.72 keV. The *in situ* measurements were done at sector 6-ID-B, where the incident energy was 17 keV. The fluorescence yield data was corrected for the detector dead-time, and for the variation of incident beam footprint on the sample with Q. The *in situ* XSW data reported is for the following solution conditions, RbOH 0.5mM pH 10.7, RbOH 1mM pH 11, RbOH 1mM NaCl 2mM pH 11, RbOH 1mM NaCl 5mM pH 11, RbOH 1mM NaCl 9mM pH 11, and RbOH 1mM with $SrCl_2$ 0.1mM pH 11.

6.1.3 Results and Discussion

The XR data measured in air is shown in Fig. 6.2B (magenta dots). We begin by a qualitative assessment of the data. Primarily, there are two distinct oscillations in the reflectivity data. The longer Q period oscillations correspond to the Bragg peaks of the multi-layer structure, i.e., the condition when reflections from each bi-layer constructively interfere. For e.g., the Q-spacing between the third and the fourth Bragg peak is $\Delta Q \sim 0.031$ Å^{-1}, this corresponds to a d-spacing of ~200 Å, as expected. The fine period oscillations have a period $\Delta Q \sim 0.0016$ Å^{-1}, this corresponds to a real space period of ~ 4000 Å. This arises from the interference from the thickness of the full structure, i.e. from the top and bottom of the full thickness which is expected to be 20 bi-layers each with a thickness of ~200 Å. The above assessment was only qualitative, and is strictly speaking valid only when the kinematical approximation is applicable. Since this is
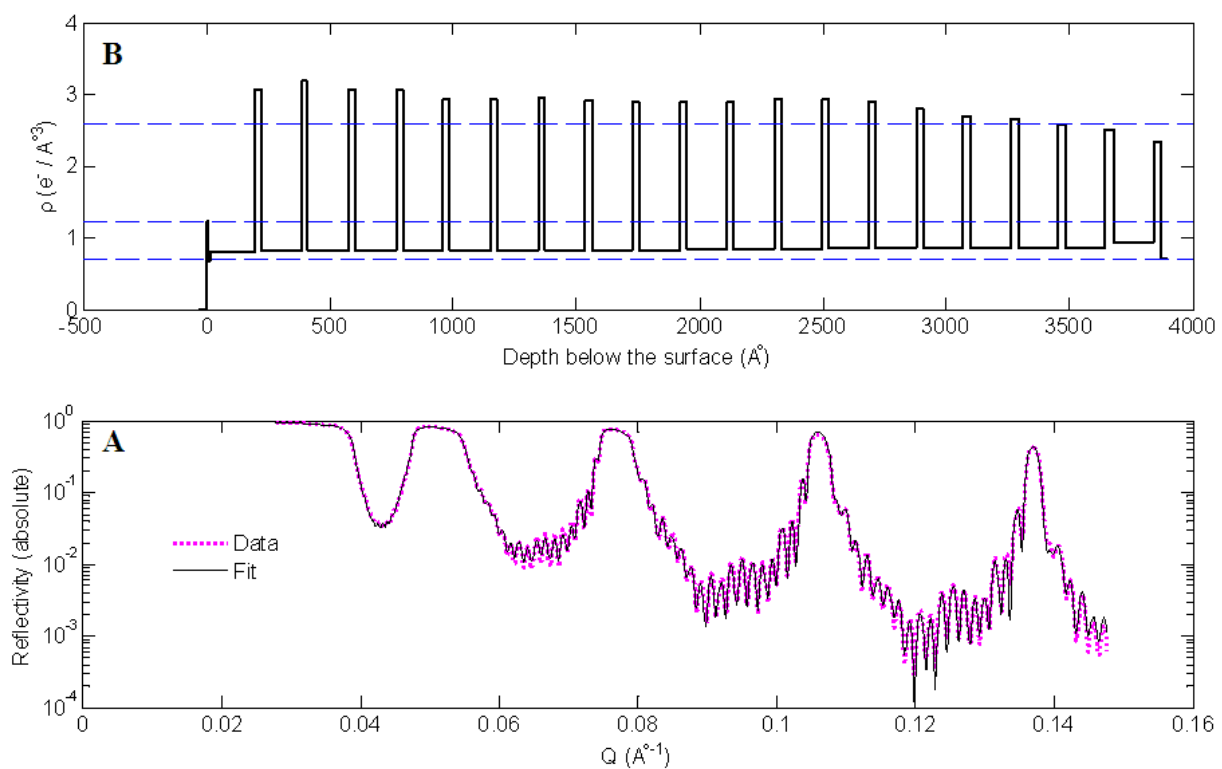
Figure 6.2: X-ray reflectivity analyses of the TiO_2 coated Si/Mo multilayer sample. (A): XR data measured in air (magenta dots), and model-based fit (black line), plotted in absolute units. (B): The total electron density profile of the model used (this model is referred to as the best-fit reflectivity structure in the text). Each layer was represented by separate parameters for thickness and density-factor (i.e. density relative to bulk material). The electron densities of the bulk materials (i.e., Si, Mo, and TiO_2) are shown as dashed horizontal blue lines.
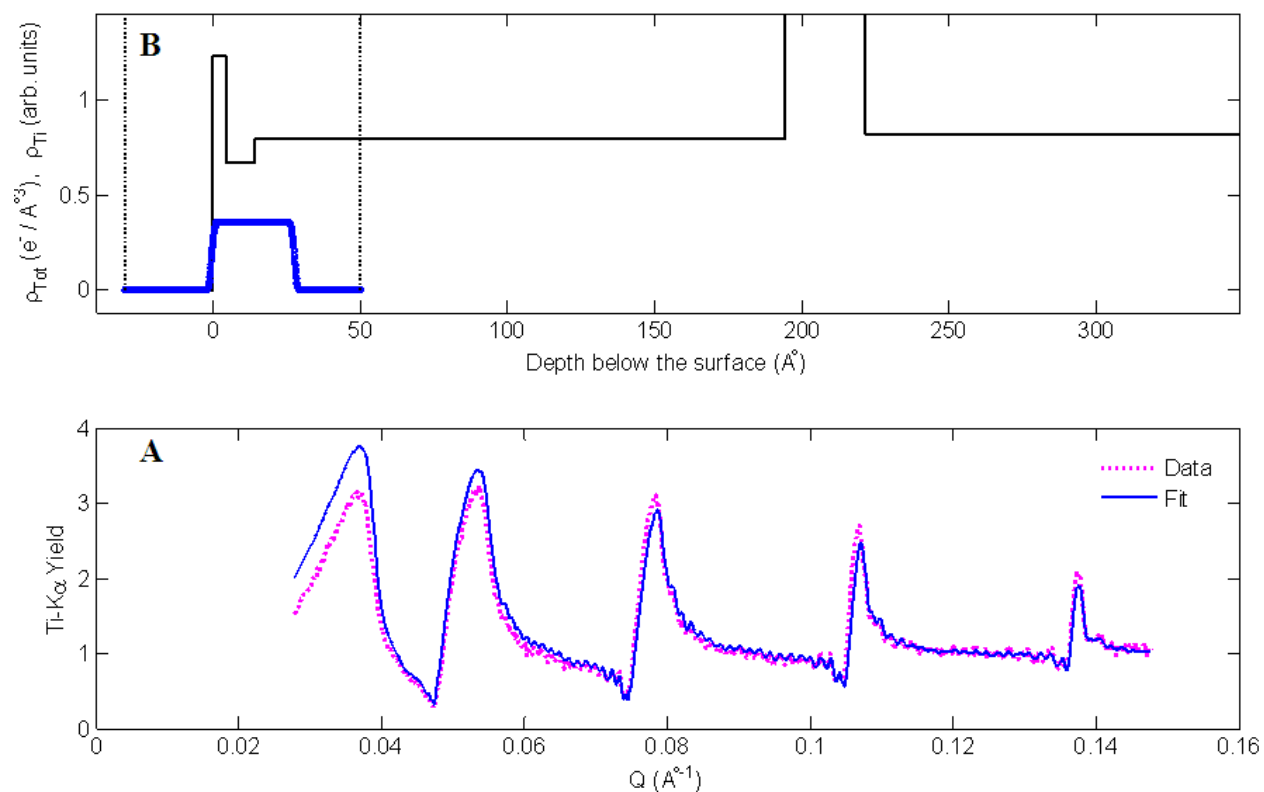
Figure 6.3: XSW analysis for the TiO$_2$ coated Si/Mo multi-layer system. (A): X-ray standing wave (XSW) data for Ti-Kα yield measured in air, and model dependent fit. (B): The total electron density profile (black line, in e/Å^3) based on the best-fit reflectivity structure, and the corresponding Ti-profile obtained from XSW analysis (blue line, in arbitrary units). Notice the disagreement in the Ti thickness between the best-fit reflectivity structure and the XSW derived structure.

Table 6.1: Structural parameters obtained from XR and XSW analysis based on the *best-fit reflectivity structure*.

A. X-ray Reflectivity Results				
Multi-Layer Structure				
Bi-layer Number	t_{Si} (Å)	t_{Mo} (Å)	X_{Si}	X_{Mo}
1	179.8 ± 3.5	27.5 ± 0.6	1.124 ± 0.010	1.147 ± 0.019
2	164.6 ± 0.5	24.9 ± 0.5	1.159 ± 0.010	1.192 ± 0.019
3	164.9 ± 0.4	26.7 ± 0.5	1.163 ± 0.010	1.148 ± 0.017
4	166.1 ± 0.5	26.5 ± 0.5	1.168 ± 0.010	1.143 ± 0.018
5	163.7 ± 0.5	28.3 ± 0.6	1.170 ± 0.010	1.095 ± 0.016
6	164.2 ± 0.5	28.0 ± 0.6	1.167 ± 0.011	1.094 ± 0.016
7	165.1 ± 0.6	27.3 ± 0.6	1.167 ± 0.011	1.107 ± 0.018
8	164.2 ± 0.6	28.1 ± 0.7	1.166 ± 0.011	1.086 ± 0.017
9	164.1 ± 0.6	28.3 ± 0.7	1.171 ± 0.012	1.083 ± 0.017
10	162.9 ± 0.6	28.1 ± 0.7	1.173 ± 0.013	1.081 ± 0.018
11	163.2 ± 0.7	27.8 ± 0.8	1.176 ± 0.013	1.081 ± 0.019
12	163.9 ± 0.8	26.7 ± 0.9	1.181 ± 0.015	1.100 ± 0.021
13	165.3 ± 0.8	26.8 ± 1.0	1.189 ± 0.016	1.093 ± 0.023
14	164.9 ± 0.9	26.8 ± 1.0	1.204 ± 0.017	1.084 ± 0.023
15	164.6 ± 1.0	27.5 ± 1.2	1.213 ± 0.018	1.048 ± 0.023
16	163.3 ± 1.1	28.5 ± 1.3	1.207 ± 0.018	1.008 ± 0.022
17	163.8 ± 1.1	29.6 ± 1.3	1.204 ± 0.019	0.994 ± 0.021
18	162.5 ± 1.1	32.4 ± 1.3	1.209 ± 0.019	0.959 ± 0.018
19	159.2 ± 1.2	32.8 ± 1.4	1.201 ± 0.023	0.940 ± 0.018
20	163.5 ± 1.6	30.4 ± 1.9	1.321 ± 0.023	0.877 ± 0.021
Additional Parameters				
t_{TiO_2} (Å)	10			
t_{SiO_2} (Å)	10			
σ (Si-Mo) (Å)	11.5 ± 0.3			
σ (Mo-Si) (Å)	1			
σ (Air-TiO$_2$) (Å)	1			
σ (TiO$_2$-SiO$_2$)(Å)	1			
σ (SiO$_2$-Si) (Å)	1			
B. X-ray Standing Waves Results				
Ti distribution				
Z_{Ti} (Å)	13.5 ± 0.3			
Δ_{Ti} (Å)	28 ± 2			

not the case for the data shown (where multiple scattering effects are important), it is important to conduct the full quantitative analysis to obtain the precise multilayer structure.

The analysis of the XR data was conducted using least-squares fitting from calculations based on two different models of the multi-layer structure. The first was a simple model that assumed that the multi-layer can be represented by a single bi-layer structure (i.e., the bi-layer thickness d, and the Mo to Si thickness fraction or f_{Mo}) throughout each of the 20 bi-layers. The top-most Si layer was assumed to have a 10 Å thick native-oxide layer of SiO_2, above which a TiO_2 layer with the expected thickness of 10 Å was assumed. This model also assumed that each of the layers had the density same as the density of the corresponding bulk materials. The fit based on this model resulted in the bi-layer structure of d = 190.7 ± 0.1 Å, and f_{Mo}= 0.169 ± 0.003. This fit however was not able to fully explain the features in the reflectivity data, with clear disagreements in the Q-locations and relative intensities of the fine-Q or subsidiary oscillations. This suggested that this simple model that assumed a single bi-layer structure throughout the 20 bi-layers was not sufficient, and a more detailed structural model was needed that allowed the variations in the bi-layer structure over the different bi-layers. We therefore used a second model which did not make any assumptions about the thickness, density or relative Si/Mo thickness fractions in any of the 20 bi-layers. The starting parameters for the fit based on this new model were based on the results obtained from the first model described above. In the new model, separate thickness and density factor parameters (i.e. density relative to bulk material) were used for each of the 40 layers (representing the Si and Mo) in the multilayer structure. The structure that gave the best fit based on this model is referred to as the *best-fit*

reflectivity structure (Fig. 6.2A shows the structure, while the line in Fig. 6.2B shows the fit, Table 6.1 shows the fit parameters).

The Ti-K$_\alpha$ yield data was fit (Fig. 6.3B) using a rectangular model as described in Chapter 4, where the position and width of the Ti layer were allowed to vary. Here the best-fit reflectivity structure was used in the calculation of the electric field intensities used in the XSW analysis. Based on this analysis, a Ti layer thickness of 28 ± 2 Å, and a Ti center of 13.5 ± 0.3 Å below the air-TiO$_2$ interface was obtained (Table 6.1). As shown in Fig. 6.3A, there is inconsistency in the Ti profile from the XSW analysis, and the TiO$_2$ structure based on the reflectivity analysis.

The reflectivity data was therefore also analyzed using an iterative procedure similar to that described in Chapter 3 for the analysis of the RAXR data. In this process, the reflectivity data was first analyzed using the TiO$_2$ layer fixed at the nominally expected value of 10 Å. For simplicity, no SiO$_2$ layer was used during these iterations. The reflectivity analyis was followed by fit of the XSW data to obtain the TiO$_2$ layer thickness. This thickness was then fed back as the new TiO$_2$ layer thickness to fit the reflectivity data. This new structure generated from the reflectivity analysis was then used to re-fit the Ti-yield data. This process was repeated until an agreement was achieved between the final Ti thickness from the XSW analysis and the Ti thickness that was assumed in the corresponding reflectivity analysis. This final total structure based on the consistency between the reflectivity and the Ti-XSW analysis is referred to as the *converged reflectivity structure* (Table 6.2). The converged structure shows an overall excellent agreement with the reflectivity data (Fig. 6.4B), with some minor disagreements around $Q = 0.12$ Å^{-1} where the fine-Q oscillations in the calculation have a smaller magnitude than the data. The
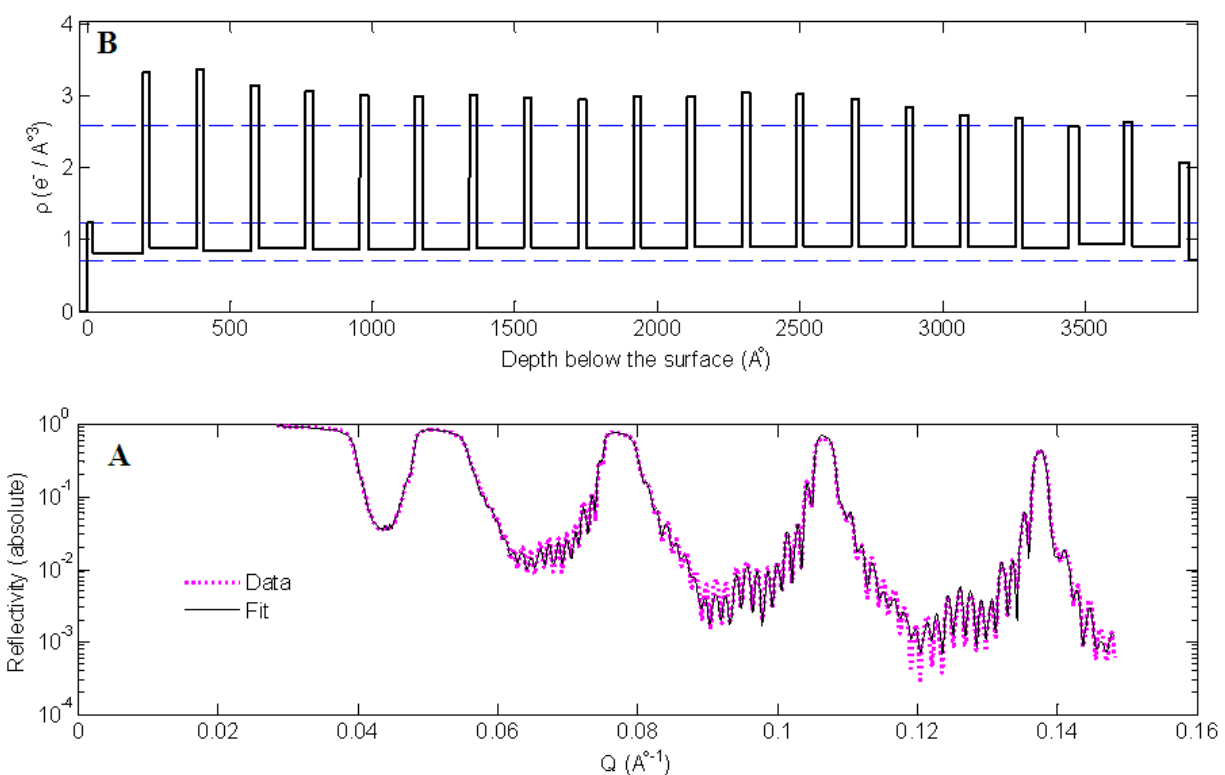
Figure 6.4: *Converged* XR analysis of the TiO_2 coated Si/Mo multi-layer system. (A): XR data measured in air, and model fit based on the *converged reflectivity structure* (see text). (B): The total electron density profile of the model used (this model is referred to as the converged reflectivity structure in the text). Each layer was represented by separate parameters for thickness and density-factor (i.e. density relative to bulk material). The dashed horizontal blue lines denote the electron densities of the bulk materials (i.e., Si, Mo, and TiO_2).
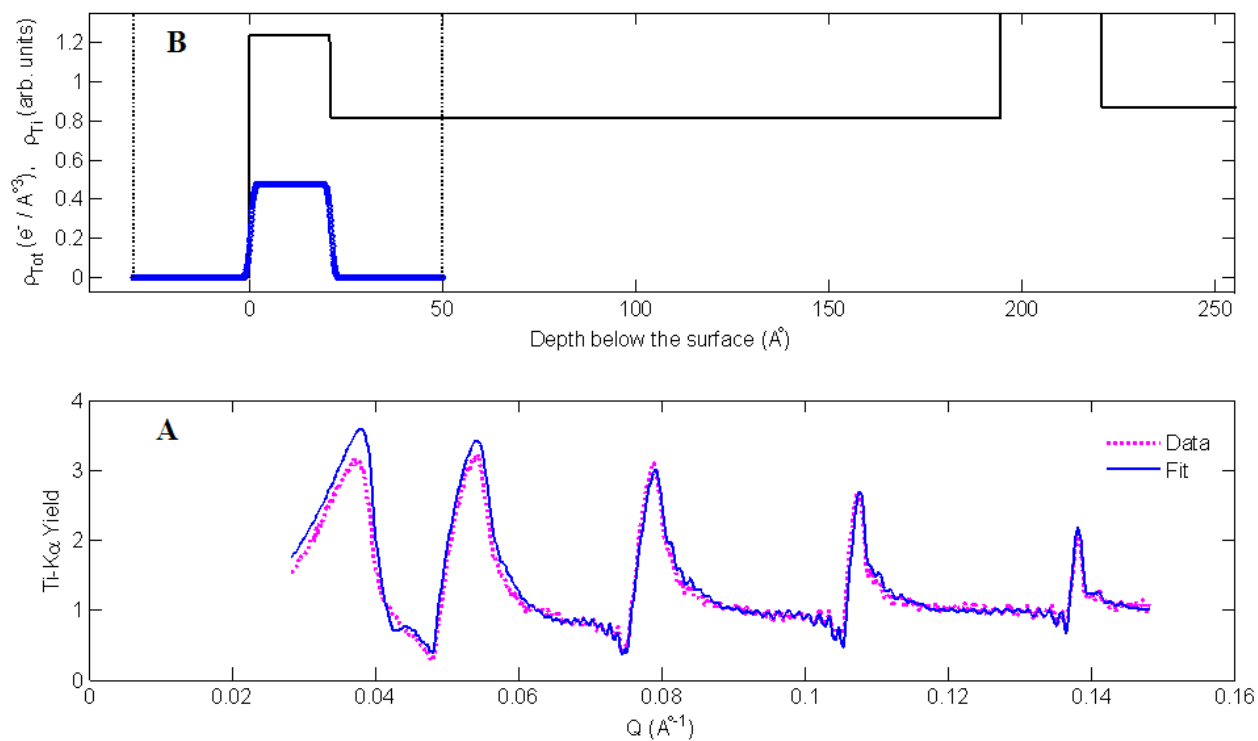
Figure 6.5: *Converged* XSW analysis of the TiO$_2$ coated Si/Mo multi-layer system. (A): X-ray standing wave (XSW) data for Ti-Kα yield measured in air, and model dependent fit based on the *converged reflectivity structure* (see text). (B): The total electron density profile (black line, in e/Å^3) based on the best-converged reflectivity structure, and the corresponding Ti-profile obtained from XSW analysis (blue line, in arbitrary units). Notice that there is consistency in the Ti thickness between the reflectivity structure and the XSW derived structure based on the XR-XSW iterative analysis, unlike the case when best-fit reflectivity structure was used.

Table 6.2: Structural parameters obtained from XR and XSW analysis based on the *converged reflectivity structure*.

A. X-ray Reflectivity Results				
Multi-Layer Structure				
Bi-layer Number	t_{Si} (Å)	t_{Mo} (Å)	X_{Si}	X_{Mo}
1	173.4 ± 0.4	25.9 ± 0.5	1.152 ± 0.008	1.249 ± 0.017
2	164.2 ± 0.3	23.5 ± 0.3	1.230 ± 0.010	1.259 ± 0.014
3	165.9 ± 0.4	26.2 ± 0.6	1.198 ± 0.010	1.179 ± 0.019
4	165.3 ± 0.4	26.8 ± 0.5	1.231 ± 0.010	1.148 ± 0.015
5	162.8 ± 0.5	28.2 ± 0.6	1.215 ± 0.010	1.122 ± 0.016
6	164.0 ± 0.5	28.0 ± 0.6	1.225 ± 0.011	1.117 ± 0.016
7	164.4 ± 0.6	27.3 ± 0.7	1.224 ± 0.012	1.124 ± 0.018
8	163.6 ± 0.6	28.1 ± 0.7	1.227 ± 0.012	1.112 ± 0.017
9	163.6 ± 0.6	28.0 ± 0.7	1.235 ± 0.013	1.104 ± 0.018
10	162.7 ± 0.7	27.5 ± 0.8	1.239 ± 0.013	1.116 ± 0.018
11	163.5 ± 0.8	26.8 ± 0.9	1.241 ± 0.014	1.120 ± 0.020
12	164.5 ± 0.9	26.2 ± 1.0	1.249 ± 0.015	1.133 ± 0.023
13	165.8 ± 1.0	25.7 ± 1.1	1.261 ± 0.018	1.128 ± 0.025
14	165.4 ± 1.0	26.1 ± 1.2	1.277 ± 0.018	1.108 ± 0.025
15	164.6 ± 1.2	26.8 ± 1.4	1.275 ± 0.020	1.062 ± 0.025
16	163.4 ± 1.2	28.1 ± 1.5	1.269 ± 0.021	1.022 ± 0.024
17	164.1 ± 1.3	29.3 ± 1.5	1.267 ± 0.021	1.007 ± 0.022
18	161.0 ± 1.3	32.8 ± 1.5	1.244 ± 0.024	0.960 ± 0.019
19	160.5 ± 1.4	30.7 ± 1.7	1.318 ± 0.023	0.983 ± 0.021
20	162.8 ± 2.0	31.9 ± 2.4	1.292 ± 0.033	0.775 ± 0.020
Additional Parameters				
t_{TiO_2} (Å)	21			
σ (Si-Mo) (Å)	12.0 ± 0.3			
σ (Mo-Si) (Å)	1			
σ (Air-TiO$_2$) (Å)	1			
B. X-ray Standing Waves Results				
Ti distribution				
Z_{Ti} (Å)	10.7 ± 0.2			
Δ_{Ti} (Å)	21 ± 2			

XSW analysis based on the *converged reflectivity structure* resulted in a Ti layer thickness of 21 ± 2 Å, and a Ti center of 10.7 ± 0.2 Å below the air-TiO$_2$ interface (Fig. 6.5A, Table 6.2).

The XR and XSW measurements were also conducted *in situ* where the multilayer sample was in contact with different electrolyte solutions, containing Rb$^+$ or Sr^{2+}. These measurements were aimed at measuring the diffuse profile of these ions at different ionic strengths, as the diffuse Debye length is expected to be a function of the total ionic strength based on the linearized Poisson Boltzmann description of the double layer (Fig. 6.6, also refer to Chapter 1.2). The solution conditions were chosen such that the expected Debye lengths were lower than the d-spacing of the multi-layer and larger than the experimental resolution of the planned measurement (~ 20 Å based on data range with Q_{max}=0.15 Å^{-1}). Figure 6.7 shows the Rb-K$_\alpha$ yield for six different solution conditions. Out of the six solutions, the Rb-yield for the RbOH 0.5mM case appears to be the most similar to the shape of the reflectivity data. This suggests that this solution has the most disordered Rb$^+$ structure as seen by PML-XSW at these scattering angles. This is not unexpected, since this solution is expected to have the largest Debye length (136 Å based on linearized PB theory) compared to the other solutions, and the length scale is comparable to the d-spacing of the multilayer (~190 Å). The solution conditions expected to have a shorter Debye length show some asymmetry in the shape of fluorescence yield around the Bragg peaks, indicating some ordering of the ion distribution. For example, the solution RbOH 1mM with NaCl 9mM (which is expected to have L$_D$ ~ 30 Å) has more asymmetry in the second Bragg peak shape in comparison to the low ionic strength solutions.
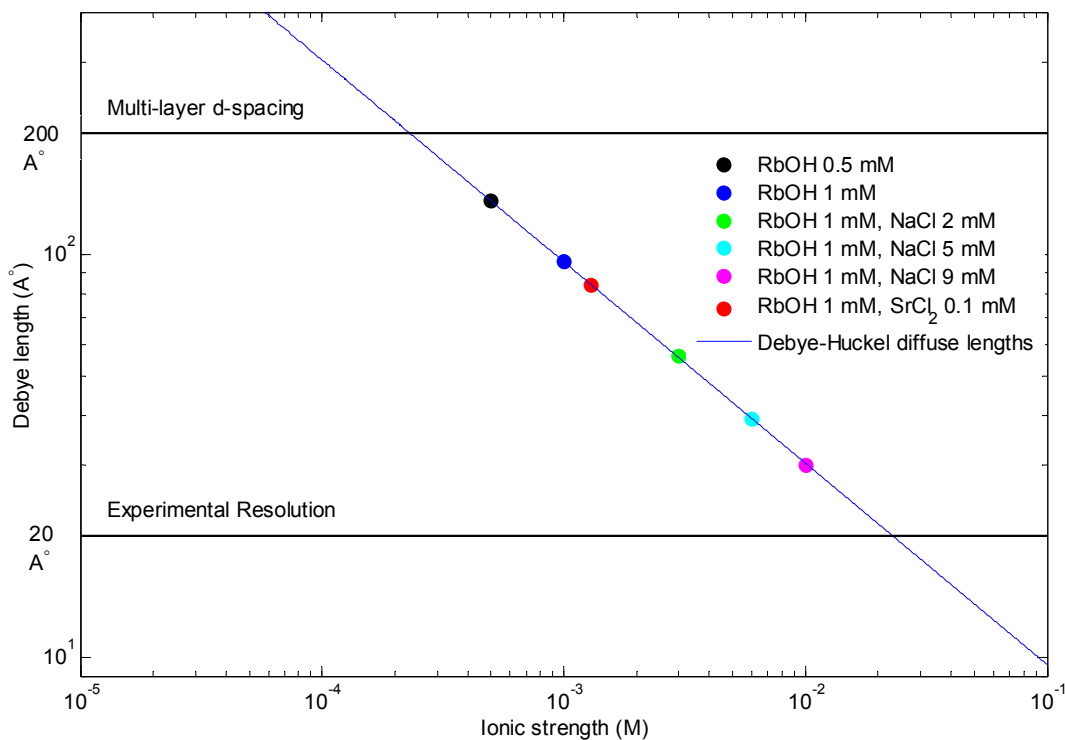
Figure 6.6: The electrolyte conditions chosen for the XSW experiments that measured Rb-Kα yield for the electrolyte-multilayer interfacial system, for different electrolytes. These ionic strengths were chosen (colored circles) to enable measurements of a series of Debye lengths of the diffuse ion profile (assuming a Debye-Huckel distribution) that are larger than the expected experimental resolution (~20 Å), and less than the period of the multi-layers (~200Å). The blue line shows the variation of Debye length with ionic strength, based on the Debye-Huckel distribution.
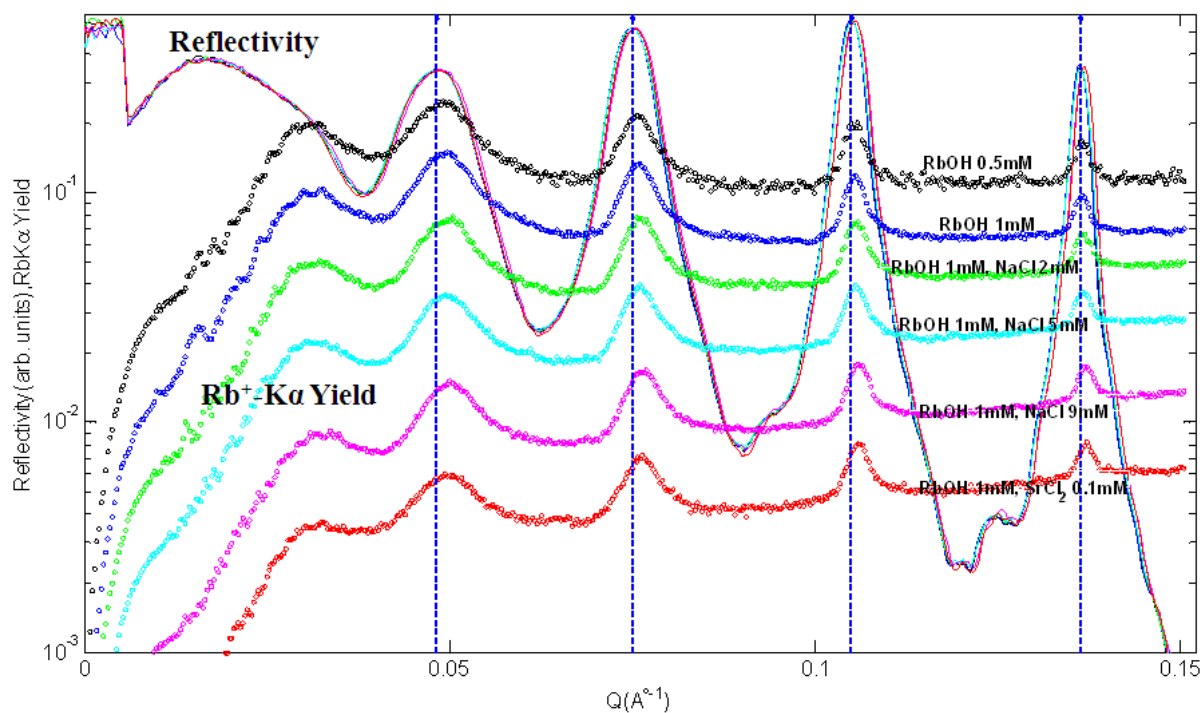
Figure 6.7: X-ray standing waves data for Rb-Kα yield, measured *in situ* for six different electrolyte conditions, for the TiO_2 coated Si/Mo multi-layer system. The XSW data (circles) from top to bottom, is respectively for the following electrolytes: 0.5mM RbOH, 1mM RbOH, 1mM RbOH with 2mM NaCl, 1mM RbOH with 5mM NaCl, 1mM RbOH with 9mM NaCl, and 1mM RbOH with 0.1mM $SrCl_2$. The *in situ* x-ray reflectivity data (thin lines) for the six cases is also shown (as indicated).

The most distinct difference in the XSW data is present in case of the Rb^+ solution with 0.1mM $SrCl_2$ (for e.g. in the shape of third Bragg peak) compared to the other solutions.

While the above assessment suggests that there could be a diffuse ordering of ions measurable with the current multi-layer for the higher ionic strength solutions, it can be ascertained only after a thorough quantitative analysis. Because the differences in the fluorescence yield for the different solution conditions appear to be slight, it is important to conduct a very careful analysis of the *in situ* reflectivity and subsequently the ion-yield data. One of the disadvantages of using such a multi-layer structure is the presence of a large number of unknowns in the structure that complicate the data analysis (for e.g. the reflectivity analysis shown for the *ex situ* case used over 80 parameters in the model fit). So far as the measurement of the diffuse ion profile is concerned, it was shown in Chapter 5 (Fig. 5.4) that most of the information concerning the exponentially decaying profiles expected at dilute ion concentrations is confined at very low scattering angles, i.e. $Q < 0.1 \text{ Å}^{-1}$, therefore most of the information about the diffuse profile may already be lost at the third and fourth Bragg peaks of these multi-layers. Because of the fact that the Q-range useful for the measurement of the diffuse profile is so limited, it is desirable to choose structures that specifically have high reflectivity throughout the $Q < 0.1 \text{ Å}^{-1}$ range. The Si/Mo bi-layer described in Chapters 4 and 5 had a simpler structure and provided a high reflectivity throughout the useful Q-range (greater than 10 percent reflectivity for $Q < 0.08 \text{ Å}^{-1}$), and therefore may be preferable for future attempts of probing the diffuse profile length scales. It is important however to minimize the bending of these samples that occurs as a result of tension from the tightened Kapton film used to enclose the electrolyte solutions in the thin film cell.

6.1.4 Conclusion

X-ray reflectivity was used to characterize the Si/Mo multilayer with minimum assumptions about the periodicity of the structure used in the analysis. The analysis showed that the individual bi-layers differed significantly not only in their thicknesses, but also in their densities, and the relative thicknesses of Si and Mo, through the extent of the multilayer. The TiO$_2$ nanofilm was characterized using PML-XSW, and the film was found to be 21 ± 2 Å thick. The Rb$^+$-yields measured under different electrolyte ionic strengths suggest that there could be a diffuse ordering of ions above the interface, although this can be confirmed only after the complete analysis of the ion-yield data. Choice of substrate will be critical for future measurements of the diffuse profile due to the limited Q-range feasible for the measurement. Minimizing the bending of these samples during the *in situ* measurements will be needed for precise analysis of the low-Q range data. An improved cell design that minimizes direct contact between the Kapton film and the sample corners will be helpful. However, it is important that such a design does not lead to an increased solution layer thickness above the sample surface as that would result in an increased incoherent signal from the bulk electrolyte ions.

6.2 Feasibility of Measuring the Diffuse Ion Profile Using a Cavity-Array Structure

6.2.1 Introduction

Resonant anomalous x-ray reflectivity (RAXR) is a valuable tool in probing the ion distribution at the liquid-solid interface, as evident from the results shown in Chapter 3 of this thesis, where it was used to measure the specifically adsorbed ion structure at the rutile-electrolyte interface. However, probing the diffuse part of the ion distribution requires measuring the RAXR signals at very low scattering angles ($Q<0.1$ Å^{-1}), where the resonant modulations are weak due to the relatively large magnitude of the non-resonant structure factor of the crystal-aqueous system at these scattering angles. The RAXR signal will be amplified if the non-resonant structure factor could somehow be reduced. One way to accomplish this is to use a periodic structure as the substrate, where each period is made of adjacent high and low density materials. The structure factor of such a substrate has Bragg peaks (at multiple orders) at the Q-positions governed simply by the period (Bragg's law). The relative strength of these reflections can be controlled by the duty cycle of the structure (i.e., the relative thicknesses of the light and dense materials) in order to have weak reflections where the RAXR signal is enhanced.

Previously Diaz et al. used a cavity array structure (made of Silicon) with a 1 μ period to study the confinement effects in colloids (Fig. 6.8)[119-121]. From diffraction experiments performed in transmission geometry, Bragg peak efficiencies were measured (for 50 orders) and Patterson function analysis was used to reveal the ordering of colloidal particles inside the cavities. Such a grating structure can also be used to measure the distribution of ions at the
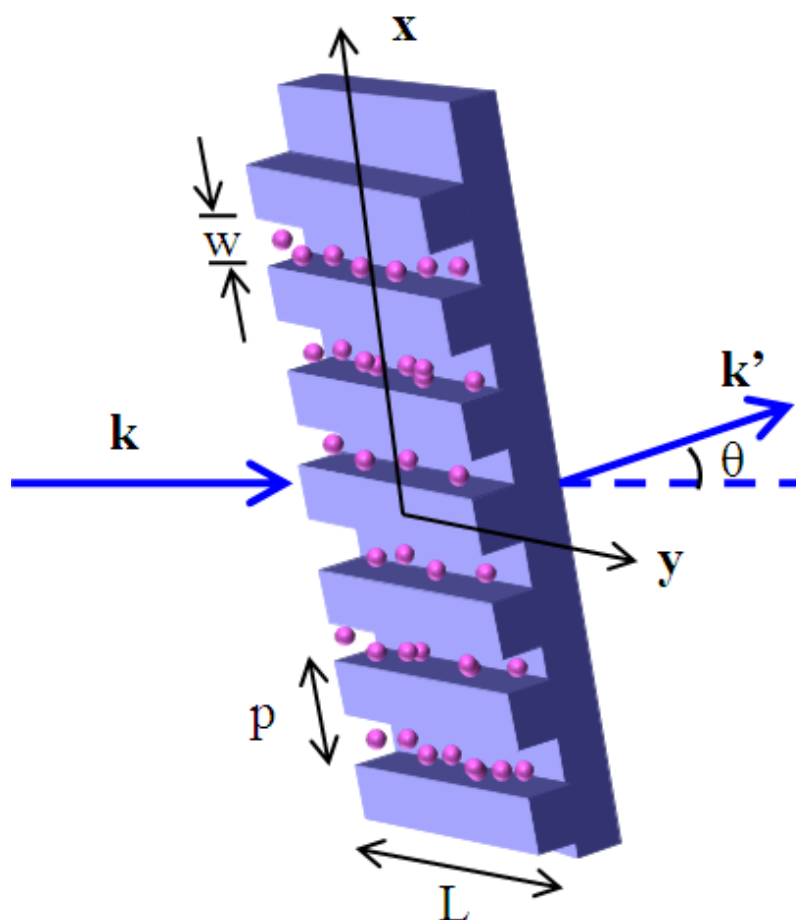
Figure 6.8: Si micro-array structure used by Diaz et al. (Reference [119]) to measure the ordering of colloids confined in the cavities. Here p denotes the period of the grating, w the width of the cavity, and L the length of the grating. The incident and scattered wave-vectors (k and k') are also shown for a diffraction experiment in transmission geometry.

liquid-solid interface using resonant scattering. For such an experiment, the cavities can be filled with ionic solutions (for e.g. containing Rb^+ or Sr^{2+}), and the RAXR signal from the ions distributing at the aqueous-SiO_2 interface (using the native oxide that forms at the Si walls adjacent to the cavities) can be probed. The duty cycle can be chosen so as to have weak order Bragg peaks where the enhanced resonant signals can be easily measured.

Here we show simulations to demonstrate that the ion density profile within the cavities can be retrieved from the non-resonant and resonant scattering intensities in a model independent way. The simulations are for the grating with a period, p=1μ, height h=6μ, and a duty cycle (w/p=0.5, where w is the width of the cavity, see Fig. 6.8 for the notations), for an incident x-ray energy of 20 keV. The reciprocal lattice unit, $L = \frac{Q}{(2\pi/p)}$, is used throughout this section, to refer to the order of the reflection (Bragg peaks). We also discuss feasibility issues including the effect of experimental resolution, tapered walls of the cavities; and, the changes in the duty cycle (associated with fabrication) that can be tolerated for these measurements.

6.2.2 Model Independent Retrieval of the Diffuse Ion Distribution

Here we consider an example for the case of the grating structure with *cavities* filled with a diffuse layer distribution of Rb^+ with a Debye length of 100 Å (equivalent to a 10^{-3} M concentration based on Debye-Huckel theory). It is shown in this example that the diffuse ion distribution can be model independently retrieved using the following:

i) Non - resonant structure factor (upto L=80)

ii) Resonant spectra at even orders upto L=80 (ie. at L=2,4,6,...80)

The density profile considered for these simulations is shown in Fig. 6.9A (only one period of the grating structure is considered in these calculations). We first calculate the non-resonant structure factor (Fig. 6.9B) at the Bragg peaks (L=0 to 80) for the above structure, for a fixed sample orientation. Notice the difference in intensities of the adjacent reflections, the even order Bragg peaks are ~10^4-10^5 times weaker than the odd order Bragg peaks. We now calculate the resonant spectra (modulus square of the total structure factor vs. E) at even orders upto the 80th order (L=2,4,6....80). Some of the spectra are shown in Fig. 6.9C. These calculations show that there are large resonant modulations (25%) at the weak even order Bragg peaks. In contrast, the resonant modulations at odd order Bragg peaks were substantially smaller (<0.1%). Here it will be shown that that the ion profile can be retrieved from the resonant spectra at just the even orders.

When both the phase and amplitude of the non-resonant structure factor are known (which can be obtained from the non-resonant scattering data using model independent or model dependent approaches; in this example they are calculated), then each of these resonant spectra (reflectivity vs. E) can be fit model independently to obtain the phase and amplitudes of the partial structure factor of the ions. We obtain the phases and amplitudes of the ion profile partial structure factor by model independent fit of the simulated resonant scattering data and the calculated non-resonant structure factor. These recovered amplitudes and phases are shown in Figs. 6.9D and 6.9E respectively. The ion profile was retrieved by Fourier inversion of the above phases and amplitudes (circles in Fig. 6.9F). It can be seen that the retrieved profile (circles) agrees well with the initially assumed distribution (ie. L_D = 100Å, shown as solid line in Fig. 6.9F).
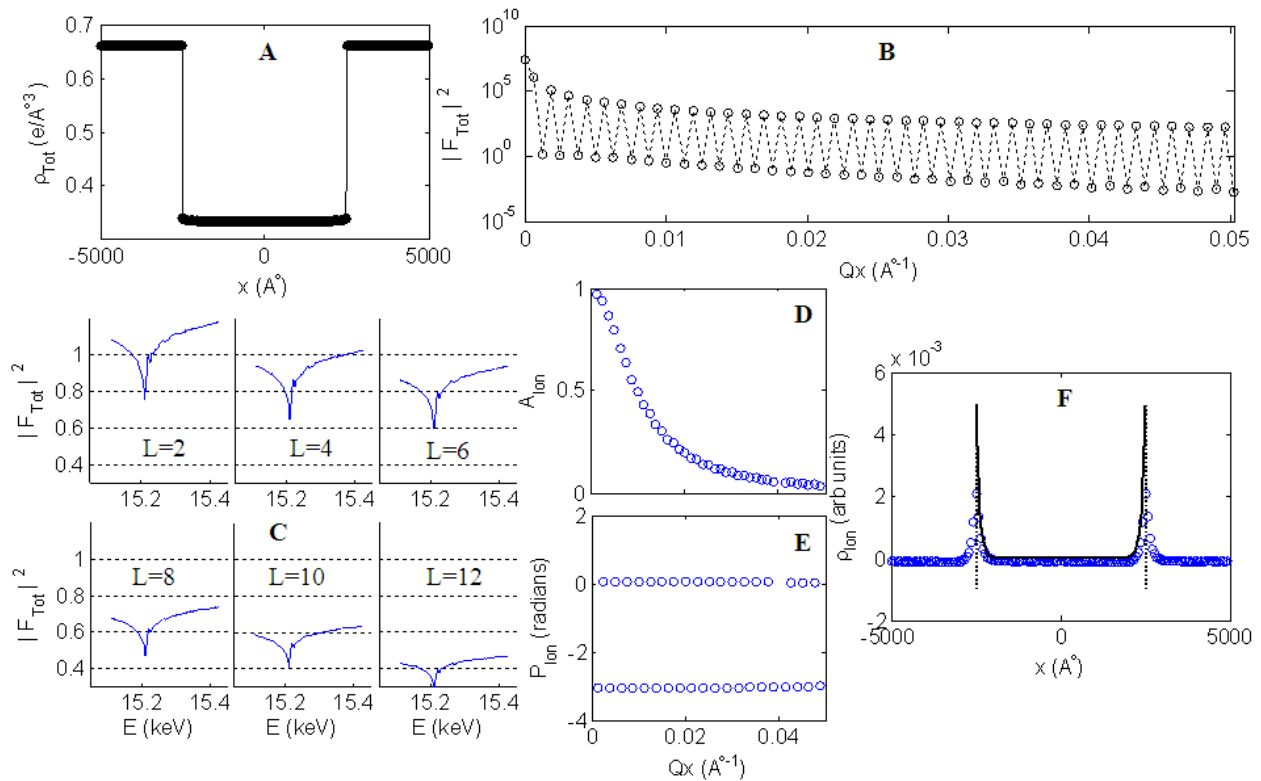
Figure 6.9: Simulation demonstrating model independent retrieval of the ion profile within the cavities, using non-resonant structure factor and resonant-scattering intensities. (A): Total electron density profile of the Si-cavity structure, with duty cycle of 0.5, and period of 1 μ, with a diffuse ion distribution of Rb$^+$ in the cavities having a Debye length of 100 Å. (B): Non-resonant structure factor (squared) of the grating, at the Bragg peaks up to 80th order. (C): Resonant anomalous x-ray reflectivity spectra for L=2,4,6,8,10, and 12. Resonant spectra at even L up to L=80 were included in this analysis. (D) & (E): The amplitudes and phases of the resonant structure factor (i.e. the ions) obtained from model-independent fit of the resonant spectra. (F): Reconstructed ion profile (circles) plotted along with the original ion distribution that was used as input (black line). Vertical dashed lines show the location of the cavity walls.

Note that we were able to retrieve a unique density distribution over the whole of cavity width (w), in spite of using the resonant spectra at only the even orders, since the real space *Fourier window* ΔX is determined by the sampling frequency ΔQ by the relation $\Delta X = 2\pi/\Delta Q = 2\pi/(2*2\pi/p) = p/2 = w$. The ion profile outside the width 'w' is therefore an artifact. The next section discusses the experimental feasibility issues associated with the measurement of the non-resonant and resonant data on these cavity-array structures, in order to have the sufficient resolution necessary to measure the diffuse ion distribution.

6.2.3 Feasibility

(a) Experimental Resolution: The resolution of the retrieved profile is limited by the Q range of the data. In the calculations in the previous section, we took into account the resonant spectra upto L = 80, hence the resolution (of the retrieved ion profile) was $\approx \pi/Q_{max} = 63$ Å. We could therefore expect to resolve the diffuse ion distribution for a Debye length of 100 Å, as seen from the previous section.

(b) Effect of Tapering of the Cavity Walls: The walls of the cavities may not be exactly vertical. Since the ion distribution will follow the tapered walls of the cavity, the effect of tapering on the partial structure factor of the ion distribution can be incorporated by multiplying it by an interference term ('tapering interference factor', Fig. 6.10). One concern is whether this interference factor will affect the RAXR measurements because this factor tends to reduce the un-tapered structure factor. This may limit the Q-range accessible to these measurements and therefore limit our ability to resolve the diffuse layer ion distribution. Fig. 6.10 shows the variation (with Q) of the structure factor of a diffuse layer of Debye length 100 Å (circles), and
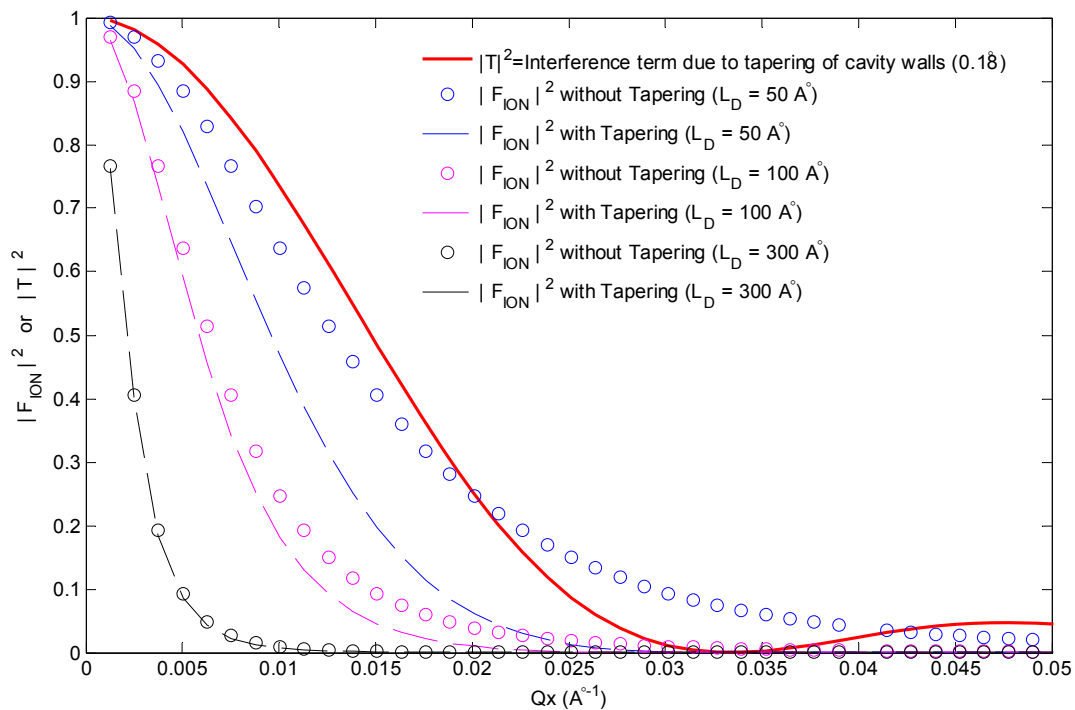
Figure 6.10: Effect of tapering of cavity walls on the measurement of diffuse ion distribution. Structure factor squared of diffuse profile with (line) and without (circles) tapering, for the following Debye lengths: 50 Å (blue), 100 Å (magenta), and 300 Å (black). Also shown is the tapering interference factor (red line) corresponding to a tapering of 0.18 degrees of the cavity walls.

the variation of the tapering factor (solid red line) for a wall-tapering angle of 0.18°. The structure factor variation of ion profiles with different Debye lengths with (dashed lines) and without (circles) the tapering interference factor included is also shown in Fig. 6.10. It is clear that the tapering interference factor reduces the grating structure factor. For shorter Debye lengths (<50 Å), this could prevent us from measuring far enough in Q and therefore restrict us from resolving the diffuse profile. However, for ion distributions with Debye lengths ≥100 Å, the structure factor is much less altered.

(c) Effect of Presence of Adsorbed Layers on Probing the Diffuse Layer: We did calculations assuming 10% of the adsorbed ions forming a condensed layer at the interface and remaining in the diffuse layer. We then reconstructed the ion profile from the model independent analysis of calculated resonant spectra at the even order Bragg peaks (using calculated non-resonant structure factor). The reconstructed profile showed a diffuse profile matching with the one that we had assumed. The presence of a condensed layer does not appear to affect our ability to probe the diffuse layer spatial variation. The presence of a condensed layer is seen clearly in the ion partial structure factor amplitude as a non-zero vertical offset at large Q.

(d) Advantage of the 0.5 Duty Cycle: The main advantage of the exact 0.5 duty cycle case is the large resonant modulations (25%) at the weak even-order Bragg peaks. However, the duty cycle of exact 0.5 offers another significant advantage. The kinematic structure factor of the grating is exactly zero at even order Bragg peaks (except L=0), when there are no ions present in the cavity. When there are ions present in the cavity, the total structure factor of the grating structure (at even L) simply equals the partial structure factor of the ion distribution. We also found that in this case, the ion distribution can be obtained by simply inverting the non-resonant
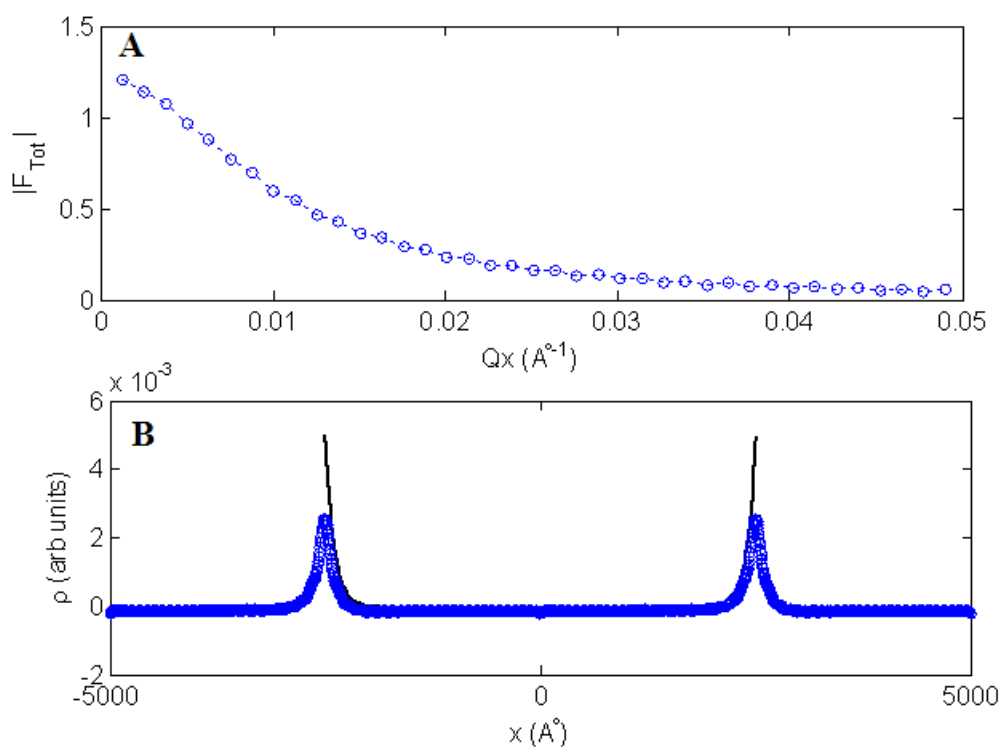
Figure 6.11: Retrieval of ion distribution from non-resonant structure factor for exact 0.5 duty

cycle case. (A): Total structure factor of the grating structure with diffuse ion distribution of

L_D=100 Å. For the exact 0.5 duty cycle, the non-resonant structure factor at the even order Bragg

peaks is equal to the ion structure factor. (B): Reconstructed ion profile (circles) using the non-

resonant amplitudes and phases, along with the originally assumed ion distribution (line).

structure factor (calculated at L=2,4,6,..80). Fig. 6.11 shows the retrieved ion profile from the non-resonant structure factor. Although the duty cycle of exact 0.5 is the ideal case from our perspective, there may be some potential feasibility problems with this case as discussed in the next section.

(e) Potential Feasibility Issues with the Exact 0.5 Duty Cycle Case: One issue that arises is the potential problem in measuring the signal at the weak reflections (from the grating structures) due to the large differences (10^4 fold) in intensities of the weak reflections and the adjacent strong reflections. In particular, it may be difficult to measure these weak reflections in presence of background signals (the background signals were 10^2 fold smaller than the typical peak Bragg intensities in Ana Diaz's thesis[119]). Deviations in the duty cycle from 0.5 increases the intensity of the weak reflections, thus making the measurement of weak reflections potentially more feasible. However, this deviation also results in smaller resonant modulations, making the resonant measurements more difficult. One proposed solution is to have a duty cycle that differs only as much from 0.5 as is required to make measuring the weak reflections feasible but not that much that it reduces the resonant modulations to less than 0.5% (considering this as a safe lower limit of fractional resonant modulations that can be measured).

(f) Tolerance in the Duty-Cycle Deviation from 0.5: Calculations for various duty cycles (up to L=80) show that a change of more than 2% from a duty cycle of 0.5 results in lower than 0.4% resonant modulations at even the weaker Bragg peaks making the measurements of resonant signal difficult. Assuming that resonant modulations as small as 0.5% can be measured (considering the statistical and systematic uncertainties of our measurements), we can tolerate a ±2% change in the duty cycle, i.e. the duty cycle must be in the range of 0.49 to 0.51. One
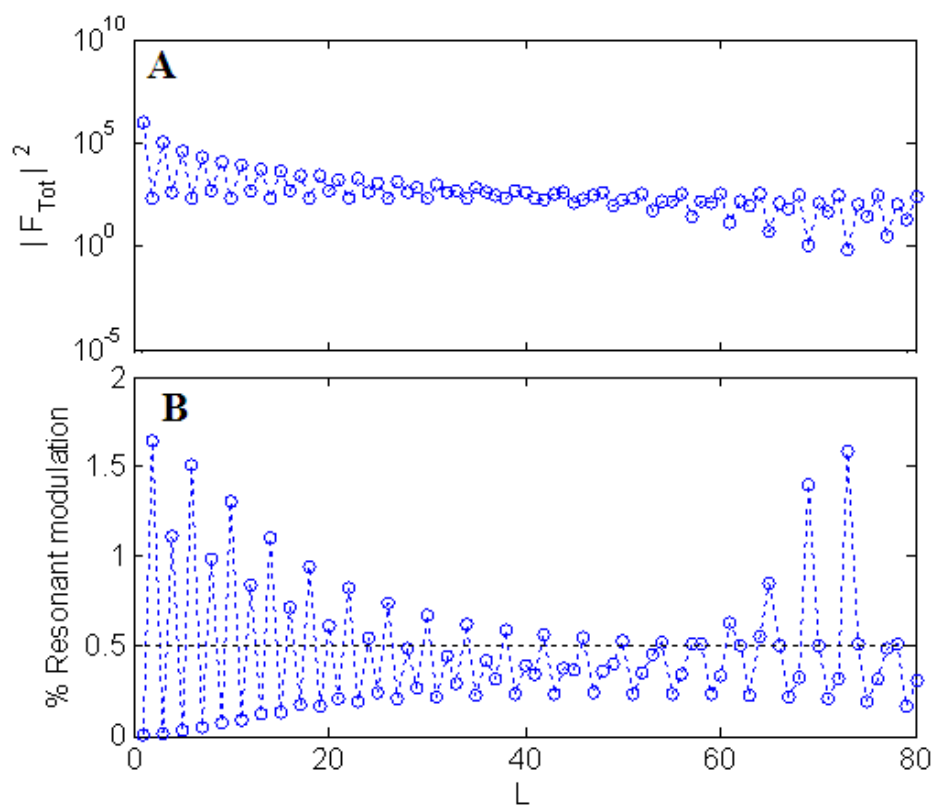
Figure 6.12: Preferred structure for the measurement of the diffuse ion distribution should have a slight deviation (1% in the case shown) of the duty cycle from 0.5. (A) Total structure factor of the grating for a duty cycle of 0.505. The relative difference between the adjacent strong and weak Bragg peaks is much reduced in comparison to a duty cycle of 0.5, making such a measurement more feasible. (B) Percentage modulations in the calculated resonant spectra (up to L=80) for the 0.505 duty cycle. Most of the even order Bragg peaks have modulations greater than 0.5%.

proposed structure is the duty cycle of 0.505 (1% deviation from 0.5), the scattering intensity calculations for this case are shown in Fig. 6.12. For this structure, the differences between the strong and weak reflections are less than two orders of magnitude, while the resonant modulations (at weak reflections) are mostly >0.5%.

6.2.4 Conclusions

These calculations show that we can directly observe the diffuse ion profiles extending from the walls of the grating structures, at least in principle, using realistic grating structures (i.e., even with tapering of the walls and with some adsorption at the interface). There are, however, a number of technical challenges described above that may compromise the feasibility of the measurements. In particular, the 0.5 duty cycle leads to even order Bragg peaks that are 10^4 fold smaller than the strong odd order peaks. This would be a challenging measurement since the even order peaks may be 10^2-fold smaller than the background signals. For structures with a duty cycle that differs from 0.5, the fraction modulation of the resonant spectra will be weak (~0.5%). Nevertheless, these experiments hold great potential in being able to provide direct information about the diffuse ion distribution, as well as in studying the effect of shear flow on the electrical double layer by flow of electrolyte solutions through the cavities while measuring the diffuse ion distribution.

Chapter 7 : Summary

Adsorbed ion structure at the rutile (110)-electrolyte interface was probed using resonant anomalous X-ray reflectivity, and crystal truncation rod reflectivity. Conventionally the specifically adsorbed inner-sphere ions are regarded as occupying a single adsorption site. Current work provides an experimental confirmation of the recent molecular dynamics prediction[56] that the adsorbed ion structure on the rutile surface is actually distributed between separate inner-sphere sites. In particular, comparison of the X-ray results with molecular dynamics simulations confirmed that both monovalent and divalent ions (Rb^+ and Sr^{2+}) occupy tetra-dentate as well as bi-dentate sites above the interface, rather than a single site as regarded previously. These results also confirm that the rutile surface is hydroxylated, in agreement with previous conclusions[33, 38]. A Rb^+ coverage of 0.080±0.003 monolayer (ML) with an average height of 3.72±0.03 Å above the interface, and a Sr^{2+} coverage of 0.40±0.07 ML and an average height of 3.05±0.16 Å is revealed from these measurements (which were conducted for 1mM Rb^+ at pH 11, and 0.1mM Sr^{2+} at pH 10.3). The Sr^{2+} distribution measured in presence of an added background electrolyte (30mM Na^+) shows that the ion average height and coverage are unchanged within experimental uncertainties, providing an additional indirect evidence of the absence of outer-sphere species. The observation of a lack of outer-sphere species on rutile is consistent with previous surface complexation models[36], which predicted that the ion solvation free energy component that opposes inner-sphere adsorption is negligible on high dielectric constant substrates, such as rutile. Therefore the difference between the inner-sphere dominant speciation on rutile in comparison to inner-sphere/outer-sphere co-existence observed on mica[20], appears to be primarily due the difference in the dielectric constants of the two

minerals. Further understanding of the multi-site inner-sphere ion distribution on rutile can be achieved by simultaneously measuring the distribution of two competing cations that are both expected to be inner-sphere adsorbed (e.g. Sr^{2+} and Zn^{2+}).

Long-period XSW is a valuable tool in obtaining information about diffuse 1D elemental distributions[19, 122]. Analysis of the long-period XSW data traditionally relied on model-based approaches, and model-independent analysis was limited to a recently developed formalism applicable to the TER-XSW regime[123]. In this thesis, a generalized model-independent method was developed that is applicable to various reflection geometries, including simple X-ray mirrors and multi-layers. This method is also applicable for XSW generated inside an attenuating medium. The formalism was demonstrated by successful model-independent retrieval of 1D profile of Ti normal to the surface of a TiO_2/Si/Mo tri-layer sample (on a Si substrate), from the low scattering angle Ti-Kα fluorescence yield data measured in air, and under an aqueous electrolyte. It was shown that the yield data plotted vs. Q can be divided into separate segments, and each segment can be analyzed to obtain an amplitude and a phase of the elemental structure factor. The elemental distribution was then recovered from Fourier inversion of the derived amplitudes and phases. The position of the model-independently recovered Ti distribution was same within experimental uncertainties as that obtained with conventional model analysis, while the width of the model-independent profile was limited by the experimental resolution. The current model-independent approach can be used to extract not only the amplitudes and phases of the elemental profile, but also their second or higher order gradients, thereby making it potentially useful in analyzing XSW data from complex multi-layered distributions. A distinguishing feature of this method is that it allows model-independent retrieval of Fourier

coefficients (of the elemental profile) at a more continuous sampling (in Q) than possible with Bragg-XSW, thus allowing imaging of more extended distributions.

Long-period XSW combined with XR were used to study the adsorption of ions (Rb^+ and Sr^{2+}) on the surface of a nano-film of titania grown using ALD. Using the XRF-measured 2D ion densities, and the XSW-measured ion distributions, the absolute coverages of both the total interacting ions (i.e., condensed and diffuse), and the specifically-adsorbed ions (i.e., condensed) were determined. These measurements revealed two novel characteristics of the nano-titania surface. First, the nano-titania had a total coverage of ions that was twice that observed previously on the rutile surface. Second, the nano-titania had a ~9-fold enhancement of specific adsorption of monovalent ions inside the pores defined by the surface roughness. Each of these revelations is an important result, with potential impact on modern energy storage devices, such as electrochemical capacitors (EC). In ECs, a higher ion coverage is desired to achieve a higher energy density. Also, the specifically-adsorbed ions are more preferable than the diffuse ions, since the latter are detrimental to the energy density. It appears that the electrode surface morphology holds a key in improving the energy density of ECs, both in terms of enhancing the total ion-electrode interaction, and in terms of controlling the distribution of ions in the condensed and diffuse layers. The current results demonstrate that use of nanometer thick layers can provide an additional control in improving EC properties.

REFERENCES

1. Hiemenz, P.C. and R. Rajagopalan, *Principles of Colloid and Surrface Chemistry*. Third ed. 1997: Marcel Dekker, Inc.

2. Masliyah, J.H. and S. Bhattacharjee, *Electrokinetic and colloid transport phenomena*. 2006: Wiley-Interscience.

3. Shchukin, E.D., A.V. Pertsov, E.A. Amelina, and A.S. Zelenev, *Colloid and surface chemistry*, ed. D. Mobius and R. Miller. 2001: Elsevier.

4. Stumm, W., *Chemistry of the solid-water interface*. 1996: John Wiley & Sons, Inc.

5. Brown, G.E., Jr. and G.A. Parks, *Sorption of trace elements on mineral surfaces: modern perspectives from spectroscopic studies, and comments on sorption in the marine environment.* Int. Geo. Rev., 2001. **43**: p. 963-1073.

6. Abruna, H.D., Y. Kiya, and J.C. Henderson, *Batteries and electrochemical capacitors*. Physics Today, 2008 **Dec.**: p. 43-47.

7. Frackowiak, E. and F. Beguin, *Carbon materials for the electrochemical storage of energy in capacitors.* Carbon, 2001. **39**: p. 937-950.

8. Burke, A.F., *Batteries and ultracapacitors for electric, hybrid, and fuel cell vehicles*. Proc. IEEE, 2007. **95**(4): p. 806.

9. Kotz, R. and M. Carlen, *Principles and applications of electrochemical capacitors*. Electrochim. Acta, 2000. **45**: p. 2483-2498.

10. Simon, P. and Y. Gogotsi, *Materials for electrochemical capacitors*. Nature Mat., 2008. **7**: p. 845.

11. Winter, M. and R.J. Brodd, *What are batteries, fuel cells, and supercapacitors.* Chem. Rev., 2004. **104**: p. 4245.

12. Zhang, Z., *Atomic scale x-ray studies of the electrical double layer structure at the rutile TiO2(110)-aqueous electrolyte interface.* PhD Thesis, Northwestern University, 2004.

13. Bu, W., D. Vaknin, and A. Travesset, *Monovalent counterion distributions at highly charged water interfaces: proton-transfer and Poisson-Boltzmann theory.* Phys. Rev. E, 2005. **72**: p. 060501.

14. Bu, W., D. Vaknin, and A. Travesset, *How accurate is Poisson-Boltzmann theory for monovalent ions near highly charged interfaces?* Langmuir, 2006. **22**: p. 5673-5681.

15. Israelachvili, J.N. and G.E. Adams, *Measurement of forces between two mica surfaces in aqueous electrolyte solution in the range 0-100 nm.* J. Chem. Soc. - Faraday Trans. I, 1978. **74**.

16. Fulton, J.M., D.M. Pfund, S.L. Wallen, M. Newville, E.A. Stern, and Y. Ma, *Rubidium ion hydration in ambient and supercritical water.* J. Chem. Phys., 1996. **105**(6): p. 2161.

17. Fenter, P., *X-ray Reflectivity: as a Probe of Mineral-Fluid Interfaces: A User Guide*, in *Reviews in Mineralogy & Geochemistry*, P. Fenter, et al., Editors. 2002. p. 149-220.

18. Fenter, P. and N.C. Sturchio, *Mineral-water interfacial structures revealed by synchrotron X-ray scattering.* Progress in Surface Science, 2004. **77**: p. 171-258.

19. Bedzyk, M.J., G.M. Bommarito, M. Caffrey, and T.L. Penner, *Diffuse double layer at a membrane-aqueous interface measured with x-ray standing waves.* Science. **248**(4951): p. 52-56.

20.   Park, C., P. Fenter, K.L. Nagy, and N.C. Sturchio, *Hydration and Distribution of Ions at the Mica-Water Interface.* Phys. Rev. Lett., 2006. **97**: p. 016101.

21.   Fenter, P., C. Park, and N.C. Sturchio, *Adsorption of Rb+ and Sr2+ at the orthoclase (001)-solution interface.* Geochim. Cosmochim. Acta, 2008. **72**: p. 1848-1863.

22.   Zhang, Z., P. Fenter, L. Cheng, N.C. Sturchio, M.J. Bedzyk, M.L. Machesky, L. Anovitz, and D.J. Wesolowski, *Zn2+ and Sr2+ adsorption at the TiO2 (110)-electrolyte interface: Influence of ionic strength, coverage and anions.* J. Coll. & Int. Sci., 2006. **295**: p. 50-64.

23.   Zhang, Z., P. Fenter, L. Cheng, N.C. Sturchio, M.J. Bedzyk, M. Predota, A. Bandura, J.D. Kubicki, S.N. Lvov, P.T. Cummings, A.A. Chialvo, M.K. Ridley, P. Benezeth, L. Anovitz, D.A. Palmer, M.L. Machesky, and D.J. Wesolowski, *Ion Adsorption at the Rutile-Water Interface: Linking Molecular and Macroscopic Properties.* Langmuir, 2004. **20**(12): p. 4954-4969.

24.   Zhang, Z., P. Fenter, S.D. Kelly, J.G. Catalano, A. Bandura, J.D. Kubicki, J.O. Sofo, D.J. Wesolowski, M.L. Machesky, N.C. Sturchio, and M.J. Bedzyk, *Structure of hydrated Zn2+ at the rutile TiO2 (110)-aqueous solution interface: Comparison of x-ray standing wave, x-ray absorption spectroscopy, and density funcitonal theory results.* Geochim. Cosmochim. Acta, 2006. **70**: p. 4039-4056.

25.   Zhang, Z., P. Fenter, N.C. Sturchio, M.J. Bedzyk, M.L. Machesky, and D.J. Wesolowski, *Structure of rutile TiO2 (110) in water and 1 molal Rb+ at pH 12: Inter-relationship among surface charge, interfacial hydration structure, and substrate structural displacements.* Surf. Sci., 2007. **601**: p. 1129-1143.

26. Catalano, J.G., C. Park, P. Fenter, and Z. Zhang, *Simultaneous inner- and outer-sphere arsenate adsorption on corundum and hematite.* Geochim. Cosmochim. Acta, 2008. **72**: p. 1986-2004.

27. Park, C., P. Fenter, N.C. Sturchio, and J.R. Regalbuto, *Probing outer-sphere adsorption of aqueous metal complexes at the oxide-water interface with resonant anomalous x-ray reflectivity.* Phys. Rev. Lett., 2005. **94**: p. 076104.

28. Cheng, L., *Atomic scale study of ion incorporation at calcite surface using synchrotron x-ray methods.* PhD Thesis, Northwestern University, 1998.

29. Fenter, P., L. Cheng, S. Rihs, M.L. Machesky, M.J. Bedzyk, and N.C. Sturchio, *Electrical double layer structure at the rutile-water interface as observed in situ with small-period x-ray standing waves.* J. Coll. & Int. Sci., 2000. **225**: p. 154-165.

30. Diebold, U., *The surface science of titanium dioxide.* Surf. Sci. Rep., 2003. **48**: p. 53-229.

31. Grant, F.A., *Properties of rutile (titanium dioxide).* Rev. Mod. Phys., 1959. **31**(3): p. 646.

32. Ramamoorthy, M., D. Vanderbilt, and R.D. King-Smith, *First - principles calculations of the energetics of stoichiometric TiO2 surfaces.* Phys. Rev. B, 1994. **49**: p. 16721.

33. Predota, M., A. Bandura, P.T. Cummings, J.D. Kubicki, D.J. Wesolowski, A.A. Chialvo, and M.L. Machesky, *Electrical Double Layer at the Rutile (110) Surface. 1. Structure of Surfaces and Interfacial Water from Molecular Dynamics by Use of ab Initio Potentials.* J. Phys. Chem. B, 2004. **108**: p. 12049-12060.

34. Machesky, M.L., D.A. Palmer, and D.J. Wesolowski, *Hydrogen ion adsorption at the rutile-water interface to 250 deg C.* Geochim. Cosmochim. Acta, 1994. **58**(24): p. 5627.

35.   Hiemstra, T., W.H.v. Riemsdijk, and G.H. Bolt, *Multisite proton adsorption modeling at the solid-solution interface of (hydr)oxides - a new approach. 1. Model description & evaluation of intrinsic reaction constants.* J. Coll. & Int. Sci., 1989. **133**(1): p. 91-104.

36.   Sverjensky, D.A., *Prediction of the speciation of alkaline earths adsorbed on mineral surfaces in salt solutions.* Geochim. Cosmochim. Acta, 2006. **70**: p. 2427-2453.

37.   S. Koppen and W. Langel, *Simulation of the interface of (100) rutile with aqueous ionic solution.* Surf. Sci., 2006. **600**: p. 2040-2050.

38.   Predota, M., Z. Zhang, P. Fenter, D.J. Wesolowski, and P.T. Cummings, *Electrical Double Layer at the Rutile (110) Surface. 2. Adsorption of Ions from Molecular Dynamics and X-ray Experiments.* J. Phys. Chem. B, 2004. **108**: p. 12061-12072.

39.   Ridley, M.K., M.L. Machesky, D.J. Wesolowski, and D.A. Palmer, *Calcium adsorption at the rutile-water interface: A potentiometric study in NaCl media to 250 degC.* Geochim. Cosmochim. Acta, 1999. **63**: p. 3087-3096.

40.   Ridley, M.K., M.L. Machesky, D.J. Wesolowski, and D.A. Palmer, *Surface complexation of neodymium at the rutile-water interface: A potentiometric and modeling study in NaCl media to 250 degC.* Geochim. Cosmochim. Acta, 2005. **69**(1): p. 63-81.

41.   O'Day, P.A., C.J. Chisholm-Brause, S.N. Towle, G.A. Parks, and G.E. Brown, Jr., *X-ray absorption spectroscopy of Co(II) sorption complexes on quarz (alpha-SiO2) and rutile (TiO2).* Geochim. Cosmochim. Acta, 1996. **60**(14): p. 2515-2532.

42.   Hiemstra, T., J.C.M. Dewit, and W.H.V. Riemsdijk, *Multisite proton adsorption modeling at the solid-solution interface of (hydr)oxides - a new approach. 2. Application to various important (hydr)oxides.* J. Coll. & Int. Sci., 1989. **133**(1): p. 105-117.

43. Bandura, A.V., D.G. Sykes, V. Shapovalov, T.N. Troung, J.D. Kubicki, and R.A. Evarestov, *Adsorption of Water on the TiO2 (Rutile) (110) Surface: A Comparison of Periodic and Embedded Cluster Calculations.* Journal of Physical Chemistry B, 2004. **108**: p. 7844-7853.

44. Hiemstra, T., P. Venema, and W.H.V. Riemsdijk, *Intrinsic proton affinity of reactive surface groups of metal (hydr)oxides: the bond valence principle.* J. Coll. & Int. Sci., 1996. **184**: p. 680-692.

45. Hiemstra, T. and W.H.V. Riemsdijk, *A Surface Structural Approach to Ion Adsorption: The Charger Distribution (CD) Model.* Journal of Colloid and Interface Science, 1996. **179**: p. 488-508.

46. Ridley, M.K., T. Hiemstra, W.H.V. Riemsdijk, and M.L. Machesky, *Inner-sphere complexation of cations at the rutile-water interface: a concise surface structural interpretation with the CD and MUSIC model.* Geochim. Cosmochim. Acta, 2009. **73**: p. 1841.

47. Hiemstra, T. and W.H.V. Riemsdijk, *On the relationship between charge distriubtion, surface hydration, and the structure of the interface of metal hydroxides.* Journal of Colloid and Interface Science, 2006. **301**: p. 1-18.

48. Sverjensky, D.A., *Physical surface-complexation models for sorption at the mineral-water interface.* Nature, 1993. **364**: p. 776-780.

49. Sverjensky, D.A., *Interpretation and prediction of triple-layer model capacitances and the structure of the oxide-electrolyte-water interface.* Geochim. Cosmochim. Acta, 2001. **65**(21): p. 3643-3655.

50. Machesky, M.L., D.J. Wesolowski, D.A. Palmer, and M.K. Ridley, *On the temperature dependence of intrinsic surface protonation equilibrium constants: an extension of the revised MUSIC model.* J. Coll. & Int. Sci., 2001. **239**(2): p. 314-327.

51. Towle, S.N., G.E. Brown, Jr., and G.A. Parks, *Sorption of Co(II) on Metal Oxide Surfaces.* J. Coll. & Int. Sci., 1999. **217**: p. 299-311.

52. Brown, G.E., Jr., V.E. Henrich, W.H. Casey, D.L. Clark, C. Eggleston, A. Felmy, D.W. Goodman, M. Gratzel, G. Maciel, M.I. McCarthy, K.H. Nealson, D.A. Sverjensky, M.F. Toney, and J.M. Zachara, *Metal Oxide Surfaces and Their Interactions with Aqueous Solutions and Microbial Organisms.* Chem. Rev., 1999. **99**: p. 77-174.

53. Machesky, M.L., D.J. Wesolowski, D.A. Palmer, and K. Ichiro-Hayashi, *Potentiometric Titrations of Rutile Suspensions to 250 degC.* Journal of Colloid and Interface Science, 1998. **200**: p. 298-309.

54. Berube, Y.G. and P.L. DeBruyn, *Adsorption at the rutile-solution interface, 1. thermodynamic and experimental study.* J. Coll. & Int. Sci., 1968. **27**(2): p. 305-318.

55. Berube, Y.G. and P.L. DeBruyn, *Adsorption at the Rutile-Solution Interface, 2. Model of the electrochemical double layer.* J. Coll. & Int. Sci., 1968. **28**(1): p. 92-105.

56. Predota, M. and L. Vlcek, *Comment on Parts 1 and 2 of the Series "Electric Double Layer at the Rutile (110) Surface".* J. Phys. Chem. B, 2007. **111**: p. 1245-1247.

57. Wang, J., M. Caffrey, M.J. Bedzyk, and T.L. Penner, *Direct profiling and reversibility of ion distribution at a charged membrane/aqueous interface: an x-ray standing wave study.* Langmuir, 2001. **17**: p. 3671-3681.

58.   Martynov, G.A. and R.R. Salem, *The dense part of the electrochemical double layer: molecular or electronic capacitor ?`.* Advances in Colloid and Interface Science, 1985. **22**: p. 229.

59.   Robinson, I.K. and D.J. Tweet, *Surface x-ray diffraction.* Rep. Prog. Phys., 1992. **55**: p. 599-651.

60.   Als-Nielsen, J. and D. McMorrow, *Elements of Modern X-Ray Physics*. 2001: John Wiley & Sons, Ltd.

61.   Warren, B.E., *X-ray Diffraction*. 1990: Dover Publicaitons.

62.   Hammond, C., *The Basics of Crystallography and Diffraction*. Second ed. 2003: Oxford University Press.

63.   Fenter, P., J.G. Catalano, C. Park, and Z. Zhang, *On the use of CCD area detectors for high-resolution specular x-ray reflectivity.* J. Synch. Rad., 2006. **13**: p. 293-303.

64.   Robinson, I.K., *Crystal truncation rods and surface roughness.* Phys. Rev. B, 1986. **33**(6): p. 3830-3836.

65.   Park, C. and P. Fenter, *Phasing of resonant anomalous X-ray reflectivity spectra and direct Fourier synthesis of element-specific partial structures at buried interaces.* J. App. Cryst., 2007. **40**: p. 290-301.

66.   Cross, J.O., M. Newville, J.J. Rehr, L.B. Sorensen, C.E. Bouldin, G. Watson, T. Gouder, G.H. Lander, and M.I. Bell, *Inclusion of local structure effects in theoretical x-ray resonant scattering amplitudes using ab initio x-ray absorption spectra calculations.* Phys. Rev. B, 1998. **58**: p. 11215.

67.   Parratt, L.G., *Surface studies of solids by total reflection of x-rays.* Phys. Rev. B, 1954. **95**: p. 359-369.

68.   Bommarito, G.M., *In situ studies of electrochemical interfaces using X-ray standing waves.* PhD Thesis, Cornell University, 1992.

69.   Batterman, B.W., *Detection of foreign atom sites by their x-ray fluorescence scattering.* Phys. Rev. Lett., 1969. **22**(14): p. 703-705.

70.   Golovchenko, J.A., B.W. Batterman, and W.L. Brown, *Observation of internal x-ray wave fields during Bragg diffraction with an application to impurity lattice location.* Phys. Rev. B, 1974. **10**(10): p. 4239.

71.   Andersen, S.K., J.A. Golovchenko, and G. Mair, *New applications of x-ray standing-wave fields to solid state physics.* Phys. Rev. Lett., 1976. **37**(17): p. 1141.

72.   Qian, Y., N.C. Sturchio, R.P. Chiarello, P.F. Lyman, T.-L. Lee, and M.J. Bedzyk, *Lattice location of trace elements within minerals and at their surfaces with x-ray standing waves.* Science, 1994. **265**: p. 1555-1557.

73.   Cheng, L., P. Fenter, N.C. Sturchio, Z. Zhong, and M.J. Bedzyk, *X-ray standing wave study of arsenite incorporation at the calcite surface.* Geochim. Cosmochim. Acta, 1999. **63**: p. 3153-3157.

74.   Zegenhagen, J., *Surface structure determination with x-ray standing waves.* Surf. Sc. Rep., 1993. **18**: p. 199-271.

75.   Woodruff, D.P., B.C.C. Cowie, and A.R.H.F. Ettema, *Surface structure determination using x-ray standing waves: a simple view.* J. Phys. : Cond. Mat., 1994. **6**: p. 10633-10645.

76.   Bedzyk, M.J. and G. Materlik, *Determination of the Position and Vibrational Amplitude of an Adsorbate by Means of Multiple-Order X-Ray Standing-Wave Measurements.* Physical Review B, 1985. **31**(6): p. 4110-4112.

77.   Golovchenko, J.A., J.R. Patel, D.R. Kaplan, P.L. Cowan, and M.J. Bedzyk, *Solution to the Surface Registration Problem Using X-Ray Standing Waves.* Physical Review Letters, 1982. **49**(8): p. 560-563.

78.   Kazimirov, A., L.X. Cao, G. Scherb, L. Cheng, M.J. Bedzyk, and J. Zegenhagen, *X-ray standing wave analysis of the rare-earth atomic positions in RBa2Cu3O7-delta thin films.* Solid State Comm., 2000. **114**: p. 271-276.

79.   Barbee Jr., T.W. and W.K. Warburton, *X-ray evanescent and standing wave fluorescence studies using a layered synthetic microstructure.* Mat. Lett., 1984. **3**: p. 17.

80.   Bedzyk, M.J., D.W. Bilderback, J.H. White, M.G. Bommarito, and H.D. Abruna, *X-Ray Standing Waves as Probes of Electrochemical Interfaces.* Journal of the Electrochemical Society, 1987. **134**(3): p. C132-C132.

81.   Bedzyk, M.J., D.H. Bilderback, G.M. Bommarito, M. Caffrey, and J.S. Schildkraut, *X-Ray Standing Waves - a Molecular Yardstick for Biological-Membranes.* Science, 1988. **241**(4874): p. 1788-1791.

82.   Libera, J.A., R.W. Gurney, C. Schwartz, H. Jin, T.L. Lee, S.T. Nguyen, J.T. Hupp, and M.J. Bedzyk, *Comparative X-ray standing wave analysis of metal-phosphonate multilayer films of dodecane and porphyrin molecular square.* Journal of Physical Chemistry B, 2005. **109**(4): p. 1441-1450.

83.   Cowan, P.L., J.A. Golovchenko, and M.F. Robbins, *X-Ray Standing Waves at Crystal-Surfaces.* Physical Review Letters, 1980. **44**(25): p. 1680-1683.

84.   Fenter, P., L. Cheng, S. Rihs, M.L. Machesky, M.J. Bedzyk, and N.C. Sturchio, *Electrical double layer structure at the rutile-water interface as observed in situ with small-period x-ray standing waves.* J. Coll. & Int. Sc., 2000. **225**: p. 154-165.

85.   Bedzyk, M.J. and L. Cheng, *X-ray Standing Wave Studies of Minerals and Mineral Surfaces: Principles and Applications*, in *Reviews in Mineralogy and Geochemistry*, P. Fenter, et al., Editors. 2002. p. 221-266.

86.   Bedzyk, M.J., G.M. Bommarito, and J.S. Schildkraut, *X-ray standing waves at a reflecting mirror surface.* Phys. Rev. Lett., 1989. **62**(12): p. 1376-1379.

87.   Templeton, A.S., T.P. Trainor, S.J. Traina, A.M. Spormann, and G.E. Brown, Jr., *Pb(II) distributions at biofilm-metal oxide interfaces.* Proc. Nat. Acad. Sc., 2001. **98**(21): p. 11897-11902.

88.   Zhang, Z., P. Fenter, L. Cheng, N.C. Sturchio, M.J. Bedzyk, M.L. Machesky, and D.J. Wesolowski, *Model-independent X-ray imaging of adsorbed cations at the crystal-water interface.* Surf. Sci., 2004. **554**: p. L95-L100.

89.   Bolzan, A.A., C. Fong, B.J. Kennedy, and C.J. Howard, *Structural studies of rutile-type metal dioxides.* Acta Cryst. , 1997. **B53**: p. 373-380.

90.   Fenter, P., L. Cheng, C. Park, Z. Zhang, and N.C. Sturchio, *Structure of orthoclase (001)- and (010)-water interfaces by high-resolution x-ray reflectivity.* Geochim. Cosmochim. Acta, 2003. **67**(22): p. 4267-4275.

91.   Park, C., P. Fenter, N.C. Sturchio, and K.L. Nagy, *Thermodynamics, interfacial structure, and pH hysteresis of Rb+ and Sr2+ adsorption at the muscovite (001) - solution interface.* Langmuir, 2008. **24**: p. 13993.

92.   Kohli, V., Z. Zhang, C. Park, and P. Fenter, *Rb+ and Sr2+ adsorption at the TiO2 (110) - water interface studied using resonant anomalous x-ray reflectivity.* Langmuir, in press, 2009.

93.   Bedzyk, M.J. and G. Materlik, *2-Beam Dynamical Diffraction Solution of the Phase Problem - a Determination with X-Ray Standing-Wave Fields.* Physical Review B, 1985. **32**(10): p. 6456-6463.

94.   Hertel, N., G. Materlik, and J. Zegenhagen, *X-ray standing wave analysis of bismuth implanted Si(110).* Z. Phys. B - Cond. Matt., 1985. **58**: p. 199-204.

95.   Cheng, L., P. Fenter, M.J. Bedzyk, and N.C. Sturchio, *Fourier-expansion solution of atom distributions in a crystal using x-ray standing waves.* Phys. Rev. Lett., 2003. **90**(25): p. 255503-1.

96.   Escuadro, A.A., D.M. Goodner, J.S. Okasinski, and M.J. Bedzyk, *X-ray standing wave analysis of the Sn/Si(111) surface.* Phys. Rev. B, 2004. **70**: p. 235416.

97.   Kim, C.-Y., J.W. Elam, M.J. Pellin, D.K. Goswami, S.T. Christensen, M.C. Hersam, P.C. Stair, and M.J. Bedzyk, *Imaging of atomic layer deposited (ALD) tungsten monolayers on alpha-TiO2 (110) by x-ray standing wave fourier inversion.* J. Phys. Chem. B, 2006. **110**: p. 12616-12620.

98. Lin, J.C., J.A. Kellar, J.H. Kim, N.L. Yoder, K.H. Bevan, S.T. Nguyen, M.C. Hersam, and M.J. Bedzyk, *Atomic-scale X-ray structural analysis of self-assembled monolayers on Silicon.* European Physical Journal-Special Topics, 2009. **167**: p. 33-39.

99. Bedzyk, M.J., *XSW at the total reflection condition*, in *arXiv:0908.2115v1   The x-ray standing wave technique: principles and applications*, J. Zegenhagen and A. Kazimirov, Editors. in press, 2009.

100. Leskela, M. and M. Ritala, *Atomic layer deposition chemistry: Recent developments and future challenges.* Angew. Chem. - Int. Ed. , 2003. **42**(45): p. 5548.

101. Boer, D.K.G.d., *Glancing incidence x-ray fluorescence of layered materials.* Phys. Rev. B, 1991. **44**(2): p. 498-511.

102. Ghose, S.K. and B.N. Dev, *X-ray standing wave and reflectometric characterization of multilayer structures.* Phys. Rev. B, 2001. **63**: p. 245409-1-11.

103. Libera, J.A., PhD Thesis, Northwestern University, 2005.

104. Batterman, B.W. and H. Cole, *Dynamical diffraction of x-rays by perfect crystals.* Rev. Mod. Phys., 1964. **36**: p. 681-717.

105. Dash, R., J. Chmiola, G. Yushin, Y. Gogotsi, G. Laudisio, J. Singer, J. Fischer, and S. Kucheyev, *Titanium carbide derived nanoporous carbon for energy-related applications.* Carbon, 2006. **44**: p. 2489.

106. Janes, A., L. Permann, M. Arulepp, and E. Lust, *Electrochemical characteristics of nanoporous carbide-derived carbon materials in non-aqueous electrolyte solutions.* Electrochem. Comm., 2004. **6**: p. 313.

107.   Sarangapani, S., B.V. Tilak, and C.-P.Chen, *Materials for electrochemical capacitors, theoretical and experimental constraints.* J. Electrochem. Soc., 1996. **143**(11): p. 3791.

108.   Pandolfo, A.G. and A.F. Hollenkamp, *Carbon properties and their role in supercapacitors.* J. Pow. Sour., 2006. **157**: p. 11-27.

109.   Chmiola, J., C. Largeot, P.-L. Taberna, P. Simon, and Y. Gogotsi, *Desolvation of ions in subnanometer pores and its effect on capacitance and double-layer theory.* Angew. Chem. Int. Ed., 2008. **47**: p. 3392.

110.   Burke, A., *Ultracapacitors: why, how and where is the technology.* J. Pow. Sour., 2000. **91**: p. 37-50.

111.   Conway, B.E., V. Birss, and J. Wojtowicz, *The role and utilization of pseudocapacitance for energy storage by supercapacitors.* J. Pow. Sour., 1997. **66**: p. 1-14.

112.   Toupin, M., T. Brousse, and D. Belanger, *Charge storage mechanism of MnO2 electrode used in aqueous electrochemical capacitor.* Chem. Mater., 2004. **16**: p. 3184-3190.

113.   Pang, S.-C., M.A. Anderson, and T.W. Chapman, *Novel electrode materials for thin-film ultracapacitors: comparison of electrochemical properties of sol-gel-derived and electrodeposited manganese dioxide.* J. Electrochem. Soc., 2000. **147**(2): p. 444.

114.   Arico, A.S., P. Bruce, B. Scrosati, J.-M. Tarascon, and W.V. Schalkwijk, *Nanostructured materials for advanced energy conversion and storage devices.* Nature Mat., 2005. **4**: p. 366.

115.   Chmiola, J., G. Yushin, Y. Gogotsi, C. Portet, P. Simon, and P.-L. Taberna, *Anomalous increase in carbon capacitance at pore sizes less than 1 nanometer.* Science, 2006. **313**: p. 1760.

116.   Towle, S.N., G.E. Brown, Jr., and G.A. Parks, *Sorption of Co(II) on Metal Oxide Surfaces.* J. Coll. & Int. Sc., 199. **217**: p. 299-311.

117.   Kohli, V., M.J. Bedzyk, and P. Fenter, *A direct-method for imaging elemental distribution profiles with long-period x-ray standing waves.* submitted to Phys. Rev. B, 2009.

118.   Kohli, V., J.K. Rosenqvist, J.A. Libera, J.W. Elam, C. Liu, M.J. Bedzyk, M.L. Machesky, D.J. Wesolowski, and P. Fenter, *Enhanced ion adsorption at the nanotitania-aqueous electrolyte interface.* in preparation, 2009.

119.   Diaz, A.D., *X-ray scattering studies of ordering phenomena in colloids confined in microcavity arrays.* PhD Thesis, ETH Zurich, 2006.

120.   Diaz, A.D. and J.F.v.d. Veen, *Theory of x-ray scattering from a complex fluid confined by a nanocavity array.* Thin Solid Films, 2007. **515**: p. 5645-5653.

121.   Diaz, A.D., C. David, H. Guo, H. Keymeulen, F. Pfeiffer, G. Wegdam, T. Weitkamp, and J.F.v.d. Veen, *Microcavity arrays for x-ray diffraction studies of ordering phenomena in confined colloid solutions.* Physica B, 2005. **357**: p. 199-203.

122.   Bedzyk, M.J., D.H. Bilderback, G.M. Bommarito, M. Caffrey, and J.S. Schildkraut, *X-ray standing waves: a molecular yardstick for biological membranes.* Science, 1988. **241**: p. 1788-1791.

123.   Bedzyk, M.J., *XSW at the total reflection condition*, in *The x-ray standing wave technique: principles and applications*, J. Zegenhagen and A. Kazimirov, Editors. in press, 2009.

APPENDIX A: MATLAB Programs for Model Independent Analysis of Long-Period X-ray Standing Waves Data

A.1 Introduction

A novel model-independent approach of analyzing long-period X-ray standing waves (XSW) data was described in Chapter 4. This approach allowed direct imaging of 1D elemental profile from the measured XSW data. The analysis procedure involved dividing the measured fluorescence yield vs. momentum transfer into segments of width ΔQ, and extracting an amplitude and a phase of the elemental structure factor from each segment. This allowed a direct reconstruction of the 1D elemental distribution using Fourier inversion of the derived amplitudes and phases. This concept was actualized using a set of programs written in MATLAB that aimed at performing the model-independent fitting of the measured XSW data that was necessary in order to recover the elemental profile. The programs can be used for the analysis of both *ex situ* and *in situ* XSW data, following the procedure described in Chapter 4. This appendix provides an overview of the software package, the steps required in the model-independent XSW analysis, and a documentation of the individual programs. The code was written in M-files, whose names carry a .m extension. The function names are represented in bold italicized font throughout this appendix.

A.2 List of Primary Functions

mimain: Main program that manages the model independent analysis of fluorescence yield data, including seeking input from M-files, calling execution functions, plotting the results and writing the output to files.

getmiinput1: Obtains input from user regarding various fitting options, and retrieves the reflectivity and fluorescence yield data from the specified files.

getmifitpara: Retrives the model independent fit parameters from the specified input file.

reduce_fitpara: Retrieves amplitudes, phases, and their gradients while sifting through the fit parameters.

yldmicalc: Calculates the model-independent fluorescence yield from the inputted reflectivity and phase of reflectivity coefficient, and the amplitude and phase of elemental structure factor, according to the formalism described in Chapter 4.

yldmifit: Activates during every fit iteration to convert the fit parameters to the input format necessary for the calculation of model independent yield through ***yldmicalc***. Also applies any correction factors (e.g. scale factor) needed to be applied to the calculation rendering the calculation to be comparable to the data.

calcROIFT: Obtains the 1D elemental profile from inputted amplitudes and phases of elemental structure factor through an inverse Fourier transform.

processAP: Obtains expanded amplitudes and phases from the amplitude, phase, and gradient parameters used in the fit. Obtains the 1D elemental profile through ***calcROIFT***.

A.3 Steps in Model Independent XSW Analysis

The first step involves setting up the input parameters required for the analysis in the M-file ***getmiinput.m***. The model independent XSW analysis requires two input data files. The first is the file containing the fluorescence yield data, which should have 3 columns of data corresponding to momentum transfer, fluorescence yield and uncertainty in the fluorescence yield. The second is the reflectivity file, also having 3 columns, containing momentum transfer, reflectivity, and phase of reflectivity coefficient, which are model calculated based on the reflectivity analysis. For the case of *in situ* data (for e.g., when the elemental distribution is located inside an aqueous medium), the momentum transfer specified in the reflectivity file should be the one inside the medium (while the momentum transfer in the fluorescence yield data file should be that in air). The directory and names of the two input files should be specified in ***getmiinput.m***. The momentum transfer range of data to be included in the analysis can be specified in the variable *trm_range*. The model independent analysis divides the data into separate segments to extract an amplitude and a phase of the elemental structure factor from each segment. The segment width (in Å^{-1}) can be specified in the variable *winwidth*. Additional input needed in *getmiinput.m* includes options specified as 'y' or 'n' for whether an angular averaging needs to be applied to the data (stored in *angle_avg*), whether separate scale factors be used for individual segments of the data during the fitting (stored in *scale_sep*), whether momentum transfer specified in the reflectivity file is that inside a non-vacuum medium (stored in *q_internal*), whether an attenuation correction needs to be included corresponding to the simple amplitude attenuation of the beam for *in situ* data (stored in *amp_correction*).

The next step involves setting up the fitting parameters in the ***fitparami.m*** M-file. The location of the ***fitparami.m*** file should be specified in ***getmifitpara.m***. Below is a sample of the parameters that can be used for the model independent fitting (stored in variable *parainfo*):

```
parainfo={...% Parameter name, initial value, initial fractional change, fractional precision, maximum fractional change
           'Scale'     1.00        0.01         0.001            1;  %scale factor
           'A'         0.90        0.01         0.001            1;  %amplitude
           'P'         0.1         0.01         0.001            1;  %phase (in units of 2π)
           'Agrad'     0           0.00         0.001            1;  %amplitude gradient
           'Pgrad'     0           0.00         0.001            1;  %phase gradient
           'avg1'      0.01        0.01         0.001            1;  %angle averaging para1
           'avg2'      0.000       0.00         0.001            1;  %ang avg para2 (not used)
           'twat_mcr'  10          0.01         0.001            1; %Water+Kapton thickness in µ
           'Q_off'     0.000       0.00         0.001            1;}; %Q-offset (not used)
```

Here, the first column of information stored in variable *parainfo* is a label of the fit parameter name, the second is the initial value of the parameter at the beginning of the fitting, third is the initial fractional change in the parameter, fourth is the fractional precision in the parameter, and fifth is the maximum fractional change allowed in the parameter in any fit iteration. *Scale* is the parameter denoting the scale factor used in comparison between the data and the calculation. *A*, *P*, *Agrad*, and *Pgrad* denote respectively the amplitude, phase, gradient in amplitude, and gradient in phase of the elemental structure factor. The initial values specified to *A*, *P*, *Agrad* and *Pgrad* are simultaneously assigned to each of the Q-segments into which the data is divided for the model independent analysis during the first iteration (for e.g., if the data is divided into 5 segments, then *A*, *P*, *Agrad* and *Pgrad* would set the initial values of 20 fitting parameters). In subsequent iterations, however, each segment is allowed to have its separate value of *A*, *P*, *Agrad* and *Pgrad*, as guided by the fit. The variable *twat_mcr* is specific to the *in situ* data fitting, and corresponds to a water-equivalent thickness of the aqueous and Kapton layers.

Once the input parameters and the fitting parameters have been set, the fitting process can be initiated by executing the *mimain* function. Additional plotting and output options may be specified within the *mimain* function (for e.g., whether to hold the plot for multiple data plotting, plot color, etc.). The routine performs fitting of each segment of the fluorescence yield data to extract an amplitude and a phase from each segment. The 1D elemental profile is obtained by calling *processAP*. The *mimain* function then plots the results including the fluorescence yield data and model independent fit based calculation, the amplitudes and phases of elemental structure factor vs. Q, and the recovered elemental 1D profile.

A.4 Documentation of Primary Functions

```
function [] = mimain ()

%%% INPUT
fit_option=1; %1 for fitting, 0 for calculation
mainfig=1;
Z=[-100:0.1:100]; %for density profile calculation
plot_col='k';
plot_hold=0;
ele='Ti';
cmmnt='';
plot_yoff=0; %y-offset in yield plot
%%% End of user input

%%% Initializations
qbegin_Dq=[]; miscinfo1={};
global Dq DR Dnu
global qair Dqair qmid_Dqair qmid_Dq scale_sep amp_corr_load angle_avg
%%% Retrieve additional input, from getmiinput.m
[q,Y,Yeb,Dq,DR,Dnu,nWin,W,miscinfo1] = getmiinput1();
for j=1:nWin, qbegin_Dq(j)=Dq{j}(1); end
for j=1:nWin, qmid_Dq(j)=mean(Dq{j}); end
for j=1:nWin, qmid_Dqair(j)=mean(Dqair{j}); end
```

```
%% Calculation
if fit_option==0
    % Retrieve A, P, Agrad, Pgrad for calculation
    [A,P,Agrad,Pgrad]=getAPmodel(qbegin_Dq);
    % Call yldmicalc and calculate DYmi
    [DYmi]=yldmicalc (Dq, DR, Dnu, A, P, Agrad, Pgrad);
    % Call Coalescer to get Ymi
    [Ymi]=Coalescer(DYmi);
else
    iter=0; x=q; y=Y; yeb=Yeb; wt=1./yeb;
    [pin,func,stol,niter,dpin,dfdp,options,parainfo_exp] = getmifitpara (nWin);
    if ~any(dpin),
        f=feval(func,q,pin); pout=pin; stdev=zeros(size(pout));
    else
        [f, pout, stdev, kvg, iter, corp, covp, covr, stdresid, Ztmp, r2]=leasqrpf(x, y, pin, func, stol,
niter, wt, dpin, dfdp, options);
    end
    Ymi=f;
    [chi2_1,r_1]=fitresults_dsp(parainfo_exp,pout,stdev,iter,niter,x,y,yeb,f,dpin);
    [A,P,Agrad,Pgrad,scale,aavg,twat,tmp4]=reduce_fitpara(pout,nWin);

[Aeb,Peb,Agrad_eb,Pgrad_eb,scale_eb,aavg_eb,twat_eb,tmp4_eb]=reduce_fitpara(stdev,nWin);
end
%% Obtain density profile
[Arel,Prel,qrel,RO] = processAP (Z,A,P,Agrad,Pgrad,Dq,qbegin_Dq,fit_option);


%% PLOTTING THE RESULTS
qtmp=q; q=qair; %for plotting purposes
plt_x=qtmp; %qtmp or q
plotsize=[3,4]; pa=plotsize(1); pb=plotsize(2);
figure(mainfig);
pc=plot_col; ph=plot_hold;
miscinfo2={interpret_color(pc),ele,cmmnt};


%% Plot#1: Calc & Data
subplot(pa,pb,[1,2]); if ph, hold on; end
if ph, h1=gca; h2=get(h1,'Title'); TMP0=get(h2,'UserData');  else h1=[]; h2=[]; TMP0=[]; end
errorbar(plt_x,Y+plot_yoff,Yeb,[pc,'o']);
hold on;
plot(plt_x,Ymi+plot_yoff,[pc,'-']);
hold off;
xlabel('Q_a_i_r(A^\circ^-^1)'); ylabel('Fluo. yield (data & calc)'); axis tight;
if plt_x==qtmp, xlabel('Q_i_n_t(A^\circ^-^1)'); end
```

```matlab
chi2_tmp=round(chi2_1*10)/10; tmp1=10^4;tmp2=10^5;
if round(r_1*10^4)/10^4, tmp=tmp1; else tmp=tmp2; end
r_tmp=round(r_1*tmp)/tmp;
twat_tmp=round(twat*10)/10;
aavg_tmp=round(aavg(1)*1000)/1000;
VALSTR1={num2str(aavg_tmp),num2str(twat_tmp),num2str(chi2_tmp),num2str(r_tmp)};
TMP1=miscinfo2;
if ~ph, h1=gca; h2=get(h1,'Title'); end
if ph
   VALSTR0=get(h1,'UserData'); for j=1:length(VALSTR1),
VALSTR1{j}=[VALSTR0{j},',',VALSTR1{j}]; end
   for j=1:length(TMP1),
      if ~isempty(TMP0{j}), TMP1{j}=[TMP0{j},',',TMP1{j}]; end
   end
end
set(h1,'UserData',VALSTR1); set(h2,'UserData',TMP1);
if amp_corr_load=='n', tmpstr1=[',twat=',VALSTR1{2},'\mu']; else tmpstr1=''; end
if angle_avg=='y', tmpstr2=[',aavg=',VALSTR1{1},'A^\circ^-^1']; else tmpstr2=''; end
tmpstr3=[',\chi^2=',VALSTR1{3},',R^2=',VALSTR1{4}];
X{1}=[TMP1{1},':',TMP1{2},',Misc:',TMP1{3}];
X{2}=['Qint=',miscinfo1{1},',Ampcorr=',miscinfo1{2},',Ampcorr
load=',miscinfo1{5},',Aavg=',miscinfo1{3},',Scale sep=',miscinfo1{4}];
X{2}=[X{2},tmpstr1,tmpstr2,tmpstr3];
set(h2,'String',X); set(h2,'Fontsize',12);
set(h2,'Units','Normalized'); tmp1=get(h2,'Position'); tmp1(1)=-.2;
set(h2,'HorizontalAlignment','Left','Position',tmp1);
v=axis;
for j=1:length(W), line([W{j}(1) W{j}(1)],[v(3),v(4)],'Linewidth',.5,'Color',pc,'Linestyle',':'); end

%%% Plot#2: A vs. Q
subplot(pa,pb,[5,6]); if ph, hold on; end
plot(plt_x,Arel,[pc,'.-']); xlabel('Q_a_i_r(A^\circ^-^1)'); ylabel('A'); xlim([v(1) v(2)]);
vtmp=axis; ylim([0 max(vtmp(4),1)]); vtmp=axis;
for j=1:length(W), line([W{j}(1)
W{j}(1)],[vtmp(3),vtmp(4)],'Linewidth',.5,'Color',pc,'Linestyle',':'); end
if plt_x==qtmp, xlabel('Q_i_n_t(A^\circ^-^1)'); end

%%% Plot#3: P vs. Q
subplot(pa,pb,[9,10]); if ph, hold on; end
plot(plt_x,angle(exp(i*2*pi*Prel))/(2*pi),[pc,'.-']); %plot(plt_x,Prel,[pc,'.-']);
xlabel('Q_a_i_r(A^\circ^-^1)'); ylabel('P (radians)'); xlim([v(1) v(2)]); vtmp=axis;
ylim([min(vtmp(3),0) max(vtmp(4),0)]); vtmp=axis;
for j=1:length(W), line([W{j}(1)
W{j}(1)],[vtmp(3),vtmp(4)],'Linewidth',.5,'Color',pc,'Linestyle',':'); end
```

```
if plt_x==qtmp, xlabel('Q_i_n_t(A^\circ^-^1)'); end
```

%% Plot#4: Density profile
```
subplot(pa,pb,11); if ph, hold on; end
if ph, tmpinfo0=get(gca,'UserData');  else tmpinfo0=[]; end
plot(Z,RO,[pc,'-']);
xlabel('distance(A^\circ)'); ylabel('Electron density(e^-/A^\circ^3)');
if any(RO), location_tmp=round(10*Z(find(RO==max(RO))))/10; else location_tmp=0; end
tmpstr1=num2str(location_tmp); if location_tmp>=0, tmpstr2='Above'; else tmpstr2='Below';
end
tmpinfo1=tmpstr1; if ph, tmpinfo1=[tmpinfo0,',',tmpinfo1]; end
set(gca,'Userdata',tmpinfo1);
title([tmpstr2,' surf: ',tmpinfo1,' A^\circ'],'Fontsize',12);
vtmp=axis; line([location_tmp location_tmp],[vtmp(3)
vtmp(4)],'Color',pc,'Linestyle',':','Linewidth',.5);
```

%% Plot#5: A vs Q (discrete)
```
subplot(pa,pb,[3,4]); if ph, hold on; end
errorbar(qmid_Dqair,A,Aeb,[pc,'o--']); xlabel('Q_a_i_r(A^\circ^-^1)'); ylabel('A'); axis tight;
v=axis; xlim([0 v(2)]);vtmp=axis; ylim([0 max(vtmp(4),1)]);
vtmp=axis; for j=1:length(W), line([W{j}(1)
W{j}(1)],[vtmp(3),vtmp(4)],'Linewidth',.5,'Color',pc,'Linestyle',':'); end
```

%% Plot#6: P vs. Q (discrete)
```
subplot(pa,pb,[7,8]); if ph, hold on; end
Ptmp=angle(exp(1i*2*pi*P))/(2*pi); Pebtmp=(Peb./P).*Ptmp;
errorbar(qmid_Dqair,Ptmp,Pebtmp,[pc,'o--']);%ensure P between -.5 and .5 and in units of 2pi.
xtmp=[0:10^-5:qbegin_Dq(1)]; ytmp=xtmp*(P(1)/qmid_Dqair(1)); hold on;
plot(xtmp,ytmp,[pc,':']); hold off;
xlabel('Q_a_i_r(A^\circ^-^1)'); ylabel('P (radians)'); xlim([0 v(2)]);vtmp=axis;
ylim([min(vtmp(3),0) max(vtmp(4),0)]);
vtmp=axis; for j=1:length(W), line([W{j}(1)
W{j}(1)],[vtmp(3),vtmp(4)],'Linewidth',.5,'Color',pc,'Linestyle',':'); end
```

%% Plot#7: Scale factor variability
```
subplot(pa,pb,12); if ph, hold on; end
if length(scale)==1, scale_tmp=repmat(scale,length(qbegin_Dq),1);
scale_tmp_eb=repmat(scale_eb,length(qbegin_Dq),1); else scale_tmp=scale;
scale_tmp_eb=scale_eb; end
plot(qbegin_Dq,scale_tmp,[pc,'.-']); errorbar(qbegin_Dq,scale_tmp,scale_tmp_eb,[pc,'o--']);
xlabel('Q_a_i_r(A^\circ^-^1)'); ylabel('Scale'); xlim([v(1) v(2)]);vtmp=axis; ylim([0.8*vtmp(3)
1.2*vtmp(4)]);
if scale_sep=='y', tmpstr1=[num2str(round((max(scale_tmp)-
min(scale_tmp))/mean(scale_tmp)*100)),' %']; else tmpstr1='n/a'; end
```

```matlab
title(['Scale, variability: ',tmpstr1],'Fontsize',12);

%%% Save results to file
%Density profile
dense_file='dense';
fid=fopen(dense_file,'w');
fprintf(fid,['%%',datestr(now, 'mmm dd, yyyy HH:MM:SS AM'),'\n']);
fprintf(fid,'%%Distance from surface    Density profile\n');
fprintf(fid,'%6.4f     %6.4f\n',[Z',RO']');
fclose(fid);
```

function [q,Y,Yeb,Dq,DR,Dnu,nWin,W,miscinfo1] = getmiinput1()

```matlab
%%% USER INPUT
%%% Initialization
global AMP_CORR amp_correction amp_corr_load angle_avg qair Dqair
global scale_sep
%%% File information, & other input
fdir='C:\Documents and Settings\...\mi\'; %Enter directory of XSW & reflectivity data files
q_internal='y';
amp_correction='y';
angle_avg='y';
scale_sep='n';
amp_corr_load='n'; %whether to load from file or to calculate
miscinfo1={q_internal;amp_correction;angle_avg;scale_sep;amp_corr_load};
%%% Input window size
winwidth=0.01;
trm=1;
trm_range=[0.01,.15];  %used to look at the data only in this range.
%%% File names
Ydata_fname='Y_1'; Rnu_fname='Rnu_1';
ampcor_fname='Fact_1';
%%% End of user input

%%% Input Y and Yeb vs. Q data
Ydata=load([fdir,Ydata_fname]);
q=Ydata(:,1); Y=Ydata(:,2); Yeb=Ydata(:,3);
qair=q; %assumes that the first column in the data file is qair
%%% Input R and nu vs Q
Rnu=load([fdir,Rnu_fname]);
if q_internal=='y', q=Rnu(:,1); end
R=Rnu(:,2); nu=Rnu(:,3);
%%% trim the vectors, if trim option is chosen
```

```matlab
if trm
    trm_indx=find(q>=trm_range(1) & q<=trm_range(2));
    q=q(trm_indx); Y=Y(trm_indx); Yeb=Yeb(trm_indx); R=R(trm_indx); nu=nu(trm_indx);
    qair=qair(trm_indx); end
%% Amp correction, apply to data or calculation
if amp_correction=='y' && amp_corr_load=='y',
    AMP_CORR=load([fdir,ampcor_fname]); if trm, AMP_CORR=AMP_CORR(trm_indx); end
end
%% Generate Divided vectors
W=Wcreator(q,winwidth);
[Dq,DR,Dnu,Dqair]=Divider(q,W,R,nu,qair);
nWin=length(Dq);
```

function [pin,func,stol,niter,dpin,dfdp,options,parainfo_exp] = getmifitpara (nWin)

```matlab
filedir='C:\Documents and Settings\...\'; %%directory of M-file that has fitting parameters
filename='fitparami'; %%name of M-file that has the fitting parameters
addpath(filedir);
eval(filename);
rmpath(filedir);
%% Calculation
%% parainfo expanded
[parainfo_exp] = expand_parainfo(parainfo,nWin);
%% INITIAL PARA OVERWRITE OPTION
inipara_load='n'; %% load initial parameters from an paraout file
inipara_dir='C:\Documents and Settings\...\';
inipara_file='paraout1';
if inipara_load=='y', tmp=read_paraout([inipara_dir,inipara_file]);
parainfo_exp(1:end,2)=tmp(1:end,4); end
%% end INI PARA OVERWRITE OPTION
pin=cell2mat(parainfo_exp(:,2)); dpin=cell2mat(parainfo_exp(:,3));
options=cell2mat(parainfo_exp(:,4:5));
```

function [A,P,Agrad,Pgrad,scale,aavg,twater,Q_off] = reduce_fitpara (p,nWin)

```matlab
if scale_sep=='y', scale=p(1:nWin); begin_rel=nWin+1; else scale=p(1); begin_rel=2; end
tmp=begin_rel-1;
A=p(tmp+1:tmp+nWin);
P=p(tmp+nWin+1:tmp+2*nWin);
Agrad=p(tmp+2*nWin+1:tmp+3*nWin);
Pgrad=p(tmp+3*nWin+1:tmp+4*nWin);
```

```
aavg=[p(tmp+4*nWin+1),p(tmp+4*nWin+2)];
twater=p(tmp+4*nWin+3);
Q_off=p(tmp+4*nWin+4);
```

function [DYmi] = yldmicalc (Dq, DR, Dnu, A, P, Agrad, Pgrad)

```
for j=1:length(Dq)

DYmi{j}=1+DR{j}+...
        2*sqrt(DR{j}) .* (A(j)+Agrad(j)*(Dq{j}-mean(Dq{j})))  .*
cos(Dnu{j}+2*pi*(P(j)+Pgrad(j)*(Dq{j}-mean(Dq{j})))));

end
```

function [Ymi] = yldmifit (q,p)

```
global Dq DR Dnu
global AMP_CORR amp_correction amp_corr_load angle_avg qair
global scale_sep
%% Calculation
nWin=length(Dq);
[A,P,Agrad,Pgrad,scale,aavg,twater,Q_off] = reduce_fitpara (p,nWin);
%% Apply any Q-offset (This option not used currently)
for j=1:length(Dq), Dq{j}=Dq{j}+Q_off; end
q=q+Q_off; qair=qair+Q_off/1.035; %% Note the exact conversion between Qair and Qoff will
depend on the density of water layer (Q-offset feature not used currently)
%% end apply offset
[DYmi] = yldmicalc (Dq, DR, Dnu, A, P, Agrad, Pgrad);
[Ymi]=Coalescer(DYmi);

if amp_correction=='y',
   if amp_corr_load~='y', AMP_CORR=attenhalf_calc(17,9402,q,twater); end % this line not
intended for generalized usage, 9402 microns is attenuation length through water at 17keV
   Ymi=Ymi.*AMP_CORR';
end
if angle_avg=='y', Ymi=angavg(qair,Ymi',aavg(1),aavg(2)); end
if scale_sep=='y'
   for j=1:nWin, Dscale{j}=repmat(scale(j),length(Dq{j}),1); end
   scale=Coalescer(Dscale);
end
Ymi=Ymi.*scale; %scale could be single entry or array depending on scale_sep
Ymi=Ymi';
```

```matlab
function [RO]=calcROIFT(Z,A,P,q)
delq=q(2:end)-q(1:end-1);
if size(q)~=size(A(1:end-1)), q=q.'; delq=delq.'; end
for j=1:length(Z)
    RO(j)=(0.5/pi) * sum(A(1:end-1) .* exp(i*2*pi*P(1:end-1)) .* exp(-i*q(1:end-1)*Z(j)) .* delq);
end
RO=real(RO);


function [Arel,Prel,qrel,RO] = processAP (Z,A,P,Agrad,Pgrad,Dq,qbegin_Dq,fit_option)
global qair Dqair qmid_Dqair qmid_Dq
nWin=length(Dq);
if ~any(Agrad) && ~any(Pgrad) && ~fit_option %%~fit_option to exclude the case where fit final parameter gave gradient terms=0
    Arel=A; Prel=P; qrel=qbegin_Dq;
else
    for j=1:nWin
        DAfull{j}=A(j)+Agrad(j)*(Dq{j}-mean(Dq{j}));
        DPfull{j}=P(j)+Pgrad(j)*(Dq{j}-mean(Dq{j}));
    end
    Arel=Coalescer(DAfull); Prel=Coalescer(DPfull); qrel=Coalescer(Dq);
end
if ~any(Pgrad) && ~any(Agrad), RO=calcROIFT(Z,A,P,qmid_Dq');
else        RO=calcROIFT(Z,Arel,Prel,q');
end
```

%% Sample fit parameter M-file: mifitpara.m

```matlab
func='yldmifit';
dfdp  = 'dfdppf';
stol  = .01;
niter  = 200;
 parainfo={...% Parameter name  %Initial value   %Initial frac. change     %Frac. precision  %Max frac. change
        'Scale'      1.00       0.01          0.001               1;   %scale factor
        'A'          0.90       0.01          0.001              .5;   %amplitude
        'P'         -0.1        0.01          0.001               5;   %phase
        'Agrad'       0         0.00          0.001               1;   %amplitude gradient
        'Pgrad'       0         0.00          0.001              1; %phase gradient
        'avg1'       0.036      0.05          0.001              5;%ang avg para1
        'avg2'       0.000      0.00          0.001              5;%ang avg para2
        'twat_mcr'    10        0.01          0.001              5;%Water+Kapton thickness (µ)
        'Q_off'      0.000      0.00          0.001              5;};%Qoffset(internal if int=='y')
```

function [W] = Wcreator (x,winwidth)

```
%% Calculation
winstart=x(1); winend=x(end)+(x(end)-x(end-1));
win_temp=[winstart:winwidth:winend];
if win_temp(end)<winend, win_temp(end+1)=win_temp(end)+winwidth; end

nwin=floor((x(end)-x(1))/winwidth);
for j=1:nwin
   W{j}=[win_temp(j),win_temp(j+1)];
   if j==nwin, W{j}(2)=win_temp(end); end
end
```

function [x] = Coalescer (Dx)

```
aindx=1;%%available index
for j=1:length(Dx)
   ntmp=length(Dx{j});
   x(aindx:aindx+ntmp-1)=Dx{j};
   aindx=aindx+ntmp;
end
```

function [Dx,varargout] = Divider (x, W, varargin)

```
for j=1:length(W)
   ind=find((x>=W{j}(1) & x<W{j}(2)));
   Dx{j}=x(ind);
   for k=1:nargin-2
      varargout{k}{j}=varargin{k}(ind);
   end
end
```